



City Research Online

City, University of London Institutional Repository

Citation: Filippaki, Evangelia (2015). Glistenings in Intraocular lenses and their effect on forward light scatter; an in vitro study. (Unpublished Doctoral thesis, City University London)

This is the accepted version of the paper.

This version of the publication may differ from the final published version.

Permanent repository link: <https://openaccess.city.ac.uk/id/eprint/13594/>

Link to published version:

Copyright: City Research Online aims to make research outputs of City, University of London available to a wider audience. Copyright and Moral Rights remain with the author(s) and/or copyright holders. URLs from City Research Online may be freely distributed and linked to.

Reuse: Copies of full items can be used for personal research or study, educational, or not-for-profit purposes without prior permission or charge. Provided that the authors, title and full bibliographic details are credited, a hyperlink and/or URL is given for the original metadata page and the content is not changed in any way.



CITY UNIVERSITY
LONDON

“Glistenings in Intraocular lenses and their effect on forward light
scatter; an in vitro study”

A Thesis submitted by

Evangelia Filippaki

For the degree of

Doctor of Philosophy

2015

Applied Vision Research Centre
School of Health Sciences
City University London

GLISTENINGS IN INTRAOCULAR LENSES AND THEIR EFFECT ON
FORWARD LIGHT SCATTER; AN IN VITRO STUDY.

First Submission: April 17th, 2015

Viva Examination: July 15th, 2015

Final Submission: September 7th, 2015

Supervised by:

Chris C. Hull

Professor of Optics of Vision

Divisional Lead for Optometry and Visual Science

City University London

Members of the examination committee:

David O'Brart

Consultant Ophthalmic Surgeon

St Thomas' Hospital, London

John Barbur

Professor of Optics and Visual Science

City University London

“neither leaves nor fruits in the absence of roots”

— Ψαραντώνης

To Renia and Theo

Table of Contents

| | |
|--|-----------|
| 1. Introduction | 27 |
| 2. Literature Review | 29 |
| 2.1 Scatter in the human eye | 29 |
| 2.2 The Glare Spread Function | 31 |
| 2.3 Impact of pupil size on light scatter | 33 |
| 2.4 Measurement of forward light scatter | 34 |
| 2.4.1 Optical Methods | 34 |
| 2.4.1.1 Detecting the angular distribution of scattered light with a photomultiplier..... | 34 |
| 2.4.1.2 Narrow-angle forward light scatter | 35 |
| 2.4.1.3 Ballistic-photon Removing Integrating-sphere Method | 37 |
| 2.4.1.4 Measurement of intraocular light scatter with a Hartmann-Shack sensor..... | 38 |
| 2.4.2 Psychophysical Methods..... | 39 |
| 2.4.2.1 Conventional Threshold Method | 40 |
| 2.4.2.2 Direct Compensation | 40 |
| 2.4.2.3 Flicker cancellation | 41 |
| 2.4.2.4 Compensation Comparison..... | 41 |
| 2.5 Glistenings in IOLs and their effect on vision..... | 42 |
| 3. Methodology | 45 |
| 3.1 Experimental set-up | 45 |
| 3.2 IOL Preparation | 49 |
| 3.3 Procedure..... | 51 |
| 3.4 Repeatability and reproducibility..... | 53 |
| 3.5 Imaging and Quantifying Glistenings..... | 57 |
| 3.5.1 Imaging Methods..... | 57 |
| 3.5.2 Slit-lamp Digital Image capture and analysis | 59 |

| | |
|---|-----------|
| 4. Association between forward light scatter and subjective grading of IOL Glistenings | 63 |
| 4.1 Introduction..... | 63 |
| 4.1.1 Clinical IOL Glistenings Grading..... | 63 |
| 4.1.2 Point Spread Function and Forward Light Scatter | 65 |
| 4.2 Methods..... | 66 |
| 4.2.1 Procedure | 66 |
| 4.2.2 Data Analysis | 67 |
| 4.3 Results..... | 70 |
| 4.3.1 Volume under PSF's skirt (VUSF) | 70 |
| 4.3.2 PSF angular distribution..... | 71 |
| 4.3.3 Scatter index n | 73 |
| 4.3.3.1 Large angle domain..... | 73 |
| 4.3.3.2 Small angle domain..... | 75 |
| 4.3.4 Straylight Parameter – log(s)..... | 76 |
| 4.4 Discussion..... | 78 |
| | |
| 5. Objective Quantification of Glistenings by Digital Image Processing.... | 81 |
| | |
| 5.1 Introduction | 81 |
| 5.2 Description of Software | 83 |
| 5.3 Software Validation Metrics..... | 87 |
| 5.4 Ground truth images..... | 93 |
| 5.5 Reproducibility of setting the Area of Interest | 95 |
| 5.6 Glistenings Detection Parameters..... | 96 |
| 5.6.1 Fixed Parameters Values..... | 96 |
| 5.6.2 Variable Detection Parameters – Moderate grade of glistenings..... | 97 |
| 5.6.3 Variable Detection Parameters – High grade of glistenings | 99 |
| 5.6.4 Variable Detection Parameters – All images with groundtruth..... | 101 |
| 5.7 Discussion | 102 |

| | |
|---|------------|
| 6. Association between forward light scatter and objective grading of IOL Glistenings..... | 105 |
| 6.1 Introduction..... | 105 |
| 6.1.1 Light Scattering by Small Particles | 105 |
| 6.1.2 Objective quantification of glistenings – previous studies..... | 110 |
| 6.2 Methods..... | 112 |
| 6.3 Results | 114 |
| 6.3.1 Morphology of glistenings..... | 114 |
| 6.3.1.1 Distribution and Density | 114 |
| 6.3.1.2 Size and Shape..... | 116 |
| 6.3.2 Objective quantification of glistenings and forward light scatter..... | 119 |
| 6.3.2.1 Number | 119 |
| 6.3.2.2 Average Area (cross-section)..... | 120 |
| 6.3.2.3 Density..... | 121 |
| 6.3.2.4 Number and Area vs. Scatter – multivariate regression..... | 122 |
| 6.4 Discussion..... | 123 |
| | |
| 7. Bilateral study between Acrysof SN60WF and Eternity Natural Uni NW-60 . | 125 |
| | |
| 7.1 Introduction..... | 125 |
| 7.2 Methods..... | 128 |
| 7.2.1 IOL Preparation and Measurement..... | 128 |
| 7.2.2 Data Analysis | 129 |
| 7.3 Results | 129 |
| 7.3.1 Number of glistenings pre vs post thermal grading..... | 129 |
| 7.3.2 Size of glistenings..... | 131 |
| 7.3.3 Volume Under Scatter Function (VUSF)..... | 132 |
| 7.3.4 PSF and Straylight parameter..... | 133 |
| 7.4 Discussion..... | 135 |

| | |
|---|------------|
| 8. Modulation Transfer Function and Wavefront Aberrations in Intraocular Lenses with Glistenings | 139 |
| 8.1 Introduction..... | 139 |
| 8.1.1 Modulation Transfer Function | 141 |
| 8.1.2 Optical performance studies on intraocular lenses with glistenings | 143 |
| 8.2 Methods..... | 144 |
| 8.2.1 Materials..... | 144 |
| 8.2.2 Procedure..... | 145 |
| 8.2.3 Wavefront aberrations calculations..... | 147 |
| 8.2.4 Reproducibility..... | 148 |
| 8.3 Results..... | 150 |
| 8.3.1 Stage One..... | 150 |
| 8.3.1.1 Wavefront aberrations | 150 |
| 8.3.1.2 Power and MTF..... | 150 |
| 8.3.1.3 Resolution limit – USAF target | 151 |
| 8.3.2 Stage Two | 152 |
| 8.3.2.1 Correlation of Glistenings with Dioptric Power..... | 152 |
| 8.3.2.2 MTF change | 153 |
| 8.3.2.3 Resolution limit..... | 153 |
| 8.4 Discussion | 155 |
| | |
| 9. Conclusions and Future Work | 157 |
| | |
| Appendix..... | 163 |
| | |
| References..... | 169 |

List of Tables

| | |
|--|----|
| Table 3.1 Detector eccentricity values for measured points on the scatter function..... | 52 |
| Table 3.2 Repeatability for an IOL with Grade 3 glistenings (4mm pupil)..... | 54 |
| Table 3.3 Procedure's Reproducibility for an IOL with Grade 3 glistenings (4mm pupil) | 56 |
| Table 3.4 NHS Diabetic Retinopathy recommended camera settings | 60 |
| Table 4.1 Tested IOLs specifications..... | 66 |
| Table 4.2 Mean values and standard deviations (mean \pm sd) of VUSFs for each grade at 3mm pupil size (normalized units) | 70 |
| Table 4.3 Correlation between VUSF and Grade of Glistenings for each pupil size.... | 71 |
| Table 4.4 No correlation was found between large angle domain scatter index and glistening grading for none of the three pupil sizes | 74 |
| Table 4.5 Mean values (and SD) of scatter index n for each pupil size in the large angle domain | 74 |
| Table 4.6 A positive correlation was found between scatter index and glistening grading for all three pupil sizes (small angle domain)..... | 75 |
| Table 4.7 Correlation between straylight parameter and glistenings grading for all pupil sizes | 77 |
| Table 5.1 Population classification fractions..... | 88 |
| Table 5.2 General area under ROC curve (AUC) descriptions | 90 |
| Table 5.3 Glistenings Detection Classification fractions | 91 |

| | |
|--|-----|
| Table 5.4 Ground truth images..... | 94 |
| Table 5.5 Detection parameters set as an initial starting point..... | 95 |
| Table 5.6 Mask Reproducibility..... | 96 |
| Table 5.7 Initial glistenings detection for all ground truth images..... | 96 |
| Table 5.8 Software performance for an image with moderate grade of glistenings and different input parameters (see text for details). | 98 |
| Table 5.9 Set of parameters applied on DSC_0776, high grade of glistenings IOL image | 99 |
| Table 5.10 Software evaluation suggested protocol | 104 |
| Table 6.1 Details of the IOLs used in the study | 113 |
| Table 6.2 Spearman coefficients and p-values for the correlation between the detected number of glistenings in an IOL and log(s) results | 120 |
| Table 6.3 Spearman coefficients and p-values for the correlation between the average glistenings cross-section in an IOL and corresponding log(s) values for 10°. | 121 |
| Table 6.4 No correlation was shown between Density and straylight parameter.... | 122 |
| Table 6.5 Multivariate regression results for Number, Area and VUSF..... | 122 |
| Table 7.1 Tested IOLs coding and description. Material specifications as provided by manufacturers to physicians; composition details are not exhaustive | 128 |
| Table 7.2 Mean VUSF values for each material among the three different pupil sizes | 132 |
| Table 7.3 Straylight parameter, log(s), for two different angles: 3.5° and 10° | 134 |
| Table 7.4 Human eye base straylight parameter values for four (4) scattering angles (van den Berg, 1995)..... | 137 |
| Table 8.1 IOLA plus reproducibility results..... | 148 |
| Table 8.2 Optocraft reproducibility results | 149 |
| Table 8.3 Optical bench reproducibility results..... | 149 |

Table 8.4 Stage 1: Wavefront metrics, pre and post treatment. All data are mean \pm SD 150

Table 8.5 Stage 1: Power and MTF, tested with Optocraft and IOLA plus..... 150

Table 8.6 Resolution limit measured with Optical Bench 151

Table 8.7 Percentage of lenses among the three dioptric groups, that developed glistenings after being subjected in same thermal grading conditions..... 152

List of Figures

Figure 2.1. Scatter effect when viewing a full moon. Courtesy of Haris Ginis (Looking at the Moon, 2009), IVO Crete 29

Figure 2.2. Forms of PSF diffraction limited, presence of coma and spherical aberrations 31

Figure 2.3. The Point-Spread function (PSF) for a normal eye, according to the CIE standard (Vos, 1984) 33

Figure 2.4 PSF in the human eye relatively to the pupil size..... 34

Figure 2.5 Schematic drawing of experimental setup (van den Berg and IJspeert, 1995) 35

Figure 2.6 Experimental setup for IOL in vitro light scatter distribution measurement, simulating the human eye by inducing an artificial cornea. 35

Figure 2.7 Schematic view of narrow-angle forward light scatter measuring system. 36

Figure 2.8 Diagram of cumulative intensity while light source radius is increasing. An asymptotic value is being reached beyond which intensity does not increase..... 36

Figure 2.9 Left: Integrating sphere schematic experimental setup. Right: BRIM arrangement..... 37

Figure 2.10 Illustration of image processing. PSF detection and separation in tiles, parameter determination for different areas of the PSF: corner, ring, centre, CAHM. (Schramm et al., 2013) 38

Figure 2.11 A modifies WASCA for intraocular light scatter evaluation (Schramm et al., 2013)..... 39

Figure 2.12 Conventional Threshold Method..... 40

Figure 2.13 Direct compensation (flicker) method..... 41

| | |
|---|----|
| Figure 2.14 Compensation Comparison method..... | 42 |
| Figure 2.15 In vitro glistenings in an intraocular lens | 43 |
| Figure 3.1 Experimental Setup. LS, Monochromatic Light Source; M, mirror; SF, Spatial Filter; CL1, collimator achromatic lens; AP (1&2), apertures; CL2, achromatic lens; S, IOL sample stage; D, detector; BS, cube beam splitter; T, target;..... | 45 |
| Figure 3.2 Lab view setup | 46 |
| Figure 3.3 Scheme of an afocal system formed using an achromatic lens and a converging (IOL) lens | 47 |
| Figure 3.4 Autodesk Platform drawing | 47 |
| Figure 3.5 Scheme of the IOL holder device | 50 |
| Figure 3.6 Angle calculator and data spreadsheet..... | 52 |
| Figure 3.7 Repeatability mean values and corresponding standard deviations. Y-axis is plotted in a logarithmic scale..... | 55 |
| Figure 3.8 Reproducibility mean values and corresponding standard deviations | 56 |
| Figure 3.9 IOL imaging with Scheimpflug photography (Rønbeck et al., 2013) | 57 |
| Figure 3.10 Methods of imaging IOL glistenings: (a) in vivo slit-lamp photography (Colin et al., 2009), (b) in vitro slit-lamp photography (Gregori et al., 2002) and (c) reflecting microscopy (Kato et al., 2001)..... | 58 |
| Figure 3.11 Slit-lamp setup | 59 |
| Figure 3.12 Images in row A were taken for a maximum beam width and angle positions of 0°,10°,20°,50°and 60° respectively. Images in row B were taken for a 2mm beam width and angle positions of 0°,10°,40°and 60° respectively | 60 |
| Figure 3.13 Example of an IOL slit-lamp digital image and analysis: (a) original photo taken with a 2mm beam width, (b) the image was analysed in BW by collaborators at Kingston University by (c) highlighting the glistening and removing background noise and reflections..... | 61 |
| Figure 3.14 Schematic representation of IOL's illumination | 62 |

| | |
|--|----|
| Figure 3.15 IOL glistening capture with a Digital Slit-lamp and uniform illumination | 62 |
| Figure 4.1 Standard photographs of the glistenings as proposed by Dhaliwal et al (1996). From left to the right: trace, 1+, 2+ and 3+. | 63 |
| Figure 4.2 a) A solid of revolution generated by a plane rotated around y axis b) illustration of a capped cone | 68 |
| Figure 4.2 Correlation between PSF skirt (beyond 1°) volume and Grade of Glistenings for all pupil sizes | 70 |
| Figure 4.3 PSF angular distribution for three different grades: white points for a grade 0 (S16), grey points for a moderate grade 3 (S5) and black points for a high grade >4 (S10). Peak values decrease and skirt levels increase while grade of glistenings increases. All results correspond to a 3mm pupil size..... | 72 |
| Figure 4.4 PSF comparison with CIE standards: green line for an young (20yrs) and red line for an old (70yrs) normal subject. Dash grey line is for a grade 0 IOL, grey line for a moderate grade 3 and black line for a high grade >4. IOL results correspond to a 3mm pupil size. Both axes are in logarithmic scale. | 72 |
| Figure 4.5 Pupil size impact on PSF for an IOL of moderate grade 3 of glistenings (S5). Both axes are in logarithmic scale | 73 |
| Figure 4.6 Linear regression of log(PSF) vs log(θ) among the large angle domain ($\geq 1^\circ$) for a grade 1 (IOL A), 3mm pupil size. Red trendline stands for negative eccentricity (L) while blue for positive..... | 74 |
| Figure 4.7 Linear regression of log(PSF) vs log(θ) for a grade 2 IOL (S4), 3mm pupil size (small angle domain) | 75 |
| Figure 4.8 Variation in small angle domain scatter index with glistenings severity .. | 76 |
| Figure 4.9 Straylight log(s) values for a grade 3 IOL (S5) vs glare angle θ for the three different pupil sizes | 77 |
| Figure 4.10 Straylight parameter angular dependence. For normal subjects, both young and old, as well as for a low grade 1 IOL, $s(\theta)$ can approximately be considered as constant beyond 1° while for a grade >4 IOL the angular dependence is evident | 78 |

Figure 5.1 Image Processing steps used by Colin et al. for the quantification of glistenings (Colin and Orignac, 2011). A) Slit-lamp image of an IOL, with the yellow rectangle showing the central zone that was used for counting. B) Inversion of colour. C) Conversion to 8-bit format. D) Subtraction of background and adjustment of contrast. E) Thresholding to recognize features of size up to 0.001 mm². F) Microvacuoles counted by the software and circled in red. Density was calculated by dividing the counted number by the initial yellow rectangular area.....81

Figure 5.2 Image Analysis Processing by Dhital et al. (2012) Left to right: Image from slit-lamp camera, reverse contrast, final image of glistenings.....82

Figure 5.3 Hard Exudates. American Academy of Ophthalmology. Available from <http://www.aaopt.org/> [accessed 15th October 2014].84

Figure 5.4 Lens Zoning for a 6mm optic diameter IOL.85

Figure 5.5 Graphical User Interface for Glistenings Detection Software.....86

Figure 5.6 Left: User is marking five (5) different points on the IOL’s edge. Right: Software calculates a best fit circle defining the mask.....86

Figure 5.7 Glistenings Detection result. Detected glistenings are marked in red, either filling each glistening area (left) or their boundaries (right). Quantification values appear on the bottom of the interface for the whole lens as well as for each of the three (3) different optical zones.87

Figure 5.8 Diseased and Normal groups distribution overlap.....88

Figure 5.9 The ROC curve.....89

Figure 5.10 True glistenings (NG) and Detected glistenings (N) are two intersecting sets where their intersection $NG \cap N$ is the number of the True Positive (TP) glistenings...
.....92

Figure 5.11 Validation metrics as appearing on the bottom right corner of our Detection Programme GUI93

Figure 5.12 Result after glistenings’ detection with the corresponding ground truth image
.....95

Figure 5.13 Comparison of GDP outcome (left) with initial image (right) for DSC_0776, high grade IOL image. The non detected true glistenings areas are likely to be in areas that glistenings overlap 100

Figure 5.14 ROC empirical curves for a moderate grade of glistenings IOL image (blue line) and a high grade of glistenings IOL image (red line) 100

Figure 5.15 Variation of Minimum Threshold value on all ground truth images.... 101

Figure 5.16 DSC_0607: For minimum threshold value 0.01, number of wrong detected glistenings is 6 times bigger than for minimum threshold value 0.02..... 102

Figure 5.17 Image of an IOL with high density and moderate size of glistenings (grade >4) 103

Figure 6.1 Scattering by an arbitrary particle..... 105

Figure 6.2 The direction of scattering at any r is characterized by the scattering angle θ measured relative to the direction of the incident beam and the azimuth angle φ . .. 106

Figure 6.3 Light possible interactions with a large size particle 109

Figure 6.4 A spheroid particle whose axis of revolution orientation has an angle of θ with the incident beam..... 110

Figure 6.5 Illustration of different glistenings sizes and densities (DeHoog and Doraiswamy, 2014)..... 111

Figure 6.6 An IOL image following detection of glistenings, which were highlighted by the GDP. Results for each circular zone are given below the image. In addition, a spreadsheet with more extensive detail is exported for further analysis 112

Figure 6.7 Glistenings Distribution (%) among the three different pupil sizes..... 115

Figure 6.8 Actual distribution median values are lower than the ones if a uniform distribution of glistenings existed..... 115

Figure 6.9 Density of glistenings among the different pupil sizes in all IOL samples .
..... 116

Figure 6.10 A difference between Major and Minor Axis of glistenings was found, implying that glistenings shape is more likely to be ellipsoid rather than spherical.....
..... 117

Figure 6.11 Distribution of the two size categories of glistenings among our tested IOLs: (a) glistenings size given from previous studies and (b) larger size of glistenings. Group b, large particles, appears in higher percentage as an average..... 118

Figure 6.12 Size distribution of all IOLs glistenings population. A very wide range of glistenings sizes was shown to exist, overcoming the so far reported boundary of 20µm 118

Figure 6.13 Spearman coefficients and p-values for the correlation between the existing number of glistenings in an IOL and VUSF results 119

Figure 6.14 Spearman coefficients and p-values for the correlation between the average area of glistenings and VUSF beyond 1°..... 120

Figure 6.15 A statistically significant correlation was shown between Density and VUSF 121

Figure 7.1 A three piece clear IOL (right) versus a single piece blue blocker (left), Alcon®. Available from: <http://www.eyecalcs.com/DWAN/pages/v6/v6c011.html> [accessed 16th November 2014] 127

Figure 7.2 Mean values of pre and post IOL treatment for each material 130

Figure 7.3 Number of induced glistenings for the Eternity Natural Uni and Acrysof materials post thermal grading treatment 130

Figure 7.4 Glistenings size classifications' distribution among Eternity Natural Uni and Acrysof, post thermal treatment. Number of glistenings scale (y axis) differs 131

Figure 7.5 Magnification (right) of a selected central area (2mm width) from an Acrysof, post treatment image. It is evident that the IOL consists of a large number of small glistenings 132

Figure 7.6 PSF mean values (logarithmic scale) for each group of IOLs and all eccentricity angles θ . Acrysof appears to have shown greater amounts of scattered light. Measurements are for a 3mm pupil size 133

Figure 7.7 PSF mean values of Acrysof and Eternity in comparison with the equivalent for a young (green line) and aged (red line) according to the CIE standards. All values appear in a logarithmic scale..... 134

| | |
|---|-----|
| Figure 7.8 Mean straylight parameter log(s) values for each material group along with the equivalent CIE standards for a young and old (red) normal subject | 135 |
| Figure 8.1 One dimension Point Spread Function (Left) and Airy disk (Right)..... | 139 |
| Figure 8.2 Birmingham, New Street Train Station, 1903 [source: Warwickshire Railways http://www.warwickshirerailways.com/ , assessed 15/12/2014]..... | 140 |
| Figure 8.3 Perfect line edges before (Left) and after (Right) passing through a Low Resolution Imaging System..... | 141 |
| Figure 8.4 (a) MTF curves for different pupil sizes, 632 nm source wavelength (Artal and Navarro, 1994). (b) MTF alterations on Zernike aberration corrections for a 3mm pupil size, 632.8 nm wavelength, spatial frequency in cycles/degree (Liang and Williams, 1997). (c) Significant difference on MTF curves among three different age groups for a 6mm pupil size, 530nm wavelength (McLellan et al., 2001)..... | 142 |
| Figure 8.5 USAF bar target resolution charts | 143 |
| Figure 8.6 SHSOphthalmic Optocraft graphical user interface | 146 |
| Figure 8.7 Optical Bench Apparatus (ISO 11979-2): 1 Microscope; 2 IOL; 3 Collimator Achromat; 4 USAF 1951 resolution target; 5 Dichroic filter; 6 Condenser; | 147 |
| Figure 8.8 Number of lenses on different glistenings grades showing a negative, a positive or no resolution change | 151 |
| Figure 8.9 Grade of glistenings vs dioptric power..... | 153 |
| Figure 8.10 MTF changes mean values and standard deviations among the three dioptric power lens groups..... | 154 |
| Figure 8.11 Resolution mean changes for each dioptric power IOL group | 154 |
| Figure 9.1 A diffraction topography of the IOL as projected on a black screen (shield) when exiting beam is diverging, offering a magnified projection of a relatively small central area of the lens. A modified version of this technique could be used for glistenings imaging and characterization..... | 159 |

Acknowledgements

A PhD is a lonely journey. However, I was lucky to come across sporadically some fellow travellers. In different ways, they contributed their own piece in helping me exploring and solving the PhD puzzle.

I would truly like to thank my supervisor Prof. Chris Hull, first of all for trusting me and giving me the opportunity to work and study at City University London and secondly, for all the academic support, guidance, experienced knowledge and critical thinking he provided throughout my PhD research. Moreover, I am grateful to City University for supporting financially my studentship.

I was fortunate to meet some excellent and bright people at City and the Division of Optometry and Visual Science. I am grateful to Prof. John Barbur, who was the first to come across my CV and encouraged me to continue my studies in London. Dr. Steve Grupetta for his technical advice and all the lab troubles we've shared. Special thanks to Dr. Evgenia Konstantakopoulou for her encouragement and help, in and out of City. At last, my dear colleagues Dr. Marisa Rodrigues Carmona, Dr. Hanna Gillespie-Gallery, Dr. Priya Dabasia and Irene Ctori for the wonderful PhD moments, troubles, uncertainties, coffees, beers and dreams we've shared!

This PhD would not have been accomplished without the contribution of AVS Inc. I am grateful to Mrs. Cynthia Bentley for giving me the opportunity to work in Santa Barbara. Special thanks to Dr. Andy Doraiswamy for his innovative ideas, enthusiasm and trust. Mrs. Nahid Izadpanah for her technical expertise. Last but not least, I would like to thank Mr. Kevin Balch for his great help and enthusiasm on the "stardust" project, but mostly for the long chats and IPAs we shared in California.

A grateful acknowledgment to Dr. Sarah Barman, Parisut Jitpakdee and Dr. Bunyarit Uyyanonvara for establishing a constructive collaboration. Their excellent work on developing the Glistenings Detection Programme made a significant contribution to my thesis.

My placement in London not only extended my educational experiences. I was blessed to meet some exceptional people, a true family, who inspired me and marked my perception, way of thinking and personal judgement. I would like to thank firstly Dr. Christina Moutsiana and secondly Professor Antonios Tzanakopoulos. Their contribution did not only rely on their great academic experience and advice; the long and deep philosophical discussions and tough situations we shared throughout those three years are equivalent of a second PhD. My life in London would not have been the same without the support in many aspects of my dearest friend Lily Kotsana, from the very first moment till the ultimate stage of my PhD. Last but not least, I would like to thank my dearests Anamaria Diana Hutanu, Genevieve Lachance and Maria Tzanakopoulos for the vital worries and the glasses of wine we shared! Thank you for always being there for me.

Crete is more than an island. It is a cradle of sounds, pictures and emotions that have accompanied me throughout my PhD. My family has always been the unfaltering base for me to stand on and create my own path. I wish to thank them for the continuous valuable supply of encouragement, love, inspiration, advice, long international skype chats, parcels and glorious Cretan food! I would also wish to thank my friends from the “Παρέα της Νταμαρόπετρας” for paying visits to London and always remembering me. Dear @DepressedPasok for making me laugh. Last, I wish to thank the artists Yiannis Aggelakas and Psarogiorgis (Giorgos Xylouris) for their lyrics and music that filled most of the dark, long and lonely laboratory hours.

Finally, I am grateful to all those who always believed in me and kept supporting me with their thoughts and care.

Declaration

I grant the power of discretion to the University Librarian to allow this thesis to be copied in whole or in part without further reference to me. This permission covers only single copies made for study purposes, subject to normal conditions of acknowledgement.

Abstract

Introduction. Glistenings are fluid-filled inclusions in the polymer matrix of an intraocular lens (IOL). Acting as refractile particles they may contribute to a reported high level of forward light scatter. However, several studies have reported that there is no significant correlation with a number of measures of visual function. The purpose of the work reported in this thesis was to test if there was an association between *in vitro* forward light scatter and grade of glistenings. The *in vitro* approach allows measurement of forward light scatter without the confounding effects of other structures in the eye and subjective responses.

Methods. Intraocular lenses were placed at the centre of rotation of a detector stage. The detector measured the forward scattered light in star space at 37 angles covering ± 18 degrees. Measurements were made for each of the test lenses at 3mm, 4mm and 5mm pupil sizes. Forward light scatter was quantified by calculating the straylight (volume under the scatter function) for the large angle domain (> 1 deg.). Images of the intraocular lenses were captured with a digital Nikon FS-2 photo slit-lamp. Having developed a Glistenings Detection Programme (GDP) in collaboration with external computer scientists, images were analysed. Results of glistening detection, which included their number, size, density and distribution, were correlated with *in vitro* forward light scatter measurements.

Results. A statistically significant correlation was found between forward light scatter and the number, size and density of glistenings. Comparing our scatter results with the CIE standards, suggests that only high glistenings severity could have an impact on visual function. In addition, results were inversely proportional to pupil size due to the non-uniform distribution of glistenings. The shape of glistenings was shown to be predominantly ellipsoidal rather than spherical. Size and number of glistenings varies in the hydrophobic acrylic materials. Despite the production of new glistenings-free materials, development of glistenings may still exist with cases of high severity giving straylight parameter values greater than those for a cortical cataract subject. A statistically

significant difference in MTF and Resolution limit was found in IOLs, pre and post thermal treatment. Finally, a correlation between IOL dioptric power and severity of glistenings was found.

Conclusion. Subjective methods for grading intraocular lens glistenings poorly describe the significance of increased light scattering. Image processing software can provide objective data on glistenings density, size and morphology, factors which are important in light scatter modelling. The impact of glistenings on visual function needs further clinical investigation.

Chapter 1

Introduction

“All that glisters is not gold”

-William Shakespeare

The Merchant of Venice, 1596

In November 1949, the first intraocular lens (Rayner Ltd, Brighton UK) was successfully implanted by Sir Harold Ridley at St. Thomas’ Hospital in London (Spalton, 1999, Apple et al., 1999). Since that date, there have been many developments in cataract surgery and intraocular lenses in particular. Nowadays, intraocular lens implantation following surgical removal of the cataractous lens is one of the most commonly performed and successful eye procedures in the developed world.

In the late 1980s the phenomenon of glistenings was first reported. These reports increased after the introduction of the hydrophobic acrylic materials in IOL manufacturing in 1993 (Bellucci, 2013). IOL glistenings are vacuoles within in the polymer matrix that develop after cataract surgery. These particles appear to sparkle under slit-lamp examination and hence are referred to as glistenings. As refractile particles, glistenings can contribute to intraocular scatter. Visual complaints have been reported linked to the presence of glistenings. However, the impact of glistenings on light scatter and the subsequent effect on visual function has been controversial.

The aim of the work presented in this thesis is to evaluate and quantify light scatter from intraocular lenses with glistenings. Ocular light scatter, although described and studied in the past, remains a phenomenon where its quantification and clinically significant threshold are still under discussion and investigation. As it is difficult to distinguish scatter caused by glistenings and scatter caused by other imperfections such as posterior capsule opacification, in vitro measurement of IOLs was preferred to avoid confounding. The overarching aim of this project was to test the hypothesis that intraocular lenses with

glistenings cause forward light scatter and to assess how this scatter is linked to objective measures of the density, size and distribution of the glistenings.

The basic principles of intraocular light scatter and methods of measurement are described in Chapter 2. Emphasis is placed on optical, *in vitro* methods since our study is *in vitro*. A detailed description is then attempted of glistenings and the mechanisms and factors that affect their development before reviewing published results on clinically reported visual complaints.

An experimental setup was developed for measuring forward light scatter in intraocular lenses with glistenings and is described in Chapter 3. Moreover, the procedure and data analysis are explained as well as the development of the imaging protocol using a photo slit-lamp with a digital camera.

The association between light scatter results and subjective grading of glistenings is evaluated in Chapter 4. We show that clinical grading, although related to light scatter, does not quantify some of the glistening parameters that could affect light scatter. Therefore software for the quantification of the glistening was developed in collaboration with Kingston University, UK and Thammasat University, Thailand. The software development and validation are described in Chapter 5.

Association between objective metrics derived from the Glistenings Detection Programme (GDP) and forward light scatter are presented in Chapter 6. In addition, an evaluation of glistenings morphology is attempted and linked with theoretical models of scattering.

New materials for intraocular lenses have been introduced recently that are promoted as being glistenings-free. A bilateral study between two hydrophobic acrylic materials is presented in Chapter 7 to evaluate the severity of the laboratory developed glistenings and the significance of the resulting light scatter.

Finally, in Chapter 8, a pilot study on the effect of intraocular lenses with glistenings on the Modulation Transfer Function (MTF) is presented.

Chapter 2

Literature Review

2.1 Scatter in the human eye

The retina of the human eye is necessarily preceded by transparent biological tissues. Nevertheless, the ocular media are not optically ideal resulting in usually small amounts of scattering. A good example of how these small amounts of scatter affect the appearance of an object is the image of a full moon on a clear night sky (figure 2.1). Ideally, edges of a luminous moon against dark sky should be sharp, as shown on the right side of figure 2.1. In reality, edges appear blurred with a halo around the moon disk, as shown on the left of the same figure.



Figure 2.1 Scatter effect when viewing a full moon. Courtesy of Haris Ginis (Looking at the Moon, 2009), IVO Crete.

The components of the human eye that an incident beam of light traverses and that can contribute to ocular scatter are:

- a) Cornea
- b) Aqueous Humour
- c) Crystalline Lens
- d) Vitreous Body
- e) Retina (comprising several layers before the photoreceptors)

Corneal light scatter, although normally small due to the regular organisation of collagen fibres, can be increased by corneal inflammation, dystrophy, oedema or after laser surgery (haze), where the regular lattice arrangement is disrupted. Aqueous humour can contribute to ocular scatter notably when there is inflammation. It is described by clinicians as “aqueous flare” and is caused by increased protein levels within the aqueous (McLaren et al., 1990). The most significant source of scattering in the eye occurs in the crystalline lens. It increases with age and accelerates under pathological conditions such as cataract, where the aggregation of proteins causes a loss of transparency. The role of the fundus in scattering lies mainly with retinal reflections and back scatter, sending the light in different directions resulting in increased overall scatter. The forward light scatter caused by the layers immediately preceding the photoreceptors is small. The iris and sclera contribute indirectly due to light transmittance through these structures (Van den Berg et al., 1991). In addition, iris pigmentation is a considerable factor as light coloured irides appear to transmit higher amounts of light compared with more heavily pigmented ones. Finally, conditions where the transparent gel structure of the vitreous degenerates can result in the collapse of the vitreous (syneresis) and can affect ocular scatter since the transparency and homogeneity of the normal young vitreous is affected (Sebag, 1987).

Scatter in the eye can be separated into two types depending on the direction of the scattered photons: ocular forward scatter is defined as the total amount of light scattered towards the retina (angular distribution between 0° and 180°), resulting in a veiling illuminance superimposed upon the retinal image and causing a reduction in contrast. This phenomenon leads to a variety of complaints, such as glare. Backscatter on the other hand is defined as the total amount of light scattered backwards towards the anterior chamber (angular distribution between 180° and 360°), reducing the amount of light reaching the retina.

In the literature (Holladay, 1927, Stiles and Crawford, 1937, Fry and Alpern, 1953, Vos, 1963), the equivalent veiling luminance of intraocular light scatter is given by the formula:

$$L_{eq} = \frac{kE}{\theta^n} \quad (2.1)$$

where E is the illuminance of the light entering the pupil from the glare source and θ the angle in object space. The scatter index n and straylight parameter k are constants, which have different values in the expressions given by various investigators. Some of the most important are:

$$L(\theta) = \frac{9.2 E}{\theta^2}, \quad 2.5^\circ \leq \theta \leq 25^\circ \quad (\text{Holladay, 1927})$$

$$L(\theta) = \frac{4.16 E}{\theta^{1.5}}, \quad 1^\circ \leq \theta \leq 10^\circ \quad (\text{Stiles, 1929})$$

$$L(\theta) = \frac{29 E}{\theta^{2.8}}, \quad 1^\circ < \theta < 8^\circ \quad (\text{Vos and Bouman, 1959})$$

$$L(\theta) = \frac{29 E}{(\theta + 0.13)^{2.8}}, \quad 0.15^\circ < \theta < 8^\circ \quad (\text{Walraven, 1973})$$

where $L(\theta)$ is in candelas per square meter (cd/m^2) and E is in lux (lm/m^2). The straylight parameter, k , has been reported to depend on angle and studies have also shown that it also depends on age, especially over the age of 45 (Whitaker et al., 1993, Hennelly et al., 1998).

As the ocular media are not perfect, a point object stimulus is not imaged on the retina as a single point image. The quality of the retinal image is defined by the point spread function (PSF) of the human eye, which is the corresponding retinal image of a point object.

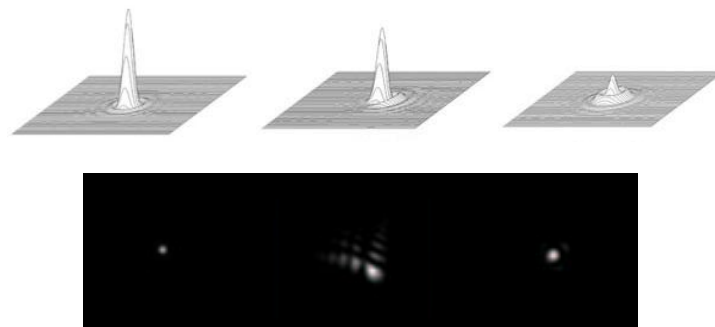


Figure 2.2. Image of a point source showing the presence of coma and spherical aberrations.

The form of the PSF depends upon diffraction, defocus, aberrations and scatter (figure 2.2). The effect of aberrations and scatter is to spread light out more than predicted by diffraction (diffraction-limited case), therefore the PSF becomes broader and the peak is lowered. The amplitude PSF is the complex amplitude of the light distribution, whereas the intensity PSF is the actual light distribution as measured with a light meter.

2.2 The Glare Light Scatter Function of the eye

In the normal eye, visual acuity is of the order of 1 minute of arc, corresponding to the very central core of the PSF. At the beginning of the 20th century it was already realized that the outer part of the PSF beyond 1° is also of functional importance (Van Den Berg

et al., 2009). This part has been called straylight. Intraocular straylight is the phenomenon where the retina receives light at locations that do not optically correspond to the direction the light is coming from. The resulting straylight reduces the quality of vision.

According to the CIE (Commissión internationale de l'éclairage) 1999 Total glare function (Vos and Van Den Berg, 1999), the PSF equation that applies to all angles is:

$$\begin{aligned}
 PSF = \left[\frac{L_{eq}}{E_{gl}} \right]_{total} &= \left[1 - 0.08 \cdot \left(\frac{A}{70} \right)^4 \right] \cdot \left[\frac{9.2 \cdot 10^6}{\left[1 + \left(\frac{\theta}{0.0046} \right)^2 \right]^{1.5}} + \frac{1.5 \cdot 10^5}{\left[1 + \left(\frac{\theta}{0.045} \right)^2 \right]^{1.5}} \right] + \\
 &\left[1 + 1.6 \cdot \left(\frac{A}{70} \right)^4 \right] \\
 &\cdot \left\{ \left[\frac{400}{1 + \left(\frac{\theta}{0.1} \right)^2} + 3 \cdot 10^{-8} \cdot \theta^2 \right] + p \right. \\
 &\left. \cdot \left[\frac{1300}{\left[1 + \left(\frac{\theta}{0.1} \right)^2 \right]^{1.5}} + \frac{0.8}{\left[1 + \left(\frac{\theta}{0.1} \right)^2 \right]^{0.5}} \right] \right\} + \\
 &2.5 \cdot 10^{-3} \cdot p \quad [sr^{-1}] \tag{2.2}
 \end{aligned}$$

where θ is the glare angle in degrees, A the age in years and p the iris pigmentation factor (van den Berg, 1995). As a general approach, pigmentation factor, p , was considered as 1 for blue-green Caucasian irides. The straylight parameter s is then defined by:

$$s(\theta) = \theta^2 \cdot \frac{L_{eq}}{E_{gl}} = \theta^2 \cdot PSF \tag{2.3}$$

using equations (2.1) and (2.2), and taking the scatter index $n=2$ and the PSF defined so that it integrates to unity (van den Berg, 1995). As forward scatter in cataract is found to decrease strongly with scattering angle (de Waard et al., 1992), the logarithm, $\log(s)$, of straylight is usually plotted (figure 2.3).

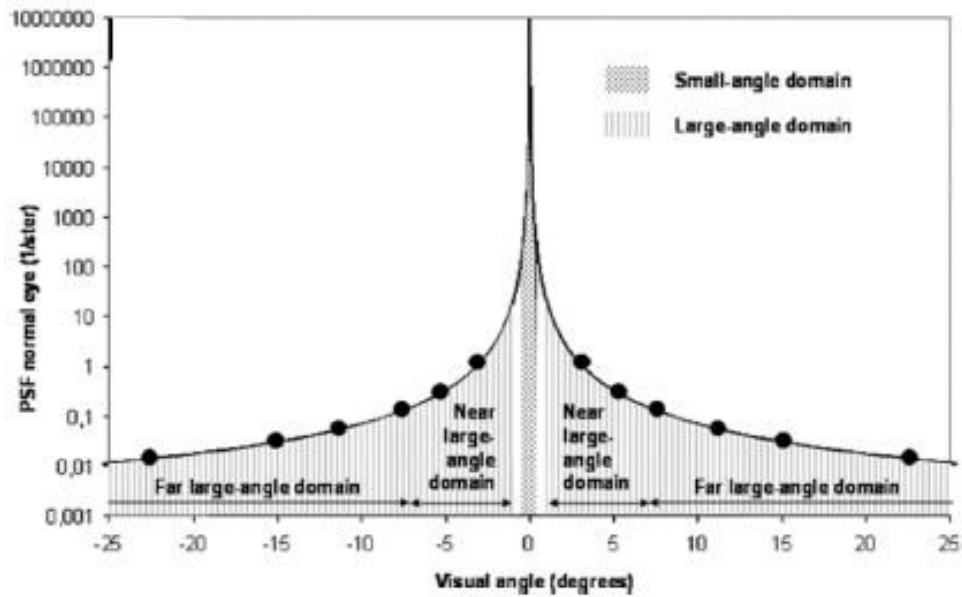


Figure 2.3. The Point-Spread function (PSF) for a normal eye, according to the CIE standard (Vos, 1984)

2.3 Impact of pupil size on light scatter

Pupil size decreases with increasing age, as well as reacting to changes in luminance (Winn et al., 1994). The Point Spread Function is related to the size of the pupil where its shape is a combination of diffraction and aberrations. The pupil size that offers the optimal resolution (lateral) is between 2mm and 3mm (Campbell and Green, 1965, Liang and Williams, 1997). Below this size, diffraction increases whereas at larger pupil sizes aberrations negatively influence the PSF as illustrated in figure 2.4 below.

A mathematical description of the foveal point spread function (Ijspeert et al., 1993), showed that although distortion of the PSF occurs within the small angle domain for pupil sizes from 2mm to 5.8mm size, no significant variation was found in the large angle domain. Hence, for straylight and for normal subjects, no dependence on the pupil size is expected. Other studies on the impact of pupil size on straylight have shown that no significant change occurs for natural pupil sizes (2mm to 7mm) and for normal human eyes (Franssen et al., 2007).

Contrary to the theoretical expectations, a psychophysical testing method (Barbur et al., 1995) showed that the retinal illuminance needed to cancel out the effects of scattered light in the eye increased with pupil size. Generally, the independency of light scattering from pupil size is a consequence of the fact that scatterers in the normal human eye are

uniform over the pupil. When this is not the case, the parameters of the scatter function of the eye can change with pupil size.

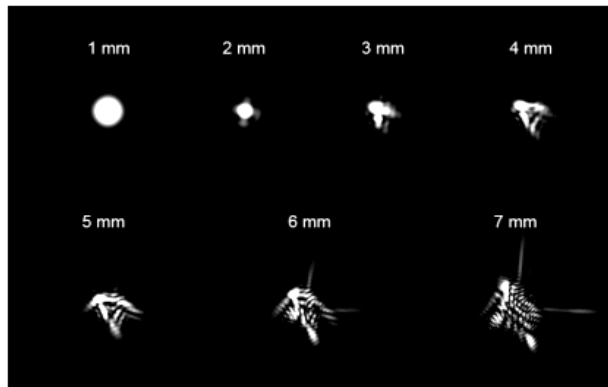


Figure 2.4 PSF in the human eye relative to the pupil size.

2.4 Measurement of forward light scatter

Methods of measuring ocular scatter can be subdivided into three categories: the optical in vitro, the optical in vivo and the psychophysical. The first is related to the direct measurement of forward scattered light using CCD cameras or other light sensors after it has passed through the scattering media. The measurement of optical in vivo scatter is achieved indirectly from light reflected back out of the eye. Finally, using psychophysical methods, scatter is quantified by estimating the amount of diffused light creating veiling glare which reduces the contrast of the retinal image.

2.4.1 Optical methods

Optical methods are in general preferred in estimating ocular light scatter as they give objective results. Methods that have been used to measure forward light scatter in vitro are reviewed in the following sections. They have relevance to the studies reported in this thesis, which are also in vitro.

2.4.1.1 Detecting the angular distribution of scattered light with a photomultiplier

A method based on measuring the angular distribution of forward light scatter in excised eyes (Boynton et al., 1954), donor lenses (Van Den Berg and Ijspeert, 1995) and spectacle lenses (De Wit and Coppens, 2003) has been described. The experimental set-up is shown in figure 2.5.

Monochromatic light, focused on diaphragm 1, passes through an optical system of a lens and the scatter sample (donor lens), which is positioned perpendicular to the incident beam. A detector is rotated in the horizontal plane, centred on the sample, recording the angular distribution of scattered light. The detector assembly consists of a diaphragm (“Diaphragm 3”), an objective lens and a photomultiplier. In this arrangement, diaphragms (1) and (3) are conjugate while the photomultiplier is conjugate with the donor lens due to the objective lens. The photomultiplier detects the intensity of light $I(\theta)$ to quantify the forward light scatter caused by the sample. The experimental setup used in our study was mainly influenced by this method as further described in Chapter 3.

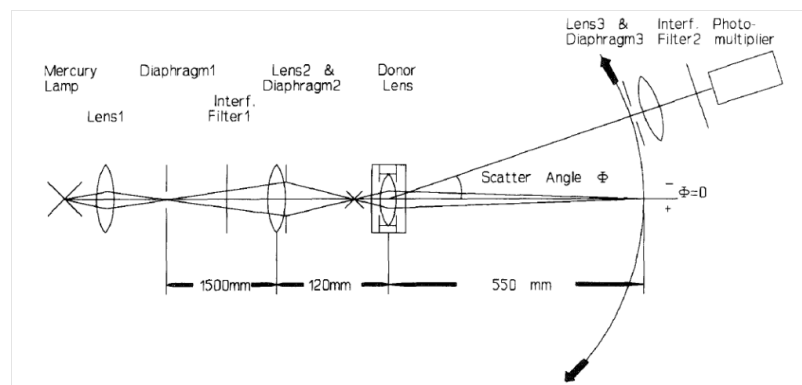


Figure 2.5 Schematic drawing of experimental setup (van den Berg and IJspeert, 1995)

A modified version of the above described setup was recently proposed by van den Mooren et al (van der Mooren et al., 2011). In this case, an experimental simulation of the human eye was developed. An artificial cornea was placed in front of the tested IOL (figure 2.6). It produces a more realistic approximation of the real PSF distribution by mimicking more exactly the optics of the cornea and lens. However, given that the back focal length of the artificial cornea and the IOL is very small ($\approx 15\text{mm}$), the objective lens and CCD camera are limited in the angle they can rotate through so as not to hit the sample cell. As a result, it was reported that the maximum angle measured was no greater than ± 3 degrees.

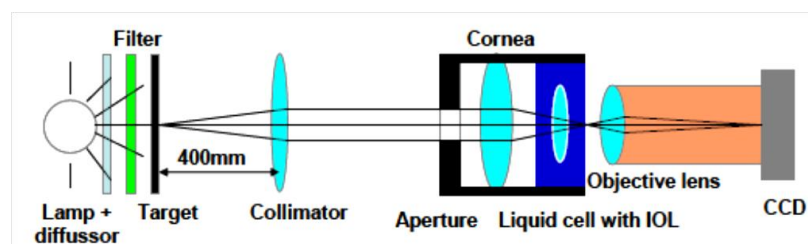


Figure 2.6 Experimental setup for IOL in vitro light scatter distribution measurement, simulating the human eye by including an artificial cornea. (van der Mooren et al., 2011)

2.4.1.2 Narrow-angle forward light scatter

An alternative method of measuring forward scatter in vitro, described below, is applicable only for narrow-angle light scatter quantification. Figure 2.7 shows the arrangement used to record the measurements. The measurement system consists of a CCD camera, a sample and a computer display which projects an image and at the same time acts as the light source.

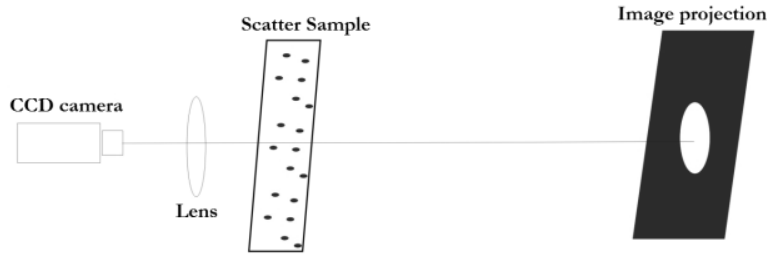


Figure 2.7 Schematic view of narrow-angle forward light scatter measuring system.

The projected image is a bright disc whose radius, r , is varied. The CCD camera detects the intensity I . Figure 2.8 shows an example of measured cumulative intensity as a function of the radius of the disk.

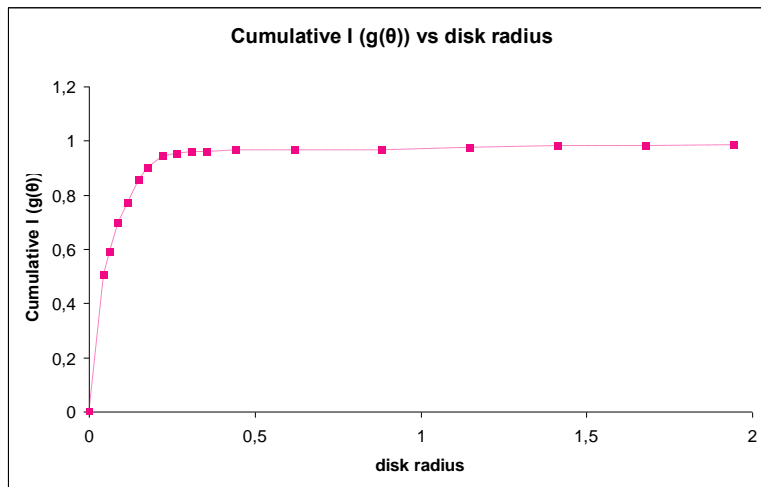


Figure 2.8 Diagram of cumulative intensity while light source radius (degrees) is increasing. An asymptotic value is being reached beyond which intensity does not increase (taken from Optics Lab notes, 2008, MSc Course in “Optics and Vision”, University of Crete).

The cumulative intensity, I , increases as the radius of the projected disc increases. For a radius $r \geq R$, where R is 0.25° , intensity remains nearly constant and tends to unity. It is expected that for an incident beam of light of intensity I_0 where a percentage α has been scattered, then the measured intensity will be:

$$I = I_0 \times (100 - \alpha)\% \quad (2.4)$$

compared to the incident intensity (figure 2.7). The horizontal asymptote of the $I(\theta)$ function, corresponding to the total cumulative intensity of forward scatter, is defined as the Scatter Ratio (SR) parameter. Scattering in an optical system affects the characteristics of the point spread function, attenuating the central region of the PSF and distributing light into the periphery, creating a halo. In the case of the luminous disk, the central PSF (peak) thus central intensity is amplified by the peripheral annuli of the PSF of nearby points which are added to that point. Saturation of intensity occurs as it is impossible for the measured intensity to exceed the original (100%) even if the diameter of the circle continues increasing.

The above method, duplicating the psychophysical Compensation Method (see paragraph 2.4.2), was used by Ginis et al (Ginis et al., 2009) to measure narrow-angle light scatter in rabbit corneas after refractive surgery. In that case, the display presented an annulus. The scatter ratio was directly detected as the light scattered into the dark central patch, which decreases as disk's radius increases.

2.4.1.3 Ballistic-photon Removing Integrating-sphere Method

Another method was introduced by Kim et al. (Kim et al., 2011) called the Ballistic-photon Removing Integrating Sphere Method (BRIM). It was used to quantify forward light scatter caused by glistenings in intraocular lenses, in vitro and was developed based on a quantitative study by Oshika et al. (Oshika et al., 2001). The method relies on detecting and quantifying scatter by removing the ballistic photons of the beam after they have passed through an IOL. Ballistic photons are the ones that follow the geometrical optical path without interacting with the glistenings and hence are not scattered.

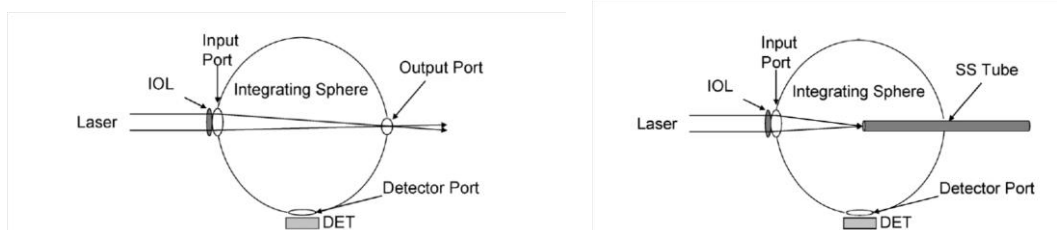


Figure 2.9 Left: Integrating sphere schematic experimental setup. Right: BRIM arrangement.(From Oshika et al. (2001)

Suppose the integrating sphere has a diameter equal to the IOL's focal length. For a collimated beam reaching the IOL, the beam will be focused at the output port (figure 2.9 left). A detector placed at the detector port, perpendicular to the direction of propagation, will detect scattered photons. Practically this setup requires an individual integrating sphere for each different IOL power. To avoid this, the authors suggested using a single integrating sphere regardless of the dioptric power of the tested IOL and removing the ballistic photons by placing the entrance aperture of a thin, optically opaque tube at the back focal point of the lens as shown in figure 2.9 (right).

The degree of scattering was defined by:

$$DS = \frac{S}{T} \times 100\% \quad (2.5)$$

where S is the amount of scattered light and T the transmission value, i.e. all of the transmitted light, direct and scattered, outgoing from the IOL. Estimation of glistenings density was determined using a digital microscope to capture images of the lenses. The counting function of the microscope was used to calculate the number of vacuoles.

Apart from some practical restrictions with this experimental setup, (the authors have reported problems in the case of severe glistenings), the main limitation is that the method doesn't provide information about the angular distribution of forward light scatter.

2.4.1.4 Measurement of intraocular light scatter with a Hartmann-Shack sensor

This technique relies on the Hartmann-Shack principle (Wong and Lim, 2011) and can be applied in vitro using a single-pass wavefront sensor (Moreno-Barriuso and Navarro, 2000, Philippaki et al., 2009). A number of recent in vivo studies have attempted to use the Hartman-Shack (Wong and Lim) method for intraocular light scatter evaluation (Cerviño et al., 2008, Mihashi et al., 2006, Schramm et al., 2013), using a modified clinical HS ocular aberrometer such as the WASCA (Panagopoulou and Pallikaris, 2001). A Hartmann-Shack sensor produces a pattern of individual PSFs as illustrated in figure 2.10. Each individual PSF can be analysed to determine parameters such as: the corner, the ring, the centre and the cross sectional area at half height (CAHM) (figure 2.10, right).

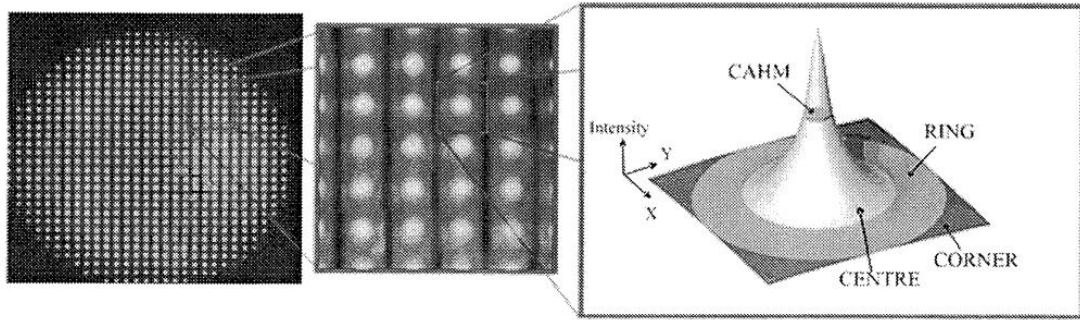


Figure 2.10 Illustration of image processing. PSF detection and separation in tiles, parameter determination for different areas of the PSF: corner, ring, centre, CAHM. (Schramm et al., 2013)

The Michelson Contrast is defined by

$$Contrast_{Michelson} = \frac{Centre - Ring}{Centre + Ring} \quad (2.6)$$

where Centre stands for the mean value of the maximum intensity value of all PSFs in the centre area and Ring represents the mean intensity value of the ring area of all PSFs. This measure of contrast should reduce with increasing light scatter.

The method has the advantage that one can evaluate the spatial distribution of scatter in the image, especially in cases when scattering centres are not uniformly distributed. On the other hand, the results of the HS method for straylight evaluation has limitations as shown in figure 2.11; in order to allow the scattered light to pass through the imaging system and reach the HS sensor, a larger pinhole than the clinical WASCA pinhole is used. Schramm et al (2013) used an 8mm aperture instead of the original 1.5mm pinhole. As a result, in the presence of significant light scatter caused by, for example, cataract, the HS images are blurred and the subsequent analysis and straylight evaluation is poor compared to other methods. In addition, the difference between PSF distortions caused by aberrations and pure scatter is not yet fully understood.

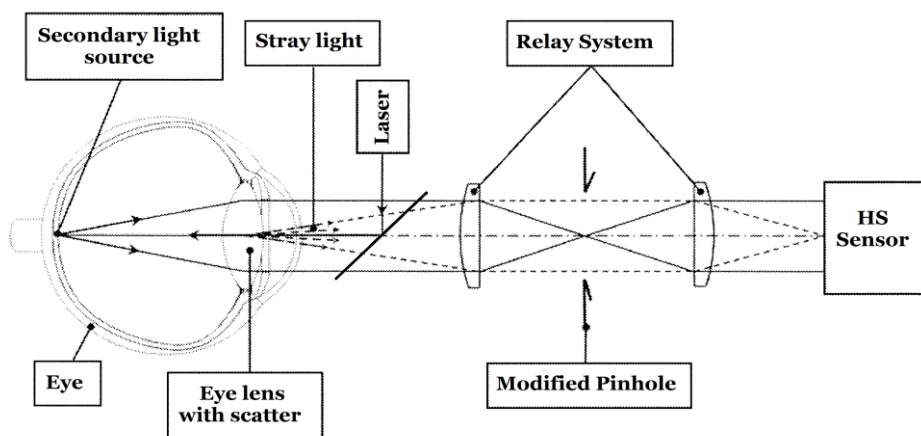


Figure 2.11 A modified WASCA for intraocular light scatter evaluation (Schramm et al., 2013)

2.4.2 Psychophysical methods

Forward light scatter can also be measured using psychophysical methods. Such methods are necessary when testing the effect of scattered light on vision for individual patients. Moreover, psychophysical methods have been used in most of the clinical glistening studies that directly relate to the work in this thesis. Most of these methods, described in further detail below, have used a modified version of the “equivalent veiling” concept introduced by Cobb (Cobb, 1911). The first researchers to apply this idea were Le Grand (Le Grand, 1937), Stiles (Stiles, 1929, Stiles and Crawford, 1937).

2.4.2.1 Conventional Threshold Method

A standard method that originates from Stiles is the “conventional threshold method” (Stiles, 1929, Stiles and Crawford, 1937). It is based on the estimation of the brightness of a homogeneously illuminated target in the presence of a glare source placed at a specific angle θ to the line of sight (figure 2.12).

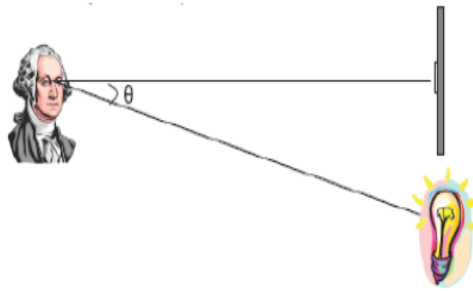


Figure 2.12 Conventional Threshold Method

The glare source, because of scattering, generates a light intensity distribution superimposed on the retinal image. This results in an increase in the retinal illuminance compared to when the target is viewed without the glare source. By turning off the glare source, the luminance of the target is varied until it produces the same threshold for detecting the central target. The luminance difference between the with glare and without glare condition is the equivalent veiling luminance caused by the off-axis glare source and can be determined for a range of angles.

2.4.2.2 Direct Compensation

A modification of the conventional threshold method was introduced in 1992 by Thomas JTP van den Berg and Jan Kees IJspeert (van den Berg and IJspeert, 1992). A device was developed, which was able to measure the in vivo light scatter in the human eye with a psychophysical technique known as the “direct compensation” method. In this method,

the subject is required to observe monocularly a dark disk (test field) surrounded by a bright ring. The test field and the bright ring are set to flicker in counterphase at a frequency of 8Hz.

Light scatter from the straylight source will add light to the test field (figure 2.13). When the straylight source is off, a variable amount of light is added to the test field until the subject does not observe any flickering of the test field. This additional light then equals the amount of scattered light from the straylight source.

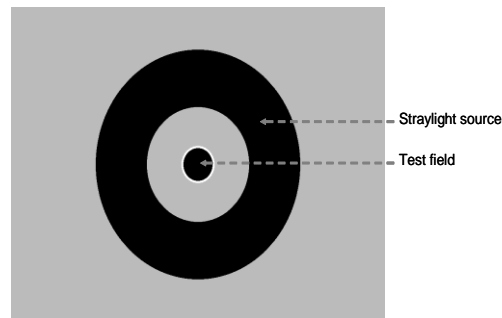


Figure 2.13 Direct compensation (flicker) method

2.4.2.3 Flicker cancellation

Similar to the flicker compensation technique introduced by van den Berg et al (1992), a flicker cancellation test was developed at City University London (Hennelly et al., 1998, Hennelly et al., 1997). The novel contribution to this intraocular scatter light measurement method was the fact that scatter is evaluated for five different eccentricities instead of only one. A new algorithm was developed to estimate the effective eccentricity of each extended annulus. This allows an estimation of not only the straylight parameter k but also the scatter index n , as described in equation 2.1. Moreover, an integrated straylight parameter k' is calculated, based on the empirical scatter function derived from k and n (Barbur et al., 1995).

2.4.2.4 Compensation Comparison

A more recent psychophysical method is the “compensation comparison” method (Franssen et al., 2006). In this method, the central test field consists of two adjoined semi-circular targets (figure 2.14) where different amounts of light are presented to each half. The subject, in a series of forced choice responses, is asked to select the semi-

circular test field with the stronger flicker. The equivalent luminance is estimated by means of the subject's responses after fitting an appropriate psychometric function. The compensation comparison method is commercially used in the C-Quant instrument (Oculus GmbH, Germany).

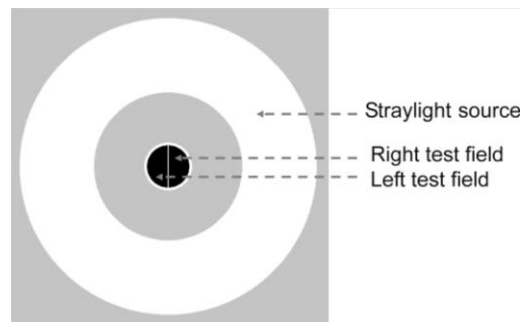


Figure 2.14 Compensation Comparison method

2.5 Glistenings in IOLs and their effect on vision

Implantation of intraocular lenses in the human eye is a widespread method of treating cataract or correcting refractive errors such as myopia. In cataract surgery the artificial lens (IOL) works as a substitute for the crystalline lens, normally being placed in the capsular bag and held in position by its haptics, which act as spacers. In the case of refractive correction, a phakic IOL is placed in the posterior chamber in front of the crystalline lens, without contacting or replacing the existing natural lens of the eye. This method is used when parameters such as high refractive error or corneal thickness is a contra-indication for laser surgery.

IOLs are manufactured from polymers that are divided into two main categories: acrylic and silicone. Acrylic lenses are further divided into rigid (PMMA) and foldable (hydrophobic or hydrophilic polymers). Several studies for uveal and capsular biocompatibility have been carried out either relating it to IOL design (Schauersberger et al., 2001) or ocular diseases and inflammation (Richter-Mueksch et al., 2007). Glass transition temperature, T_g (the temperature at which a polymer changes from a hard, glassy material to a soft, rubbery material), of foldable acrylics is close to room temperature while for silicone-based materials it is significantly lower. Temperature is a significant factor in generating glistenings, as described later. Acrylic lenses in general unfold in a more controlled manner, while silicone lenses tend to spring open more rapidly. Another important difference is the refractive index: silicone materials provide

low refractive index varying from 1.41 to 1.46, while acrylics start from 1.47 and can be found up to 1.56. As a result, acrylic lenses are thinner than silicone lenses for the same refractive power.

Glistenings are fluid-filled microvacuoles that form within the IOL when in an aqueous environment. Hydrophobic acrylic IOLs have been known to be most susceptible to developing glistenings although they have also been observed by slitlamp examination in many different IOL materials (Klos et al., 1999, Tognetto et al., 2002, Werner, 2010). Although there have been reports about patients' reduced contrast sensitivity due to glistenings (Dhaliwal et al., 1996), there are discrepancies among reports about whether glistenings affect a patient's vision (Oshika et al., 2001, Christiansen et al., 2001, Gunenc et al., 2001).

The mechanism of glistening formation relies on the fact that polymers generally absorb water when immersed in an aqueous environment for an extended time. Absorbed water exists in the form of vapour, which makes it invisible. However, a phase separation within the polymer matrix can result in the formation of a visible water droplet. The refractive index difference of these water droplets ($n = 1.333$) and the IOL polymer material causes refraction and scatter, giving a sparkling appearance to these fluid-filled vacuoles hence their name "glistenings" (figure 2.15). Polymer water absorption is associated with temperature (Miyata, 2007). For hydrophobic acrylics, when the temperature is below the glass transition temperature (T_g), water absorption is minimised. On the other hand, when the temperature is above T_g , the material softens and water absorption increases. As a result, temperature fluctuations in the aqueous humour may cause formation of glistenings (Kato et al., 2001).



Figure 2.15 In vitro glistenings in an intraocular lens.

Although the mechanism of glistening formation is widely accepted, factors that influence the formation remain unclear. The most likely factors to have an impact on the

development of glistenings currently include: IOL manufacturing techniques, IOL packaging, pathological conditions such as glaucoma or breakdown of blood-aqueous barrier (BAB) and ocular medication.

In phakic IOLs (PIOL), glistenings have rarely been reported. An individual case study for the Artiflex foldable iris-fixated phakic intraocular lens by Cisneros-Lanuza et al (Cisneros-Lanuza et al., 2007) reported the appearance of glistenings and evaluated their visual significance. Twenty eyes of thirteen patients were examined with a slit-lamp while visual acuity was also measured. No significant visual disturbances and no complaints from patients were reported for any of the cases. However, an interesting observation, which could contribute to the investigation of the factors influencing the formation of glistenings, was that a curious distribution of glistenings along the implantation axis was observed. This is an area that the insertion spatula comes in contact with during implantation. Interaction of surgical devices with intraocular lenses has also been reported by Sher et al (Sher et al., 2008) suggesting that the intra-operative use of Viscoat is associated with the development of late calcification and opacification of the Hydroview hydrogel IOL.

Chapter 3

Methodology

3.1 Experimental set-up

Although an experimental setup had already been developed for use with tissue samples (Hull et al., 2009), a revised setup was necessary to measure intraocular lenses. Three main areas have been examined in the development of the current system:

- a) Modification of the system to measure IOLs with optical power.
- b) Improvement in the alignment and calibration procedures to improve repeatability.
- c) Use of new optomechanics to improve precision and stability.

The newly developed experimental setup is shown schematically in figure 3.1 (plan view) and figure 3.2. The whole system is mounted on an optical breadboard (Thorlabs Ltd, Ely Cambridgeshire, UK) that in turn is placed on an air-damped antivibration workstation (Intracel Ltd, Royston, UK). The importance of this table is that it isolates the system from external vibration, a problem that was noted in the original development of the system. Further details for each component follow:

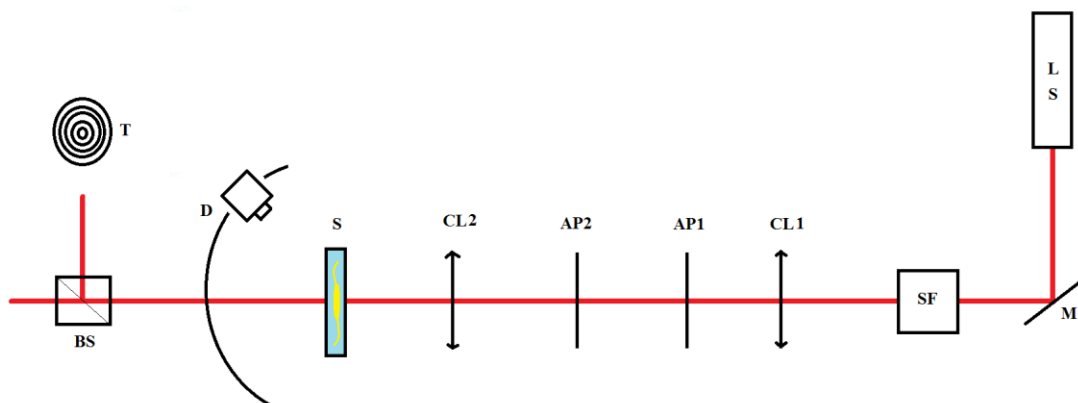


Figure 3.1. Experimental Setup. LS, Monochromatic Light Source; M, mirror; SF, Spatial Filter; CL1, collimator achromatic lens; AP (1&2), apertures; CL2, achromatic lens; S, IOL sample stage; D, detector; BS, cube beam splitter; T, target;

A He-Ne laser (543 nm wavelength) emits a beam of coherent monochromatic light. The wavelength, λ , is 543nm and was chosen to give a measure of light scatter more closely related to in vivo scattering since the wavelength approximates the peak of the human eye's photopic sensitivity at 555nm and is closer to the centre of the visible spectrum than for example a 633nm red He-Ne laser. The laser beam strikes the surface of an alignment mirror (M). It is a plane, front-surfaced mirror which is used to turn the beam through 90° and allow a longer beam path while keeping within the horizontal width of the air-damped table. The purpose of the mirror is also to remove any slight beam misalignment. A spatial filter assembly, consisting of an objective microscope lens and a pinhole set precisely at the objective lens' focus, rapidly diverges the beam and removes spatial imperfections. An achromatic collimating lens (CL) of focal length $f=160\text{mm}$ collimates the beam resulting in a Gaussian beam profile with a spot size of 1cm diameter approximately. The use of an aberration-controlled achromat provides reduced spherical aberration even though there is only one wavelength present. An aperture (AP1) "top-hats" the Gaussian beam, resulting in an approximately uniform beam intensity across its diameter. A second aperture (AP2) is used to control the test beam diameter and is varied to allow different volumes of the IOL to be measured for light scatter. It acts as a surrogate for the pupil in the human eye, which is a main factor controlling the amount of light reaching the IOL. This development allows us to explore variations with pupil size and potentially link our results to visual performance under photopic and mesopic conditions.

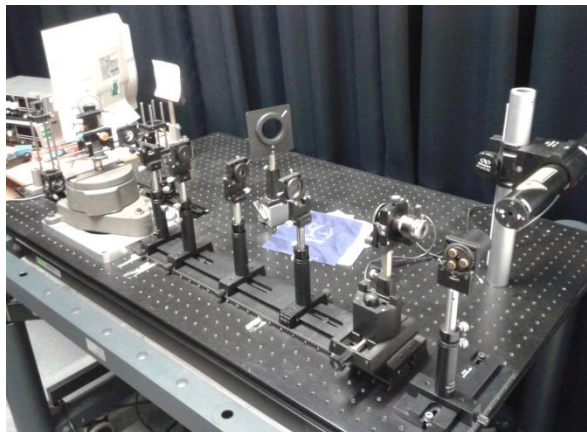


Figure 3.2 Lab view setup

The measurements that our scatter measurement system makes are in "star space" i.e. the beam transmitted by the IOL is collimated within the geometrical optics approximation. The detector therefore measures the scattered light irradiance profile in two dimensions. If a collimated beam was incident on the IOL, the result would be a focused beam which would be impractical for the detector to measure (the focus would fall too close to the

centre of rotation of the detector stage) and not provide information about the irradiance distribution of the scattered light. To avoid this, an afocal system similar to that shown in figure 3.3 is formed using an achromatic lens (CL2) of focal length $f=80\text{mm}$ to focus the test beam at the anterior focal point of the IOL. This results in a magnified collimated beam exiting the IOL and incident on the detector assembly. The consequence is that the angular distribution of scattered light can now be measured in star space for each IOL irrespective of its power. All optical components are wiped gently with premium optical cleaning tissues dampened with isopropyl alcohol at the beginning of every study, preventing any dust and therefore scatter contribution.

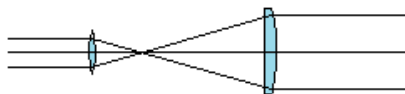


Figure 3.3. Scheme of an afocal system formed using an achromatic lens and a converging (IOL) lens.

To achieve collimation, the focusing lens (CL2) is adjusted longitudinally given that the IOL remains in a fixed location at the centre of rotation of the detector assembly. Collimation is verified with the use of a shear plate (parallel vertical interference fringes are seen when the beam is collimated). The IOL sample stage (S) consists of a fluorimeter cell (Starna Scientific Ltd, Hainault, UK) and customized holder. The cell is held by a plate holder (LINOS, Qioptiq Photonics GmbH & Co. KG, Germany) with a leaf spring for gentle clamping of the rectangular quartz cell. The entire sample stage has X-Y-Z freedom to allow alignment of the intraocular lens at the centre of detector's rotary stage.

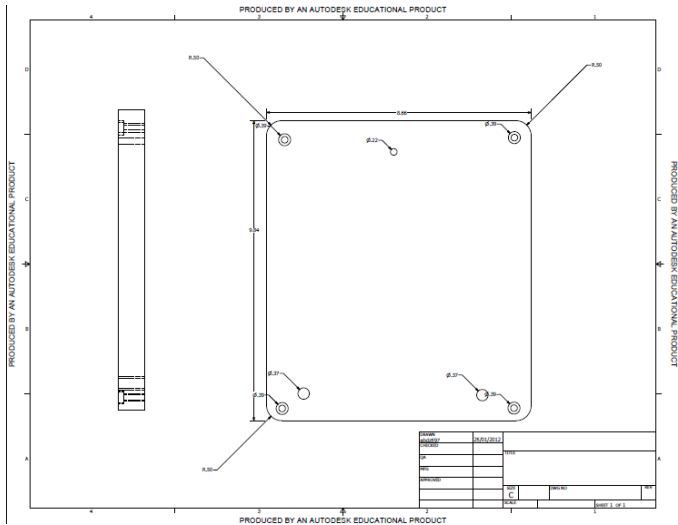


Figure 3.4. Autodesk Platform drawing

Control of the beam diameter at the IOL could not be set directly since our system is telescopic hence AP2 could not be placed between lens L and the IOL. Furthermore the

diameter of AP2 is not the size of the beam reaching the IOL due to magnification. In fact, magnification M is defined as:

$$M = \frac{f_2}{f_1} \quad (3.1)$$

where f_2 is the focal length of the IOL and f_1 the focal length of lens (L). An IOL of 23.0D will result in a 0.54 times magnification of the initial beam size while an 18.0D IOL would give a 0.70 times beam diameter. The power of the IOL affects the beam diameter because the focal length affects how much the beam will have diverged before hitting the sample. Therefore, a cube beam splitter is used during alignment to set the desired beam diameter for each tested IOL by projecting the outgoing beam on to a target (T). Since the IOL's thickness is small, usually just under or close to 1mm, a thin lens approximation was assumed for the IOL accepting that beam size arriving at the front surface of the IOL was equal with the beam size exiting the back surface.

The detector assembly (D) is based on a 5" diameter spectrometer base (The Precision tool & Instrument Co Ltd, Surrey UK) with an angular resolution of 1' of arc. A customised aluminium plate was manufactured to secure the spectrometer table to the breadboard (figure 3.4). The detector itself, which consists of a microscope objective, a pinhole (200 μm), a silicon photodiode and an amplifier (Picoammeter Type SP043, Vinculum, UK), is mounted on one of the spectrometer arms allowing its angle to be precisely controlled. The IOL is placed at the centre of rotation of the spectrometer table.

To check the relative size of the focused spot at the pinhole of the detector the following calculations were performed: The detector is set-up to receive collimated light hence the Airy disc diameter at the focus of the microscope objective is given by

$$\Delta l = 1.22 \times \lambda \times N \quad (3.2)$$

where λ is the wavelength and N is the f-number of the objective lens, defined as $N=f/D$, where f is the focal length and D the diameter of the entrance pupil. This is the minimum beam spot size diameter (BSSD) to which a collimated beam of light can be focused. In our case we have $\lambda=543\text{nm}$, $f=16\text{mm}$ and hence for a 5mm pupil size the BSSD is 21 microns increasing to 35 microns for a 3mm input beam diameter:

The minimum pinhole diameter (MPD) for which the maximum amount of energy is passed, while eliminating as much spatial noise as possible, has been experimentally determined (Cox, 1979):

$$MPD \cong 2 \times BSSD \quad (3.3)$$

hence, for the setup described, the pinhole size should be equal or greater than $2 \times 35\mu m = 70\mu m$.

The pinhole size used initially was 100 μm to provide greater angular sensitivity but following some pilot studies this resulted in a significant reduction of light intensity that exceeded our amplifier's sensitivity. Light collection is our primary objective, therefore it was necessary to maximise that even if that would lead to some spatial impurities in the beam. The next commercially available pinhole size was a 200 μm (Wey Scientific & Photonics Ltd, Surrey, UK), consequently this pinhole size was finally chosen and used throughout the study.

3.2 IOL preparation

One of the fundamental goals was to develop a method where our IOL samples could be tested in a vertical rather than a horizontal plane as was the case for the original setup. This would automatically remove the 45 degree mirrors that were needed to deflect the beam vertically through the culture medium and tissue sample, which had to be horizontal. Removing these mirrors simplifies the alignment and avoids any extra surfaces and sources of scatter. A rectangular, quartz glass fluorimeter cell (Starna Scientific Ltd, Hainault, UK) was chosen to house the sample (figure 3.5). All sides are optical quality to minimize scatter. Additional care was taken to keep the cell clean; Latex gloves were used whenever holding the cell, which was rinsed several times with copious distilled water after each measurement to remove all traces of saline and left open to dry before it was covered with a new clean lens tissue. When the cell was not in use, it was stored in a well-sealed container to avoid dust and damage.

IOLs were delivered to our labs and kept in micro glass vials. Before and after every use, each IOL was carefully washed with distilled water to remove any salt stains or other deposits on their surfaces. To support the IOL, two customised plastic holders as shown in figure 3.5, were designed and manufactured. Each one has a circular central aperture with an inner groove. Two different fixtures were used to accommodate IOLs with 7mm

and 6mm optic diameters. The haptics of the IOL were placed within the grooves of the central aperture using forceps. The elastic properties of the IOL haptics were used to keep the IOL stable and centered within the fixture. The IOL holder is submerged in the fluorimeter cell containing saline. Fresh saline (Sensitive Eyes Plus, Bausch & Lomb, Rochester NY) was used for every measurement.

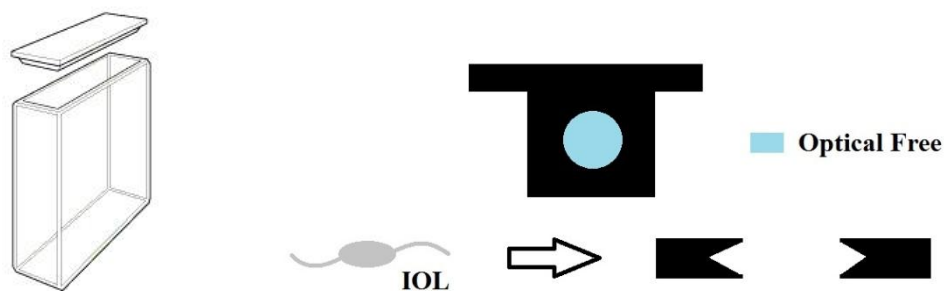


Figure 3.5. Scheme of the IOL holder device

For different parts of the project, IOLs were delivered to our labs either pre-treated to induce glistenings or untreated within the manufacturer's packaging. Pre-treated IOLs were kept prior to testing in an incubator (Heraeus Heracell, Kendro, Germany) under constant 35°C temperature and a 5% CO₂ level, maintaining the optimum physiological pH for Balanced Salts Solutions (BSS). Such a controlled and stable environment for the IOL has been reported to preserve the glistenings size, density and pattern (Thomes and Callaghan, 2013).

Formation of glistenings *ex vivo* can be achieved by subjecting IOLs to thermal gradients. Various protocols have been suggested and followed in previous *in vitro* studies (Gregori et al., 2002, Matsui, 2006, Kato et al., 2001, Miyata et al., 2001, van der Mooren et al., 2013, Shiba et al., 2002, Oshika et al., 2001, Pagnouille et al., 2012, Omar et al., 1998). In general the thermal gradient protocols can be categorized into those with high temperature fluctuations over a short period of time or smaller fluctuations near the normal human body temperature but over a longer period. For example, recently Pagnouille et al (2012) followed a protocol of incubating the IOLs in saline at 60°C for 1 hour, observing under a microscope at 23°C (room temperature), reheating and observing again at 60°C and finally drying at 65°C for 48 hours. In contrast, Omar et al (1998) had followed a protocol of 336 hours (14 days) of incubation at a constant 37°C. The argument between the different temperature ranges is whether such environmental conditions exist in reality in the human eye; normal fluctuations are small, usually within

$\pm 1^{\circ}\text{C}$ while even in the case of high fever, the temperature does not exceed 41°C . However, for laboratory studies due to time limitations, accelerated methods are more practical.

In our study, glistenings were induced by following the thermal grading protocol devised by our collaborators, Advanced Vision Science Inc.:

- 1) IOLs are removed from their container
- 2) Transfer to sealed glass vials containing fresh saline
- 3) Vials are placed in 50°C for 5 days (120 hours)
- 4) Lenses are cooled down to room temperature and then inspected/measured

After step 3 ($50^{\circ}\text{C}/5\text{days}$) if lenses are not to be measured directly, vials are kept in a constant 35°C environment as is the case for all treated IOLs. Before testing, the IOL is carefully rinsed using distilled water at room temperature, to remove any saline crystallization on the lens surfaces.

3.3 Procedure

Before any test, our light source is turned on in advance for at least 3 hours. This allows the laser output to stabilize, avoiding significant fluctuations that could affect our measurements. The IOL to be tested is placed in the fluorimeter cell as previously described. The cell is clipped on to the plate holder, hanging above the detector's centre of rotation. The IOL is centred and aligned with the experimental setup by restoring the beam's propagation according to our target, T (figure 3.1).

Collimation of the outgoing beam was achieved by adjusting the longitudinal position of lens L, and assessed using the shear plate test as well as comparing the beam size arriving at a near (10cm) and a far (1m) target. Lights were turned off and black curtains surrounding our optical bench were drawn, creating dark environmental conditions. The amplifier was turned on and the zero reading was found by adjusting the angular position of the detector to give a peak reading on the microammeter (coarse adjustment). The pinhole position for the detector was then adjusted to maximise the reading (fine adjustment). The spectrometer reading was entered into a spreadsheet (figure 3.6) which automatically produces the spectrometer table values for the detector arm to give a range of values up to ± 18 degrees.

| Degrees | | Minutes | Degrees | | Minutes | Degrees | | Minutes |
|------------|----------|----------------------|-------------|--------------|-------------|-------------|--|---------|
| Left edge: | | | Point Zero: | | | Right edge: | | |
| 258 | | 50 | 259 | | 40/60 | 260 | | 30 |
| Step | Angle | Individual Positions | | Measurements | Sensitivity | Results | | |
| -18 | -18 | 241 | 40/60 | 0.015 | 0.0000001 | 1.5E-09 | | |
| -17 | -14 | 245 | 40/60 | 0.03 | 0.0000001 | 0.00000003 | | |
| -16 | -10 | 249 | 40/60 | 0.083 | 0.0000001 | 8.3E-09 | | |
| -15 | -7 | 252 | 40/60 | 0.223 | 0.0000001 | 2.23E-08 | | |
| -14 | -5 | 254 | 40/60 | 0.743 | 0.0000001 | 7.43E-08 | | |
| -13 | -4 | 255 | 40/60 | 0.134 | 0.0000001 | 0.000000134 | | |
| -12 | -3 30/60 | 256 | 10/60 | 0.218 | 0.0000001 | 0.000000218 | | |
| -11 | -3 | 256 | 40/60 | 0.287 | 0.0000001 | 0.000000287 | | |
| -10 | -2 30/60 | 257 | 10/60 | 0.459 | 0.0000001 | 0.000000459 | | |
| -9 | -2 | 257 | 40/60 | 0.769 | 0.0000001 | 0.000000769 | | |
| -8 | -1 45/60 | 257 | 55/60 | 0.101 | 0.0000001 | 0.000000101 | | |
| -7 | -1 30/60 | 258 | 10/60 | 0.139 | 0.0000001 | 0.000000139 | | |
| -6 | -1 15/60 | 258 | 25/60 | 0.21 | 0.0000001 | 0.00000021 | | |
| -5 | -1 | 258 | 40/60 | 0.371 | 0.0000001 | 0.000000371 | | |
| -4 | - 50/60 | 258 | 50/60 | 0.611 | 0.0000001 | 0.000000611 | | |
| -3 | - 40/60 | 259 | | 0.101 | 0.0001 | 0.00000101 | | |
| -2 | - 30/60 | 259 | 10/60 | 0.107 | 0.001 | 0.00000107 | | |
| -1 | - 20/60 | 259 | 20/60 | 0.105 | 0.01 | 0.00000105 | | |
| 0 | 0 | 259 | 40/60 | 0.143 | 1.00E-02 | 0.00000143 | | |
| 1 | 20/60 | 260 | | 0.678 | 0.0001 | 0.00000678 | | |
| 2 | 30/60 | 260 | 10/60 | 0.974 | 0.0000001 | 0.000000974 | | |
| 3 | 40/60 | 260 | 20/60 | 0.564 | 0.0000001 | 0.000000564 | | |
| 4 | 50/60 | 260 | 30/60 | 0.406 | 0.0000001 | 0.000000406 | | |
| 5 | 1 | 260 | 40/60 | 0.254 | 0.0000001 | 0.000000254 | | |

Figure 3.6. Angle calculator and data spreadsheet.

In total, thirty seven (37) eccentricity values are used; eighteen (18) from each side (right and left) plus the zero angle corresponding to the centre of the peak. Steps, as shown in Table 3.1, are non-linear due to the shape of the scatter function being every 10 arcmin near the peak and dropping to every 4 degrees in the periphery of the scatter function.

| Step | Angle |
|------|--------|
| 0 | 0 |
| 1 | 0° 20' |
| 2 | 0° 30' |
| 3 | 0° 40' |
| 4 | 0° 50' |
| 5 | 1° |
| 6 | 1° 15' |
| 7 | 1° 30' |
| 8 | 1° 45' |
| 9 | 2° |
| 10 | 2° 30' |
| 11 | 3° |
| 12 | 3° 30' |
| 13 | 4° |
| 14 | 5° |
| 15 | 7° |
| 16 | 10° |
| 17 | 14° |
| 18 | 18° |

Table 3.1 Detector eccentricity values for measured points on the scatter function.

A computer programme written in Java reports running average and instantaneous values from the detector and allows us to view fluctuating readings and record stable output values. Results were recorded directly on to the spreadsheet, with a ± 0.001 precision for the amplifier's reading. The amplifier sensitivity and gain was also noted and multiplied with the reading to produce the actual detector output.

When a measurement run was completed, the spreadsheet was saved with the IOL code name. For each IOL, the procedure described above was repeated three times, one for each pupil size: 3mm, 4mm and 5mm. A typical measurement run for one pupil size would take an hour, therefore to repeat the procedure for the three pupil sizes would take up to three hours.

3.4 Repeatability and Reproducibility

Prior to starting collection of our main experimental data, it was important to test whether the measurement system produced valid data that meets the needs of the study. Specifically we have sought to determine the repeatability and reproducibility of the scatter measurement system.

Repeatability is the variation that results from repeat measurements of the same parameter. Measurements are taken within a short period of time; in this case, no changes are made to the system set-up and calibration and the sample is not moved between measurements. Reproducibility measures the variation in a parameter when an attempt is made to reproduce measurements at different time points. It therefore includes variation caused by the system set-up and calibration, sample preparation and placement as well as environmental factors.

For repeatability, five sets of measurements for an IOL with a moderate level of glistenings (grade 3) and average pupil size of 4mm were taken without displacing the IOL's position in the setup. Mean output and standard deviation for each eccentricity was calculated from the five measurements. Since the light intensity varies typically over a 4 log unit range, variation for each of the measurement points is compared by calculating the coefficient of variation (CV), defined as the ratio of the standard deviation to the mean.

Results are shown in Table 3.2. Right [+] Output stands for the positive eccentricities while Left [-] Output for the negative ones.

| Eccentricity (°) | Mean Output Right [+] (A) | SD (A) | CV | Mean Output Left [-] (A) | SD (A) | CV |
|------------------|---------------------------|-----------------------|------|--------------------------|-----------------------|------|
| 0 | 1.06×10^{-3} | 0.34×10^{-3} | 0.32 | | | |
| 0° 20' | 5.58×10^{-4} | 2.93×10^{-4} | 0.53 | 8.01×10^{-5} | 3.11×10^{-5} | 0.39 |
| 0° 30' | 7.95×10^{-5} | 3.71×10^{-5} | 0.47 | 8.57×10^{-6} | 4.32×10^{-6} | 0.50 |
| 0° 40' | 2.37×10^{-5} | 0.61×10^{-5} | 0.26 | 3.89×10^{-6} | 1.45×10^{-6} | 0.37 |
| 0° 50' | 5.38×10^{-6} | 1.48×10^{-6} | 0.27 | 2.08×10^{-6} | 0.69×10^{-6} | 0.33 |
| 1° | 2.89×10^{-6} | 0.66×10^{-6} | 0.23 | 1.43×10^{-6} | 0.44×10^{-6} | 0.31 |
| 1° 15' | 2.76×10^{-6} | 1.35×10^{-6} | 0.49 | 1.01×10^{-6} | 0.33×10^{-6} | 0.33 |
| 1° 30' | 1.04×10^{-6} | 0.11×10^{-6} | 0.11 | 6.44×10^{-7} | 2.39×10^{-7} | 0.37 |
| 1° 45' | 7.12×10^{-7} | 1.37×10^{-7} | 0.19 | 4.69×10^{-7} | 1.83×10^{-7} | 0.39 |
| 2° | 5.44×10^{-7} | 1.22×10^{-7} | 0.22 | 3.50×10^{-7} | 1.45×10^{-7} | 0.41 |
| 2° 30' | 3.52×10^{-7} | 0.83×10^{-7} | 0.23 | 2.61×10^{-7} | 1.06×10^{-7} | 0.40 |
| 3° | 2.91×10^{-7} | 0.64×10^{-7} | 0.22 | 2.31×10^{-7} | 0.89×10^{-7} | 0.38 |
| 3° 30' | 2.21×10^{-7} | 0.53×10^{-7} | 0.24 | 1.85×10^{-7} | 0.71×10^{-7} | 0.38 |
| 4° | 1.56×10^{-7} | 0.38×10^{-7} | 0.24 | 1.38×10^{-7} | 0.51×10^{-7} | 0.37 |
| 5° | 8.57×10^{-8} | 2.40×10^{-8} | 0.28 | 7.03×10^{-8} | 3.22×10^{-8} | 0.46 |
| 7° | 4.12×10^{-8} | 1.11×10^{-8} | 0.27 | 3.36×10^{-8} | 1.30×10^{-8} | 0.39 |
| 10° | 1.61×10^{-8} | 0.38×10^{-8} | 0.24 | 1.67×10^{-8} | 0.55×10^{-8} | 0.33 |
| 14° | 7.14×10^{-9} | 1.74×10^{-9} | 0.24 | 8.48×10^{-9} | 2.45×10^{-9} | 0.29 |
| 18° | 3.04×10^{-9} | 0.71×10^{-9} | 0.23 | 3.62×10^{-9} | 1.34×10^{-9} | 0.37 |

Table 3.2 Repeatability for an IOL with Grade 3 glistenings (4mm pupil)

Coefficients of variation, CV, gave a mean value of 0.33 ± 0.09 . This means that actual measurements have a mean relative variability of 33%. CV values are generally similar across the range. When measurements are very small (close to zero), as in our case, the CV value is very sensitive to changes and therefore appears to be sizable. On the steeper slopes of the scatter function, variation is higher since very small differences in setting the angle will cause larger differences in repeat readings. Therefore, the fact that the CV is smaller than 1 in all cases is evidence that the distribution can be considered as having a low-variance, regarding the low values of our measurements combined with the scatter function steepness.

Results in Table 3.2 demonstrate that our experimental measurements are repeatable. A graphical representation of the results is shown in figure 3.7, which demonstrates good repeatability for measured data points on the scatter function.

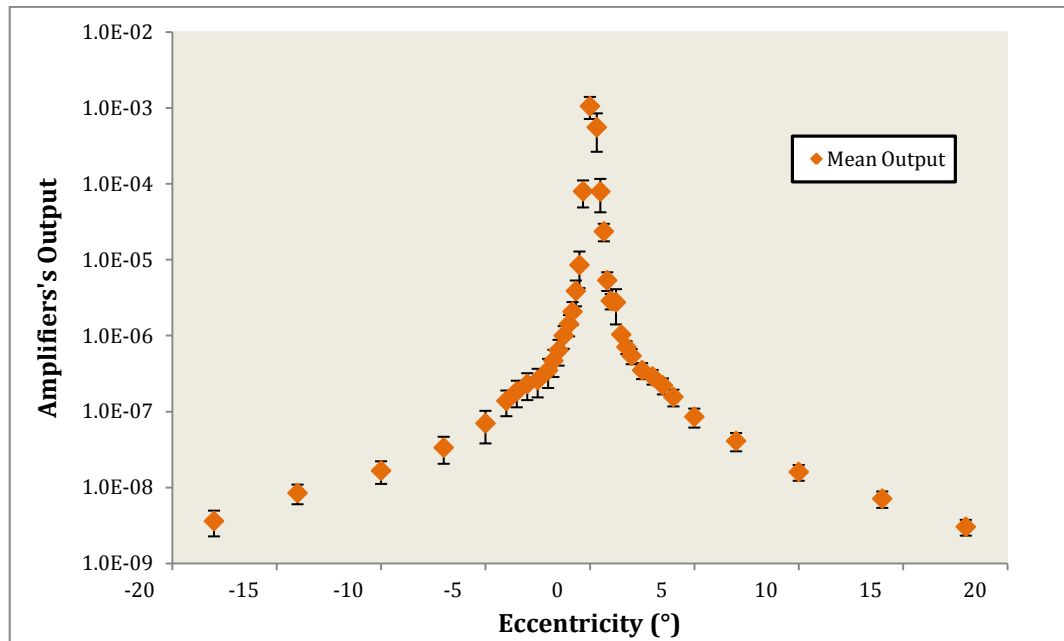


Figure 3.7 Repeatability mean values and corresponding standard deviations. Y-axis is plotted in a logarithmic scale.

For reproducibility, once again 5 different sets of measurements were taken for the same IOL with a moderate level of glistenings (grade 3) and average pupil size (4mm). Before each measurement run, the IOL was removed from the setup and replaced following the procedure described in section 3.3. The mean values, standard deviations and coefficients of variation were calculated for each eccentricity using the five readings. The results are shown in Table 3.3.

The coefficients of variation, CV, have a mean value of 0.31 ± 0.18 , hence when reproducing our measurements there is $\pm 31\%$ variability between IOLs with a moderate glistenings grade. Repeatability and reproducibility of our procedure showed a similar CV mean value of 0.33 and 0.31 respectively. This result indicates that the extra procedures required when testing reproducibility did not add additional measurement variation hence our procedure can be considered reliable. The standard deviations, however, showed that the variation of measurements for reproducibility was double the variation of repeatability (± 0.18 and ± 0.09 respectively). This is an expected result as reproducing a procedure involves additional external factors than repeating a measurement which reflects random fluctuations in the measurement system only.

Figure 3.8 shows the measured scatter function for reproducibility with mean output values and their corresponding standard deviations represented as error bars.

| Eccentricity (°) | Mean Output Right [+] (A) | SD (A) | CV | Mean Output Left [-] (A) | SD (A) | CV |
|------------------|---------------------------|-----------------------|------|--------------------------|-----------------------|------|
| 0 | 1.07×10^{-3} | 0.26×10^{-3} | 0.24 | | | |
| 0° 20' | 4.12×10^{-4} | 3.24×10^{-4} | 0.79 | 2.14×10^{-4} | 1.58×10^{-4} | 0.74 |
| 0° 30' | 4.92×10^{-5} | 2.12×10^{-5} | 0.43 | 2.29×10^{-5} | 2.02×10^{-5} | 0.88 |
| 0° 40' | 1.40×10^{-5} | 0.68×10^{-5} | 0.48 | 5.41×10^{-6} | 2.05×10^{-6} | 0.38 |
| 0° 50' | 4.17×10^{-6} | 1.45×10^{-6} | 0.35 | 2.51×10^{-6} | 0.69×10^{-6} | 0.27 |
| 1° | 2.84×10^{-6} | 1.07×10^{-6} | 0.38 | 1.67×10^{-6} | 0.42×10^{-6} | 0.25 |
| 1° 15' | 2.17×10^{-6} | 1.28×10^{-6} | 0.59 | 1.03×10^{-6} | 0.22×10^{-6} | 0.21 |
| 1° 30' | 9.66×10^{-7} | 1.68×10^{-7} | 0.17 | 6.60×10^{-7} | 1.67×10^{-7} | 0.25 |
| 1° 45' | 6.93×10^{-7} | 1.26×10^{-7} | 0.18 | 4.72×10^{-7} | 1.24×10^{-7} | 0.26 |
| 2° | 5.33×10^{-7} | 1.01×10^{-7} | 0.19 | 3.69×10^{-7} | 1.08×10^{-7} | 0.29 |
| 2° 30' | 3.63×10^{-7} | 0.53×10^{-7} | 0.15 | 2.91×10^{-7} | 0.86×10^{-7} | 0.30 |
| 3° | 2.91×10^{-7} | 0.44×10^{-7} | 0.15 | 2.52×10^{-7} | 0.70×10^{-7} | 0.28 |
| 3° 30' | 2.15×10^{-7} | 0.38×10^{-7} | 0.18 | 1.92×10^{-7} | 0.54×10^{-7} | 0.28 |
| 4° | 1.45×10^{-7} | 0.33×10^{-7} | 0.23 | 1.34×10^{-7} | 0.38×10^{-7} | 0.28 |
| 5° | 7.94×10^{-8} | 2.02×10^{-8} | 0.25 | 7.23×10^{-8} | 2.08×10^{-8} | 0.29 |
| 7° | 4.08×10^{-8} | 0.94×10^{-8} | 0.23 | 3.28×10^{-8} | 0.85×10^{-8} | 0.26 |
| 10° | 1.70×10^{-8} | 0.19×10^{-8} | 0.11 | 1.72×10^{-8} | 0.42×10^{-8} | 0.24 |
| 14° | 7.28×10^{-9} | 1.35×10^{-9} | 0.19 | 8.56×10^{-9} | 2.27×10^{-9} | 0.12 |
| 18° | 3.24×10^{-9} | 0.65×10^{-9} | 0.20 | 4.00×10^{-9} | 1.53×10^{-9} | 0.38 |

Table 3.3 Reproducibility for an IOL with Grade 3 glistenings (4mm pupil)

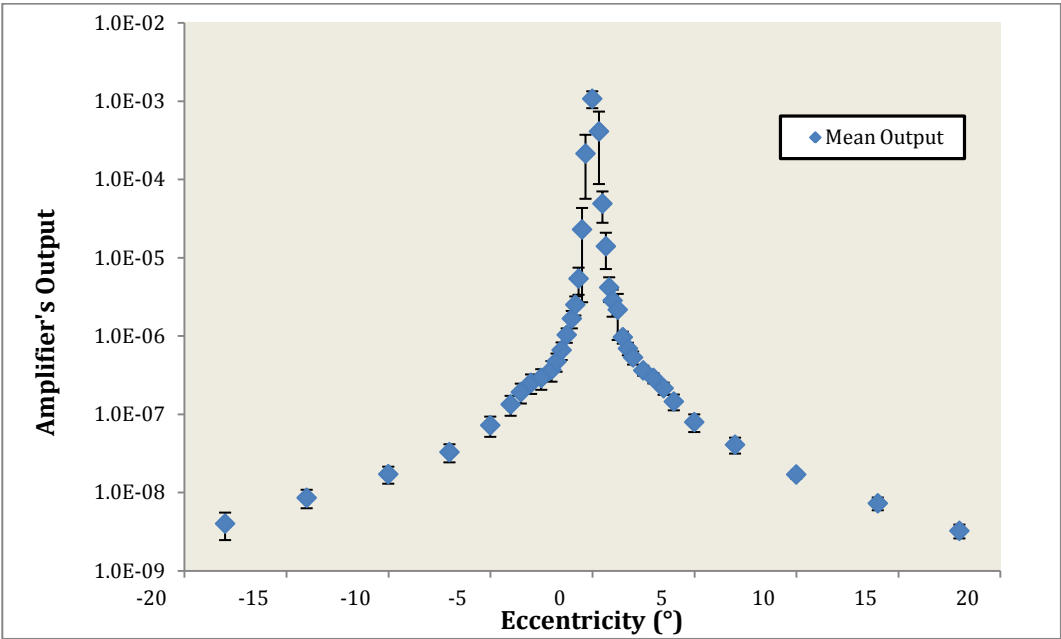


Figure 3.8 Reproducibility; mean values and corresponding standard deviations.

3.5 Imaging and Quantifying Glistenings

3.5.1 Imaging Methods

One of the fundamental aims of this study was to investigate the association between the measured scatter function and the size, density and distribution of the glistenings in the IOLs. Our approach was to capture digital images of the IOLs using a standardised protocol and carry out image processing to extract these metrics.

Different methods for imaging intraocular lenses and glistenings have been used in previous studies. These can be categorized first as either *in vivo* or *in vitro*. *In vivo* studies have used either the Scheimpflug photography (Klos et al., 1999, Ayaki et al., 2006, Behndig et al., 2009, Mönestam et al., 2011, Rønbeck et al., 2013, Miyata et al., 2012) or slit-lamp imaging (Christiansen et al., 2001, Colin et al., 2009, Dhaliwal et al., 1996, Miyata et al., 2001, Tognetto et al., 2002, Waite et al., 2007). Studies reporting *in vitro* imaging have also used slit-lamp photography (Gregori et al., 2002, Omar et al., 1998, Oshika et al., 2001), optical microscopes (Kato et al., 2001, Kim et al., 2011, Pagnouille et al., 2012, Saylor et al., 2010) or confocal light and dark field microscopy (van der Mooren et al., 2013).

Scheimpflug photography is used for evaluation and study of the anterior segment. It can display sections of the anterior eye segment from cornea to posterior lens pole, (figure 3.9). Any reflective structures appear white, like the lens anterior and posterior surfaces. Therefore, glistenings which act as refractive particles appear as white specks. This allows a depth evaluation of the glistenings, i.e. whether their location is near the surface or the centre of the lens volume and also whether located centrally or in the periphery of the lens.

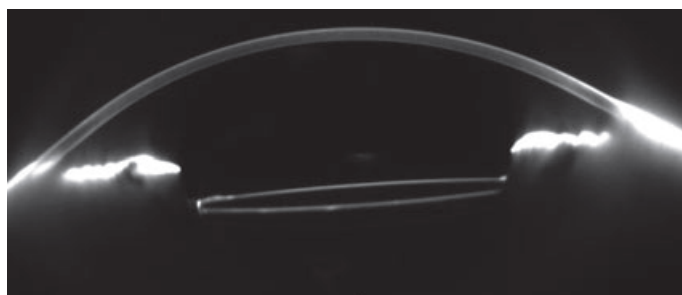


Figure 3.9 IOL imaging with Scheimpflug photography (Rønbeck et al., 2013)

The slit-lamp is one of the fundamental tools for a clinician to assess the anterior segment, and with an additional lens, the retina. Therefore, it can be used for glistenings inspection and IOL imaging. For *in vivo* slit-lamp photography, clinicians usually

illuminate part of the IOL with a narrow slit beam, around 2mm in width and at maximum height. The illuminating slit beam angle is between 30° and 40° , similar to that shown in figure 3.10 (left). The illuminated volume of the lens is defined by the reflections of light from the front and back surface of the IOL, while glistenings that lie in between, appear as shining bright structures.

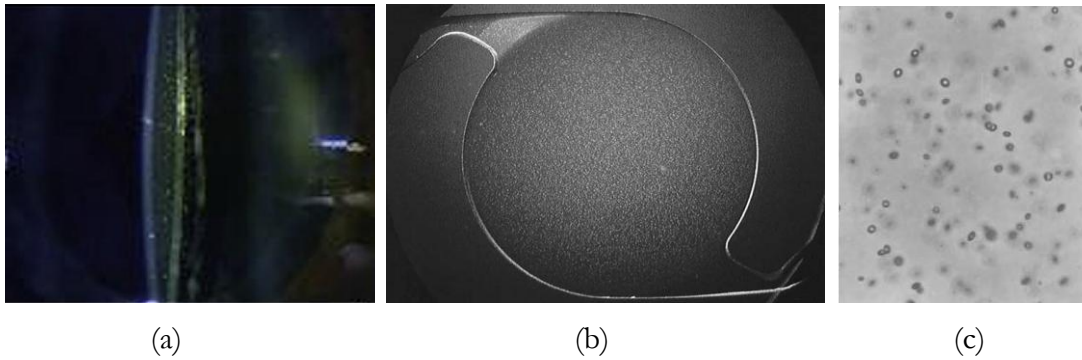


Figure 3.10 Methods of imaging IOL glistenings: (a) in vivo slit-lamp photography (Colin et al., 2009), (b) in vitro slit-lamp photography (Gregori et al., 2002) and (c) reflecting microscopy (Kato et al., 2001)

Slit-lamp imaging for the in vivo case records backscatter, whereas the retina perceives forward scatter; It has been shown (van der Mooren et al., 2013) that although for small size particles (less than the wavelength of light) scatter is distributed uniformly in all directions, the ratio of backward to forward scatter for large particles is poor, i.e. the amount of scattered light observed by a clinician is not representative of what the retina perceives. For in vitro quantification of glistening, this is not a major factor since imaging is used only to quantify the size and pattern of the glistenings. In vitro slit-lamp imaging can provide illumination of the full lens diameter, as shown in figure 3.10 (centre), where position and light illumination direction can be adjusted as desired.

A microscope can provide high magnification imaging of the IOL and is consequently able to observe in high definition the structure of the glistenings (figure 3.10, right). Confocal microscopy can also provide information about the depth location within the lens of any glistenings. In addition, if the illumination comes from behind the sample, the camera receives the forward light scatter caused by the glistenings which reduces the contrast of the image; weak and small glistenings can therefore be hard to detect. A study of posterior capsule opacification imaging has shown that reflected-light photography has a better performance when compared with retroillumination images to perceive and display the presence and severity of the PCO (Camparini et al., 2000). Another disadvantage of microscopes is that in order to have a focused and detailed view of the

glistenings, the field of view of the lens is reduced; an attempt has been made to overcome this limitation using dark field microscopy (van der Mooren et al., 2013) where the lens is still retroilluminated. The advantage of dark field microscopy though is that the unscattered light is excluded so it is easier to distinguish the glistenings.

3.5.2 Slit-lamp Digital Image capture and analysis

Slit-lamp photography as previously described is widely used by clinicians. In vivo images differ from the in vitro situation as irregularities from the cornea and anterior chamber contribute to scatter and light absorption affecting the image of the IOL and hence glistenings. However, it is easier to link and compare in vivo and in vitro slit-lamp images than other methods, for example, Scheimpflug photography with microscopy where in one case the image is a wide field coronal view while the other produces a narrow, en face, field of view. All the parameters described below have been chosen to produce images that permit quantification of glistenings in terms of size, density and distribution within the lens and for different pupil sizes.

A high resolution digital camera Nikon D90 (body only) was attached to a Nikon FS-2 photo slit-lamp (figure 3.11). Eye piece adjustment was set so that both the camera's optical path and observer's image were in focus simultaneously, by comparing with the camera's outcome image as appearing on the digital screen.



Figure 3.11 Slit-lamp setup

The IOL under test was placed within its holder and submerged in the fluorimeter cell containing fresh saline, as described in paragraph 3.2. The cell was then held, from its left and right sides, by a retort stand clamp in front of the slit-lamp objectives, with supportive foam cushions to minimize the risk of damage to the glass cell. The laboratory

lights were turned off and blackout curtains were drawn; only the slit-lamp’s light source was used. The slit-lamp’s position was adjusted until the IOL was in clear focus and centred in the field of view. Magnification was varied between 16x and 30x, depending on IOL’s optical diameter (7mm or 6mm optic diameter). This ensured that the tested IOL covered as much of the image as possible. Initial camera settings (Table 3.4) were chosen based on recommendations from the NHS National Screening Programmes for Diabetic Retinopathy (June 2009):

| | |
|---------------|-------------|
| ISO | 200 |
| White Balance | AWB |
| Resolution | Medium |
| Size | 3216 x 2136 |
| Compression | Fine |

Table 3.4 NHS Diabetic Retinopathy recommended camera settings

A number of different trials were attempted to find the optimal angle of illumination and shutter speed when using the above settings. Images were captured not only for different angles of slit illumination but for two different conditions: maximum beam width, hence uniform IOL illumination and a 2mm beam width, corresponding to the in vivo slit-lamp IOL imaging methods. The results and steps followed are shown in figure 3.12.

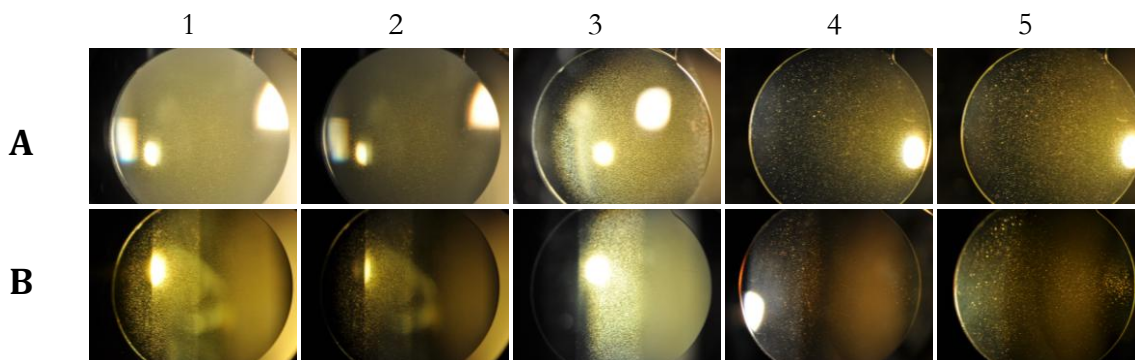


Figure 3.12 Images in row A were taken for a maximum beam width and angle positions of 0°,10°,20°,50°and 60° respectively. Images in row B were taken for a 2mm beam width and angle positions of 0°,10°,40°and 60° respectively.

Reflections from the cuvette’s front surface were evident in most cases. Images least affected by reflections are evident for angles around 60°. The wider the illumination angle used, the higher the shutter speed because of less specularly reflected light. For the images in fig. 3.12, the shutter speed varied between ½ sec to 3.0 sec. Increased exposure time made the image capture more sensitive to blur. To avoid blurring and prevent camera shake during shutter release, a remote shutter release (Nikon MC-DC2) was used.

For angles greater than 65° there is a limitation caused by the presence of the claw holding the cell and blocking the light.

An initial evaluation of our images was undertaken by our collaborators at the Department of Computing and Information Systems, Kingston University to ensure that image processing could be applied to the images to quantify glistenings. Image analysis of a test image is shown in figure 3.13. This demonstrated that it was possible with our images to highlight the area of interest, remove any noise and reflections and identify glistenings for further quantification. The conclusion from this evaluation of image capture methods was that image analysis requires uniform illumination and that using the slit-lamp beam was inadequate as shown in figure 3.12. Therefore an external light source was developed, providing a wider field of illumination.

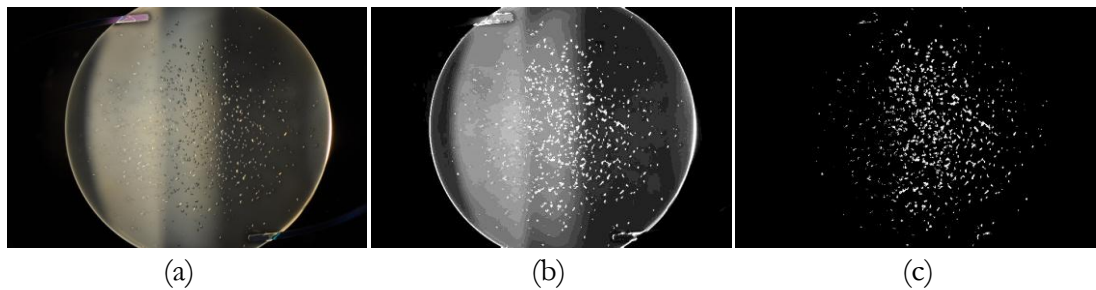


Figure 3.13 Example of an IOL slit-lamp digital image and analysis: (a) original photo taken with a 2mm beam width, (b) the image was analysed in BW by collaborators at Kingston University by (c) highlighting the glistening and removing background noise and reflections.

In our study, images were taken by illuminating the lens with an external custom-made light-emitting diode source. Illumination was from below (bottom to top) with a front angle of 30 degrees, as shown in figure 3.14.

Examples of the resulting images are shown in figure 3.15. It is important to note that although conditions of lighting are fixed and the image capture procedure remains the same, there is a slight variation in the final outcome in terms of colour, brightness and contrast. We assume that this is the result of the different lens materials, their dioptric power and design, thus lens thickness/volume and finally scatter levels caused by the induced glistenings, occurring in the lens interior. A possible limitation of this method is that information about the depth location of the glistenings is not captured. However, the images represent the scattering cross-sections the light interacts with and volume scattering affects are likely to be small, given the thickness of the IOL, size and density of the glistenings. This is further discussed on Chapter 6.

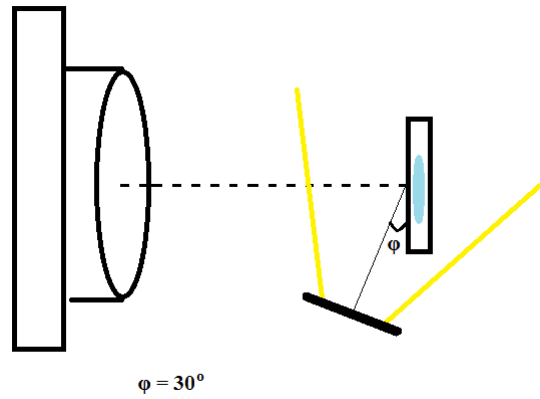


Figure 3.14 Schematic representation of IOL's illumination

For each tested IOL, 10-12 images were captured. The best images in terms of focus and clarity were selected for use by our collaborators at Kingston University, UK and Thammasat University, Thailand who developed the glistenings detection software. This Glistenings Detection Programme is explained in detail in Chapter 5. Our first study described in the next chapter is based on subjective methods of grading the severity of the glistenings. Use of objective quantification is described in Chapter 6.

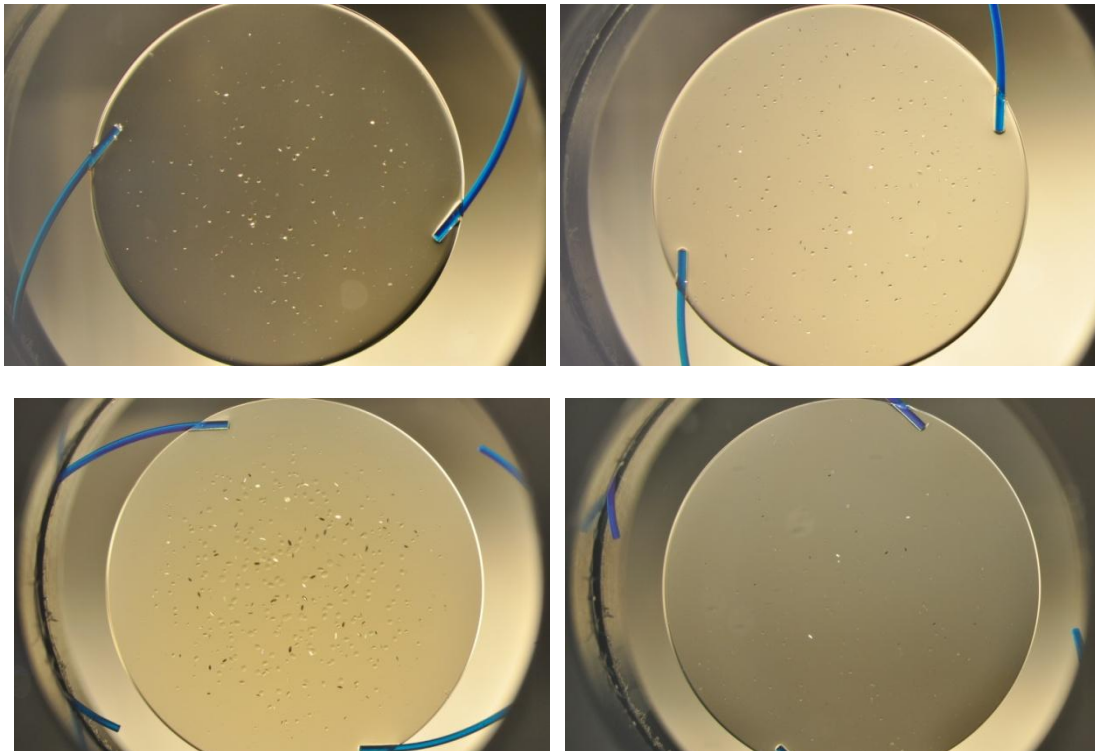


Figure 3.15 IOL glistening capture with a Digital Slit-lamp and uniform illumination

Chapter 4

Association between forward light scatter and subjective grading of IOL Glistenings.

4.1 Introduction

4.1.1 Clinical IOL Glistenings Grading

It is reasonable to expect that characteristics of glistenings have some impact on forward light scatter and hence visual performance. One method to quantify glistenings is to use a clinical grading scale. Clinical grading is subjectively assessed by clinicians observing in vivo the glistenings through a slit-lamp. Several studies (Dhaliwal et al., 1996, Wilkins and Olson, 2001, Cisneros-Lanuza et al., 2007, Mönestam et al., 2011, Colin et al., 2012) have used different grading scales, mostly attempting to grade the number of glistenings present. However, there is no common agreement on a grading scale and grades can represent different numbers of glistening on different scales. In fact, a scale of trace, 1 +, 2 + and 3 + based on standard photographs (figure 4.1) has been proposed by Dhaliwal et al. (1996), a scale from 0 to 3+ with 0 for no glistenings, 1+ for less than 10, 2+ for 10 to 50 and 3+ for more than 50 was used by Wilkins and Olson (2001), a scale of trace for fewer than 10, 1+ for 10 to 20, 2+ for 20 to 30, 3+ for 30 to 40 and 4+ for more than 40 was used by Cisneros-Lanuza et al. (2007), another scale from 0 to 4 where 0 was no glistenings, 1 standing for trace or few, 2 for a minor number, 3 for a moderate number and 4 for an intense amount was used by Mönestam, Behndig (2011) and finally the simple scale of 0 for absent, 1 for moderate and 2 for dense glistenings was used recently by Colin et al (2012).

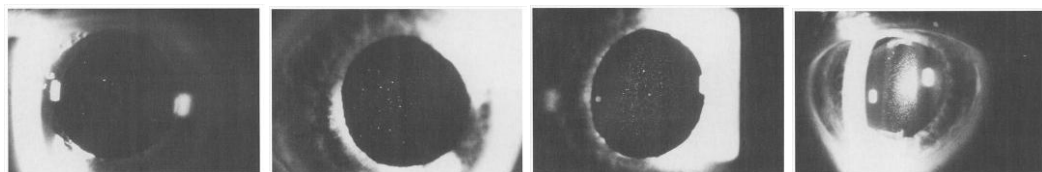


Figure 4.1 Standard photographs of the glistenings as proposed by Dhaliwal et al (1996). From left to the right: trace, 1+, 2+ and 3+.

Glistenings grading is not only limited by to the different scales used, it also assumes there is a uniform distribution of glistenings within the IOL. In vivo, it is based on backward scatter where a different angle, slit width and intensity of lighting can cause the glistenings to sparkle in different ways depending on their size and nature. Therefore, clinical grading of glistenings remains a subjective method having limitations. However, it is readily available using standard equipment and hence is has been widely used in glistenings research.

Although visual complaints have been reported, such as reduced contrast sensitivity, due to glistenings (Farbowitz et al., 2000, Dhaliwal et al., 1996), there are discrepancies among reports about whether glistenings affect the optical quality of the patient's vision with (Oshika et al., 2001, Christiansen et al., 2001, Gunenc et al., 2001). In vivo studies have reported that there is no significant correlation between grade of glistenings and a number of measures of visual function such as best corrected visual acuity and contrast sensitivity (Mönestam et al., 2011, Colin et al., 2012, Oshika et al., 2001, Colin and Orignac, 2011).

Although a decrease in VA has been reported with increased density of glistenings (Christiansen et al., 2001, Colin et al., 2012) it is generally considered that visual acuity is unaffected (Dhaliwal et al., 1996, Gunenc et al., 2001, Waite et al., 2007, Colin and Orignac, 2011, Mönestam et al., 2011, Hayashi et al., 2012, Colin et al., 2009, Moreno-Montañés et al., 2003, Wilkins and Olson, 2001, Werner, 2010). However, high contrast visual acuity has long been known to show little deficit in the presence of light scatter (Klein et al., 1995, Koch, 1989) so it is possible other measures of vision may show a greater deficit. Association between grade of glistenings and IOL optical performance in vitro has been examined by Oshika et al (2001) who demonstrated that there was no significant correlation between grade of glistenings and glare sensitivity, Modulation Transfer Function or spectral transmittance, although high grade glistenings would cause mild to moderate deterioration of lens performance (Oshika et al., 2001). In vivo measurements include light scatter from other components of the human eye, such as the cornea, as well as the neural response. Therefore, assessment of directly measuring in vitro forward light scatter without the confounding effects of other structures in the eye and subjective responses is less prone to these confounding factors.

4.1.2 Point Spread Function and Forward Light Scatter

For any optical disturbances such as refractive errors, aberrations or scatter, the point spread function, in order to satisfy the law of conservation of energy, behaves like a water mattress resulting in a lower and broader central peak with a wider skirt. According to theory, the point spread function is divided into two functional areas: the large angle and the small angle domains.

Straylight, which results from forward light scatter, is defined as the functional area of the PSF beyond 1° . This is called the large angle domain and hence an objective way to quantify scattered light is by evaluating the volume under the PSF's skirt, i.e. the straylight beyond 1° . The higher the volume, the greater the amount of scattered light.

The small angle domain of the PSF, corresponding to angles less than 1° , is affected by optical aberrations that alter visual acuity and contrast sensitivity. According to the CIE standard (Van den Berg et al. 2009), this domain is subdivided into the central peak up to 1.2 min of arc (0.02°), which dominates visual acuity, and the area from 1.2 to 10 min of arc (0.06° to 0.33°), which dominates contrast sensitivity.

The point spread function is considered as the ratio of intraocular light scatter veiling luminance L to the illuminance of the light from the glare source E , according to the Glare Spread Function (equation 2.2). A logarithmic transformation of equation 2.1 gives

$$\log(L/E) = \log(k) - n \log(\theta) \quad (4.1)$$

hence $\log(\text{PSF})$ is linearly related to the logarithm of the eccentricity θ . If we assume that the straylight parameter k remains constant for all angles, the slope of the function described by equation (4.1) determines the scatter index, n . Light scatter is expected to have a different effect on the central peak of the point spread function compared to the PSF's skirt. Therefore, the scatter index, n , was investigated separately in the two angle domains: a) the large angle domain beyond 1° and b) the small angle domain from 0.33° to 0.83° .

4.2 Methods

4.2.1 Procedure

Twenty hydrophobic acrylic, 3-piece intraocular lenses ranging in power from +18.5D to +23.0D (Mean +21.2D STDV \pm 1.5D) were tested (Table 4.1). They were subjected to thermal gradients by our collaborators at AVS Inc., Goleta, CA to induce glistenings. The glistenings were graded using a scale from 0 (no or few glistenings) up to >4 (severe glistenings) by uniformly illuminating the whole of the IOL and viewing through a high precision microscope.

| Code | Dioptric Power (D) | Optic Diameter (mm) | Glistenings Grade |
|------|--------------------|---------------------|-------------------|
| A | +19.0 | 6 | 1 |
| B | +20.5 | 6 | >4 |
| C | +20.0 | 6 | 4 |
| D | +21.0 | 6 | 2 |
| E | +19.0 | 6 | 3 |
| F | +18.5 | 6 | 2 |
| G | +21.5 | 6 | 0 |
| S1 | +21.0 | 7 | 1 |
| S2 | +18.5 | 7 | 1 |
| S3 | +23.0 | 7 | 2 |
| S4 | +22.0 | 7 | 2 |
| S5 | +23.0 | 7 | 3 |
| S6 | +23.0 | 7 | 3 |
| S7 | +23.0 | 7 | 4 |
| S8 | +21.0 | 7 | 4 |
| S9 | +22.0 | 6 | >4 |
| S10 | +22.0 | 6 | >4 |
| S15 | +22.0 | 6 | 0 |
| S16 | +22.0 | 6 | 0 |
| S17 | +21.5 | 7 | 0 |

Table 4.1 Tested IOLs specifications

Once delivered to our labs, lenses were kept in an incubator at a constant 35°C before and after being tested. For each IOL, following the imaging procedure described in Chapter 3, approximately 10 slit-lamp images were captured. Following the testing procedure described in Chapter 3, the IOL was positioned at the centre of rotation of the detector. After alignment, the detector was moved to measure the forward scattered light in star space at 37 different angles covering ± 18 degrees. Measurements were made for each of the lenses at 3mm, 4mm and 5mm pupil sizes by adjusting the size of the incident beam with an artificial aperture. Forward light scatter was quantified as explained in paragraph 4.2.2 below.

Statistical analysis was performed using Minitab version 16® (Minitab Ltd., Coventry, United Kingdom). A P value of less than 0.05 was considered statistically significant.

4.2.2 Data Analysis

Forward light scatter was measured with a silicon photodiode that generates a photocurrent proportional to the light intensity. For a given wavelength, if incident light intensity is P and the photodiode's spectral responsivity is S then photocurrent I_p is given by:

$$I_p = S \times P . \quad (4.2)$$

Therefore, our scatter function, which represents the angular distribution of the experimentally measured photocurrent, is proportional to the light intensity $I(\theta)$. By calculating the Scatter Function's volume per steradian (conversion of eccentricity θ in radians) and normalizing to unity gives by default the corresponding integral of PSF per steradian (Van Den Berg and Ijspeert, 1995, van den Berg, 1995, Van Den Berg et al., 2009).

$$\int_0^{\pi} PSF(\theta) d\omega = 1 \quad (4.3)$$

Normalization of the volume under the scatter function is determined for our measurement range of $\pm 18^\circ$, thus for a central 36° cone in forward space. Most of the volume of the PSF is located around the peak; 98% of the volume of the of the CIE Total Glare formula for a young 20 years-old subject is found within $\pm 18^\circ$. The error is therefore $< 2\%$ and is considered negligible.

A solid of revolution is defined as the solid generated by revolving a plane region around an axis. Following the Disk Method (Finney et al., 2001) the volume of a solid of revolution defined by a continuous function $x = R(y)$, for $\alpha \leq y \leq \beta$, about the y-axis (Figure 4.2a) is given by

$$V_{rev} = \int_{\alpha}^{\beta} \pi [R(y)]^2 dy. \quad (4.4)$$

The equivalent veiling luminance L of intraocular light scatter is given by the formula

$$L(\theta) = \frac{sE}{\theta^2}, \quad (4.5)$$

which is the rearranged version of equation 2.3. Equivalent veiling luminance, L , is normally plotted on the y-axis and θ on the x-axis. Equation (4.5) can be expressed in the form of $x=R(y)$ by rewriting it as

$$\theta = \sqrt{\frac{sE}{L(\theta)}} \quad (4.6)$$

Substituting (4.6) into (4.4) and evaluating the integral gives

$$V_{rev} = \pi sE (\ln \beta - \ln \alpha) \quad (4.7)$$

In reality, the straylight parameter s and scatter index n are not constant for all angles, experimental measurements do not directly measure luminance and angular distribution is not perfectly symmetric about the y-axis. Hence, the exact mathematical form of the scatter function is unknown so a numerical method is used to carry out the integration. Calculation of volume under the data points that form the scatter function can be approximated by the sum of a series of individual capped cones. The volume of a capped cone is given by

$$V_{cc} = \frac{\pi h}{3} (r^2 + rR + R^2) \quad (4.8)$$

where r is the minor radius, R the major radius and h the height (figure 4.2b). For the case where r is zero equation (4.8) reduces to the well know result for the volume of a cone.

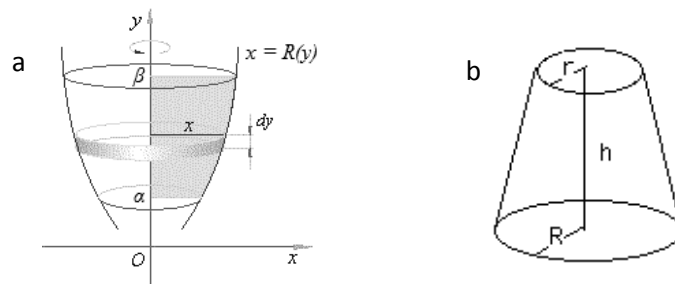


Figure 4.2 a) A solid of revolution generated by a plane rotated around y axis b) illustration of a capped cone

The capped cone volume bounded by two points of the measured scatter function $P_1(x_1, y_1)$ and $P_2(x_2, y_2)$ is therefore given by

$$V = \frac{\pi |y_1 - y_2|}{3} (x_1^2 + x_1 x_2 + x_2^2) \quad (4.9)$$

Since the measured scatter function is not perfectly symmetric about the y-axis, for each pair of points, half the volume of a capped cone (180° revolution) is calculated. Therefore, the total volume under the scatter function is given:

$$V_{SF} = \sum_{i=1}^n \frac{\pi|y_i - y_{i+1}|}{6} (x_i^2 + x_i x_{i+1} + x_{i+1}^2) \quad (4.10)$$

where y_i stands for the amplifier's outcome and x_i the angular eccentricity θ in radians. The total volume V_{SF} is calculated and used to scale each individual detector output reading so that the volume is normalised.

The closer to the peak, the steeper the PSF slope. Therefore, a small change in eccentricity causes a large variation in PSF values. This is the reason why standard deviation errors for both repeatability and reproducibility (Chapter 3) appeared greater for small angles. Consequently, experimental measurement of the area near the peak requires high precision rotational stages for setting the angle. In our setup, the rotational stage has an angular resolution of 1 min of arc. Hence, measurements were taken beyond the angle of 20 min of arc (0.33°) for which angular resolution is equal to a minimum $\delta x = 1/20 = 0.05$ (or 5%) relative error.

The straylight parameter, s , is a function of angle θ , therefore s values must always be accompanied by the corresponding glare angle. The straylight parameter values for 5 different angles were chosen (van den Berg, 1995), following the sequence of 3.5°, 7°, 10°, 14° and including angle 18° as the last step of our eccentricity range. Weight was given to $s(\theta)$ for 10° as it is the glare source angle used by C-Quant, the in vivo straylight meter considered as a “standard” for intraocular scatter evaluation (Franssen et al., 2006, Van der Mooren et al., 2007, Michael et al., 2010, Colin and Orignac, 2011). The straylight parameter is calculated according to equation 2.3, given on Chapter 2.

4.3 Results

4.3.1 Volume under PSF's skirt (VUSF)

The skirt of the PSF is considered to be the region beyond 1° eccentricity. The normalized individual volumes under this area were aggregated for each IOL and correlated with the subjective grade for the glistenings for all three pupil sizes. Figure 4.2 shows how the scattered light volume changes with glistenings grade.

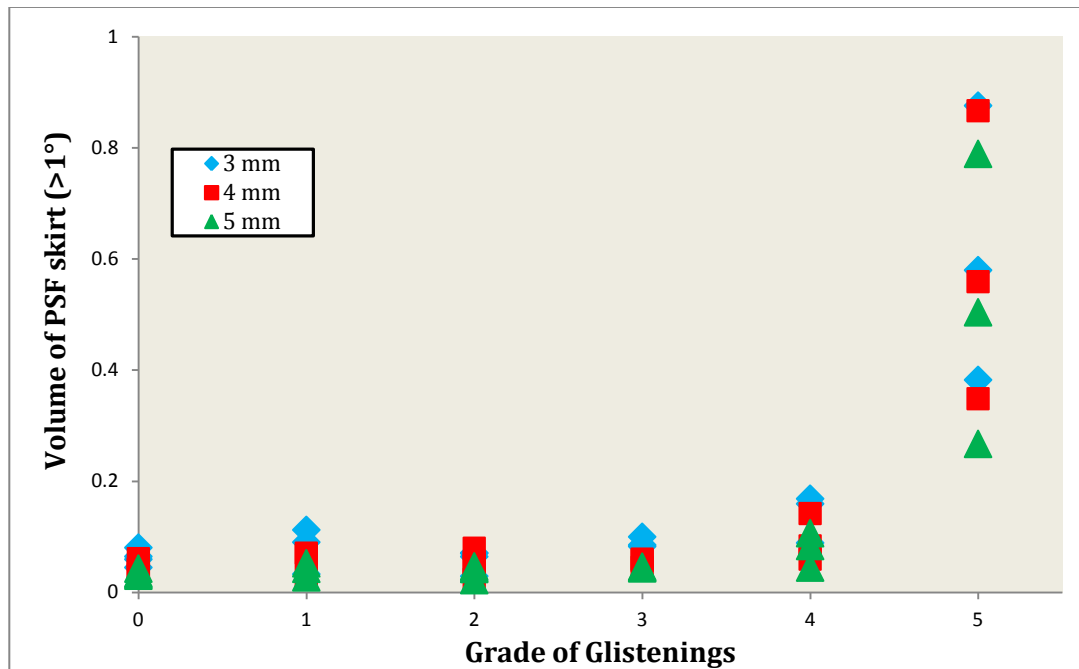


Figure 4.2 Correlation between PSF skirt (beyond 1°) volume and Grade of Glistenings for all pupil sizes.

In all cases, VUSF beyond 1° was decreasing as pupil size was increasing. For the 3 mm pupil size, where VUSF values were shown to be higher among the three different pupil sizes, the mean and standard deviations of volumes under the scatter function were calculated for each grade of glistenings, (Table 4.2). Results were noteworthy for two reasons: firstly, the mean values did not all increase monotonically with grade; secondly, standard deviations were significant in some cases, e.g. in the case of Grade 1.

| Grade 0 | Grade 1 | Grade 2 | Grade 3 | Grade 4 | Grade >4 |
|------------------|------------------|------------------|------------------|------------------|------------------|
| 0.062 ± 0.015 | 0.079 ± 0.041 | 0.059 ± 0.020 | 0.089 ± 0.009 | 0.139 ± 0.043 | 0.613 ± 0.248 |

Table 4.2 Mean values and standard deviations (mean \pm sd) of VUSFs for each grade at 3mm pupil size (normalized units).

For all pupil sizes a statistically significant relationship ($p < 0.05$) between Grade of Glistenings and VUSF (beyond 1°) was shown with a positive Spearman correlation (Table 4.3). This indicates that when glistenings grade increases, VUSF in the large angle domain (straylight) tends to increase as well. For an extreme case (IOL S10 – grade >4) the straylight volume increases up to 0.87, i.e. the 87% of the PSF volume lies under the skirt, thus a large part of the PSF has been transposed to the peripheral areas. The increase though appears to be non-linear, with a sudden sharp increase from grade 4 to grade >4 (shown as grade 5 on our graphs scale).

| Pupil Size | Spearman coefficient | p-value |
|------------|----------------------|---------|
| 3 mm | 0.743 | 0.000 |
| 4 mm | 0.659 | 0.002 |
| 5 mm | 0.781 | 0.000 |

Table 4.3 Correlation between VUSF and Grade of Glistenings for each pupil size.

4.3.2 PSF angular distribution

The angular distribution of scattered light was evaluated by plotting our normalized data against the angular eccentricity θ . Figure 4.3 shows the difference in the angular distribution of scattered light for IOLs with different grades of glistening. The measured scatter functions were normalised as described in section 4.2 and represent the point spread function.

PSF variations between grade 0 and grade 3 appear small with a tendency towards increased scatter. The PSF for grade >4 is distinctly broader with a lower peak, flatter slopes and a superimposed skirt indicating a marked increase in light scatter.

The significance of these results can be further evaluated by comparing them to the CIE Total Glare Function (equation 2.2) for normal subjects (figure 4.4) where the green line represents a young subject of 20 years-old and the red line an old subject of 70 years-old. For the glistening of grade 0 (grey dashed line), PSF levels are below (better) than those measured for a young subject; for grade 3 (grey line) the PSF lies between the young and old CIE standards; however, for glistening grade >4 (black line) the PSF values are much higher (worse) than the old subject.

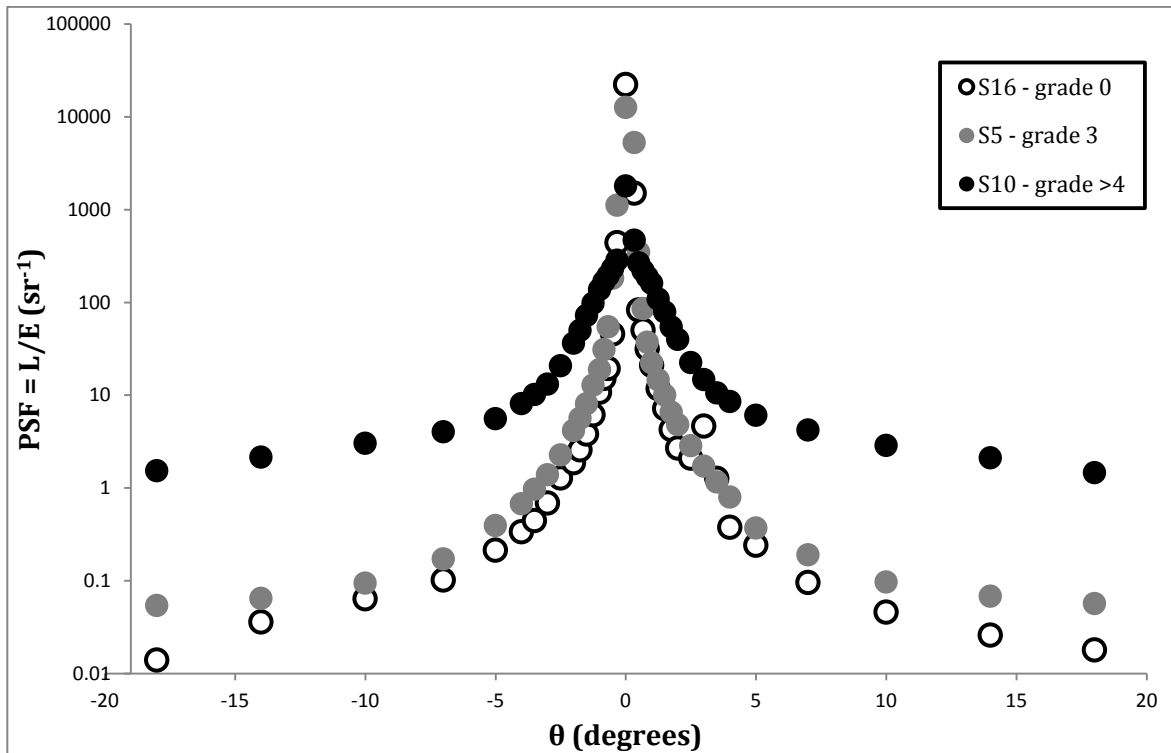


Figure 4.3 PSF angular distribution for three different grades: white points for a grade 0 (S16), grey points for a moderate grade 3 (S5) and black points for a high grade >4 (S10). Peak values decrease and skirt levels increase while grade of glistenings increases. All results correspond to a 3mm pupil size.

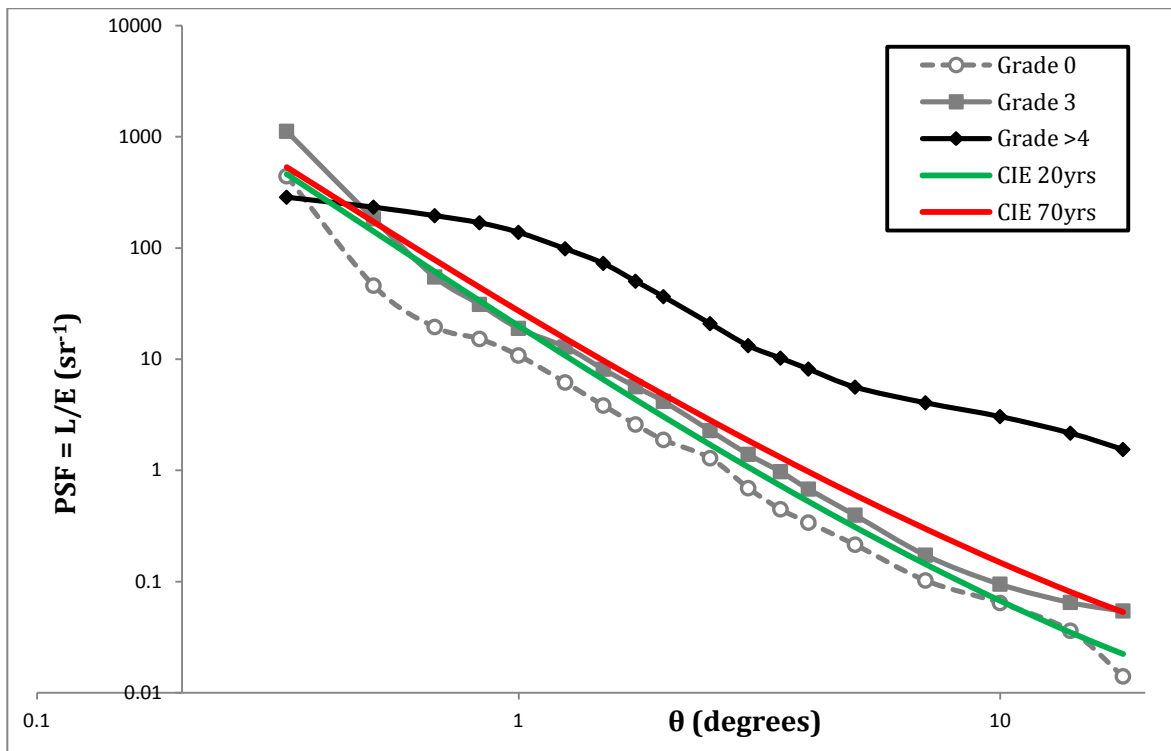


Figure 4.4 PSF comparison with CIE standards: green line for a young (20yrs) subject and red line for an old (70yrs) normal subject. The dashed grey line is for a grade 0 IOL, solid grey line for a moderate grade 3 and black line for a high grade >4. IOL results correspond to a 3mm pupil size.

Finally, the impact of pupil size on the Point-Spread Function is illustrated in figure 4.5. For an IOL of moderate grade of glistenings (grade 3), the PSF values decrease with increasing pupil size for the large angle domain. For the small angle domain the opposite occurs with higher PSF values for larger pupil sizes. It has been suggested that the slope of the PSF might differ not only between the different glistenings grades but also between different pupil sizes. This hypothesis is investigated below (Section 4.3.3) by evaluating the scatter index for the small angle ($<1^\circ$) and large ($>1^\circ$) angle domains.

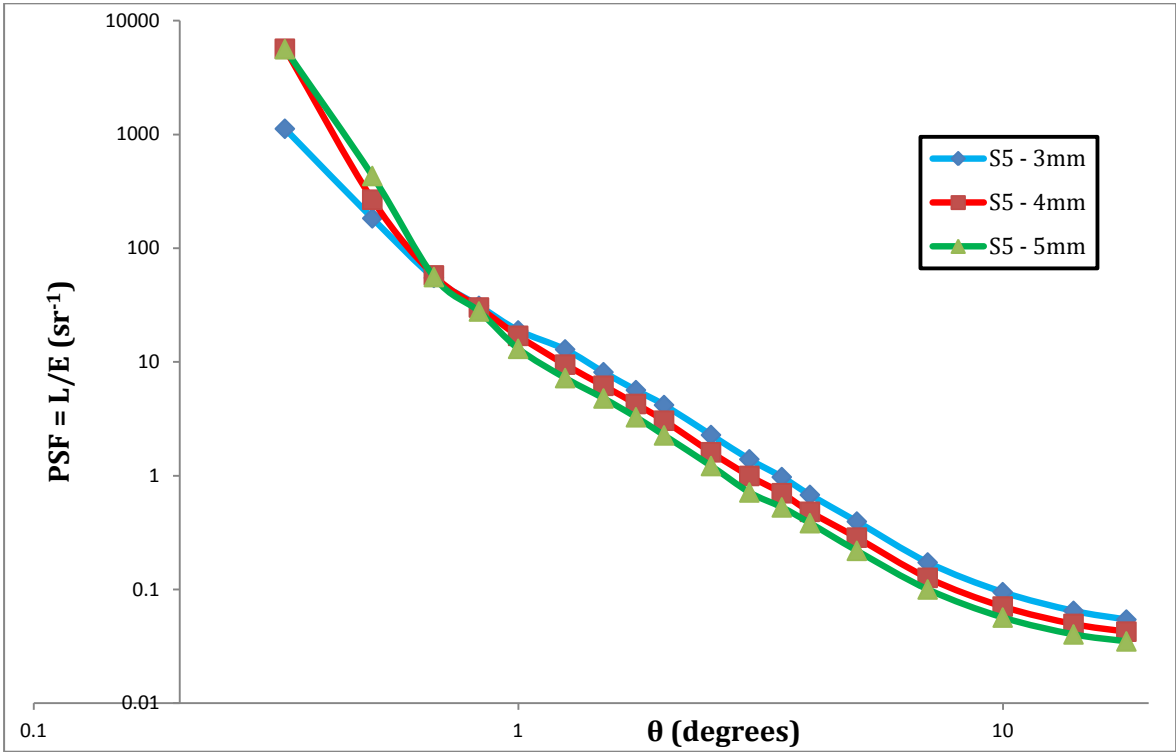


Figure 4.5 Pupil size impact on PSF for an IOL of moderate grade 3 of glistenings (S5).

4.3.3 Scatter index n

4.3.3.1 Large angle domain

Equation (4.1) demonstrates that the gradient of the relationship when the logarithm of eccentricity is plotted against the logarithm of the equivalent veiling luminance is the scatter index, n . Figure 4.9 shows a typical plot for an IOL with Grade 1 glistenings. Linearity was evaluated separately for negative (L) and positive eccentricity (R) with the average of these values then taken as a measure of the scatter index.

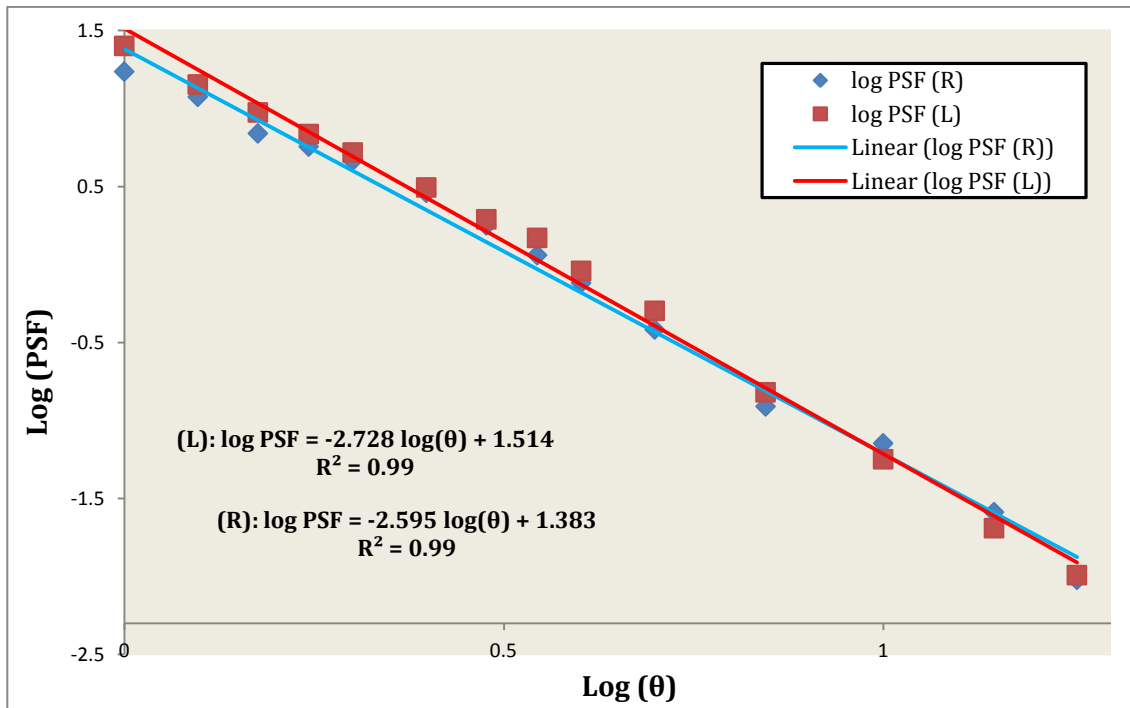


Figure 4.6 Linear regression of $\log(\text{PSF})$ vs $\log(\theta)$ among the large angle domain ($\geq 1^\circ$) for a grade 1 (IOL A), 3mm pupil size. Red trendline stands for negative eccentricity (L) while blue for positive.

For all pupil sizes, no statistically significant relationship ($p > 0.05$) between grade of glistenings and scatter index was found with a negative correlation coefficients close to zero (Table 4.4). This indicates that grade of glistenings is not associated with scatter index, n .

| Pupil size | Spearman coefficient | p-value |
|------------|----------------------|---------|
| 3 mm | -0.031 | 0.896 |
| 4 mm | -0.028 | 0.906 |
| 5 mm | -0.146 | 0.538 |

Table 4.4 No correlation was found between large angle domain scatter index and glistening grading for none of the three pupil sizes.

Given that no correlation was found between scatter index and glistening severity, the mean value for all tested intraocular lenses was calculated (Table 4.5). For all pupil sizes, the scatter index was found to be close to -2.0, as suggested from literature.

| Pupil size | 3 mm | 4 mm | 5 mm |
|-------------------------------|--------------------|--------------------|--------------------|
| Scatter index (mean \pm sd) | -2.217 \pm 0.342 | -2.201 \pm 0.336 | -2.191 \pm 0.337 |

Table 4.5 Mean values (and SD) of scatter index n for each pupil size in the large angle domain.

4.3.3.2 Small angle domain

The scatter index for the small angle domain ($0.33^\circ - 0.83^\circ$) was evaluated by calculating the linear regression between $\log(\text{PSF})$ and $\log(\theta)$. Again, slopes were calculated separately for the negative eccentricity (L) and positive eccentricity (R) (figure 4.7) and the mean values were calculated and further analyzed.

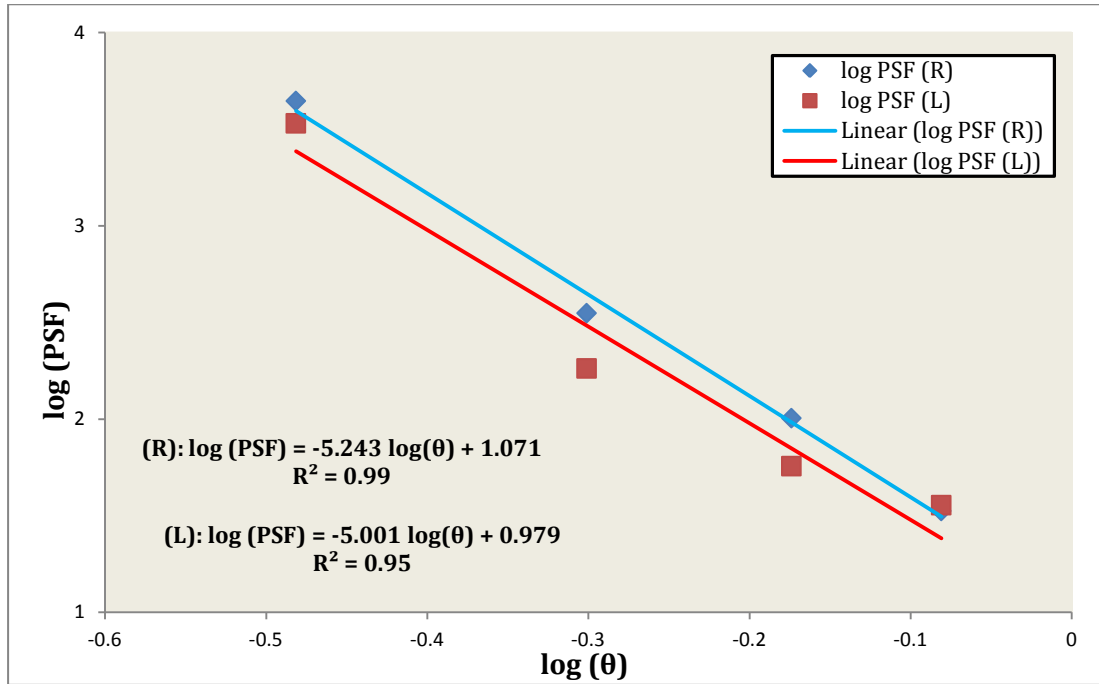


Figure 4.7 Linear regression of $\log(\text{PSF})$ vs $\log(\theta)$ for a grade 2 IOL (S4), 3mm pupil size (small angle domain)

Contrary to the large angle domain, a statistically significant ($p < 0.05$) but weak correlation between grade of glistenings and scatter index was found for both the 3mm and 5mm pupil sizes (Table 4.6). This indicates that when the grade of glistenings increases, scatter index n for the small angle domain tends also to increase.

| Pupil size | Spearman coefficient | p-value |
|------------|----------------------|---------|
| 3 mm | 0.485 | 0.030 |
| 4 mm | 0.425 | 0.062 |
| 5 mm | 0.642 | 0.029 |

Table 4.6 A positive correlation was found between scatter index and glistening grading for all three pupil sizes (small angle domain).

The change in scatter index (small angle domain) with grade of glistenings is shown in figure 4.8 for the 3mm and 5mm pupil sizes. There is a tendency for the scatter index to remain at the same levels (-6.0 approximately) for the low to moderate grades (0 to 3)

while rapidly increasing (-3.0 approximately) for the higher grades (4 and >4). This could be linked to our earlier results (paragraph 4.3.1) where light scatter was shown to increase significantly only when there was a significant amount of glistenings. In all cases, the scatter index for the small angle domain was very different than the -2.0 value proposed in the literature for the straylight. Therefore, the linearity assumption in equation 4.1 appears to breakdown closer to the centre of the PSF. A lower magnitude for the scatter index (e.g. 2) implies more light in the skirt of the PSF whereas a higher magnitude (e.g. 6) implies that light is concentrated close to the centre of the PSF. In addition, contrary to the large angle domain, the scatter index for the small angle domain was shown to increase when pupil size increases.

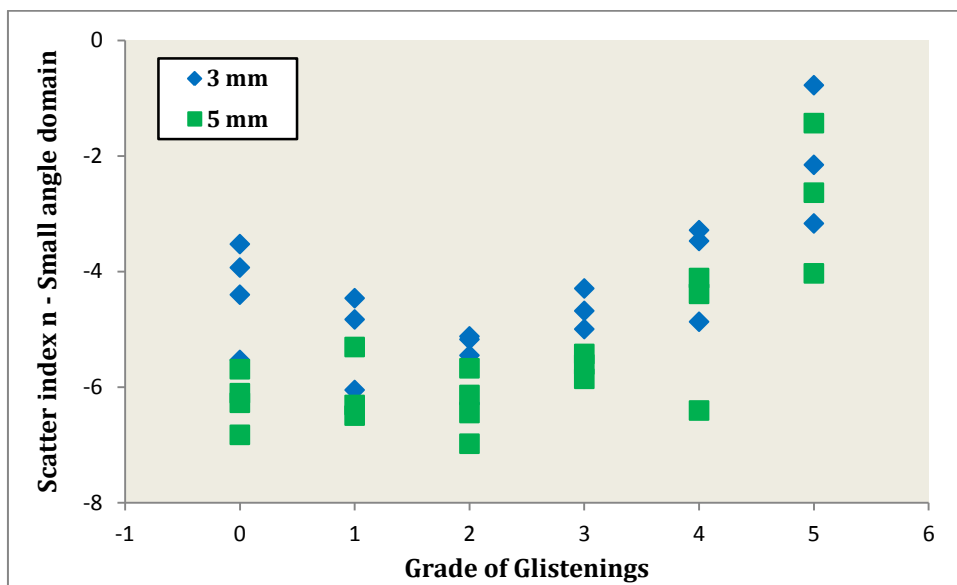


Figure 4.8 Variation in small angle domain scatter index with glistenings severity.

4.3.4 Straylight Parameter – log(s)

Straylight parameter, log(s), was calculated for a 10° angle, for all IOLs and all three pupil sizes. A statistically significant relationship ($p < 0.05$) between grade of glistenings and straylight parameter was found with positive Spearman correlation coefficients (Table 4.7). This indicates that when the grade of glistenings increases, the straylight parameter tends to increase.

| Pupil size | Spearman coefficient | p-value |
|------------|----------------------|---------|
| 3 mm | 0.516 | 0.020 |
| 4 mm | 0.506 | 0.023 |
| 5 mm | 0.615 | 0.004 |

Table 4.7 Correlation between straylight parameter and glistenings grade for all three pupil sizes

For all IOLs straylight parameter values were found to decrease with increasing pupil size; figure 4.9 below shows an example for a grade 3 IOL. This result is contrary to the theoretical prediction of straylight independency of pupil size in the normal human eye. This finding may be explained if glistenings have a non-uniform distribution across the IOL.

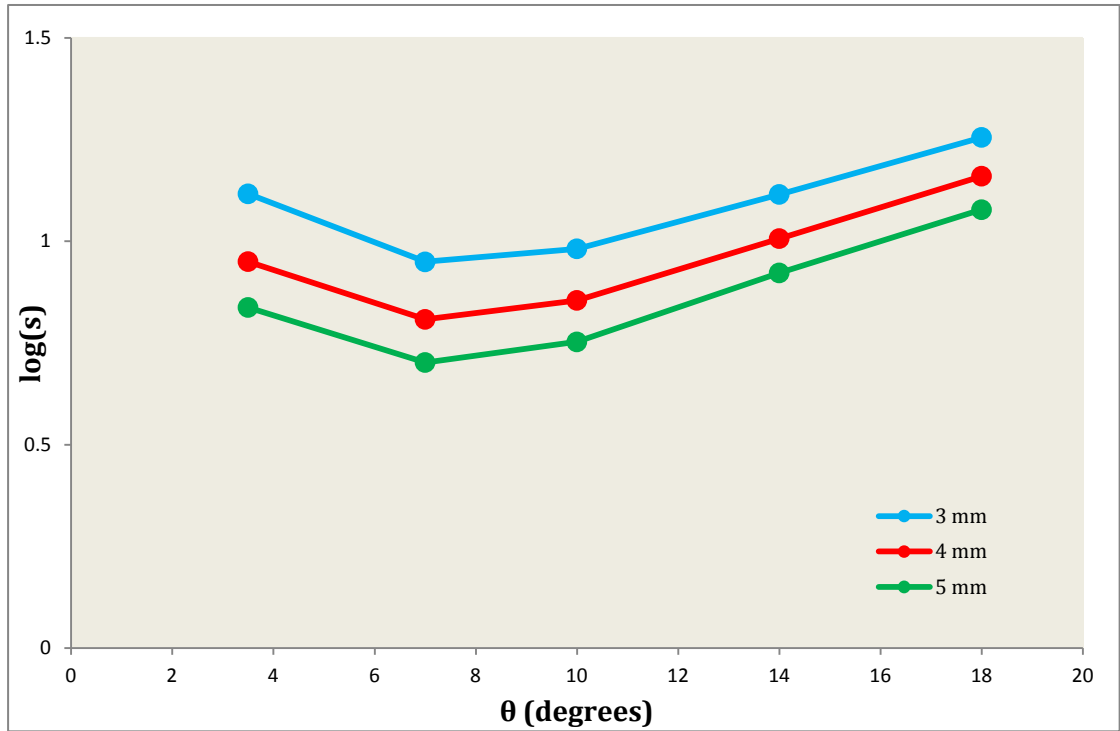


Figure 4.9 Straylight $\log(s)$ values for a grade 3 IOL (S5) vs glare angle θ for the three different pupil sizes.

Straylight parameter values were calculated for angles 1° for a low (grade 1 - grey line) and a high grade (grade >4 - black line) from data for a 3mm pupil size. The change in straylight parameter is illustrated in figure 4.10 and compared with the corresponding CIE values for a young 20 year-old (green line) and an old 70 year-old (red line) normal subject.

It is evident that the prediction that the straylight parameter is constant for angles beyond 1° is correct in cases of low or normal light scattering levels. When light scattering levels increase as in the case of a grade >4 IOL, the straylight parameter has a strong angular dependence. In addition, the straylight parameter was found to have a peak value around the 3.5° angular eccentricity for intraocular lenses with high severity of glistenings.

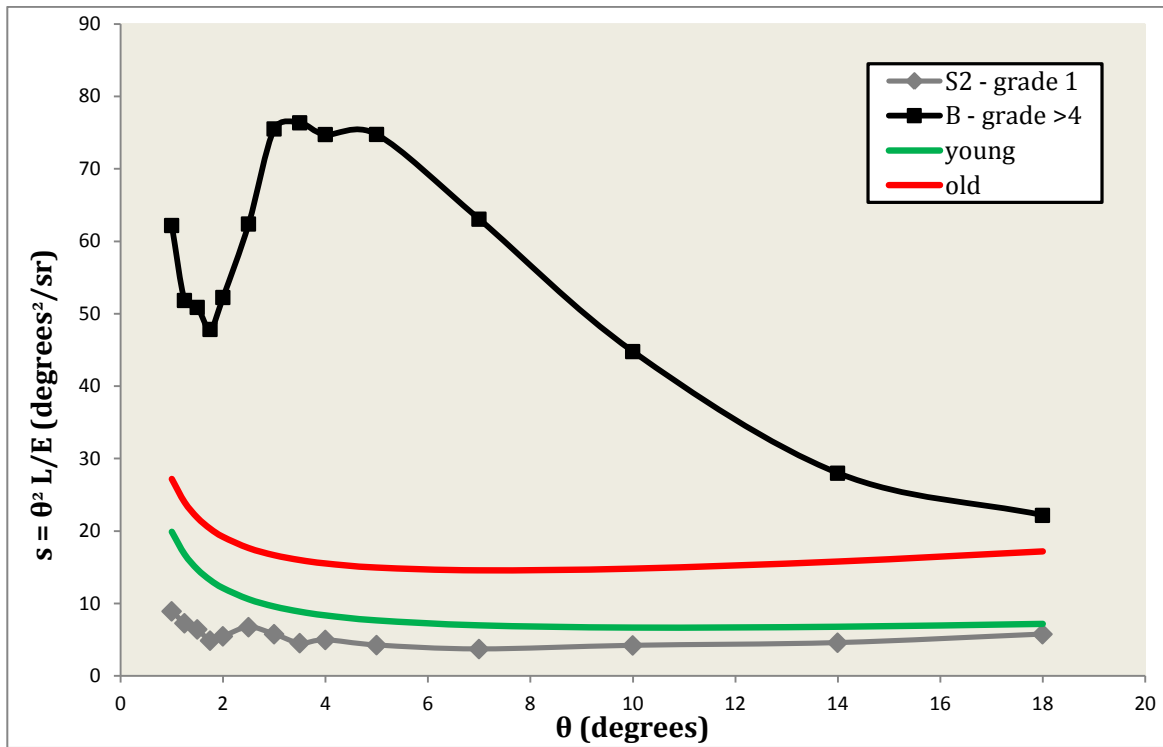


Figure 4.10 Straylight parameter angular dependence. For normal subjects, both young and old, as well as for a low grade 1 IOL, $s(\theta)$ can approximately be considered as constant beyond 1° while for a grade >4 IOL the angular dependence is evident.

4.4 Discussion

Lack of correlation between our results and grade of glistenings indicates that light scatter produced by glistenings is poorly represented by clinical grading, which is possibly due to method's subjectivity. Although light scatter tends to increase as grade of glistenings increases, this increase is small for IOLs of grades 0 to 4 (Table 4.2) while it is clearly evident for the grade >4 IOLs. The size of glistenings may be a significant factor affecting the angular distribution of forward light scatter; large refractile particles, for example, don't produce scatter in the same way as small particles such as protein aggregates in cataract. To investigate this hypothesis, an objective method is needed to quantify glistenings rather than categorizing subjectively their severity.

In all cases, volume under the scatter function beyond 1° was shown to decrease as pupil size increases; this result is contrary to the theoretical studies, which have suggested that PSF variations with pupil size in the large angle domain are insignificant for normal human eyes (Ijspeert et al., 1993, Franssen et al., 2007). A potential explanation could not only be the nature of glistenings but also the distribution and density of glistenings for

different pupil sizes. Other factors that could contribute to the non uniform distribution of glistening, for example overlap, could affect the results. However, overlap is only clearly evident in the higher grades of glistening. Further investigation is warranted by objectively quantifying these parameters for IOLs with glistenings.

Scatter index for the large angle domain remains close to the predicted constant value of -2.0 for all IOLs and all pupil sizes (Van Den Berg et al., 2009, Vos and Van Den Berg, 1999, IJspeert et al., 1990, van den Berg, 1995). Contrary to the large angle domain results, the scatter index for the small angle domain has a much greater magnitude. Pupil size dependency, as well as correlation with grade of glistenings, needs further study and investigation since the small angle domain is directly associated with visual performance and image quality functions such as Modulation Transfer Function (MTF) and Contrast Sensitivity Function (CSF), although the latter depends upon neural factors as well as optical effects.

Straylight parameter values for the 10° glare angle were found to be positively correlated with glistenings grade. No previous study has investigated the potential correlation between subjective grading and straylight parameter values. In addition, the angular distribution of the straylight parameter for a high severity of glistenings, was found not to follow the pattern seen in the CIE standard glare observers; the rapid increase of the straylight value near 3.5° may indicate that evaluation of straylight is worth investigating at glare angles other than 10° .

For all comparisons with the CIE standard for a young and an old subject, it is important to consider that these functions model the total ocular straylight distribution; since our measurements of IOLs are in vitro, light scatter contributions from components such as the cornea don't occur and therefore the equivalent in vivo results would be expected to be slightly higher. This may be the reason why a clear IOL or one with low grade glistenings, when measured in vitro, seems to scatter light less than a young normal human eye.

Chapter 5

Objective Quantification of Glistenings by Digital Image Processing

5.1 Introduction

Subjective grading of glistenings, as described in 4.1, has been widely used but has several problems: Firstly, there is no agreed grading scale; secondly, it is highly likely that light scattering depends on the size and distribution of glistenings, factors that may not be directly linked to a subjective grade. As a result there is a need to objectively quantify glistenings. The most logical approach is to use image processing of the digital images taken with our slit-lamp camera under standard settings and conditions, as described in paragraph 3.5.2.

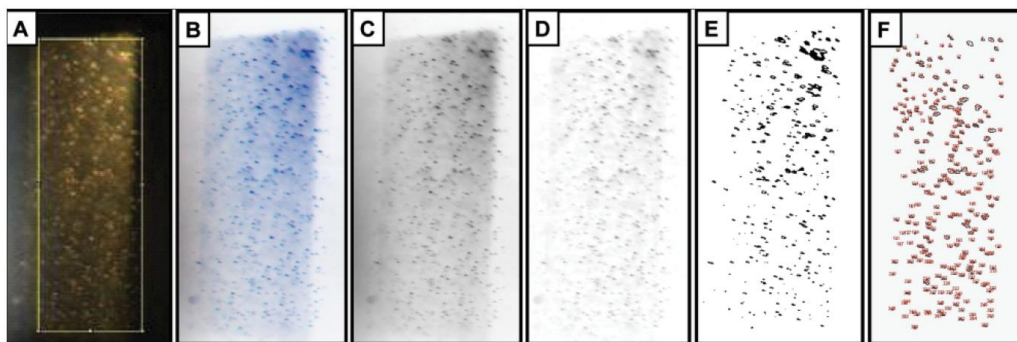


Figure 5.1 Image Processing steps used by Colin et al. for the quantification of glistenings (Colin and Orignac, 2011). A) Slit-lamp image of an IOL, with the yellow rectangle showing the central zone that was used for counting. B) Inversion of colour. C) Conversion to 8-bit format. D) Subtraction of background and adjustment of contrast. E) Thresholding to recognize features of size up to 0.001 mm². F) Microvacuoles counted by the software and circled in red. Density was calculated by dividing the counted number by the initial yellow rectangular area.

Several workers have previously described objective quantification methods. The public domain image processing program, ImageJ, has been used in several studies as a means of objectively quantifying glistenings (Waite et al., 2007, Behndig et al., 2009, Mönestam et al., 2011, Rønbeck et al., 2013, Colin and Orignac, 2011, van der Mooren et al., 2013). ImageJ is a Java-based program developed by the National Institutes of Health (NIH),

Maryland, US (<http://rsbweb.nih.gov/ij/>). Waite et al (2007) used ImageJ to evaluate size, density and severity index, (defined as the product of size and density), of glistenings using in vivo slit-lamp images of a 2 x 2 mm area centred on the visual axis. Behnidig and Mönestam (2009) used ImageJ to quantify light scattering by analysing Scheimpflug images. The method was questioned by Mackool and Colin (Mackool and Colin, 2009), mostly for the suitability of Scheimpflug imaging for the evaluation of light scattering. Nevertheless it was used again by the same authors in 2011 as well as more recently by Rønbeck et al (2013) who referred to the studies of Klos et al. (1999) and Ayaki et al. (2006). In 2011, Colin et al. described a method of image analysis to quantify objectively the grade of glistenings. In this study, slit-lamp (BQ-900) images of a 2mm wide slit of the IOL were processed as described in figure 5.1 by ImageJ v1.37. The resulting metric was the density of the glistenings expressed as the number of microvacuoles per square millimetre. The most recent study that used ImageJ software for glistenings quantification was published by van der Mooren et al in 2013. Intraocular lens imaging was performed with a confocal microscope to provide information about the glistenings location within lens volume and dark field microscopy for a wider field of view of the lens. Glistenings density was expressed as the number of microvacuoles per cubic millimetre.

Conference presentations also refer to the analysis of digital images of glistenings in vivo, although the algorithms have not been published in detail to the best of our knowledge. In April 2010 and April 2012, Dhital et al. gave presentations at the American Society of Cataract and Refractive Surgery (ASCRS) Annual Symposium about their IOL glistenings study at St. Thomas' Hospital. An objective method of glistenings quantification was described based on in vivo slit-lamp images, taken with a BQ-900 slit-lamp and IM900 imaging module (figure 5.2).

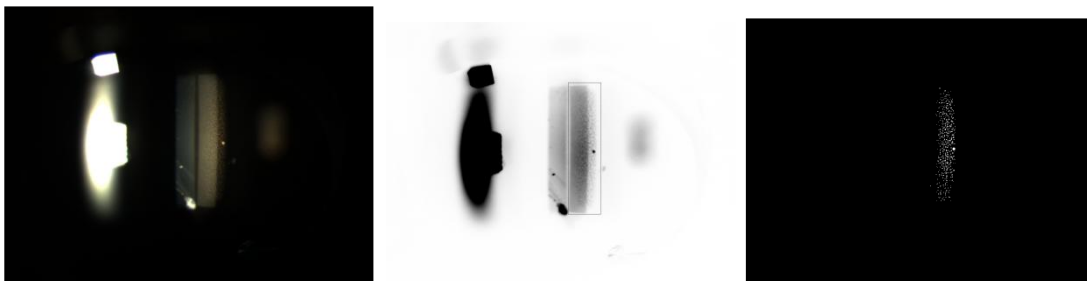


Figure 5.2 Image Analysis Processing by Dhital et al. (2012) Left to right: image from slit-lamp camera, reverse contrast, final image of glistenings.

The *in vivo* IOL was illuminated with a slit beam of 1.3 mm width and digital images were captured for analysis. The image contrast was reversed such that all reflections appear black. The area of interest was localized and framed for analysis with a box of 150 x 600 pixels. Any reflections greater than 40 pixels size are excluded as noise. The remaining spots were considered to represent glistenings and their number can be calculated. Similar to the work of Colin and Orignac (2011), the number of glistenings is a representative number assuming that distribution of glistenings is uniform. This is because the images are only of a narrow slit section of the IOL.

ImageJ software has also been used with acceptable results in many different medical imaging applications including *in vivo* specimens (Eliceiri and Rueden, 2005) and radiology (Barboriak et al., 2005). Nevertheless, the fact that it is a general image processing program makes it possible that specialized software for analysis of glistenings in intraocular lenses could be advantageous. For example, for detection with ImageJ, glistenings are considered particles that appear bright but it is possible that due to their position and orientation in combination with the illumination angle, they will appear dark. In addition, although previous studies have quantified the size of glistenings, none has evaluated their shape and distribution within the IOL. We have evidence from our studies, which has also been reported by other *in vitro* and *in vivo* studies, that glistenings can be ellipsoidal in shape (Saylor et al., 2010) and have a non-uniform distribution (Werner et al., 2008). Consequently, it would be advantageous to develop a program that quantifies the dimensions (major and minor axes) of the glistenings. In addition, most of the previous studies use images that illuminate a 1.0-2.0 mm wide section of the IOL thereby missing information about the glistenings distribution in the periphery of the IOL. The aim is therefore to derive spatial information about glistenings in the whole of the lens using *en face* images. In addition, it is desirable to quantify glistenings for different pupil sizes so that results can be related to *in vivo* studies.

5.2 Description of Software

Collaborators at Kingston University, UK and Thammasat University, Thailand, have developed the Glistenings Detection Program (GDP) under our guidance (Japunya et al., 2014) (see Appendix). The software, written in Matlab, semi-automatically scans the slit-lamp images and detects glistenings. The technique used for glistenings detection is based on previous work related to vessel segmentation and for detecting exudates and blobs

found in retinal images (Fraz et al., 2012, Sopharak et al., 2009, Duanggate et al., 2011). Retinal exudates are lipid residues of serous leakage of proteins from damaged capillaries (Youssef et al., 2010, Harangi et al., 2012). Hard exudates are seen as bright yellow lesions with sharp margins and of different sizes, shapes and locations (Youssef et al., 2010, Khan et al., 2011). Blobs (illumination artefacts) appear as a brighter or darker region compared with the surrounding area and in the same colour in a retinal image (Wang and Ju, 2008, Zhou et al., 2014). The image analysis techniques used for the detection of exudates and blobs can be adjusted and used for glistenings detection; the similarity of glistenings with retinal exudates and blobs relies on their bright appearance and sharp contrast with the surrounding area.

The glistenings edges are detected and identified using the Sobel edge detection algorithm (Gupta and Mazumdar, 2013). The Sobel Operator is commonly used for edge detection and is based on calculating the gradient of the image intensity function at each point. The function takes a binary image, I , as its input and returns a binary image BW of the same size as I , generating 1 where the function detects edges and 0 elsewhere. The outcome of the Sobel operator is a black and white map of the gradient at each image point, where the areas of high gradient (edges) appear in white. The edges that tend to intersect are considered as the glistening boundaries where the dilation operation is used for connecting them. The area contained within the boundaries is filled in white and defined as the glistenings area. After these operations, a BW outcome image is generated but it also contains irrelevant smaller areas as a result of image noise. This image is then post-processed, using the erosion operator, to remove areas which are smaller or larger than the expected target sizes. The final BW outcome is evaluated by calculating the size, density and distribution of all white spots, which should represent glistenings.

In vivo, observed glistenings usually appear spherical and about 1-10 μm in diameter but in *in vitro* studies, where glistenings are artificially induced by subjecting the lens to thermal gradients, larger diameters up to 20 μm have been produced (Behndig et al., 2009, Miyata et al., 2001, Werner, 2010). The GDP software does not consider glistenings as spherical particles, but assumes the glistenings are ellipsoidal and provides information about the major and minor axes of the ellipse.

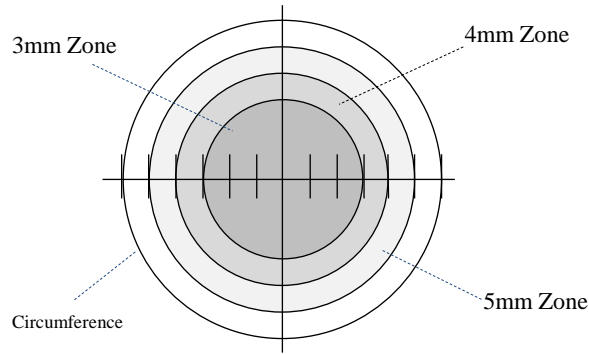


Figure 5.4 Lens zones for a 6mm optic diameter IOL.

Quantification metrics for glistenings density (equation 5.1), distribution (equation 5.2) and average area (equation 5.3), were calculated for four different optical zones: the whole lens and 3mm, 4mm and 5mm diameter concentric circular zones as shown in figure 5.4.

$$\text{Density} = \frac{\text{sum of all glistenings' areas included in zone}}{\text{Zone's area}} (\times 100\%) \quad (5.1)$$

$$\text{Distribution} = \frac{\text{number of glistenings in optical zone}}{\text{number of glistenings in whole IOL}} (\times 100\%) \quad (5.2)$$

$$\text{Average Area} = \frac{\text{sum of all glistenings' areas included in zone}}{\text{number of glistenings in zone}} \quad (5.3)$$

The objective was to create an effective glistenings detection program with a simple Graphical User Interface (GUI). The detection and quantification steps proceed as follows:

- 1) The image to be analysed is loaded from a file and appears on the software's interface as shown on figure 5.5. The lens size is selected as either a 6mm or 7mm optic diameter.

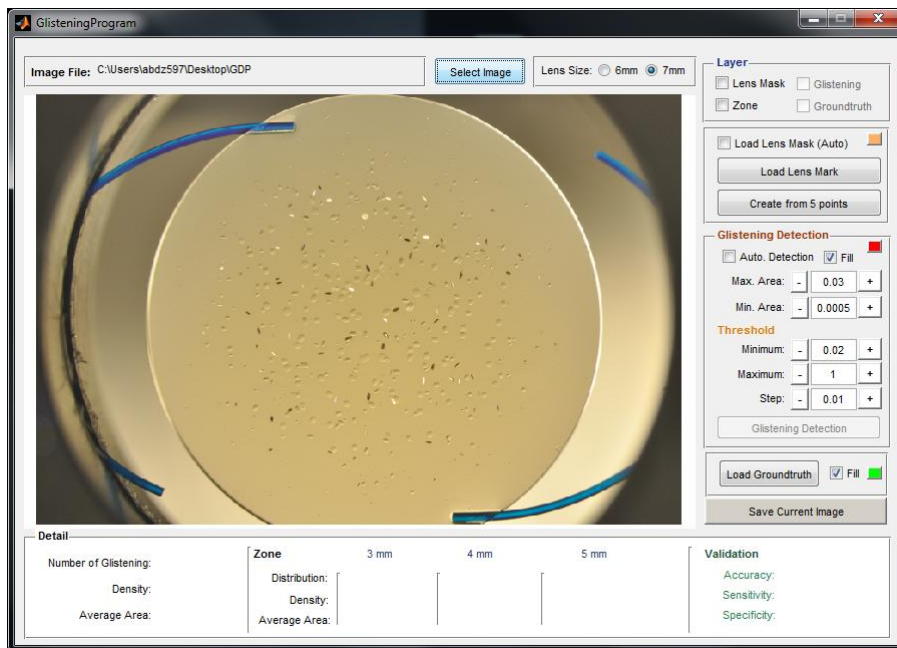


Figure 5.5 Graphical User Interface for Glistenings Detection Software

- 2) The lens edge is defined by either choosing from a list of custom-made masks for known images created by the software developer or can be manually determined by marking 5 different points on the IOL's edge. The software then calculates a best fit circle based on these points (figure 5.6).

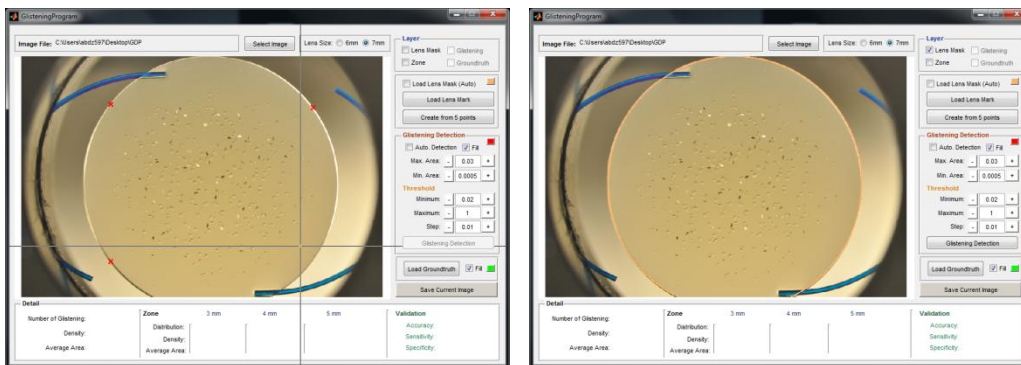


Figure 5.6 Left: 5 different points manually marked on the IOL's edge. Right: Software calculates a best fit circle defining the mask.

- 3) Parameters affecting detection appear in the right-hand control panel and fall into two categories: glistenings area and threshold. Glistenings area refers to the expected area of glistenings expressed in mm^2 . The detection parameters are Max. Area and Min. Area. Max. Area can be changed in steps of $\pm 0.005 \text{ mm}^2$ while Min. Area has steps of $\pm 0.0001 \text{ mm}^2$. The second category, Threshold, refers to the intensity gradient that the Sobel operator uses to recognize and detect the edge of the glistenings; it specifies the upper (Max) and lower (Min)

sensitivity thresholds for the Sobel method. Function “edge” ignores all edges that are not stronger than the threshold. The threshold can change with a step of ± 0.01 .

- 4) During glistenings detection, the software follows the steps in the loop using the detection parameters set by the user. Detected glistenings are marked in red and superimposed on the lens image. Quantification metrics are reported following detection. In addition, an Excel file is generated containing the calculated dimensions for each glistening as detected by the software for further evaluation and analysis.

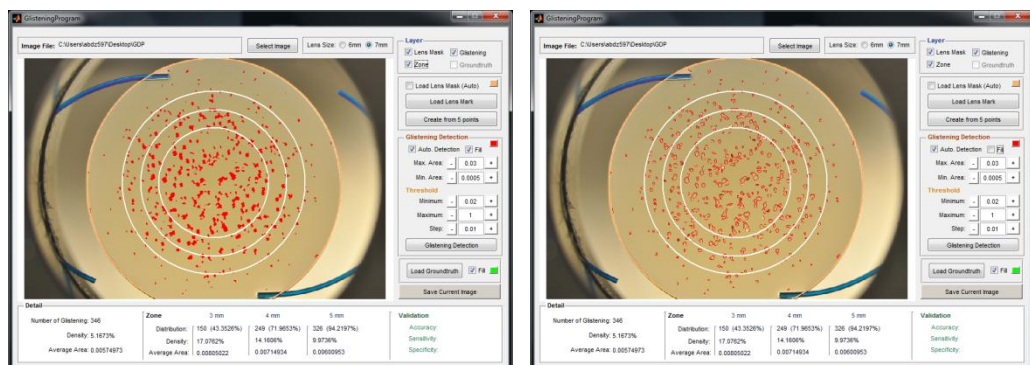


Figure 5.7 Output from the Glistenings Detection Program. Detected glistenings are marked in red, either filling each glistening area (left) or just showing their boundaries (right). Quantification values appear at the bottom of the interface for the whole lens as well as for each of the three different optical zones.

5.3 Software Validation

In diagnostic tests, distinguishing diseased from normal groups is of great importance and indicates the efficiency of the test (Attia, 2003, Zhou et al., 2011, Wong and Lim, 2011, Altman, 1990). As shown in figure 5.8, distributions of these two groups usually overlap. Cases are classified as True Positive (TP) if they have the condition and are correctly identified as such whereas those that don't have the condition and are correctly identified without it are True Negative. The overlap of the two distributions, depending on the test cut-off or criterion value, can be classified into False Positive (FP) for cases wrongly identified as having the condition and False Negative (FN) for those with the condition that are not identified.

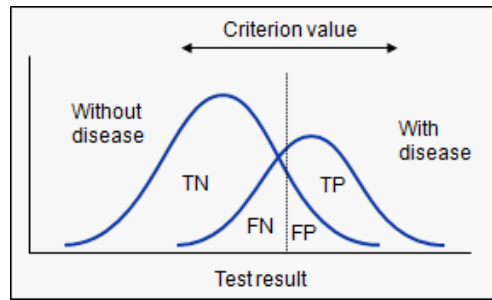


Figure 5.8 Diseased and Normal groups distribution overlap.

The different values related to this approach are shown in table 5.1.

| | Identified | Not Identified | Total |
|-----------------|------------|----------------|-------|
| With Disease | TP | FN | TP+FN |
| Without Disease | FP | TN | FP+TN |
| Total | TP+FP | FN+TN | |

Table 5.1 Population classification fractions.

A number of measures based on this approach can be used to describe the ability of a diagnostic test to identify the true patient status:

Accuracy: is the proportion of all test results that are correct; it refers to the ability of the test to actually measure what it claims to measure and is defined as the fraction of all correct assessments among all assessments, i.e. $TP+TN/TP+FN+FP+TN$

Positive Predictive Value: is the proportion of true positives among all the positives identified by the test. When expressed as a percentage, it shows the probability that a test result will correctly identify the diseased cases and is defined by the fraction of the True Positives among the total positively identified population, i.e. $TP/TP+FP$

Sensitivity: is the proportion of true positives that are correctly identified by the test; expressed as a percentage it shows the probability that a test result will be positive when the disease is present and is defined by the fraction of the True Positives among the total diseased population, i.e. $TP/TP+FN$

Specificity: is the proportion of negatives that are correctly identified by the test; expressed as a percentage it shows the probability that a test result will be negative when the disease is not present and is defined by the fraction of the True Negative among the total Normal (without disease) population, i.e. $TN/FP+TN$

Positive and Negative likelihood ratios: are independent of the disease prevalence as they combine all four different classifications. The purpose is to evaluate for the diagnostic test what the chances are for a patient who tests positive to be true positive rather than false positive (PLR – equation 5.4) and conversely for a patient who tests negative, whether it is true negative or false negative (NLR – equation 5.5). Therefore:

$$PLR = \frac{\text{probability of positive test given the presence of the disease}}{\text{probability of a positive test given the absence of the disease}} \quad (5.4)$$

$$NLR = \frac{\text{probability of a negative test given the presence of the disease}}{\text{probability of a negative test given the absence of the disease}} \quad (5.5)$$

Consequently, PLR is the ratio between Sensitivity and the fall-out, i.e. Sensitivity/(1-Specificity) while NLR is the ratio (1-Sensitivity)/Specificity.

While the Positive Predicted Value should be high (close to 1), it can well be misleading if treated as an indicator of accuracy as it doesn't consider the positive cases that haven't been identified (FN). Plotting the Positive Likelihood ratio (PLR), i.e. sensitivity against 1-specificity, for different cut-off values (parameters) produces a curve (figure 5.9) known as Receiver Operating Characteristic (Zweig and Campbell, 1993, Greiner et al., 2000).

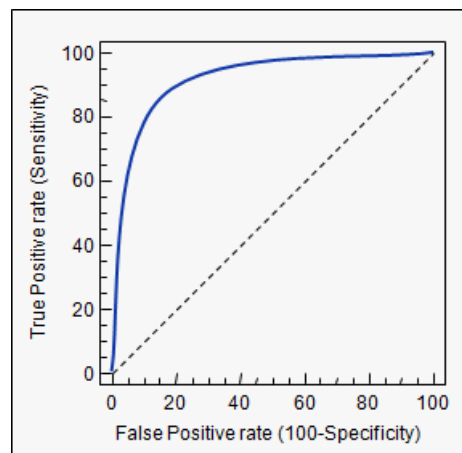


Figure 5.9 The ROC curve.

The importance of the ROC curve relies on the fact that it can be used as an indicator of the diagnostic test accuracy; ideally, if there is perfect discrimination between the diseased and non diseased distributions, both sensitivity and specificity would be 1 and the curve would reach the upper left corner of the plot. If there is no ability to discriminate between the two groups, the ROC curve would coincide with the plot's diagonal. As a result, the area under ROC is ideally 1 while in the worst case scenario it will equal 0.5 (Lalkhen and McCluskey, 2008). The descriptions related to different values for the area under the ROC curve (AUC) are shown in Table 5.2 (Hosmer Jr and Lemeshow, 2004).

| | |
|---------------------------|-----------------------------------|
| AUC \geq 0.9 | Outstanding discrimination (rare) |
| 0.9 \geq AUC \geq 0.8 | Excellent |
| 0.8 \geq AUC \geq 0.7 | Good (acceptable) |
| 0.7 \geq AUC $>$ 0.5 | Poor |
| AUC = 0.5 | No discrimination |

Table 5.2 General area under ROC curve (AUC) descriptions.

The area under the ROC curve can be calculated from numerical data using the trapezoidal rule, although it is expected that the AUC under the empirical curve is underestimated when compared with the AUC under the Gaussian-based ROC curve (Hanley and McNeil, 1982, Bradley, 1997). According to the trapezoidal approach, for a number of empirical pairs of (x_i, y_i) , where x_i stands for (1-specificity) and y_i for sensitivity, the area under the ROC curve will be given by the sum of the individual trapezoids, hence:

$$AUC = \sum_{i=0}^n \frac{1}{2} (y_i + y_{i+1})(x_{i+1} - x_i) \quad (5.6)$$

while the Standard Error of the empirical AUC (Bamber, 1975) is given by the formula 5.7, below:

$$SE = \sqrt{\frac{A(1-A) + (n_a - 1)(Q_1 - A^2) + (n_n - 1)(Q_2 - A^2)}{n_a n_n}} \quad (5.7)$$

where A is the calculated AUC, n_a and n_n the number of abnormal (diseased) and normal (non-diseased) conditions respectively and Q_1 and Q_2 are two distribution-specific quantities, defined as:

$$Q_1 = \frac{A}{(2-A)} \quad (5.8)$$

$$Q_2 = \frac{2A^2}{(1+A)} \quad (5.9)$$

In the case of glistenings detection, the number of True Negatives cannot be specified. This is due to the fact that there is no population of “non-glistenings” since there are no specified objects on the IOL image apart from the glistenings. In contrast, there might

be image disturbances that the programme might mistake for glistenings. There are two different approaches to overcome this difficulty:

a) Object-based classification

The evaluation metrics can to be adjusted to describe the significance and validity of our software results, based on the glistenings values and classification fractions as defined for this specific task by treating glistenings as individual objects (Table 5.3).

| | Detected | Not Detected | Total |
|-------------------|----------|--------------|-------|
| True glistenings | TP | FN | NG |
| False glistenings | FP | - | |
| Total | N | | |

Table 5.3 Glistenings Detection Classification fractions.

True Positive (TP) is the number of true glistenings detected as glistenings, False Positive (FP) is the number of false glistenings detected as glistenings and False Negative (FN) is the number of true glistenings that were not detected. Therefore:

Accuracy: the Glistenings Detection Programme defines accuracy as the equivalent of the Positive Predicted Value, hence the number of true detected glistenings among the number of detected, i.e. TP/N . Therefore, from now on, accuracy will refer to this definition used by the software.

Sensitivity: is the same as defined above i.e. the number of true glistenings detected as glistenings among the number of true glistenings, i.e. TP/NG

Error: as Specificity cannot be calculated due to the lack of True Negatives, an error needs to be defined, indicating the ability of our programme not to miss detecting true glistenings as well as not detecting other image areas as glistenings. As shown in figure 5.10, a value for the error can be approached through Set Theory.

Considering the number of True Glistenings among the image as the set NG (black circle) and the number of Detected Glistenings from programme as the set N (purple circle), then these are two intersecting sets. The intersection of NG with N is the True Positive glistenings (TP), i.e. $NG \cap N = TP$. The difference $NG - N$ is the False Negative

glistenings (FN), i.e. $NG - N = FN$ while the difference of $N - NG$ is the False Positive glistenings (FP), i.e. $N - NG = FP$.

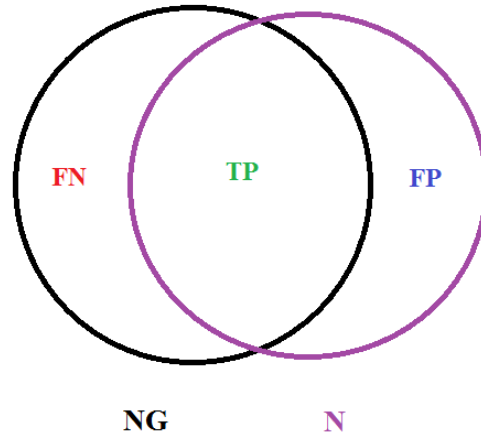


Figure 5.10 True glistenings (NG) and Detected glistenings (N) are two intersecting sets where their intersection $NG \cap N$ is the number of the True Positive (TP) glistenings.

The error can therefore be defined as the union of the sets' differences divided by the union of the sets:

$$Error = \frac{(NG - N) \cup (N - NG)}{NG \cup N} = \frac{FN + FP}{FN + TP + FP} \quad (5.5)$$

In other words, this error is a measure of the discrepancy between the detected glistenings (N) and the true glistenings (NG).

b) Pixel-based classification

This is a common approach for image processing and has also been used for retinal vessel segmentation process (Fraz et al., 2012) where any pixel is classified either as vessel or as surrounding tissue. In our case, image pixels can be classified either as glistenings or as surrounding lens. Consequently, True Positive (TP) is the number of pixels within true glistenings which are correctly identified as glistenings, False Positive (FP) is the number of pixels wrongly identified to belong in the area of glistenings, False Negative (FN) is the number of pixels that belong in true glistenings but were not detected and True Negatives is the number of pixels that covers all surrounding area of the lens and which are not identified as glistenings.

Accuracy, Sensitivity and Specificity (figure 5.11) are calculated as described above, but based on the number of pixels instead of the number of glistenings. We wish to have a high accuracy and at the same time high sensitivity and specificity (close to 1). Accuracy (Positive Predicted Value) itself might be misleading as it doesn't take into account the number of false negative glistenings. The downside to this approach is that, for images with small numbers of glistening, specificity is expected to be extremely high by default since the clear area within the lens is significant.

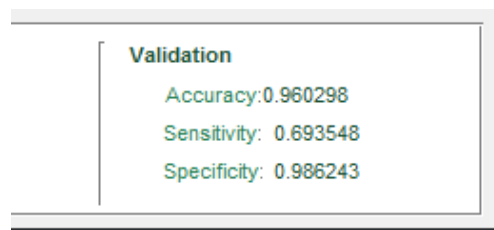


Figure 5.11 Validation metrics as appearing on the bottom right corner of our Detection Programme GUI.

Nevertheless, the pixel-based classification system was chosen as it enables us to provide statistics used when evaluating diagnostic tests and also to evaluate the software using normal image processing evaluation techniques.

5.4 Ground truth images

Six ground truth images of IOLs with glistenings grades between 1 and 4 (Table 5.4), were generated by the author. For each image, glistenings were manually identified using image handling software (Microsoft Paint) and converted into a black and white ground truth image. These ground truth images were used to test the performance of the glistenings detection programme.

After following the software's detection procedure as described in paragraph 5.2, the corresponding ground truth image can be selected for comparison. The areas of glistenings on the ground truth image that overlap with the image resulting from the detection software are highlighted in yellow. The areas that are defined as glistenings in the ground truth image but the software has failed to detect, i.e. the FN glistenings, are highlighted in green. Finally, the areas that the software identified as glistenings but are not according to the ground truth image, (FP), are shown in red. An example of the outcome of this method is shown in figure 5.12.

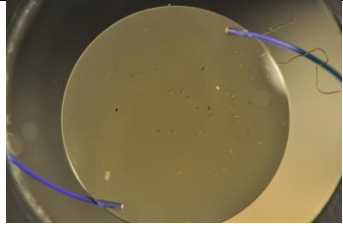
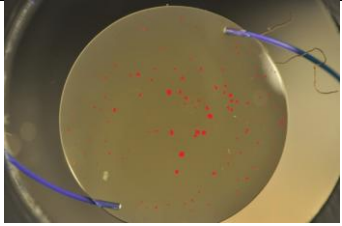
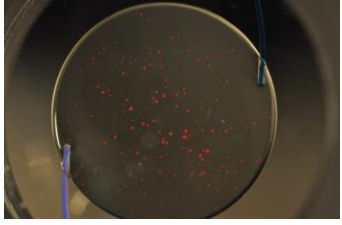
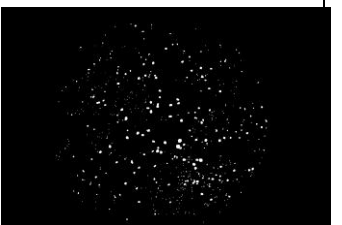
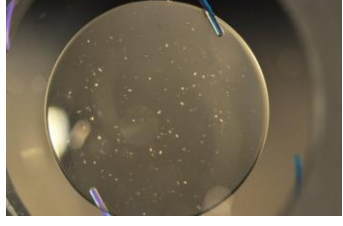
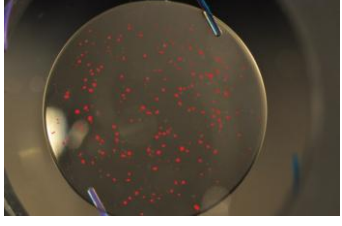
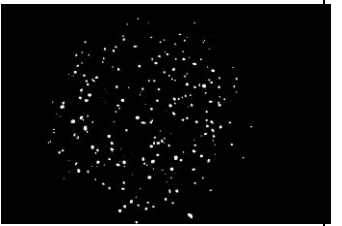
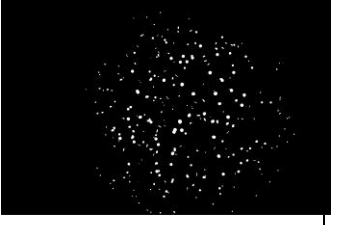
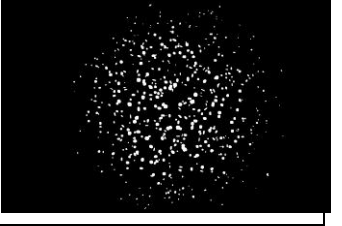
| File name/ Code | Image | Hand-drawn GT | BW Ground Truth |
|--------------------------|---|--|---|
| DSC_0582 A – grade 1 |  |  |  |
| DSC_0607 E – grade 3 |  |  |  |
| DSC_0614 F – grade 2 |  |  |  |
| DSC_0737 S3 – grade 2 |  |  |  |
| DSC_0759 S6 – grade 3 |  |  |  |
| DSC_0776 S8 – grade 4 |  |  |  |

Table 5.4 Ground truth images.

Validation metrics as described in paragraph 5.3, according to the pixel-based classification, appear in bottom right side of the software's interface. Following this procedure for all available images with a corresponding ground truth image, the validation metrics were used to evaluate the software and the role of the input parameters.

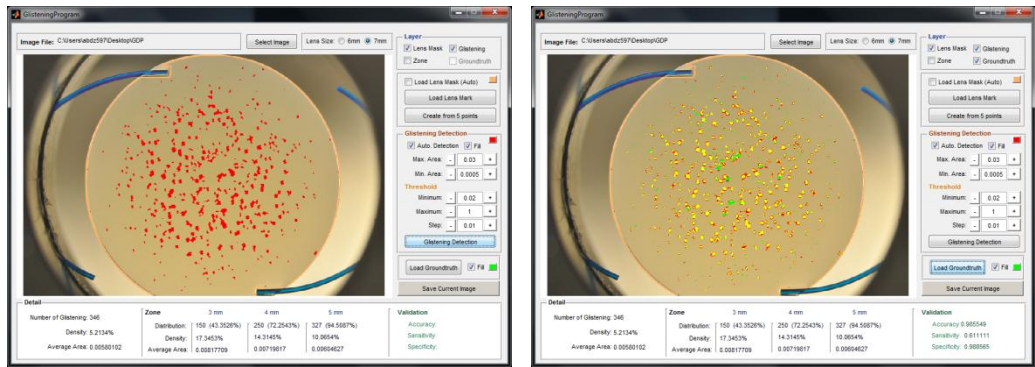


Figure 5.12 Result after glistenings' detection with the corresponding ground truth image.

5.5 Reproducibility of setting the Area of Interest

A number of evaluation and reliability tests were carried out to determine the range of input parameters that are appropriate to apply in our images to produce an accurate result. Values for the detection parameters used as a starting point were the ones set by the program developer (Table 5.5).

| Glistenings Detection | |
|------------------------------|--------|
| Max. Area: | 0.03 |
| Min. Area: | 0.0005 |
| Threshold | |
| Minimum | 0.02 |
| Maximum | 1 |
| Step | 0.01 |

Table 5.5 Detection parameters set as an initial starting point.

After loading the desired IOL image for detection, the area of interest was set for the IOL. This was achieved by manually marking five equally spaced points on the IOL's edge. The program then calculated a best fit circle to the points to define the mask. Detection of glistenings then occurred within the area of interest defined by the mask. Reproducibility of this procedure was evaluated by repeating the steps five different times for the same image (DSC_0776) using the same values for the detection parameters (glistenings area and threshold). The results are shown on Table 5.6:

| Test | Glistenings | Accuracy | sensitivity | Specificity |
|-------------------|--------------|--------------|--------------|--------------|
| 1 | 348 | 0.977 | 0.609 | 0.989 |
| 2 | 345 | 0.988 | 0.611 | 0.989 |
| 3 | 346 | 0.986 | 0.611 | 0.989 |
| 4 | 349 | 0.977 | 0.611 | 0.988 |
| 5 | 349 | 0.977 | 0.611 | 0.988 |
| Mean Value | 347 | 0.981 | 0.611 | 0.989 |
| STDV | 2 | 0.006 | 0.001 | 0.001 |
| CV | 0.58% | 0.61% | 0.16% | 0.10% |

Table 5.6 Mask Reproducibility.

Fluctuation of results depends on how concentric the drawn mask is with the actual IOL as well as the difference in diameter. In all cases standard deviation values are small with a coefficient of variation less than 1% (0.01). This indicates that the procedure is highly reproducible and setting the mask has minimal effect on glistenings detection.

5.6 Glistenings Detection Parameters

5.6.1 Fixed Parameter Values

Initially, the default detection parameters were used to see how the software performed on different images. There were five images with various sizes and densities of glistenings available together with their corresponding ground truth images. For all images, the customized mask created by the software developer was used. As a result, no variability was introduced by manually setting the mask. Results are shown in table 5.7.

| GT | Accuracy | Sensitivity | Specificity |
|-------------------|--------------|--------------|--------------|
| DSC_0582 | 0.905 | 0.496 | 0.997 |
| DSC_0607 | 0.760 | 0.507 | 0.991 |
| DSC_0614 | 0.655 | 0.793 | 0.989 |
| DSC_0737 | 0.995 | 0.510 | 0.998 |
| DSC_0759 | 0.922 | 0.784 | 0.995 |
| DSC_0776 | 0.986 | 0.611 | 0.988 |
| Mean Value | 0.871 | 0.617 | 0.993 |
| SD | 0.135 | 0.139 | 0.004 |

Table 5.7 Initial glistenings detection for all ground truth images

The results indicate that for the same (fixed) parameters, different results are achieved in terms of accuracy, sensitivity and specificity. Specificity is high in all cases; sensitivity on

the other hand showed a wider variation with a range from 0.496 to 0.793, (low to moderate values). Accuracy levels were good for most images but in some cases (DSC_0607 and DSC_0614) needs to be improved, hence the detection parameters become optimal so the number of False Positives are reduced. The choice of software detection parameters to optimise the metrics is investigated in the next section to see if better validation metrics can be achieved.

5.6.2 Detection Parameters – Moderate grade of glistenings

The aim of the study in this section was to determine the parameter combinations that give the best sensitivity, accuracy and specificity for a given image. The image chosen for this section had a moderate glistenings grade (grade 3) and all tests were recorded for the same mask to avoid reproducibility errors described previously (paragraph 5.5.2). The size of glistenings was defined according to previous glistenings studies to be between 1 μ m for the minimum expected and 20 μ m as the maximum. Threshold parameters can be varied and lead to an infinite number of different combinations. Three representative values were chosen for each parameter that consequently generated twenty-seven different tests: The “Min. Threshold” values, had values of 0, 0.01 and 0.02. The “Max. Threshold” values, were 1, 0.9 and 0.8. Finally, the “Step” parameter had values of 0.01, 0.02 and 0.03. In addition, three more tests of extreme cases were undertaken to produce data for the ROC curve evaluation. For these extreme cases, the intensity grading was set to a low level hence the test criterion value would produce a very low specificity. Step was fixed at a moderate value (0.02), Max. Threshold was chosen as the lowest from the above cases (0.8) while Min. Threshold was increased to values of 0.05, 0.1 and 0.2. The results for all parameter combinations are shown in Table 5.8.

For the 27 different tests, all gave accuracy and specificity values close to 1. Sensitivity on the other hand, varied (0.704 ± 0.217). Changing the Maximum Threshold value from 1 to 0.8 did not affect the results. For example, the results in tests 1, 7 and 10 are identical. Therefore, the value of Max. Threshold was set at 1.

Increasing the Minimum Threshold value did affect the results; a value of 0.1 produced more consistent results compared to a value of 0, for all validation metrics. At higher values, sensitivity decreases, which can also be seen in the extreme case tests (28-30). Further investigation for the Min. Threshold parameter is required to produce more definitive results.

As the parameter value for “Step” increased, the sensitivity reduced markedly. For example for tests 1, 2 and 3, the sensitivity fell rapidly from 0.85 to 0.50. Therefore, the value of the parameter Step was taken as 0.01.

The ROC curve was generated by joining the empirical pairs of 1-Specificity (x-axis) and Sensitivity (y-axis) with the points of (0,0) and (1,1) part of the data by definition. Following the trapezoidal approach, the calculated area under the ROC curve was 0.923 \pm 0.003 SE, indicating a likely outstanding discrimination between the distributions of glistenings and non-glistenings.

| test | Min Thres | Max Thres | Step | Accuracy | Sensitivity | Specificity |
|------|-----------|-----------|------|----------|-------------|-------------|
| 1 | 0 | 1 | 0.01 | 0.838 | 0.853 | 0.991 |
| 2 | 0 | 1 | 0.02 | 0.949 | 0.751 | 0.995 |
| 3 | 0 | 1 | 0.03 | 0.986 | 0.505 | 0.997 |
| 4 | 0 | 0.9 | 0.01 | 0.838 | 0.853 | 0.991 |
| 5 | 0 | 0.9 | 0.02 | 0.949 | 0.751 | 0.995 |
| 6 | 0 | 0.9 | 0.03 | 0.986 | 0.505 | 0.997 |
| 7 | 0 | 0.8 | 0.01 | 0.838 | 0.853 | 0.991 |
| 8 | 0 | 0.8 | 0.02 | 0.949 | 0.751 | 0.995 |
| 9 | 0 | 0.8 | 0.03 | 0.986 | 0.505 | 0.997 |
| 10 | 0.01 | 1 | 0.01 | 0.838 | 0.853 | 0.991 |
| 11 | 0.01 | 1 | 0.02 | 0.836 | 0.842 | 0.991 |
| 12 | 0.01 | 1 | 0.03 | 0.836 | 0.842 | 0.991 |
| 13 | 0.01 | 0.9 | 0.01 | 0.838 | 0.853 | 0.991 |
| 14 | 0.01 | 0.9 | 0.02 | 0.836 | 0.842 | 0.991 |
| 15 | 0.01 | 0.9 | 0.03 | 0.836 | 0.842 | 0.991 |
| 16 | 0.01 | 0.8 | 0.01 | 0.838 | 0.853 | 0.991 |
| 17 | 0.01 | 0.8 | 0.02 | 0.836 | 0.842 | 0.991 |
| 18 | 0.01 | 0.8 | 0.03 | 0.836 | 0.842 | 0.991 |
| 19 | 0.02 | 1 | 0.01 | 0.949 | 0.751 | 0.995 |
| 20 | 0.02 | 1 | 0.02 | 0.949 | 0.751 | 0.995 |
| 21 | 0.02 | 1 | 0.03 | 0.949 | 0.751 | 0.995 |
| 22 | 0.02 | 0.9 | 0.01 | 0.949 | 0.751 | 0.995 |
| 23 | 0.02 | 0.9 | 0.02 | 0.949 | 0.751 | 0.995 |
| 24 | 0.02 | 0.9 | 0.03 | 0.949 | 0.751 | 0.995 |
| 25 | 0.02 | 0.8 | 0.01 | 0.949 | 0.751 | 0.995 |
| 26 | 0.02 | 0.8 | 0.02 | 0.949 | 0.751 | 0.995 |
| 27 | 0.02 | 0.8 | 0.03 | 0.949 | 0.751 | 0.995 |
| 28 | 0.2 | 0.8 | 0.02 | 1.000 | 0.059 | 0.999 |
| 29 | 0.1 | 0.8 | 0.02 | 0.969 | 0.117 | 0.999 |
| 30 | 0.05 | 0.8 | 0.02 | 0.985 | 0.249 | 0.998 |

Table 5.8 Software performance for an image with moderate grade of glistenings and different input parameters (see text for details).

5.6.3 Detection Parameters – High grade of glistenings

The method described in the previous paragraph was repeated for an image with high (grade 4) severity glistenings. This provides a useful comparison with the results in the previous section as not only are there a higher number of glistenings but also their size appeared to be larger resulting in an overlap of glistenings in some cases. The aim was to determine how well the detection software can discriminate such cases. The results are shown in Table 5.9.

| test | Min Thres | Max Thres | Step | Accuracy | Sensitivity | Specificity |
|------|-----------|-----------|------|----------|-------------|-------------|
| 1 | 0 | 1 | 0.01 | 0.960 | 0.693 | 0.986 |
| 2 | 0 | 1 | 0.02 | 0.985 | 0.600 | 0.989 |
| 3 | 0 | 1 | 0.03 | 0.987 | 0.547 | 0.991 |
| 4 | 0 | 0.9 | 0.01 | 0.960 | 0.693 | 0.986 |
| 5 | 0 | 0.9 | 0.02 | 0.985 | 0.600 | 0.989 |
| 6 | 0 | 0.9 | 0.03 | 0.987 | 0.546 | 0.991 |
| 7 | 0 | 0.8 | 0.01 | 0.960 | 0.694 | 0.986 |
| 8 | 0 | 0.8 | 0.02 | 0.985 | 0.600 | 0.989 |
| 9 | 0 | 0.8 | 0.03 | 0.987 | 0.547 | 0.991 |
| 10 | 0.01 | 1 | 0.01 | 0.963 | 0.694 | 0.986 |
| 11 | 0.01 | 1 | 0.02 | 0.962 | 0.686 | 0.987 |
| 12 | 0.01 | 1 | 0.03 | 0.960 | 0.686 | 0.987 |
| 13 | 0.01 | 0.9 | 0.01 | 0.963 | 0.694 | 0.986 |
| 14 | 0.01 | 0.9 | 0.02 | 0.962 | 0.686 | 0.987 |
| 15 | 0.01 | 0.9 | 0.03 | 0.960 | 0.686 | 0.987 |
| 16 | 0.01 | 0.8 | 0.01 | 0.963 | 0.694 | 0.986 |
| 17 | 0.01 | 0.8 | 0.02 | 0.962 | 0.686 | 0.987 |
| 18 | 0.01 | 0.8 | 0.03 | 0.960 | 0.686 | 0.987 |
| 19 | 0.02 | 1 | 0.01 | 0.988 | 0.608 | 0.989 |
| 20 | 0.02 | 1 | 0.02 | 0.988 | 0.600 | 0.989 |
| 21 | 0.02 | 1 | 0.03 | 0.988 | 0.595 | 0.990 |
| 22 | 0.02 | 0.9 | 0.01 | 0.988 | 0.607 | 0.989 |
| 23 | 0.02 | 0.9 | 0.02 | 0.988 | 0.600 | 0.989 |
| 24 | 0.02 | 0.9 | 0.03 | 0.988 | 0.595 | 0.990 |
| 25 | 0.02 | 0.8 | 0.01 | 0.988 | 0.608 | 0.989 |
| 26 | 0.02 | 0.8 | 0.02 | 0.988 | 0.600 | 0.989 |
| 27 | 0.02 | 0.8 | 0.03 | 0.988 | 0.595 | 0.990 |
| 28 | 0.2 | 0.8 | 0.02 | 1.000 | 0.009 | 0.999 |
| 29 | 0.1 | 0.8 | 0.02 | 0.983 | 0.104 | 0.999 |
| 30 | 0.05 | 0.8 | 0.02 | 0.980 | 0.444 | 0.996 |

Table 5.9 Set of parameters applied on DSC_0776, high grade of glistenings IOL image

The optimal detection parameter values are the same as found in section 5.6.2. However, the sensitivity values in all cases were lower for the high grade IOL compared with the moderate grade. This indicates that the number of not detected true glistenings (FN) is proportionally greater. Comparing the programme's result with the initial image (figure

5.13) it appears that the areas marked in green (false negatives) are likely to be in areas where glistenings overlap.

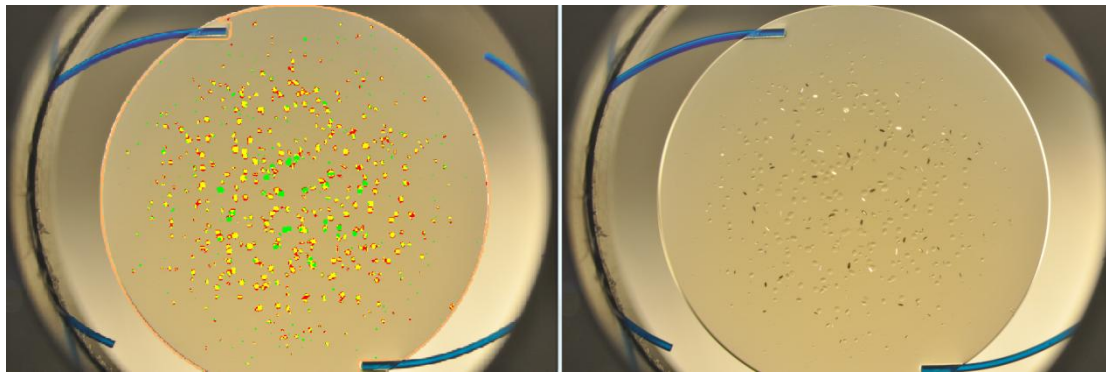


Figure 5.13 Comparison of GDP outcome (left) with initial image (right) for DSC_0776, high grade IOL image. The undetected true glistenings areas are likely to be in areas that glistenings overlap.

The empirical area under the ROC curve was calculated as 0.841 ± 0.002 SD indicating an excellent discrimination between the distributions of glistenings and non-glistenings. Both ROC curves for the moderate and high grade of glistenings IOLs are plotted in figure 5.14. The sharp transition from the empirical points to the (1,1) point can be explained by the fact that specificity is always high, hence the value of $1 - \text{Specificity}$ is close to 0 in all cases.

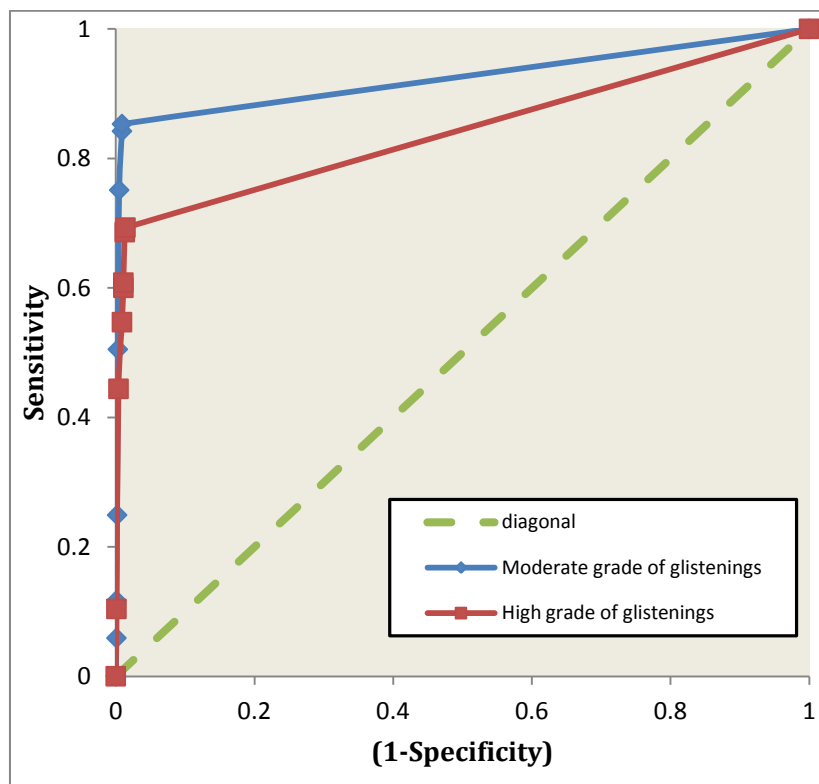


Figure 5.14 ROC empirical curves for a moderate grade of glistenings IOL image (blue line) and a high grade of glistenings IOL image (red line).

5.6.4 Detection Parameters – All images with groundtruth

Given that not all images are identical in terms of brightness and contrast, further investigation on the minimum threshold parameter was necessary. Keeping the other input parameters fixed, all images with associated groundtruth images were evaluated by the detection software for four different Minimum Threshold values of 0, 0.01, 0.02 and 0.03. To compare the outcomes, the product of accuracy, sensitivity and specificity (Jin and Dunbrack, 2005) is calculated as an outcome measure since all three statistics are required to be close to the 1, hence their product will also vary from 0 to 1. This product is then plotted against the Minimum Threshold Values for each image (figure 5.15).

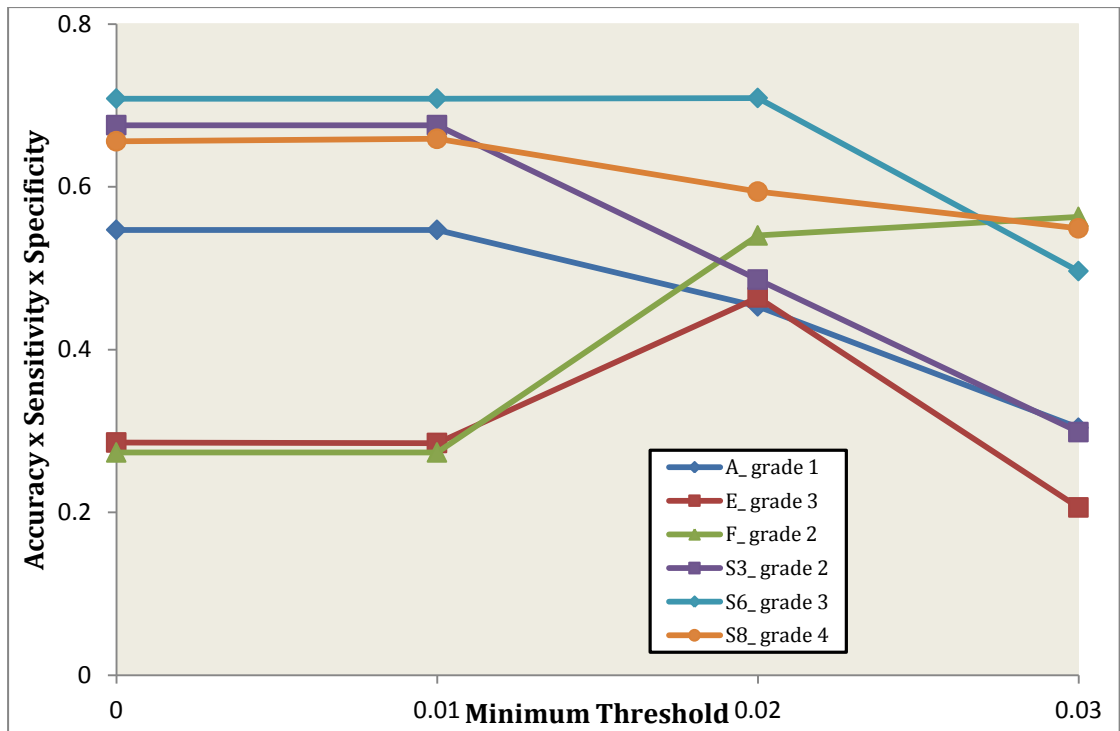


Figure 5.15 Variation of Minimum Threshold value on all ground truth images.

The graph in figure 5.15 indicates that in all cases, Minimum Threshold values from 0 to 0.01 did not alter the detection ability of the software. However, the transition from 0.02 to 0.03 changes the software's performance decreasing it for some images and improving performance for others. Furthermore, for images DSC_0607 and DSC_0614 the best results occur for a 0.02 Minimum Threshold value in contrast to the rest of the images. This can be explained by the fact that in both DSC_0607 and DSC_0614 the background to the glistenings is dark whereas for all other groundtruth images the surrounding area is bright. The gradient of image intensity that the Sobel operator detects is lower in the case

of the images with a bright background than images with a dark background. As a result, the Sobel operator could detect image noise as glistenings (figure 5.16), increasing the number of FP pixels (red).

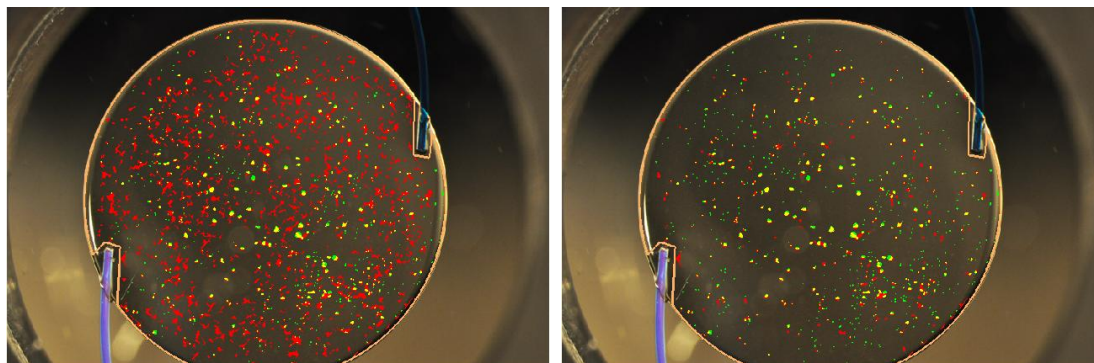


Figure 5.16 DSC_0607: For minimum threshold value 0.01, the number of incorrectly detected glistenings is 6 times bigger than for a minimum threshold value 0.02.

It was therefore decided that for bright images, a Min. Threshold of 0.01 was to be used, while for dark images the Min. Threshold was taken as 0.02. Using this protocol for all images with associated groundtruth images, accuracy was found to be 0.847 ± 0.110 , sensitivity is 0.716 ± 0.094 and specificity is 0.992 ± 0.004 (all values mean \pm SD).

5.7 Discussion

Several studies have been published that indicate interest in an objective way of quantifying and grading the severity of glistening (Waite et al., 2007, Behndig et al., 2009, Mönestam et al., 2011, Rønbeck et al., 2013, Colin and Orignac, 2011, van der Mooren et al., 2013). Metrics include density and size since there is strong evidence from Mie theory that smaller glistenings can have a significant effect on light scattering. Although a number of studies have indicated that they have used a method for objectively quantifying glistenings, there is no specific publication about the development and validation of detection software.

Our Glistenings Detection Program, was developed to quantify objectively glistenings in intraocular lenses by analyzing in vitro slit-lamp images through an image segmentation process and edge detection using a Sobel operator, a method that has also been used in retinal images studies.

The evaluation reported in this chapter showed a strong reproducibility, indicating a reliable procedure. Sensitivity and specificity values and the resulting empirical ROC

curve suggest an excellent discrimination by the algorithm between true glistenings and non-glistenings. The validation could be considered limited because specificity is always very high due to the fact that the number of “non glistening” pixels on images is usually very high. However, as was discussed in section 5.3, validation metrics all have their limitations.

In clinical tests it is generally preferred to have a high sensitivity and low specificity (Lalkhen and McCluskey, 2008). It is important to note that groundtruth images are hand-drawn (Microsoft Paint), hence there is a random error derived from hand stability as well as subjective judgement of what is and isn't a glistening.

The comparison of the ROC curves between a moderate severity of glistenings (grade 3) and a high one (grade 4) suggests that the software is likely to have difficulty in discriminating glistenings when they overlap. This can potentially cause poorer detection for images of intraocular lenses with large size and higher density of glistenings (figure 5.17).

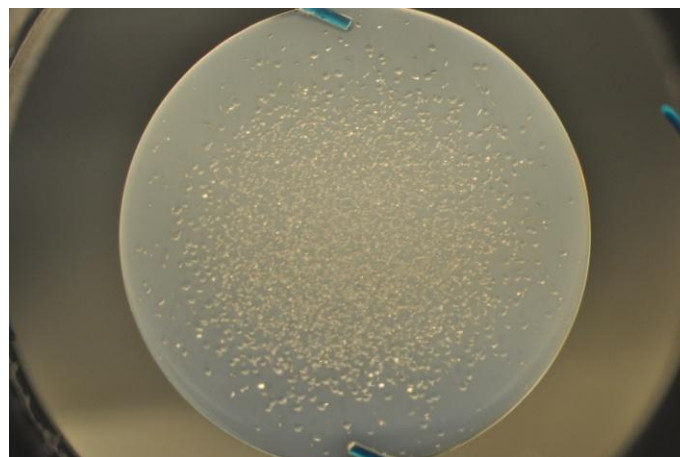


Figure 5.17 Image of an IOL with high density and moderate size of glistenings (grade >4).

The protocol chosen from this validation study for the detection parameters (Table 5.10) has been shown to be efficient for all groundtruth images. In the case of the Min. Threshold, the software operator has to change its value based on the judgement of an image having a dark or bright background; indeed, the experience of an expert is required. However as shown in figure 5.16 the discrepancy between picking wrong pixels as glistenings and detecting true ones for the two threshold values can be visually perceived.

| Glistenings Detection | |
|------------------------------|-------|
| Max. Area: | 0.02 |
| Min. Area: | 0.001 |
| Threshold | |
| Minimum (if bright) | 0.01 |
| Minimum (if dark) | 0.02 |
| Maximum | 1 |
| Step | 0.01 |

Table 5.10 Software evaluation suggested protocol.

The Glistenings Detection Programme is semi-automatic and further development is required for a fully automatic version. Creating and validating additional groundtruth images would strengthen the accuracy of the software. Moreover, validation of en face IOL images captured with different methods such as optical microscopy or in vivo slit-lamp imaging could lead to the development of a unique tool specialized for IOL glistenings studies.

Chapter 6

Association between forward light scatter and objective grading of IOL Glistenings

6.1 Introduction

The results from Chapter 4 demonstrated that subjective grading may not fully quantify glistenings since there was a weak correlation with scattered light. An objective method to quantify glistenings has been described in Chapter 5 to better understand the role of glistenings in forward light scatter by relating light scatter to their nature and morphology. In this chapter, data from the same IOLs measured in Chapter 4 were used and association between light scatter and the metrics produced by the Glistenings Detection Programme investigated.

6.1.1 Light Scattering by Small Particles

Glistenings have been shown to be fluid-filled microvacuoles within an IOL. Their contribution to light scatter depends on the refractive index difference between the vacuoles and the lens material, as well as the size, density and shape of the glistenings. The effect of these parameters on light scatter are described below in order to understand the propagation of a light beam when passing through an IOL with glistenings. When particles interact with light, two different processes can occur: elastic scattering where the energy received can be reradiated by the particle in different directions as shown in figure 6.1, or inelastic scattering where different intensities are scattered in different directions so the scattering is more directional. In addition, the radiant energy can be transformed into other forms of energy, such as heat, which is the process of absorption.

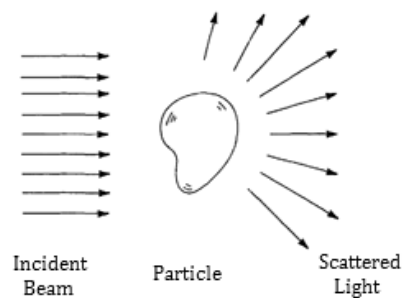


Figure 6.1 Scattering by an arbitrary particle.

Light attenuation is analyzed by considering a single particle of arbitrary size and shape, irradiated by a plane electromagnetic wave (figure 6.2). At a large distance, r , compared with the particle diameter and wavelength, the scattered energy appears as a spherical wave around the particle. The total energy lost by the plane wave, defined as the extinction energy, is equal to the scattered energy in the spherical wave plus the energy of absorption. If I_0 is the intensity of the incident beam and I the scattered wave's intensity, it can be shown that

$$I r^2 \sin \theta d\theta d\varphi = I_0 \left(\frac{\lambda}{2\pi}\right)^2 F(\theta, \varphi, \lambda) \sin \theta d\theta d\varphi \quad (6.1)$$

hence

$$I = \frac{I_0 F(\theta, \varphi, \lambda)}{(2\pi r/\lambda)^2} \quad (6.2)$$

where $F(\theta, \varphi, \lambda)$ is the dimensionless scattering function, dependent on the wavelength of the incident beam, the size, shape and optical properties of the particle but not on distance r . For spherical particles there is no φ dependence, therefore scatter is uniform in all directions. The relative values of F can be plotted on a polar diagram as a function of θ for a plane in the direction of the incident beam, called the scattering diagram for the particle.

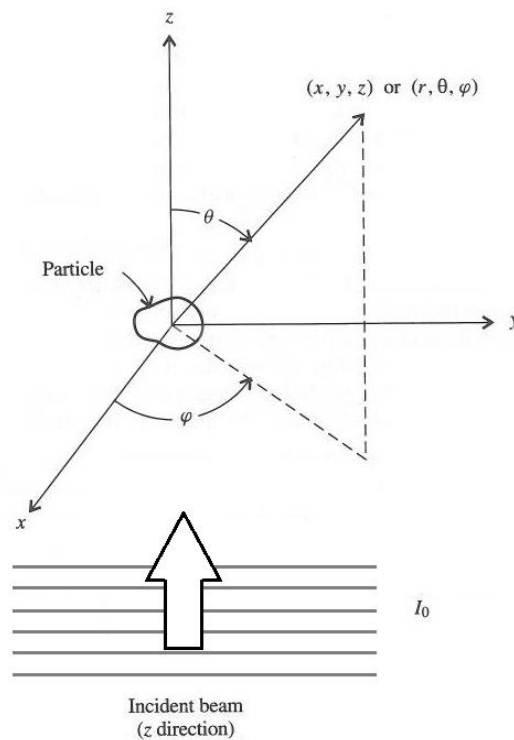


Figure 6.2 The direction of scattering at any r is characterized by the scattering angle θ measured relative to the direction of the incident beam and the azimuth angle φ .

Having a cloud of many similar particles and assuming that the depth of the cloud is minimal, i.e. all particles receive the same incident intensity I_o , the total scatter function, $F(\theta, \varphi)$, is the summation of each particle individual $F_i(\theta, \varphi)$, hence:

$$F(\theta, \varphi) = \sum_i F_i(\theta, \varphi) . \quad (6.3)$$

If N is the number of particles per unit volume and V the volume of the scattering medium, the total number of particles is NV and the scattered intensity now at a distance r is given by

$$I = \frac{NV}{(2\pi r/\lambda)^2} F(\theta, \varphi) I_o. \quad (6.4)$$

Therefore, for identical particles, the greater their total number in a fixed volume, the more the scattered light. Apart from the intensity function I , other parameters need to be defined and to characterize the scattered light. The scattering cross section C_{sca} is an area defined by normalising the total energy scattered in all directions by the particle to the energy of the incident beam:

$$C_{sca} = \frac{1}{I_o} \int_0^{2\pi} \int_0^\pi I r^2 \sin \theta d\theta d\varphi \quad (6.5)$$

which is not in general equal to the particle cross-sectional area. For that reason, the scattering efficiency is defined:

$$Q_{sca} = C_{sca}/S_g \quad (6.6)$$

where S_g is the geometric cross section of a single particle. From theory, models of elastic light scattering caused by particles can be divided into three categories based on a dimensionless size parameter (Van De Hulst, 1957), x which is defined by

$$x = \frac{2\pi a n_m}{\lambda} \quad (6.7)$$

where a is the radius of a single particle, λ the wavelength of incident light and n_m the refractive index of surrounding medium. The three categories are:

- 1) For $x \ll 1$, Rayleigh scattering occurs (particle dimensions small compared to the wavelength).
- 2) For $x \approx 1$, Mie scattering occurs (particle about the same size with the wavelength).

- 3) For $x \gg 1$, the geometric models of scattering apply since the particle is much larger than the wavelength.

In the case of glistenings, Rayleigh scattering is small as the size of glistenings is of the order of microns, which is larger than visible spectrum wavelength (380nm – 780nm).

Mie theory, introduced by Gustav Mie (Mie, 1908), is a solution of Maxwell's equations used to compute light scattering in the case of small spherical particles. These expressions take the form of an infinite series expansion of vector harmonics from which cross sections, efficiency factor and intensity distribution from a particle can be derived. Computational work for evaluating scattering problems using Mie theory involves solving differential equations and functions such as the Riccati-Bessel function (Wriedt, 1998). A number of programs are available in codes like Fortran, Matlab and Mathematica. A freely available program for Windows is MiePlot (Laven, 2006) created by Philip Laven for use in water drop optics (Laven, 2003). It has recently been used in glistenings studies (van der Mooren et al., 2013) for evaluating the intensity distribution $I(\theta)$ and extinction coefficient γ according to the formula

$$\gamma = \int_0^\infty \pi \alpha^2 Q(a) N(a) da \quad (6.8)$$

where Q , the scatter extinction efficiency factor (non absorbing spherical particles), is given by

$$Q(\rho) = 2 - \left(\frac{4}{\rho}\right) \sin \rho + \left(\frac{4}{\rho^2}\right) (1 - \cos \rho). \quad (6.9)$$

In equations (6.8) and (6.9) N is the glistenings distribution per volume and ρ the wavefront's phase lag.

In the case of large particles, as mentioned above, geometrical (ray) optics is used to describe the propagation of light. Figure 6.3 shows a representative example of this case; part of the incident beam can be reflected from particle's surface whereas other rays will be refracted, sometimes after several internal reflections.

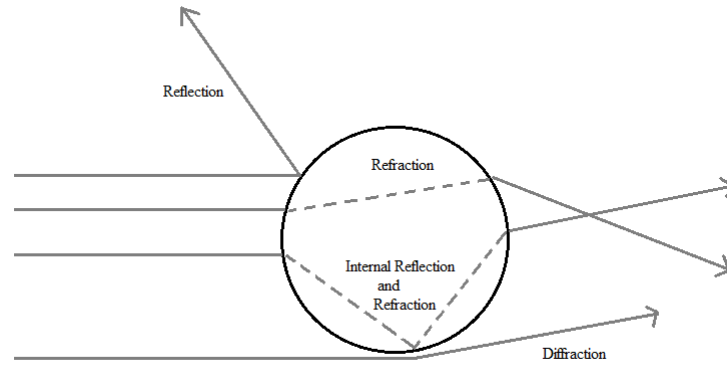


Figure 6.3 Light possible interactions with a large size particle.

Both the light directly reflected and the light refracted contribute to the total scattering by the particle. In addition, in the case of large particles, diffraction also occurs. The intensity distribution caused by diffraction is independent of the nature and composition of the particle; it only depends on its form and size. Due to this property, laser diffraction is widely used for particle size characterization (Ma et al., 2000, Eshel et al., 2004) by measuring the angular variation in scattered light intensity where large particles are expected to scatter light at small angles whereas smaller particles scatter light in wider angles, in principle.

The phenomenon of diffraction by large particles also explains the Extinction Paradox; when the distance of a detector from a scattering particle is large compared to the particle size, the total energy removed from the incident wave is twice the amount of light intercepted by its geometric cross-sectional area. Hence, for $x \gg 1$, $Q_{sca} \rightarrow 2$.

Following the geometrical path l of rays, the probability distribution function $p(l)$ for a particle at a fixed orientation is the Fourier cosine transform of the spectrum of the extinction efficiency (Kokhanovsky, 2008)

$$p(l) = \frac{\pi}{2} \int [1 - Q_{ext}(k)] \cos(kl) dk \quad (6.10)$$

where k is the wave number $2\pi/\lambda$. For a randomly oriented particle, the ray distribution is given by

$$p_r = \frac{\int p(l)\Sigma(\Omega)d\Omega}{\int \Sigma(\Omega)d\Omega} \quad (6.11)$$

where $\Sigma(\Omega)$ is the projection area of the particle at the orientation Ω .

Consider an ellipsoidal particle centered at the origin of a 3D Cartesian coordinate system (x, y, z) and a second rotated coordinate system (x', y, z') , where θ is the angle of rotation.

For a plane wavefront passing through an ellipsoid at the (x',y) orientation with a z' direction (figure 6.4), the geometrical path on the $z'=0$ plane is given by:

$$l = \frac{2ab}{\sqrt{a^2 \cos^2 \theta + b^2 \sin^2 \theta}} \sqrt{1 - (a^2 \cos^2 \theta + b^2 \sin^2 \theta)^{-1} \chi'^2 - a^{-2} y^2} \quad (6.12)$$

where θ is the angle of the incident beam with the 3D Cartesian coordinate system of the particle and a and b the ellipse semi-axes. The projected area of the ellipsoid is given by:

$$\Sigma = \pi a \sqrt{a^2 \cos^2 \theta + b^2 \sin^2 \theta}. \quad (6.13)$$

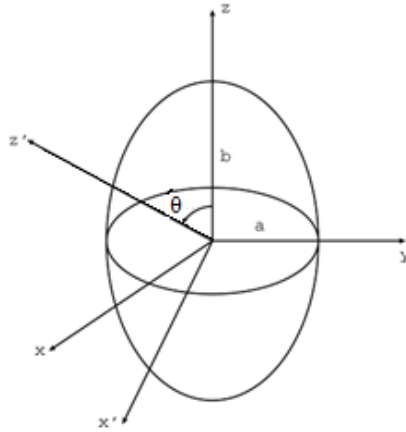


Figure 6.4 A spheroid particle whose axis of revolution orientation has an angle of θ with the incident beam.

If ϵ is the ratio of the semi-axes such that $a=\epsilon b$, the geometrical path distribution of the rays for a spheroid particle is defined by (Xu et al., 2003)

$$p_{sph}(l) = \frac{d\Sigma}{\Sigma} = \frac{1}{2\epsilon^2 b^2} (\epsilon^2 \cos^2 \theta + \sin^2 \theta) l \mathbf{H} \left(\frac{2\epsilon b}{\sqrt{\epsilon^2 \cos^2 \theta + \sin^2 \theta}} - l \right) \quad (6.14)$$

where \mathbf{H} is a Heaviside step function. In the case of a sphere, where $a=b$, hence $\epsilon=1$, the above equation is simplified to

$$p_{sph}(l) = \frac{1}{2b^2} l \mathbf{H}(2b - l). \quad (6.15)$$

6.1.2 Objective quantification of glistenings – previous studies

Previous studies have demonstrated ways of objectively quantifying IOL glistening. These can be categorised into three different groups, depending on their methods and scope:

a) Evaluation of glistenings size, morphology and nature (Kato et al., 2001, Miyata et al., 2001, Gregori et al., 2002, Saylor et al., 2010, Thomes and Callaghan, 2013). Glistenings were reported to be between 1 μ m and 20 μ m in diameter. Size has been shown to increase when IOLs are cooled to room temperature. The shape of glistenings is not always spherical; ellipsoidal shapes have also been observed.

b) In vivo studies associating size, number or density of glistenings with visual test results, such as best-corrected logMAR visual acuity, contrast sensitivity, glare testing, higher order wavefront aberrations and intraocular straylight using the C-Quant (Waite et al., 2007, Colin and Orignac, 2011, Schweitzer et al., 2013). In all cases, no statistically significant correlation was found between quantification of glistenings and the visual tests used.

c) In vitro studies with direct correlation of objective measures of glistenings with light scattering results (Kim et al., 2011, van der Mooren et al., 2013). In both cases, a positive association was found between the number of glistenings and light scatter. This result is in agreement with other in vitro studies of IOL glistenings and forward light scatter (Van der Mooren et al., 2007, Oshika et al., 2001, Das et al., 2013).

A recent study, using mathematical modelling (DeHoog and Doraiswamy, 2014) based on Mie scatter theory and implemented in Zeemax, attempted to evaluate the impact of light scatter from IOL glistenings. Twelve different combinations of glistenings size and volume concentrations in the lens were investigated as illustrated in figure 6.5.

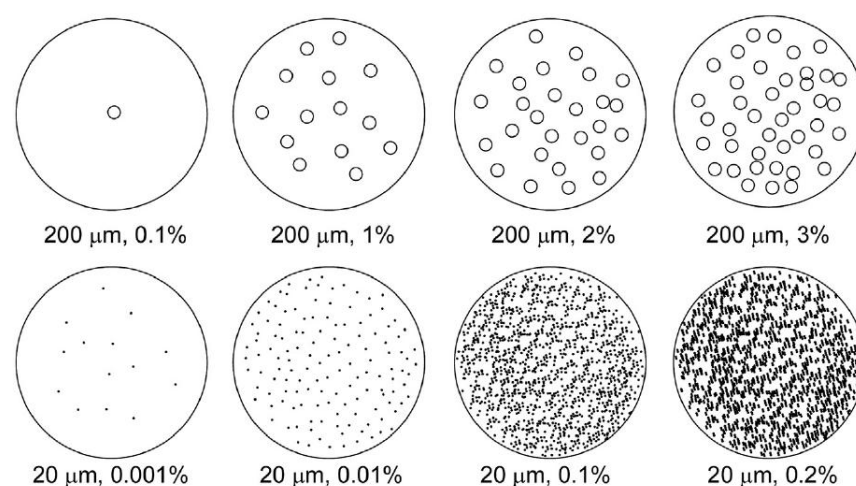


Figure 6.5 Illustration of different glistenings sizes and densities (DeHoog and Doraiswamy, 2014)

The computational results from this study demonstrated that light scatter is inversely proportional to the particle size, hence the smaller the size of glistenings the greater the effect of scatter. In addition, light scatter appears to be proportional to the volume concentration of the glistenings; the total volume of glistenings in the lens not only depends on their size but their number as well. Consequently, it is clear that for the same size of glistenings, the greater their number the more the scattered light; but yet if there is an equilibrium between a small size of glistenings with great number on the one hand and large size with a small total number on the other hand giving the same total volumes, the difference between the two cases in light scatter is not clear.

6.2 Methods

Images collected during the study described in Chapter 4 had their glistenings objectively quantified using the Glistenings Detection Programme. Forward light scatter measurements were taken following the procedure described in Chapter 3 (3.2 and 3.3). Data were further analyzed as described in Chapter 4 (4.2.2) while the Glistenings Detection Program is described in Chapter 5 (5.2). Figure 6.6 illustrates how the software detection results appear in GDP's interface for a lens (IOL F).

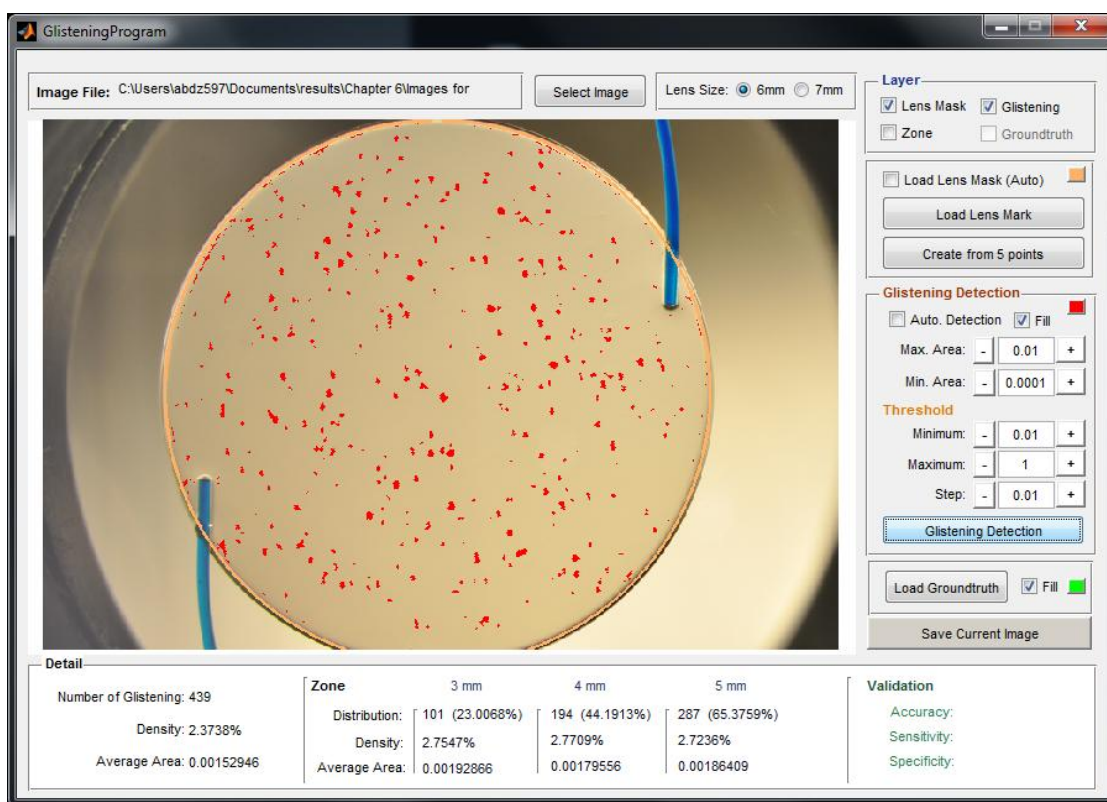


Figure 6.6 An IOL image following detection of glistenings, which were highlighted by the GDP. Results for each circular zone are given below the image. In addition, a spreadsheet with more extensive detail is exported for further analysis.

Details of the 20 IOL samples that were used in this study are given in Table 6.1. All lenses were made of a hydrophobic acrylic material. The number of glistenings was derived from the GDP. The total number of glistenings included some false positive results. This was due to the fact that near the edges of an IOL, because of the brightness change, the Sobel Operator used in the glistenings detection software regards these gradients as glistening. However, this doesn't affect the results as we limit our metrics to a maximum circular zone of 5mm, therefore these false glistenings were excluded.

| Code | Dioptric Power (D) | Optic Diameter (mm) | Total Number of Glistenings |
|------|--------------------|---------------------|-----------------------------|
| A | +19.0 | 6 | 318 |
| B | +20.5 | 6 | 1586 |
| C | +20.0 | 6 | 715 |
| D | +21.0 | 6 | 628 |
| E | +19.0 | 6 | 278 |
| F | +18.5 | 6 | 439 |
| G | +21.5 | 6 | 157 |
| S1 | +21.0 | 7 | 351 |
| S2 | +18.5 | 7 | 186 |
| S3 | +23.0 | 7 | 423 |
| S4 | +22.0 | 7 | 413 |
| S5 | +23.0 | 7 | 764 |
| S6 | +23.0 | 7 | 433 |
| S7 | +23.0 | 7 | 718 |
| S8 | +21.0 | 7 | 529 |
| S9 | +22.0 | 6 | 1321 |
| S10 | +22.0 | 6 | 3190 |
| S15 | +22.0 | 6 | 296 |
| S16 | +22.0 | 6 | 187 |
| S17 | +21.5 | 7 | 101 |

Table 6.1 Details of the IOLs used in the study.

Exported spreadsheets, as described in paragraph 5.2, from each IOL's GDP evaluation were further analyzed to derive data about the morphology of glistenings in terms of size and shape. In addition, the detected number of glistenings as well as the distribution, density and average size were calculated using equations 5.1 to 5.3 for each different circular zone.

The association between each of these values and the volume under the scatter function for angles greater than 1° was assessed by calculating the Spearman correlation

coefficient using Minitab v16. In addition, the association between the straylight parameter $\log(s)$, for the 10° eccentricity and the number of glistenings and glistening density was similarly assessed. The angle of 10° was chosen since it corresponds to the C-Quant straylight values (Franssen et al., 2006, Michael et al., 2010) and has been used in another related in vitro study (Van der Mooren et al., 2007).

As demonstrated in Chapter 5, our Glistenings Detection Program provides, for each IOL image and for each different circular zone, the average area of a single glistening. Considering the cross-sectional area of a single glistening as a circle of area A , the equivalent diameter of the specific glistening is given by

$$D = 2 \sqrt{\frac{A}{\pi}} \quad (6.16)$$

The surface area of a sphere is

$$S = 4\pi r^2 \quad (6.17)$$

which can be rewritten as

$$S = 4 \times A \quad (6.18)$$

In the case that a multiple correlation was necessary, coefficient R was calculated by formula below (equation 6.19)

$$R_{z,xy} = \sqrt{\frac{r_{xz}^2 + r_{yz}^2 - 2r_{xz}r_{yz}r_{xy}}{1 - r_{xy}^2}} \quad (6.19)$$

where x and y are viewed as the independent variables and z is the dependent variable.

6.3 Results

6.3.1 Morphology of glistenings

6.3.1.1 Distribution and Density

The assumption that glistenings are uniformly distributed within an IOL is often found in intraocular lens studies. The distribution of glistenings was expressed as a ratio (%) between the number of glistenings in each circular zone and the total number of glistenings. Results for all tested IOLs are shown in figure 6.7.

Distribution of glistenings was in all cases proportional to the pupil size giving a strong statistically significant Spearman correlation coefficient 0.856 ($p=0.000$), indicating (as expected) that the greater the pupil size the greater percentage of glistenings included.

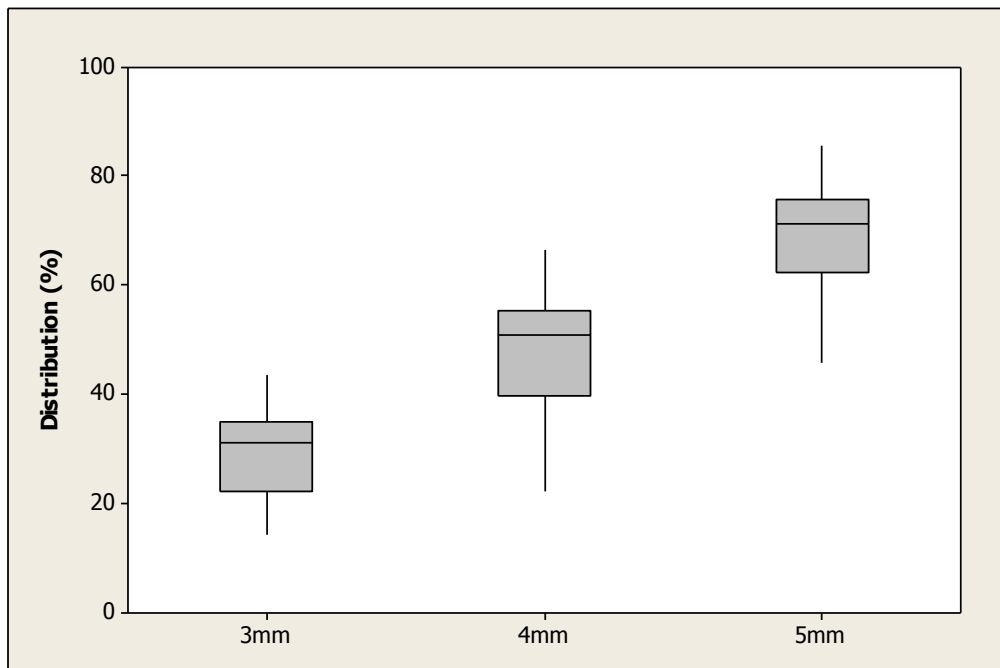


Figure 6.7 Glistenings Distribution (%) among the three different pupil sizes

The question is whether the distribution of glistenings is higher or lower, proportionally to the zone's area. For a uniform distribution, the number glistenings will be proportional to the zone area i.e. would increase in the ratio 9:16:25. Taking this into account, the actual median distribution values were compared with a theoretical uniform distribution, as illustrated in figure 6.8.

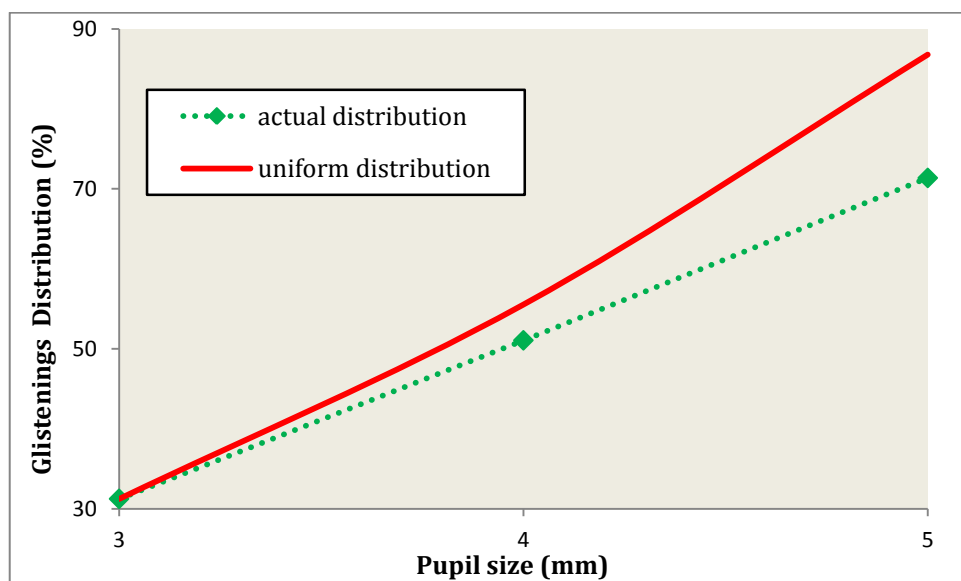


Figure 6.8 Actual distribution median values are lower than the ones if a uniform distribution of glistenings existed.

In all cases, the measured distribution appeared less than the predicted uniform values indicating that in intraocular lenses the glistenings distribution is not totally uniform among the lens but tends to show more glistenings in the centre rather than the periphery.

Taking this into account, the density of glistenings for different pupil sizes was also evaluated and compared. Density was expressed as the ratio between the sum of the area covered by the glistenings and the equivalent zone's total area. Figure 6.9 shows the density of glistenings for each IOL arranged in rank order for the 3mm zone size. Although the IOLs were ordered for increasing density of glistenings in the central 3mm zone, there is sometimes a large difference between the density in the 4mm and 5mm zones.

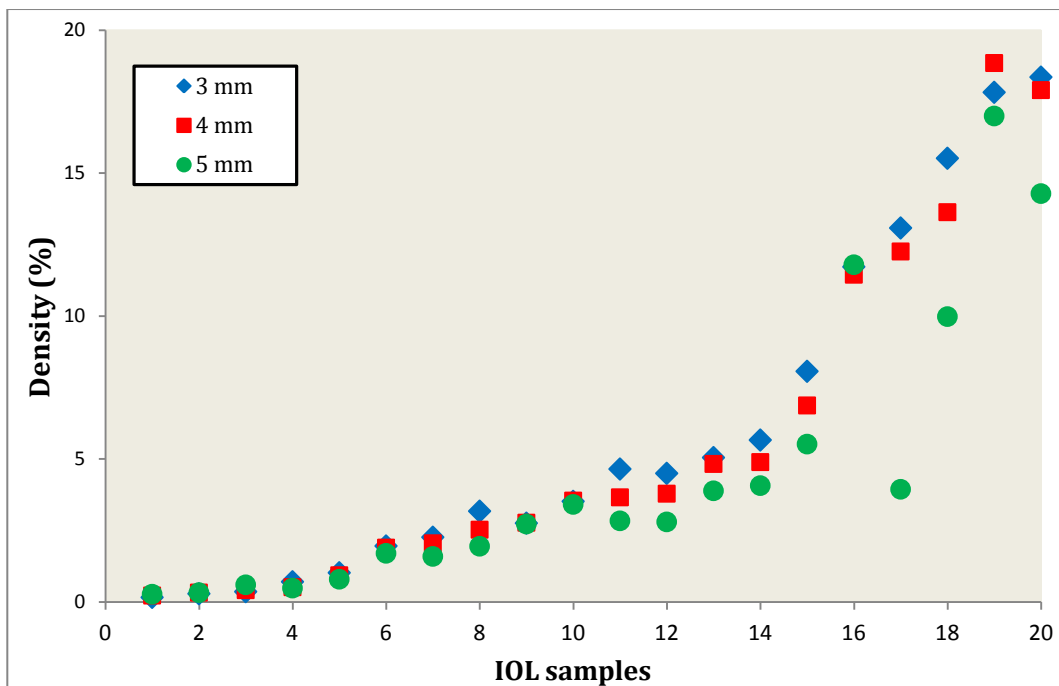


Figure 6.9 Density of glistenings among the different pupil sizes in all IOL samples

6.3.1.2 Size and Shape

Many of the IOL slit-lamp images showed an elliptical cross-section of the glistenings. The GDP software provides the dimensions of each glistening as mentioned in paragraph 5.2. In order to evaluate glistenings shape, the mean values of the major and minor axes were calculated for each IOL, as illustrated in figure 6.10. Analysis of the descriptive

statistics indicated some skewness in the data and so median results are quoted. For the minor axis the median was at 32 μm (11 μm interquartile range) while for the major axis the median was at 51 μm with a 21 μm interquartile range.

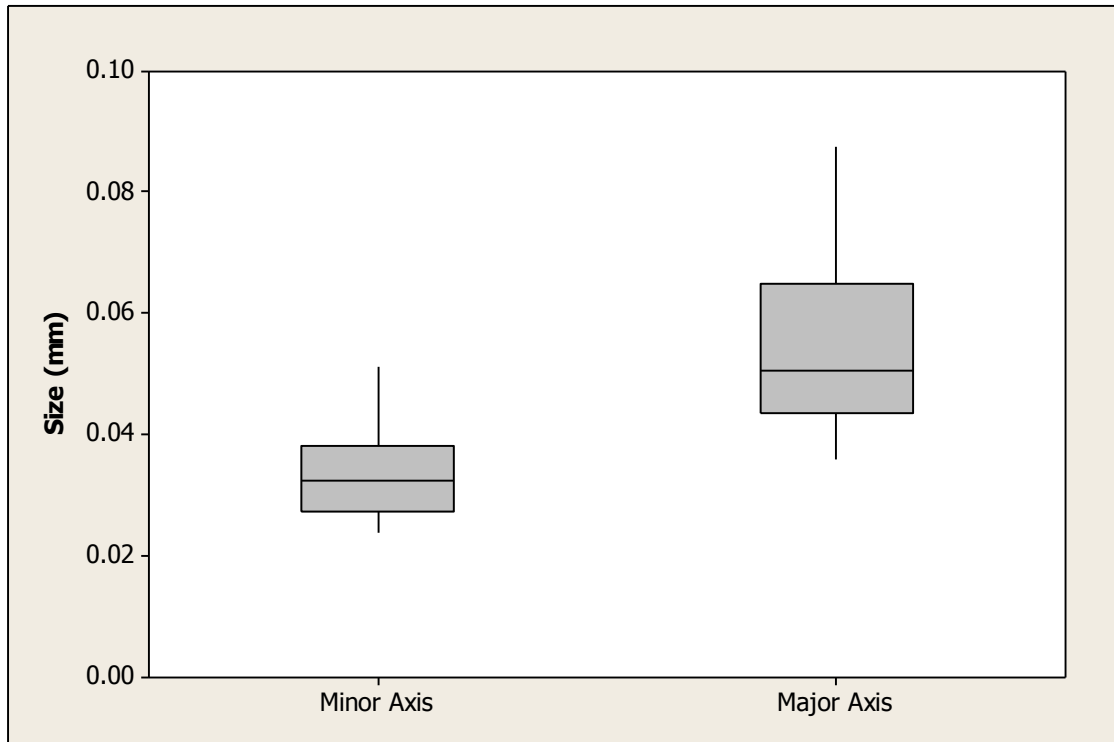


Figure 6.10 A difference between major and minor axis values was found, implying that glistenings shape is more likely to be ellipsoidal rather than spherical.

In addition, the difference between the two axes indicates that glistenings are more likely to have elliptical cross-sections rather than circular. This outcome could be of relevance to theoretical modelling of light scatter caused by glistenings.

The average size of a glistening in our study was 45 μm ; based on the area of each glistening, as described in 6.2, the glistenings representative sizes were classified in two categories:

- a) Small: less than 20 μm
- b) Large particles: greater than 20 μm

Classification was derived from the fact that the reported size of glistenings is up to 20 μm (Kato et al., 2001, Miyata et al., 2001, Gregori et al., 2002). For each IOL, the percentage of the above two groups was calculated. These percentages are illustrated in

figure 6.11. The size distributions on the other hand are shown in figure 6.12. Different lenses showed various proportions of glistenings diameters, indicating that a wide range of different sizes exists within an IOL.

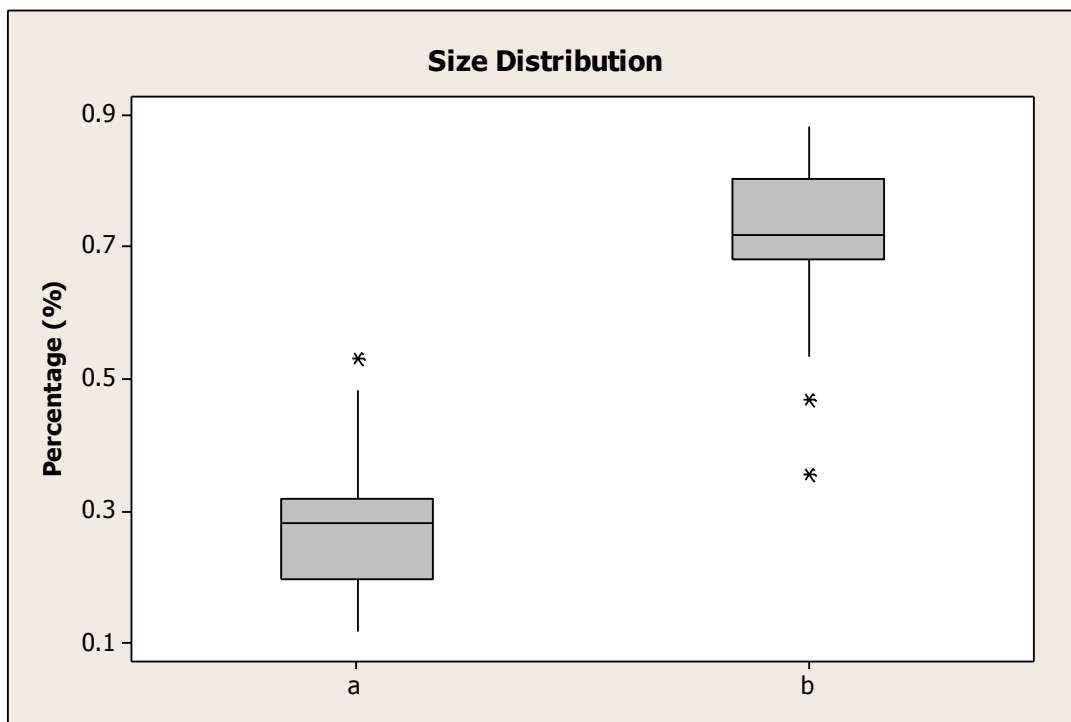


Figure 6.11 Distribution of the two size categories of glistenings among our tested IOLs: (a) glistenings size given from previous studies and (b) larger size of glistenings. Group b, large particles, appears in higher percentage as an average.

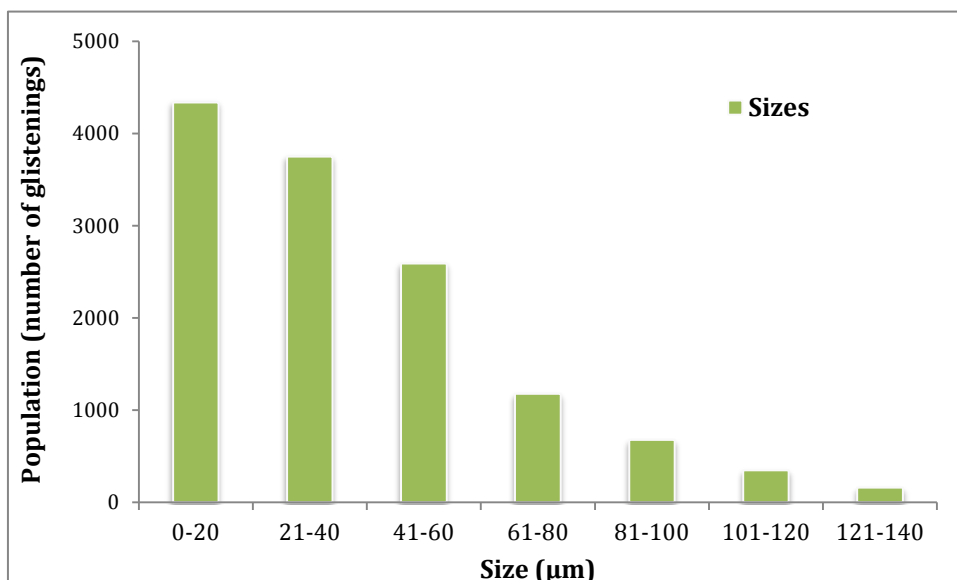


Figure 6.12 Size distribution of all IOLs glistenings population. A wide range of glistenings sizes was shown to exist, exceeding the commonly reported boundary of 20μm.

Figure 6.11 shows that larger than 20 μm particles are more likely to be found among the glistenings population; however Figure 6.12 shows that the peak of size distribution is in the range less than 20 μm . A broad wide range of glistenings sizes was shown to exist that has not been previously reported and could well be a factor influencing our light scatter measurements, as described in the theory above.

6.3.2 Objective quantification of glistenings and forward light scatter

6.3.2.1 Number

Association between the number of glistenings per circular zone and the corresponding volume under the scatter function (VUSF) values for each different pupil size was assessed with Spearman rank correlation coefficients. Results are shown in figure 6.13 together with correlation coefficients and associated p-values for each pupil size.

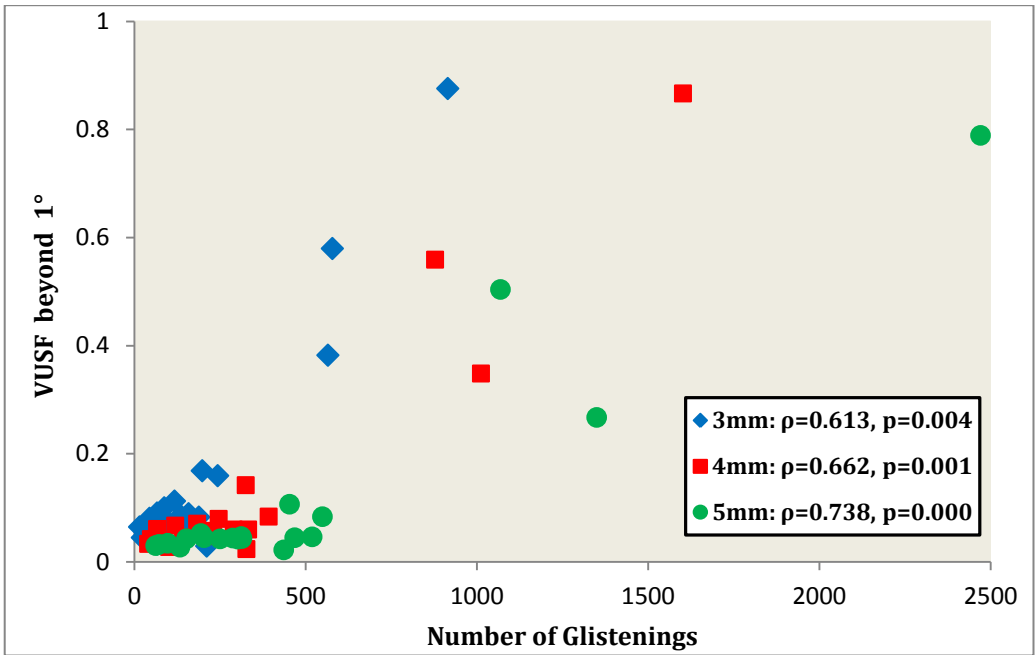


Figure 6.13 Spearman coefficients and p-values for the correlation between the existing number of glistenings in an IOL and VUSF results.

A statistically significant association is present for all pupil sizes. This indicates that the greater the number of glistenings, the higher the light scatter as measured by the volume under the scatter function.

Moreover, the logarithmic values of straylight parameter, s , for the 10° eccentricity were correlated with the detected number of glistenings in each circular zone (Table 6.2).

| Pupil size | Spearman coefficient | p-value |
|------------|----------------------|---------|
| 3 mm | 0.357 | 0.123 |
| 4 mm | 0.478 | 0.033 |
| 5 mm | 0.594 | 0.006 |

Table 6.2 Spearman coefficients and p-values for the correlation between the detected number of glistenings in an IOL and $\log(s)$ results.

Correlation between straylight parameter $\log(s)$ and the number of glistenings was not always statistically significant.

6.3.2.2 Average Area (cross-section)

The average area of glistenings per IOL and for the three different circular zones was evaluated and correlated with the corresponding VUSF experimental values (figure 6.14). The area was considered as an indicator of size, as explained in equation 6.16.

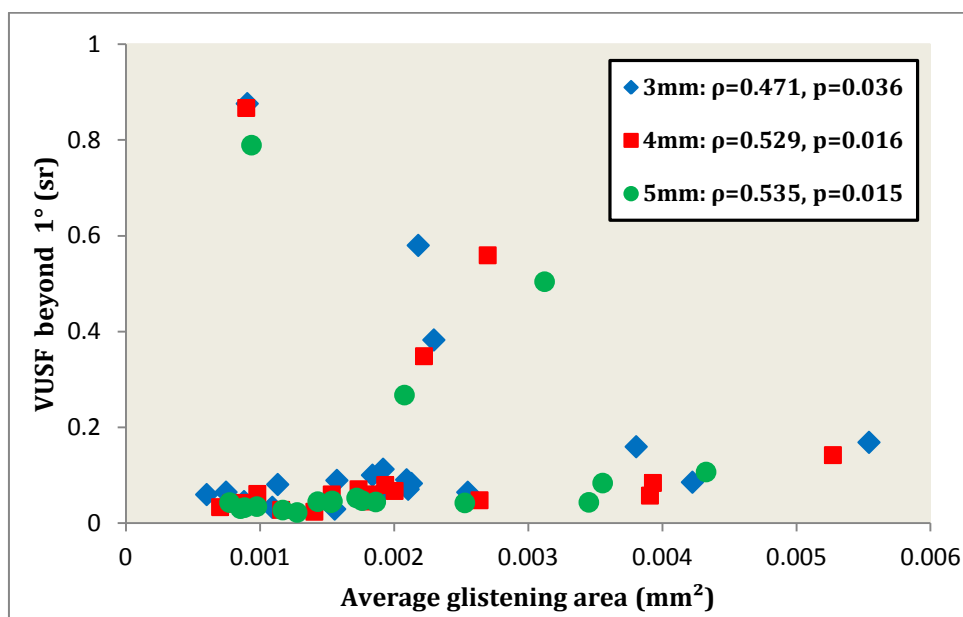


Figure 6.14 Spearman coefficients and p-values for the correlation between the average area of glistenings and VUSF beyond 1° .

A statistically significant correlation ($p < 0.05$) was shown between the average area of glistenings and the VUSF values, in all cases. However, this result is open to interpretation; an IOL with only a few small glistenings is unlikely to cause the same level

of light scattering as an IOL with a large number of glistenings of the same size (figure 6.14). In order to realize the importance of glistenings size as a factor for light scattering, IOLs with similar numbers of glistenings but different sizes must be examined. In our study, this principle could not be used due to the limited number of lenses.

Glistenings cross-section was correlated with the $\log(s)$ value for 10° eccentricity. As shown in Table 6.3, no statistically significant correlation was found for any of the three pupil sizes, supporting the argument above that cross-section warrants further study using IOLs with same number of glistenings.

| Pupil size | Spearman coefficient | p value |
|------------|----------------------|---------|
| 3 mm | -0.015 | 0.950 |
| 4 mm | 0.071 | 0.767 |
| 5 mm | 0.083 | 0.729 |

Table 6.3 Spearman coefficients and p-values for the correlation between the average glistenings cross-section in an IOL and corresponding $\log(s)$ values for 10° .

6.3.2.3 Density

Area density of glistenings for the three different circular zones was evaluated and correlated with the corresponding VUSF experimental values (figure 6.15).

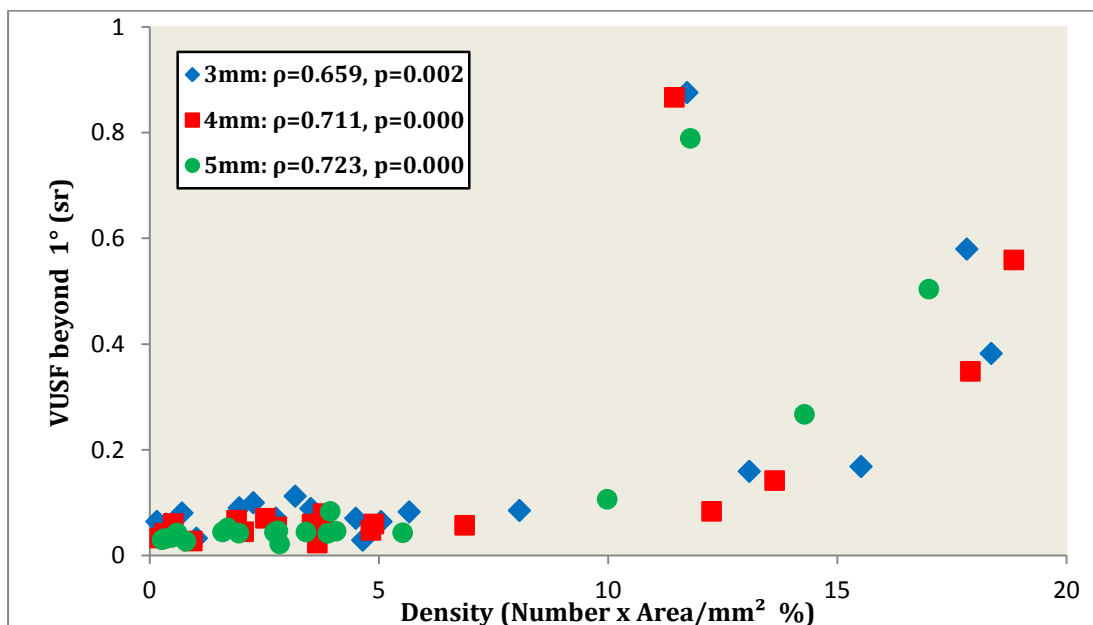


Figure 6.15 A statistically significant correlation was shown between Density and VUSF

A positive correlation (close to 0.7), which was statistically significant ($p < 0.05$), was found in all cases implying that area density is associated with light scatter.

| Pupil size | Spearman coefficient | p value |
|-------------------|-----------------------------|----------------|
| 3 mm | 0.305 | 0.191 |
| 4 mm | 0.405 | 0.077 |
| 5 mm | 0.471 | 0.036 |

Table 6.4 No correlation was shown between Density and straylight parameter

However, no statistically significant correlation was found for any pupil size between straylight parameter, $\log(s)$, and the area density of glistenings, apart from for the 5mm pupil size ($p=0.036$) (Table 6.4).

6.3.2.4 Number and Area vs. Scatter – multivariate regression

Given that both number and area of glistenings are factors that affect light scattering, a multivariate regression analysis was undertaken. Although our data didn't meet the assumptions for such an analysis i.e. our results are not expected to follow the assumptions necessary for linear regression, the purpose was to estimate the sign and weight of the regression slopes. Number and area were the predictors and VUSF the response variable. Linear regression factors are shown in Table 6.5.

| Pupil size (mm) | Number factor | Area factor | Multiple correlation coefficient |
|------------------------|----------------------|--------------------|---|
| 3 | 0.009 | -12.9 | 0.92 |
| 4 | 0.005 | -13.1 | 0.91 |
| 5 | 0.003 | -1.6 | 0.88 |

Table 6.5 Multivariate regression results for Number, Area and VUSF

A strong linear association was shown in all cases (R close to 0.9). The positive factor for the number of glistenings indicates that an increase in the number of particles tends to increase volume under the scatter function. The negative factor for the area of glistenings, implies that the smaller the size of glistenings the greater the effect on light scattering.

6.4 Discussion

The number of glistenings appears to be a significant factor contributing to light scatter, as predicted from theory (equation 6.4) and reported in the literature (Beiko and Grzybowski, 2013, Mamalis, 2012). This result also agrees with the fact that there is a positive correlation ($\rho=0.935$, $p=0.000$) between clinical grading and the actual number of glistenings, (figure 6.16).

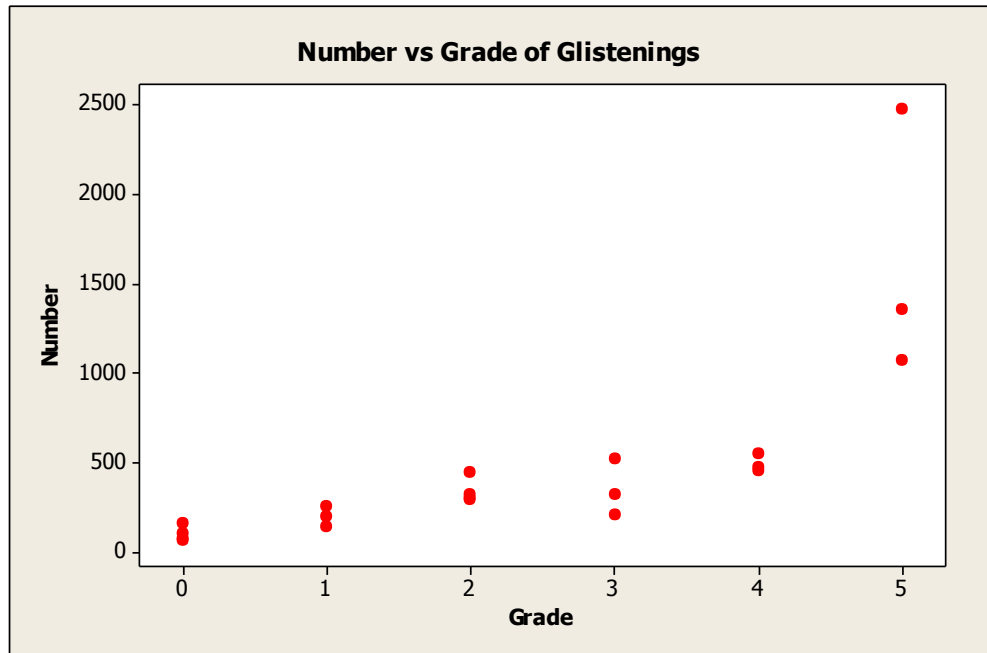


Figure 6.16 Association between clinical grade and number of glistenings.

Observed cases of high numbers of glistenings, associated with higher VUSF levels, implies that the size of glistenings could play a role as well; for a finite lens volume, the presence of a large number of glistenings is not possible unless the size of glistenings is small. Indeed, this argument is supported by the results of multivariate regression between light scatter and the number and area of the glistenings. Unlike the slope for glistenings number, which was positive, the regression coefficient was negative in all cases for area of glistenings, a surrogate of size. This result indicates that small size glistenings influence light scattering much more than the large size glistenings.

In agreement with previous studies (Colin and Orignac, 2011) the straylight parameter $\log(s)$ did not show any correlation with the number or the density of glistenings. A possible explanation for this result could be that although increase in straylight has been observed with increased number of glistenings, the straylight parameter $\log(s)$ is calculated for a fixed eccentricity angle (10°). The straylight function, as shown in Chapter 4 and from literature (van den Berg et al., 2013) does not follow a Normal

distribution; peaks and valleys are not only shifted along the y-axis but the x-axis as well. Hence, the straylight parameter derived from a single angle θ may not be sufficient to indicate the amount of scattered light and hence changes caused by a wide range of different sizes and distributions of particles. Clinically though this argument might become insignificant; scatter in the human eye is normally caused by identical or similar order of magnitude particles and disturbances.

Distribution of glistenings was shown to be denser in the centre of the lens rather the periphery; this could possibly explain the outcome from Chapter 4 that light scatter tends to decrease when pupil size increases in all cases. A physical explanation for this could be the fact that the IOL has a higher central thickness than in the periphery, hence there is more available lens volume for glistenings centrally. However, the pattern of decreasing glistenings with increased zone size does not apply for all IOLs tested.

Finally, the shape of glistenings, as already reported in literature (Saylor et al., 2010, van der Mooren et al., 2013), was shown to be ellipsoidal rather than spherical. This should be considered in any modelling of light scattering caused by glistenings. In addition, the depth location of glistenings might be a considerable factor affecting cases of high severity glistenings. As illustrated in figure 6.17, if glistenings' z-axis position differs and density is high, a cross-section overlap may occur limiting our glistenings characterization and quantification process.

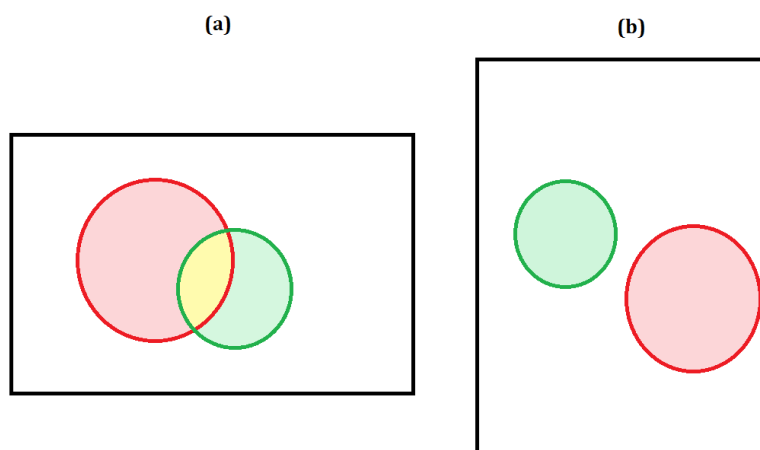


Figure 6.17 (a) Coronal plane (en face view) of two particles where their 2D projection on image (cross-section areas) overlap. (b) The same particles as shown in transaxial plane (view from top)

Chapter 7

Bilateral study between Acrysof SN60WF and Eternity Natural Uni NW-60

7.1 Introduction

Glistenings have been observed in all types of IOL materials. However, a recent multilateral 12 year follow up study, comparing the development of glistenings among polymethylmethacrylate (809C, Pharmacia & Upjohn), silicone (Phavoflex SI-40NB, AMO) and hydrophobic acrylic (Acrysof MA60BM, Alcon) IOLs, showed that the hydrophobic acrylic lens had significantly higher severity of glistenings than the PMMA and the silicone lenses (Rønbeck et al., 2013). The hydrophobic acrylic material though attracts great interest among the ophthalmic community; according to Leaming (Leaming, 2004), it has been the IOL material of choice for cataract and refractive surgeons. Reports in the literature (Werner, 2010), state that there is a difference in the manufacturing methods for Acrysof and Eternity hydrophobic acrylic materials:

- a) For Acrysof, the polymer is cast into ready-made moulds and the individual IOL removed after curing.
- b) For Eternity, the polymer is cast into thick flat sheets. After being cured, buttons are cut out and then each one is lathed according to the desired IOL design.

A study by Nishihara et al (2000), attempted to compare these two manufacturing methods by treating IOLs manufactured by both processes with thermal gradients and observing the formation of glistenings with a stereoscopic microscope. The conclusion of the study was that the lathe cut IOLs showed significantly fewer glistenings than the cast moulded ones (Nishihara et al., 2000).

Packaging between the two models also differs. The Acrysof IOL is kept dry in a plastic container (Wagon Wheel) with a central ring, within which the IOL is accommodated. Once opened, the physician can easily remove the lens and use it directly in surgery. In

contrast, the Eternity IOL is kept hydrated in 0.9% saline; the packaging consists of a plastic cylindrical vial divided into two chambers: the bottom one is open and empty, providing only length and volume to the vial for practical use while the top chamber is sealed. The top chamber is conical in shape and holds the IOL and saline solution. To date, no association has been reported between glistenings and the hydrated packaging of the IOL (Tetz et al., 2009). In contrast, dry packaging is considered as one of the factors influencing glistenings formation (Omar et al., 1998, Christiansen et al., 2001, Waite et al., 2007).

A large amount of literature exists for earlier Acrysof models, due to the fact that Acrysof was the first commercially available hydrophobic acrylic IOL (1995). Since then more than 40 million hydrophobic acrylic IOLs have been implanted globally (Werner, 2010, Christiansen et al., 2001, Dhaliwal et al., 1996, Farbowitz et al., 2000, Gunenc et al., 2001, Kato et al., 2001, Moreno-Montañés et al., 2003, Omar et al., 1998, Sacu et al., 2004, Yaguchi et al., 2007, Yaguchi et al., 2008, Chang et al., 2013, Colin et al., 2009). An *in vivo* study by Colin et al (2012) reported that among 111 eyes implanted with the Acrysof SN60WF, 96 of them developed glistenings. Grading of glistenings was subjective and used a 3 point scale: 0=absent; 1=moderate; 2=dense. No significant difference was found between corrected distance visual acuity (CDVA) and glistenings severity using this subjective scale although a significantly positive trend was shown for the grade 2 IOLs (Colin et al., 2012). In an *in vitro* comparison study of the Acrysof SB30AL (2003 model) and Acrysof SN60WF (2012 model) it was shown that a significant reduction of 87% in glistenings density occurred for the SN60WF IOL (Thomes and Callaghan, 2013). A recent *in vivo* comparison study between two, single piece hydrophobic acrylic IOLs, (Acrysof SN60WF and iMics1 NY-60), found no glistenings in iMics1 Ny-60 IOLs compared to Acrysof SN60WF where 97% of the lenses developed glistenings (Leydolt et al., 2013). No equivalent or similar published studies exist so far for Eternity Natural Uni NW-60. However, the enVista IOL, manufactured by Bausch & Lomb using the same material as Eternity Natural Uni, has been reported to be a glistening-free hydrophobic acrylic new material, approved by US Food and Drug Administration, FDA (Packer et al., 2014, Tetz et al., 2009, Packer et al., 2013). This leads us to hypothesise that the Eternity Natural Uni NW-60 IOL could also be glistening free or have reduced severity of glistenings.

In addition to the light scattering caused by the microvacuoles in the bulk of the lens (glistenings), hydrophobic acrylic IOLs manufactured by cast moulding have also been

reported to show surface light scattering. This phenomenon is caused by the formation of nano water aggregates (referred to as nanoglistenings) on the surface of the lens, which can be clinically observed using a slit-lamp when the incident beam angle is around 30°. A recent study by Minami et al (2014), found that although the Acrysof SN60WF shows light scattering, this does not increase in time, contrary to older versions. Two studies on the effect of surface light scattering on visual performance, one by Miyata et al (2012) and the other from Hayashi et al (2012), showed no significant impact on visual acuity. Miyata et al though, reported that in cases where surface light scattering was severe, a negative impact on visual acuity was found (Nishihara et al., 2003, Yaguchi et al., 2007, Yaguchi et al., 2008, Miyata et al., 2012, Hayashi et al., 2012, Ong et al., 2012, Minami et al., 2014).

Apart from the fact that both models are manufactured from hydrophobic acrylic materials, both types of IOLs were single piece and also their materials were 'blue blockers' (yellow tinted). Blue blocking intraocular lenses, which imitate the natural characteristics of the aging crystalline lens,, have reported effects on visual performance (impact on contrast sensitivity and glare due to the yellow tint) or retinal health risks, notably prevention of AMD) (Gray et al., 2011, Cuthbertson et al., 2009, Mainster and Turner, 2010, Nolan et al., 2009). However, blue blocking IOLs remain controversial and there is no common consensus among surgeons over their use..

Cataract surgeons also prefer the use of single piece IOLs, rather than the classic 3 piece design (figure 7.1), due to their greater ability to fold, requiring smaller incision injectors thereby reducing postoperative astigmatism (Chang, 2004, Kohnen et al., 1995). However, it has been shown that the 1-piece lenses are more likely to generate PCO, a disadvantage that has been eliminated with new enhanced optic edge design IOLs (Sacu et al., 2004, Wallin et al., 2003, Nishi et al., 2007).

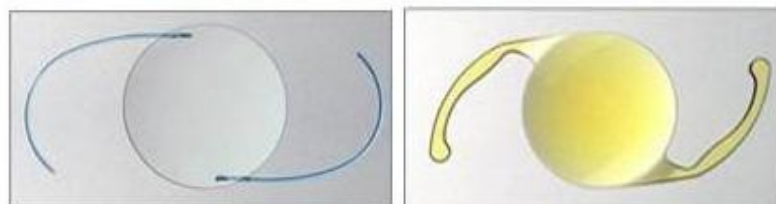


Figure 7.1 A three piece clear IOL (right) versus a single piece blue blocker (left), Alcon®.

Available from: <http://www.eyecalcs.com/DWAN/pages/v6/v6c011.html> [accessed 16th

November 2014].

The aim of this study was to evaluate the difference in incidence and severity of glistenings, generated using thermal gradients, between the Alcon Acrysof SN60WF and Santen Eternity Natural Uni NW-60 intraocular lenses. Both IOLs are made of hydrophobic acrylic materials, however they have a different composition and manufacturing process. In addition, both IOLs are currently among the latest intraocular lenses on the market. To date, no study has attempted to compare the incidence of glistenings between these two lenses; the only comparison study found evaluated the uveal and capsular biocompatibility of Eternity Natural Uni NW-60 as a new hydrophobic acrylic material (Ollerton et al., 2012).

7.2 Methods

7.2.1 IOL Preparation and Measurement

Ten IOLs in total were studied. Five were Alcon Acrysof SN60WF (from now on referred to as Acrysof) and the other half Santen Eternity Natural Uni NW-60 (from now on referred as Eternity Natural Uni or simply Eternity). Both sets of IOLs had the same dioptic power of 20D and optic diameter 6.0mm. IOLs were coded according to the Greek numeral system, as shown in Table 7.1. The IOLs were delivered to our labs in October 2013, in sealed packages as provided by the manufacturer.

| Code | Description | Material | Power and Diameter |
|---------------|--|---|--|
| α' | Santen® Eternity Natural Uni NW-60 | Cross-linked acrylate <i>ester</i> <i>copolymer</i> Ultraviolet absorber: Benzophenones Coloring agent: Azo and Methacrylamide | +20.0D Optic: 6.0 Ø Total length: 12.5 Ø |
| β' | | | |
| γ' | | | |
| δ' | | | |
| ϵ' | | | |
| $\sigma\tau'$ | Alcon® Acrysof SN60WF | Acrylate/Methacrylate copolymer Ultraviolet and blue light filtering chromophore | +20.0D Optic: 6.0 Ø Total length: 13.0 Ø |
| ζ' | | | |
| η' | | | |
| θ' | | | |
| ι' | | | |

Table 7.1 Tested IOLs coding and description. Material specifications as provided by manufacturers to physicians; composition details are not exhaustive.

Once the IOLs were removed from their packaging they were kept immersed in saline solution. This ensured that all tested IOLs were fully hydrated prior to light scatter measurements. All IOLs were subjected to thermal cycling as described in section 3.2: a

50°C/5days thermal grading protocol was followed and thereafter IOLs were kept at a constant temperature of 35°C. Eight to ten images were captured for each of the tested IOLs pre and post treatment. The images were subjectively assessed for uniformity and focus and the best selected for objective quantification of glistenings, using our Glistenings Detection Program, which was described in Chapter 5.

Scatter measurements were obtained post treatment following the same process and experimental setup described in Chapters 3 & 4.

7.2.2 Data Analysis

The scatter function was numerically integrated over steradians and normalized to unity, therefore deriving the PSF (van den Berg et al., 2013), as described in paragraph 4.2.2. The volume under the scatter function, VUSF, was calculated for the skirt of the PSF beyond 1°. The mean values and standard deviations for each category of lens were calculated and compared. Straylight parameter values were also calculated for 5 different angles. Results for PSF and straylight parameter log(s) were compared with the CIE standards for a young (20 year old) and an older (70 year old) normal subject.

7.3 Results

7.3.1 Number of glistenings pre vs post thermal grading

The number of glistenings found by the Glistenings Detection Program for each IOL is shown in fig. 7.2. An increase of glistenings number was shown in all lenses post-treatment. Pre-treatment, all IOLs had similar numbers of glistenings. Post-treatment, the Acrysof material appeared to develop a greater number of glistenings than the Eternity Natural Uni, as shown in figure 7.3. The large spread of values in Acrysof lenses post-treatment, indicates that not all lenses developed glistenings to the same extent. The number of additionally developed glistenings was evaluated by calculating the mean difference between pre and post treatment. The number of glistenings in the case of Acrysof is around seventeen times the number for the Eternity Natural Uni.

The resistance of each material to developing glistenings under thermal cycling was compared by analysing the difference in total number of glistenings before and after treatment. A Mann-Whitney U test showed that there was no statistical difference between the number of glistenings for the two materials pre-treatment ($p=0.21$) but that post treatment there was a statistically significant increase in the number of glistenings for

the Acrysof ($p=0.01$) but not for the Eternity ($p=0.09$). Data were analysed using non-parametric methods because of the low N value hence it being difficult to establish normality.

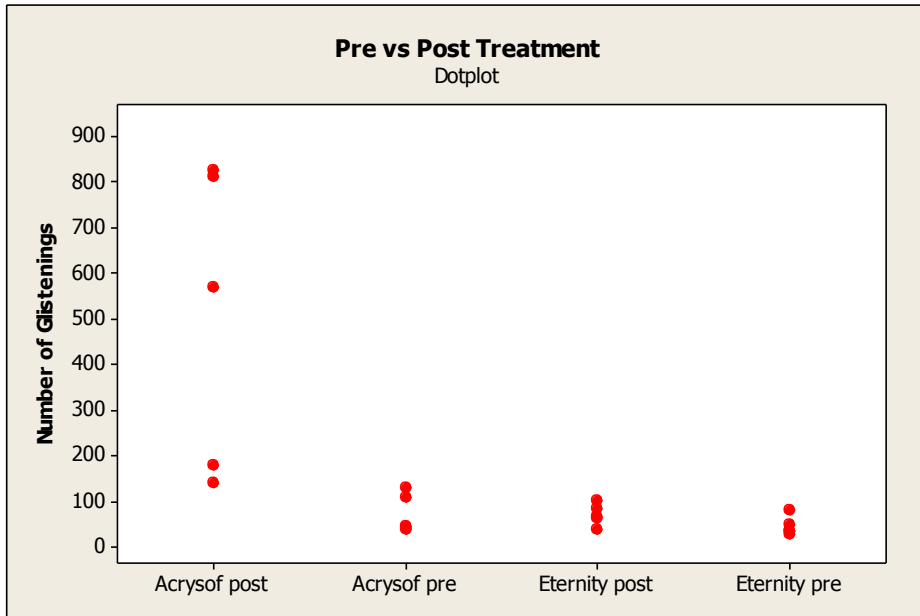


Figure 7.2 Mean values of pre and post IOL treatment for each material.

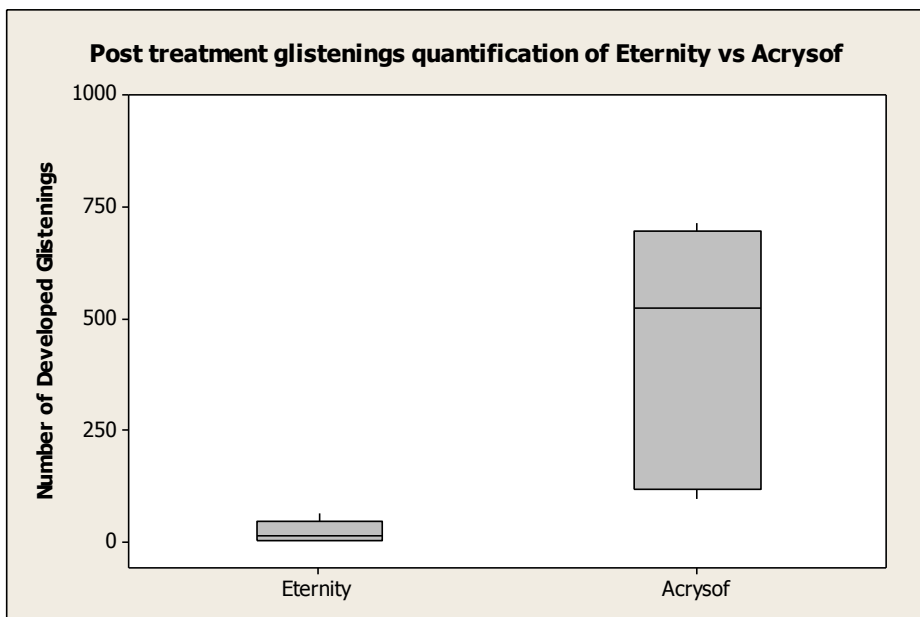


Figure 7.3 Number of induced glistenings for the Eternity Natural Uni and Acrysof materials post thermal grading treatment.

7.3.2 Size of glistenings

Apart from the number of glistenings, size was also evaluated. Glistenings were categorised using the size classification described in Chapter 6, section 6.3.1.2. Data were taken from the output of the Glistenings Detection Program on each of the post-treatment images. Distribution of the size classifications is shown in figure 7.4.

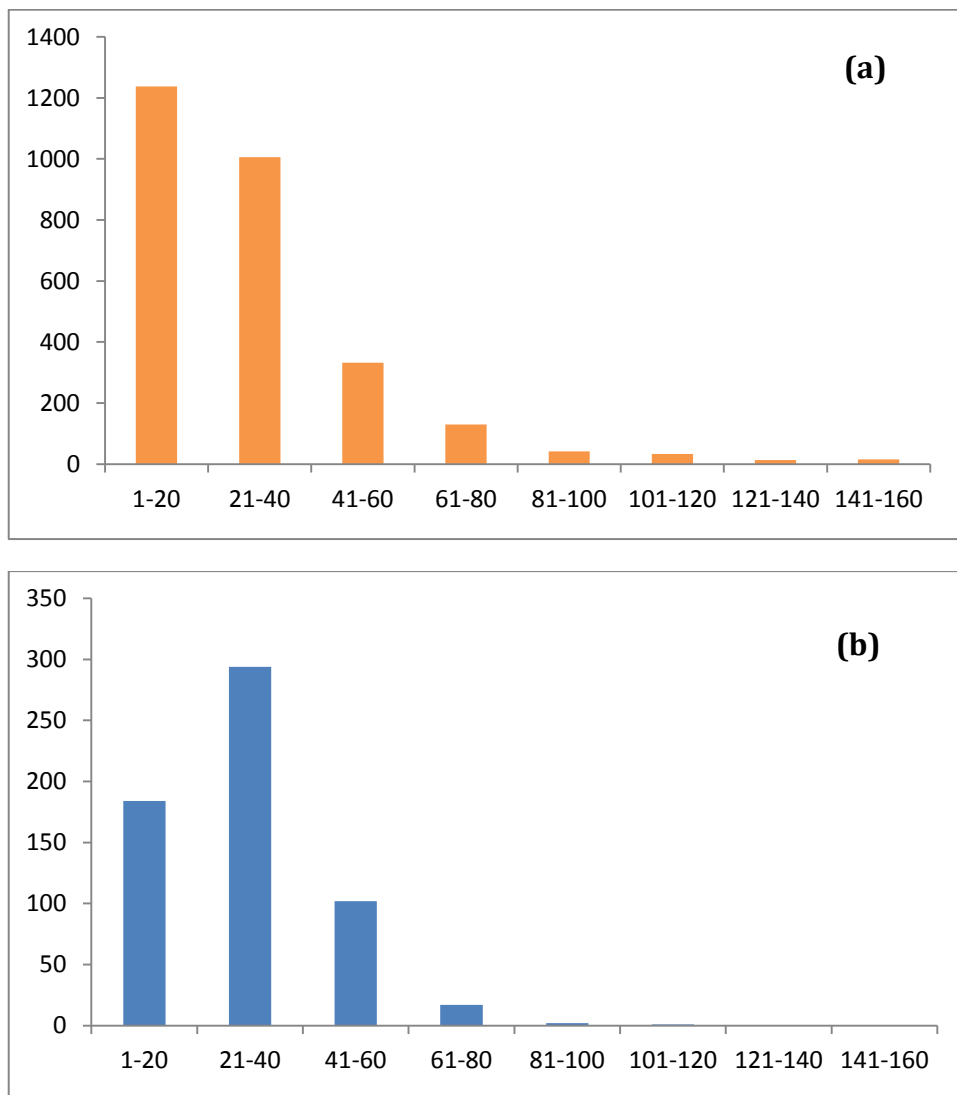


Figure 7.4 Glistenings size classifications' distribution among a) Acrysof and b) Eternity Natural Uni, post thermal treatment. Number of glistenings scale (y axis) differs.

According to our detection software, the Eternity Natural Uni developed a larger proportion of 20 μ m to 40 μ m size of glistenings compared to Acrysof, which developed a higher proportion of 1-20 micron size glistenings. In addition, the range of glistenings sizes was found to be wider (range 1 μ m – 160 μ m) in Acrysof rather than for the Eternity lenses (range 1 μ m – 100 μ m).

Figure 7.5 illustrates the large proportion of small glistening in the Acrysof material; selecting a small central area of the IOL's image and magnifying it, demonstrates that the post treatment IOL consists of a dense cluster of small particles. The impact of this result on the forward light scatter was investigated by evaluating the in vitro light scatter function (7.3.3).

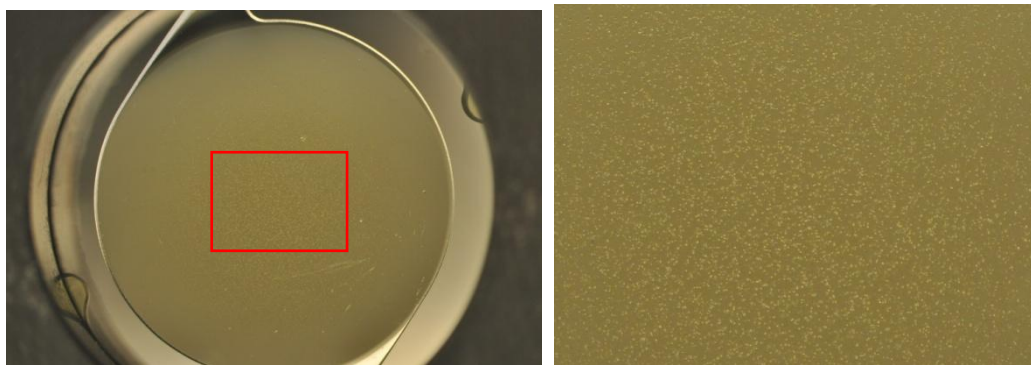


Figure 7.5 Magnification (right) of a selected central area (2mm width) from an Acrysof, post treatment image. It is evident that the IOL consists of a large number of small glistenings.

7.3.3 Volume Under Scatter Function (VUSF)

Forward light scatter light levels were evaluated by calculating the volume under the scatter function for eccentricity angles greater than 1°. The VUSF values were calculated for the three different pupil sizes. Mean values with standard deviations for each material are shown in Table 7.2 below.

| Pupil size | Eternity (Mean±SD) (sr) | Acrysof (Mean±SD) (sr) |
|------------|-------------------------|------------------------|
| 3 mm | 0.027 ± 0.009 | 0.200 ± 0.161 |
| 4 mm | 0.032 ± 0.004 | 0.195 ± 0.128 |
| 5 mm | 0.029 ± 0.007 | 0.151 ± 0.093 |

Table 7.2 Mean VUSF values for each material among the three different pupil sizes.

VUSF mean values are 5-7 times greater in Acrysof than Eternity Natural Uni for all three pupil sizes, indicating that there is more scattered light beyond 1 degree in the case of the Acrysof lenses. This is also illustrated in figure 7.6, where forward light scatter levels were greater in the case of Acrysof than Eternity Natural Uni. Figure 7.6 shows the mean light distribution, as measured experimentally, between the two materials for the small pupil size of 3mm. The importance and potential impact on visual function of this level of light scatter is evaluated in next section.

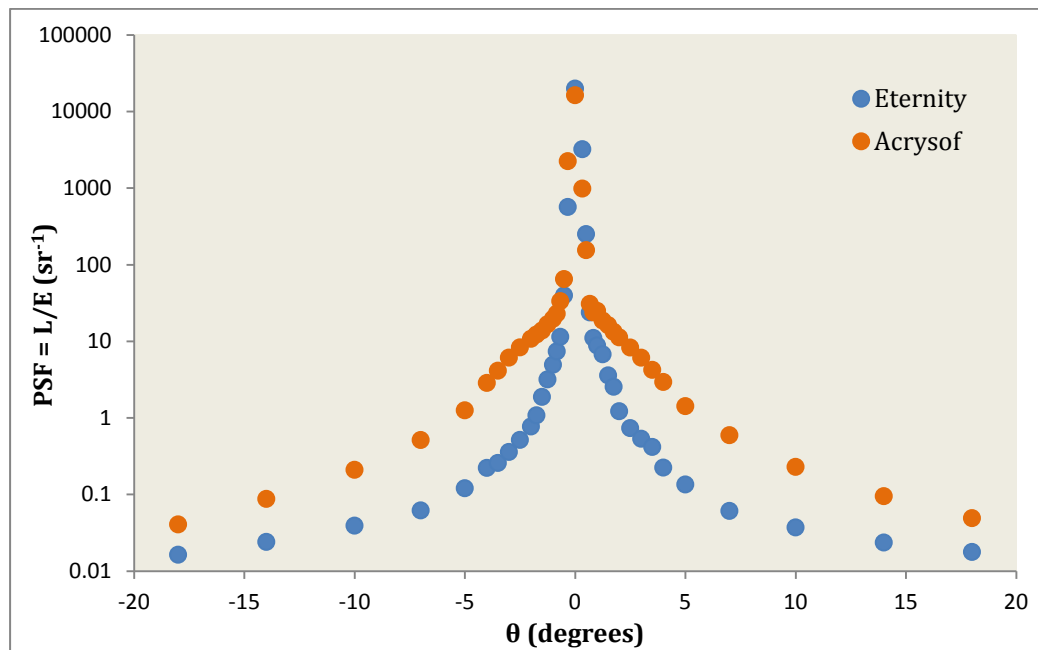


Figure 7.6 PSF mean values (logarithmic scale) for each group of IOLs and all eccentricity angles θ . Acrysof appears to have shown greater amounts of scattered light. Measurements are for a 3mm pupil size.

7.3.4 PSF and Straylight parameter

Using the CIE standards derived from the Total glare function (Vos and Van Den Berg, 1999, van den Berg et al., 2013), a comparison was undertaken between:

- a) the PSF and straylight parameter results given by the mean of Eternity Natural Uni and Acrysof measurements
- b) the equivalent CIE standards for a young (20 year old) and old (70 year old) normal subject.

Although our measurements were in vitro, hence the scatter contribution from the cornea and other eye components was not included, this evaluation attempted to indicate the significance of light scatter caused by the glistenings in the two different materials. Figure 7.7 illustrates the PSF beyond 1° based on the mean values for each of the two materials.

It is evident that, on average, the Eternity Natural Uni resulted in a lower PSF than that of a normal young subject while the Acrysof lenses produced values worse than an old normal subject. If the increased number and size of glistenings within Acrysof materials in vivo is similar to our results, light scatter caused by Acrysof is likely to be significant and may affect vision.

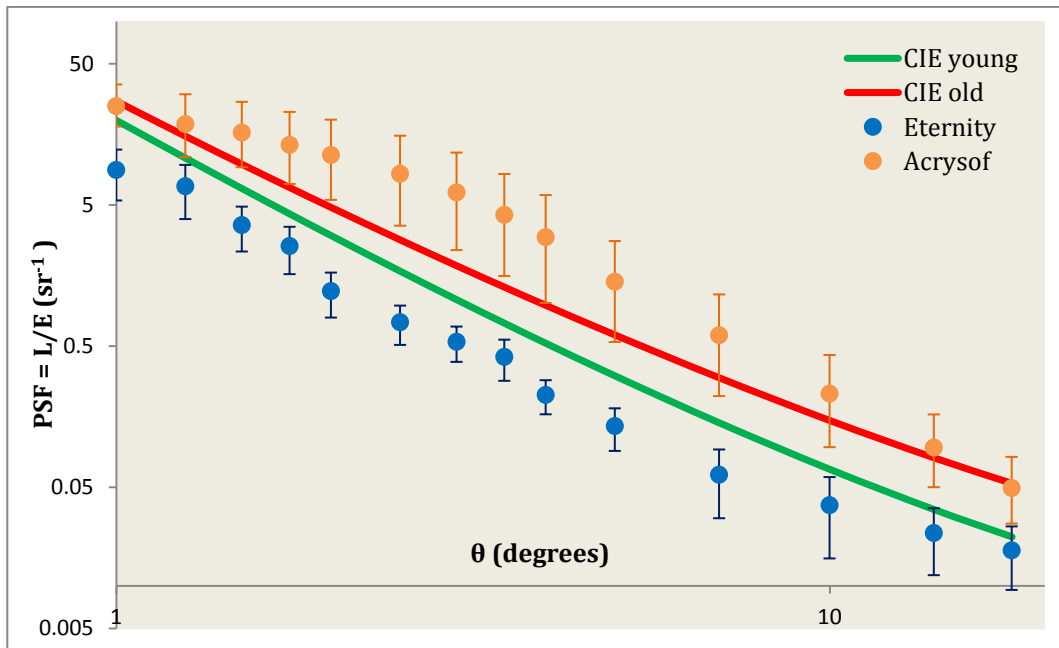


Figure 7.7 PSF mean values of Acrysof and Eternity in comparison with the equivalent for a young (green line) and aged (red line) according to the CIE standards. All values appear in a logarithmic scale.

Furthermore, the straylight parameter $\log(s)$ was calculated for 5 different angles: 3.5° , 7° , 10° , 14° and 18° . The mean values for each material and for all five angles are shown in figure 7.10. As a representative indicator, the straylight parameter values for 3.5° and 10° angles are shown for all tested IOLs in Table 7.3 and compared with the equivalent CIE values for a young and old normal subject, respectively.

| Type | Code | $\log(s)$ on 3.5° | $\log(s)$ on 10° |
|-------------------------|---------------|--------------------------|-------------------------|
| Eternity Natural Uni | α' | 0.49 | 0.18 |
| | β' | 0.56 | 0.75 |
| | γ' | 0.72 | 0.51 |
| | δ' | 0.42 | 0.51 |
| | ϵ' | 0.79 | 0.75 |
| Acrysof | $\sigma\tau'$ | 1.01 | 0.77 |
| | ζ' | 2.00 | 1.56 |
| | η' | 1.21 | 0.98 |
| | θ' | 1.33 | 0.96 |
| | ι' | 2.04 | 1.70 |
| CIE young | | 0.95 | 0.86 |
| CIE old | | 1.20 | 1.22 |

Table 7.3 Straylight parameter, $\log(s)$, for two different angles: 3.5° and 10°

Straylight parameter $\log(s)$ was found to be less than the normal young subject in all cases for the Eternity Natural Uni lenses. On the other hand, although Acrysof gave straylight parameters greater than an old subject (apart from one IOL) for an angle of 3.5° , the equivalent values for the 10° varied between the levels of a young and an old subject. In fact, one IOL was below the normal young ($\sigma\tau'$) CIE value, 2 out of 5 were between the normal young and normal old and 2 out of 5 were above the normal old straylight parameter value.

A more comprehensive way of examining the results for how the straylight values for Acrysof IOLs compare to the CIE standards, is shown in figure 7.8 below for all five angles. On average, Acrysof $\log(s)$ results exceeded those of a 70 year old subject for the angles below 10° but were found equivalent to a 70 year old subject for all other angles.

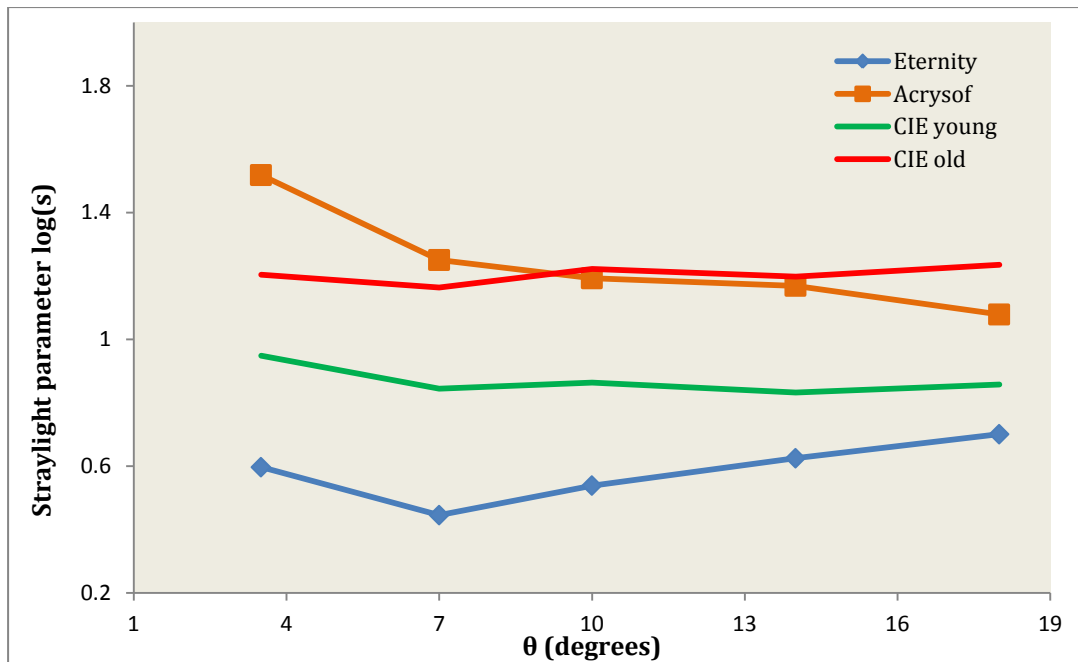


Figure 7.8 Mean straylight parameter $\log(s)$ values for each material group along with the equivalent CIE standards for a young and old (red) normal subject.

7.4 Discussion

A large number of glistening appeared in all Acrysof SN60SF IOLs, a result supported by the in vivo studies of Colin et al in (2012) and Leydolt et al (2013). The variation of the total number of glistening for each IOL was notable (figure 7.2), hence the impact on visual function is likely to be difficult to determine unambiguously. In contrast, Eternity

Natural Uni NW-60 showed a minimal number of glistenings, significantly less than Acrysof, in all cases (figure 7.3). This suggests that the Eternity Natural Uni is strongly resistant to developing glistenings.

In 2012, Alcon reported a continuous improvement of its manufacturing procedures, including environmental controls, cast moulding and curing operations (Thomes and Callaghan, 2013). However, the exact details of these improvements remains unknown to the public. In addition, as noted in our Methods section 7.2.1, current Acrysof lenses were delivered to our labs in 2013 but it is not clear whether the IOLs were manufactured before, during or after these improvements.

The fact that there is a slight (although not significant) difference in the number of glistenings between the two types of lenses pre-treatment might indicate a sensitivity of Acrysof's material to developing glistenings even while still in the manufacturer's packaging, for example due to temperature fluctuations. The association of glistenings development and Acrysof packaging has already been reported (Omar et al., 1998, Christiansen et al., 2001, Waite et al., 2007).

An essential question though, is why do virgin IOLs appear to have a notable number of glistenings? One explanation is that, as investigated in Chapter 5, our software does detect false glistenings on images. Images are taken by focusing on the edges of the lenses, therefore these in-focus imperfections are by default in the core of the lens and not on the surfaces. However, by comparing the detected outcomes with the original images, some of the false glistenings were caused by the “swimming” salts of the saline solution. Even though they are out of focus, they can still cause disturbances. A way to eliminate this “noise” would be to use filtered BSS in future. The difference between the post and pre-treatment glistenings gives the number developed during the thermal cycling treatment process, and a majority of false glistenings will be removed from the analysis. Moreover, whether true or false glistenings are detected, their contribution to scatter is minimal, as supported by our scatter function results.

A majority of the glistenings that developed in the Acrysof material were of small size, (less than 20 μ m), in agreement with previous studies and illustrated in figure 7.4 (Kato et al., 2001, Miyata et al., 2001, Gregori et al., 2002, Thomes and Callaghan, 2013). The Eternity Natural Uni IOL material, although much less susceptible to developing glistenings, was more likely to develop larger size glistenings (greater than 20 μ m). This result indicates that not only the number but the size of glistenings may differ among

different materials; to our best knowledge, no such outcome has been reported previously. An explanation could be that glistenings generated by thermal cycling in vitro are different to those found in vivo. It has been reported that the size of glistenings may differ when created under laboratory conditions rather than in vivo, with the laboratory induced ones shown to be slightly larger (Miura et al., 2004). Size of glistenings is likely to be an additional factor contributing in the nature of forward scattered light as demonstrated in Chapter 6. Therefore, whether a material tends to develop small or large size glistenings could be important when determining the impact of the glistenings on visual performance.

No significant variation of VUSF among the different pupil sizes was found for the Eternity Natural Uni material, confirming reports in the literature which suggest that for normal eyes, straylight only weakly depends upon pupil size (Franssen et al., 2007). Results for the Acrysof material confirmed the studies reported in Chapters 4 and 6, with a decrease in VUSF with increasing pupil size. As noted in Chapter 6, this may be because the induced glistenings were found to be denser in the centre of the IOL.

The fact that VUSF mean values for Acrysof were higher than for the Eternity Natural Uni lenses, can be seen in the mean scatter functions in figure 7.6. Light scattering was therefore greater in the Acrysof material than for Eternity Natural Uni, but the question of whether the impact on vision is significant remains unclear. Comparison with the normal PSF values derived from the CIE Total Glare Function, indicated that Acrysof IOL, even tested in vitro without the addition of other ocular media, has PSF values that exceed those of a 70 year old human eye. Given that for a cortical cataract subject, the straylight parameter for 10° is $\log(s)=1.37$ (de Wit et al., 2006), it was found (Table 7.3) that in two cases (both Acrysof IOLs) the straylight parameter $\log(s)$ exceeded this level. This outcome is consistent with the results of Miyata et al, where cases of decreased visual acuity were reported (Miyata et al., 2012). We would therefore hypothesise that the levels of light scatter measured in vitro in some Acrysof lenses could produce a measurable difference in visual performance.

The straylight of the human eye, as defined by van den Berg (van den Berg, 1995), is considered to include contributions from the cornea, the translucency of the ocular wall, the reflectance from the fundus and the crystalline lens of a newborn human (age=0). Taking into account that $\log(s)$ for the base is varied between 0.6 and 0.75 log units for angles from 3.5° up to 25.4° (Table 7.4), the Acrysof straylight values would be increased

further surpassing the values of the CIE 70 year old normal subject. In contrast, the Eternity Natural Uni would reach the values of a young normal subject.

| | | | | |
|----------------|------|------|-------|-------|
| Angle θ | 3.5° | 7° | 13.6° | 25.4° |
| Base log(s) | 0.70 | 0.60 | 0.65 | 0.75 |

Table 7.4 Human eye base straylight parameter values for four (4) scattering angles (van den Berg, 1995)

Chapter 8

Modulation Transfer Function and Wavefront Aberrations in Intraocular Lenses with Glistenings.

8.1 Introduction

Results from our studies have shown that glistenings have an impact on forward light scatter. However, the impact of glistenings and light scatter on visual function is still controversial (Miyata, 2014). It is therefore possible that light scatter might not be the most appropriate metric. In this study other metrics such as the Modulation Transfer Function (MTF) and wavefront higher-order aberrations will be investigated.

Image formation and the quality of any optical system can be expressed by the Point Spread Function, (PSF). In a perfect optical system the point spread function is limited by diffraction and is an Airy pattern for a circular pupil. The pattern consists of a central peak (the Airy disc), surrounded by a number of rings of ever-decreasing light level as illustrated in figure 8.1.

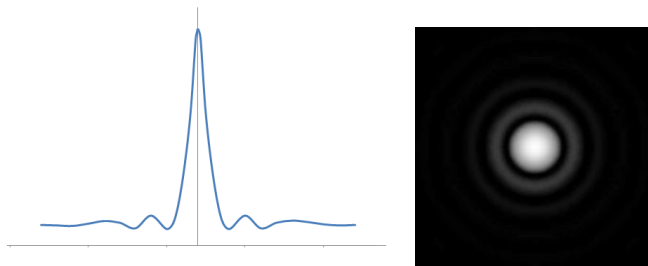


Figure 8.1 Line Point Spread Function (Left) and Airy pattern (Right).

For a monochromatic source, the diffraction-limited PSF is mathematically described by:

$$PSF(\zeta) = [2J_1(\zeta)]^2/\zeta^2 \quad (8.1)$$

where $J_1(\zeta)$ is a first-order Bessel function of the first kind and ζ the distance from the centre of the PSF.

The angular radius of the Airy disk (location of the first minimum in the Airy pattern) is given by:

$$\theta = \frac{1.22 \lambda}{D} \quad (8.2)$$

where λ is the source wavelength and D the diameter of the entrance pupil. This equation also gives the angular separation of two point sources that are just resolved according to the Rayleigh criterion (Atchison et al., 2000, Burton and Haig, 1984). Light scatter is not considered to influence the central region of a PSF (Van Den Berg et al., 2009); it mainly increases light levels at larger angles (paragraph 4.1). The summation of neighbouring PSFs, when light scatter is present, can cause blurring of an image, especially at sharp edges and hence rapid contrast transitions (Ginis et al., 2009). In pathological conditions causing ocular light scatter, for example in the presence of cataract, contrast sensitivity loss is known to occur (Chylack Jr et al., 1993, Kuroda et al., 2002).

Everyday images are better analyzed in the spatial frequency domain rather than as individual point objects. This is illustrated in figure 8.2, where the roof steelwork and surrounding design consist of a grating structure of various spatial frequencies, contrasts and orientations.



Figure 8.2 Birmingham, New Street Train Station, 1903 [source: Warwickshire Railways <http://www.warwickshirerailways.com/>, assessed 15/12/2014]

Through Fourier analysis, it is possible to consider any image as a collection of different spatial frequencies, contrasts and orientations. The ability of an imaging system to distinguish and transfer through its optics the details, edges and contrast of an image, is described by the Modulation Transfer Function. The purpose of this study was the evaluation of intraocular lenses optical performance when glisterings occur.

8.1.1 Modulation Transfer Function

An object can be considered as a collection of point sources each producing a point spread function in the image (Hecht, 2002). The image is therefore the convolution of the PSF with the intensity distribution of the object. In frequency space this becomes the product of the Optical Transfer Function (OTF) and the Fourier Transform of the object. The OTF consists of two components: 1) MTF and 2) phase-transfer function (PTF), as shown in equation 8.3. The former is its modulus, expressing the relative change in contrast of the pattern image compared to an aberration-free aperture, whereas the PTF quantifies the linear lateral shift of this pattern.

$$OTF = |OTF|e^{iPTF} = MTFe^{iPTF} \quad (8.3)$$

The Modulation Transfer Function (MTF), is the most widely used method of describing the performance of an imaging system. The MTF is the magnitude of the OTF, which itself is the Fourier Transform of the PSF. Image modulation (contrast) is defined by

$$M = \frac{I_{max} - I_{min}}{I_{max} + I_{min}} \quad (8.4)$$

where I_{min} and I_{max} are the corresponding intensities for minimum and maximum values within an image. For a grating target comprising white and black line bars, I_{min} stands for the intensity of the black bars at the image and I_{max} for the intensity of the white bars. A target such as that shown in figure 8.3, will be blurred when passing through a low resolution imaging system. This blurriness is typically due to the loss of high spatial frequencies needed to clearly define the sharp edges. The Modulation Transfer Function, defined as the ratio of the image modulation to the object modulation at all spatial frequencies, would therefore be low for the higher spatial frequencies in this example.

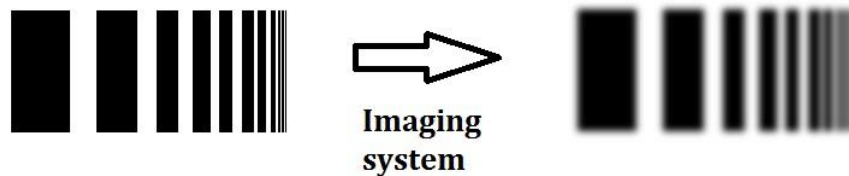


Figure 8.3 Perfect line edges before (Left) and after (Right) passing through a Low Resolution Imaging System.

An aberration-free (diffraction-limited) MTF curve starts from the value of 1.0 for a frequency of zero and drops almost linearly towards the cutoff frequency.

The cutoff frequency is given by

$$f_c = \frac{2NA}{\lambda} \quad (8.5)$$

where NA is the numerical aperture and λ the wavelength. Another factor that can limit the frequency response of an optical system is the Nyquist limit of the detector, which is theoretically defined as half a cycle or line pair per pixel. For the human eye, the Nyquist limit imposed by the cone spacing is considered as 60 cycles/deg, although there is a variation in this value depending on the eccentricity from the foveal centre and the spatial density of the photoreceptor mosaic (Curcio et al., 1993, Rossi and Roorda, 2010, Yellott, 1983).

Studies investigating the effect of pupil size on ocular MTF (figure 8.4a) show that as pupil size increases the MTF decreases for all spatial frequencies (Artal and Navarro, 1994). Wavefront aberration correction can considerably improve MTF; (Liang and Williams, 1997), showed that the higher the order of corrected aberrations, the closer the MTF approaches the diffraction limit, (figure 8.4b). This suggests that MTF loss at larger pupil sizes is largely caused by increased higher-order aberrations. Wavefront aberrations have also been shown to increase with age and as a result the MTF decreases with age (figure 8.4c) (Guirao et al., 1999, McLellan et al., 2001, Guirao et al., 2002).

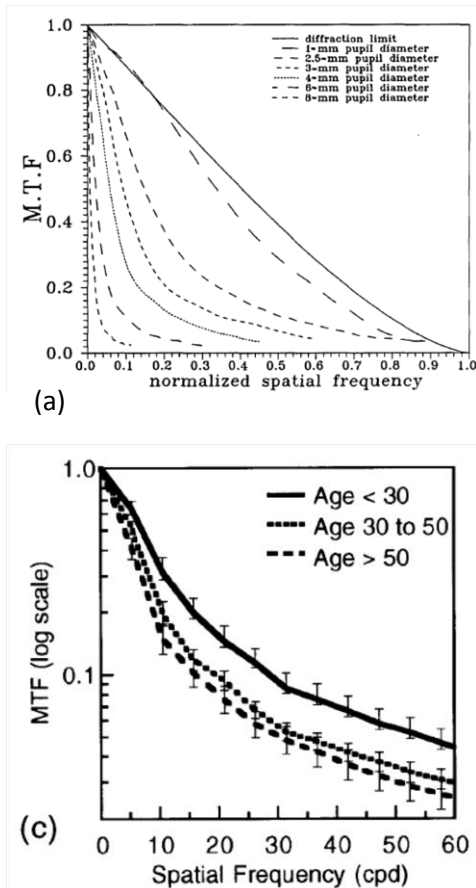


Figure 8.4 (a) MTF curves for different pupil sizes, 632 nm source wavelength (Artal and Navarro, 1994). (b) MTF alterations on Zernike aberration corrections for a 3mm pupil size, 632.8 nm wavelength, spatial frequency in cycles/degree (Liang and Williams, 1997). (c) Significant difference on MTF curves among three different age groups for a 6mm pupil size, 530nm wavelength (McLellan et al., 2001)

MTF performance of lenses and imaging systems is sometimes evaluated with the use of bar target resolution charts, the most popular of which is the USAF 1951 Test Chart (figure 8.5). The target consists of a pattern of 3 bar targets, with both horizontal and vertical orientations for each spatial frequency. The patterns spiral in towards the centre for increasing spatial frequencies. Bars are divided into Groups and Elements. Each group consists of six elements. Both groups and elements are numbered. The resolution limit is determined by reading the group and element number of the first element which the observer cannot resolve. Equation 8.6 is then used to derive the resolution limit in line pairs per mm,

$$Resolution (lp / mm) = 2^{Group-(Element-1)/6} . \quad (8.6)$$

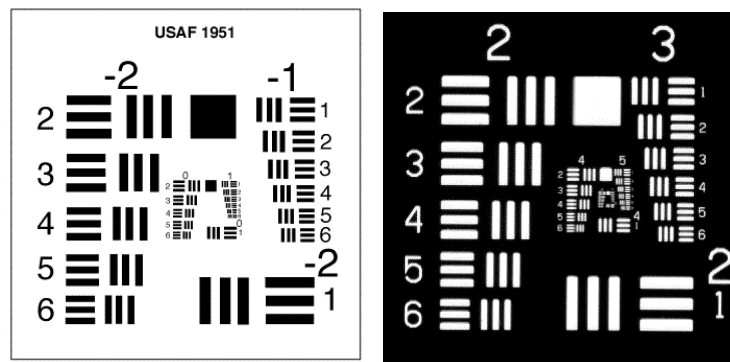


Figure 8.5 USAF bar target resolution charts.

Although it is known that increased higher-order aberrations have a negative impact on visual function (Williams et al., 2000), the effect of glistenings on the measurement of higher order aberrations has not been investigated.

8.1.2 Optical performance studies on intraocular lenses with glistenings

Apart from studies on both the MTF performance and wavefront aberrations of different intraocular lenses designs (Sakuraba, 2006, Navarro et al., 1993, Kawamorita and Uozato, 2005, Bellucci et al., 2004, Barbero et al., 2003, Lee et al., 2013, Nanavaty et al., 2011, Kasper et al., 2006), few studies have investigated the influence of glistenings on these metrics.

Oshika et al (2001), tested IOLs with glistenings in vitro and showed that a moderate level of glistenings, commonly found clinically, did not have a significant negative impact on MTF, resolving power, transmittance or glare sensitivity. However, IOLs with a 4+ subjective grade for glistenings, did show a significant performance decrease. This result

has been confirmed by a case study in 2011, where a decrease in the visual function of a subject implanted with a hydrophobic acrylic IOL with high level light scattering, has been reported (Yoshida et al., 2011).

Kawai (2012), in a conference presentation, submitted hydrophobic acrylic IOLs of various materials and designs, to a process of thermal accelerated aging equivalent to 20 years. The MTF was evaluated with a commercial optical bench (specifications not provided) and showed that in some of the materials both resolving power and MTF had been significantly decreased (Kawai, 2012).

In a mathematical modelling study by DeHoog and Doraiswamy (2014), MTF decreased for IOLs with glistenings and the loss was more evident in IOLs with a high density of glistenings (DeHoog and Doraiswamy, 2014).

A recent study of seven explanted hydrophobic acrylic IOLs with significant amounts of surface light scatter that had been evaluated with Scheimpflug imaging, showed no significant impact on MTF and image resolution, when tested on a Badal optical bench (Ogura et al., 2014).

The question our study attempted to answer, is whether glistenings have an impact on MTF and wavefront aberrations. Secondly, if glistenings do have an impact on MTF and wavefront aberrations, at what level of glistenings severity does this attenuation occur.

8.2 Methods

The study was split into two stages: the purpose of the first part was to evaluate the impact of glistenings on MTF and wavefront aberrations, by testing a wide range of almost identical intraocular lenses, in terms of material, diameter size, design and dioptric power. In the second part, we attempted to evaluate the impact of glistenings on MTF only using a wider range of different intraocular lenses in terms of diameter size and dioptric power. Therefore, an association between glistenings and lens power, i.e. thickness, was attempted.

8.2.1 Materials

One hundred and twelve intraocular lenses were tested during this project. All lenses were products rejected after quality assurance inspection, due to functional imperfections such as damaged or wrongly positioned haptics. Such imperfections would not have any impact on our study since we were testing the optical properties of the lenses.

For the first part of the study, 50 IOLs were tested. All of them were three-piece lenses with a 6.0mm optic diameter. Half of them (25) were clear and the other half (25) were yellow tinted, blue blockers. The average Dioptric power was $19.9D \pm 0.4D$ (mean \pm SD). IOLs were coded with the letter “A”, followed by a number from 1 to 50, chosen randomly.

For the second part of the study, 63 lenses were tested and subdivided into three dioptric power categories, each of 21 lenses. The categories were:

- 1) $+15.0D \pm 0.5D$, (Mean 14.9D, SD $\pm 0.5D$)
- 2) $+20.0D \pm 0.5D$, (Mean 20.0D, SD $\pm 0.3D$)
- 3) $+25.0D \pm 0.5D$, (Mean 25.0D, SD $\pm 0.2D$)

IOLs were all named with the letter “B” and numbered, as in part one of our project.

8.2.2 Procedure

All lenses were subjected to thermal gradients for laboratory induction of glistenings. The cycling protocol is proprietary and only known to Advanced Vision Science Inc. However, the details are of secondary importance given the purpose of the study is to investigate the impact of glistenings on the optical properties of intraocular lenses provided a range of severity of glistenings is produced.

Having grouped the lenses, according to each stage of the project, they were all inspected and measured prior to thermal gradients. After treatment, only the lenses with glistenings were measured again. Pre versus post treatment results were compared for the following measurements:

Modulation Transfer Function, MTF, was evaluated for a 100 lp/mm frequency by testing all lenses using two different intraocular lensometers:

- a) IOLA plus (ROTLEX Ltd, Omer, Israel)
- b) SHSOphthalmic (Optocraft GmbH, Erlangen, Germany).

In addition, the wavefront aberrations were evaluated using the SHSOphthalmic device.

The IOLA plus is an automatic wavefront sensor based on the Lau effect and shearing interferometry (Jahns and Lohmann, 1979). The SHSOphthalmic instrument, referred to as the Optocraft (figure 8.6) from this point on, is also an automatic wavefront sensor but based on the Hartman-Shack principle (Thibos, 2000). For both wavefront

measurements, IOLs were supported in cuvettes approved by the manufacturers and filled with filtered BSS solution. Cuvettes were washed with copious quantities of distilled water at the end of each session. For each measurement, the lenses were transferred carefully from their vials to the custom-made cuvette with the use of stainless steel laboratory forceps. The cuvette, containing the IOL, was placed in the sensor. The IOL was centred, according to the guiding target of each instrument’s software. Fine adjustments were made with an X-Y micropositioner stage in the case of the Optocraft or a Y-axis adjustment in the case of the IOLA plus. Lights in the room were turned off. Measurements were taken for a 3mm pupil size. Data files were named with the corresponding IOL’s coded number and an abbreviation, “pre” or “post” regarding whether measurement was taken pre or post thermal treatment.

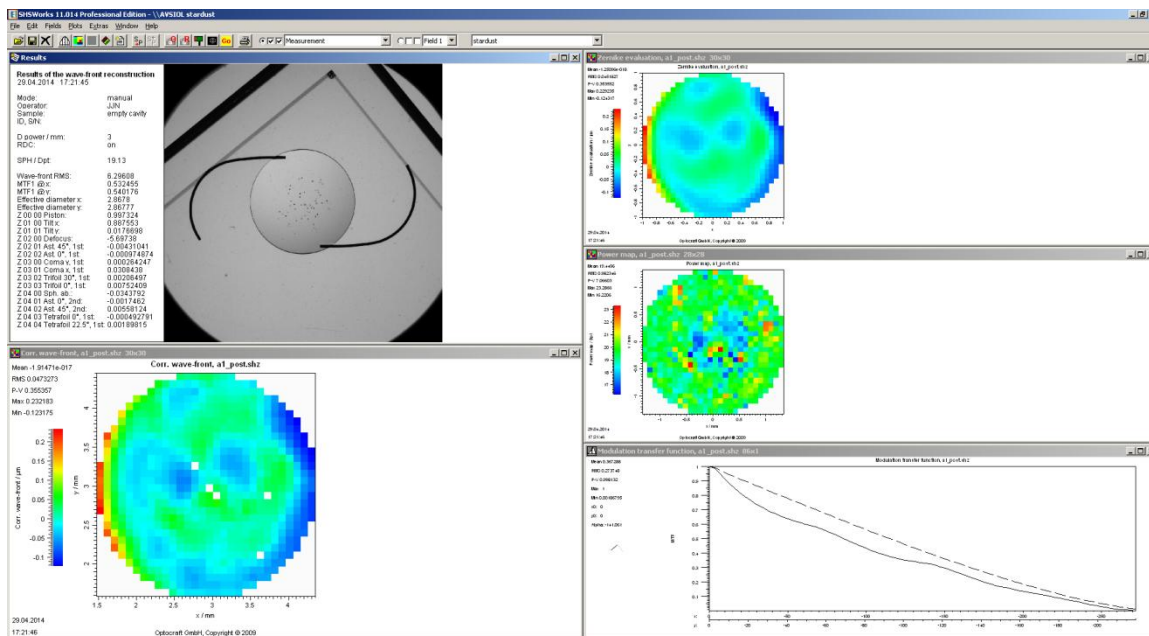


Figure 8.6 SHSOphthalmic Optocraft graphical user interface.

The optical resolution limit of all lenses was evaluated with the MB104Z Manual Optical Bench (Optical Testing Laboratory, Corvallis, US). This apparatus is designed for dioptric power and optical resolution measurement of intraocular lenses, according to ISO 11979-2 guidelines (figure 8.7). It will be referred to as “Optical Bench” in the rest of this thesis. The bench is operated manually although the testing procedure is software driven. The IOL to be tested was positioned and centred under the microscope. Power was determined by measuring the back focal length of the IOL. The observer determines the finest pattern (group, element) on an illuminated USAF 1951 target (light lines against black background) for which both horizontal and vertical bars are resolved. The manufacturer’s specifications for lens refractive index, curvature and thickness are input

to the software. The optical resolution limit, expressed as a percentage of the diffraction-limited cut-off spatial frequency of an ideal lens having the same focal length and specifications, was determined from

$$Resolution = 100 \times 2^{[G + \frac{E-1}{6}]} \times \frac{f\lambda}{nd} \quad (8.7)$$

where G is the group, E the element, f the collimator's focal length, λ the wavelength, n the surrounding medium refractive index (hence 1) and d the aperture. Identical conditions were used for all lenses with $d = 3\text{mm}$, $\lambda = 550\text{nm}$ and $n = 1$.

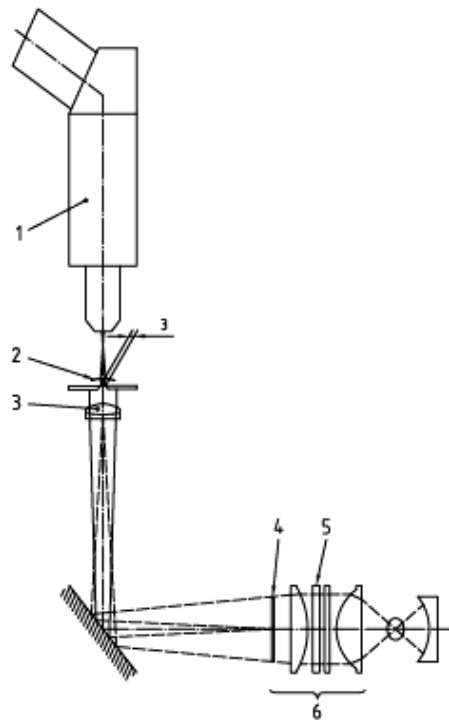


Figure 8.7 Optical Bench Apparatus (ISO 11979-2): 1 Microscope; 2 IOL; 3 Collimator Achromat; 4 USAF 1951 resolution target; 5 Dichroic filter; 6 Condenser;

All measurements were taken under normal ambient lighting conditions of a laboratory. Lenses were divided into groups of the same dioptric power and tested respectively. Each result was saved with screenshots and manually recorded.

8.2.3 Wavefront aberrations calculations

For the first part of the study, the wavefront aberrations were evaluated by calculating the Zernike coefficients up to the 4th order (Thibos et al., 2002).

The Seidel defocus, M , is derived from defocus, Z_2^0 and spherical aberration, Z_4^0 , divided by the square of measured pupil's radius, r and is given by

$$M = \frac{1}{r^2} (-4\sqrt{3}Z_2^0 + 12\sqrt{5}Z_4^0) \quad (8.8)$$

- a) Spherical RMS was derived from the square root of the sum of the defocus, Z_2^0 and spherical aberration, Z_4^0

$$RMS_{sph} = \sqrt{(Z_2^0)^2 + (Z_4^0)^2} \quad (8.9)$$

- b) Higher Order (HO) RMS, was derived from the square root of the sum of all 3rd and 4th order Zernike coefficients ($Z_{-3}^3, Z_{-1}^3, Z_1^3, Z_3^3, Z_{-4}^4, Z_{-2}^4, Z_0^4, Z_2^4, Z_4^4$), respectively

$$RMS_{HO} = \sqrt{\sum_{n,m} (Z_n^m)^2} \quad (8.10)$$

8.2.4 Reproducibility

All three intraocular lensometers are considered by their manufacturers to give accurate and repeatable results. In addition, performance results have been reported in previous intraocular lenses studies (Chou et al., 1995, Amaral and Monteiro, 2013, Eppig et al., 2013). We evaluated the reproducibility of our procedure since it depends on both machine and operator error.

For the IOLA plus, 5 trials were undertaken for a 24.5D, three piece, blue blocking IOL, 7mm optic diameter. Results are shown in Table 8.1.

| Trial | Measured Power (D) | MTF |
|-------|--------------------|---------------|
| 1 | 24.91 | 0.611 |
| 2 | 25.34 | 0.571 |
| 3 | 25.38 | 0.585 |
| 4 | 24.86 | 0.606 |
| 5 | 25.19 | 0.609 |
| Mean | 25.14 | 0.596 |
| SD | ±0.24 | ±0.018 |
| CV | 0.01 | 0.030 |

Table 8.1 IOLA plus reproducibility results

For the Optocraft, again 5 trials were undertaken for a 20.0D, three piece, blue blocking IOL, 6mm optic diameter. Results are shown in Table 8.2.

| Trial | Power (D) | MTF | Seidel Defocus (D) | Spherical RMS | HO RMS |
|-------|--------------|---------------|--------------------|---------------|---------------|
| 1 | 19.63 | 0.596 | 17.707 | 5.845 | 0.031 |
| 2 | 19.60 | 0.575 | 17.667 | 5.837 | 0.038 |
| 3 | 19.61 | 0.574 | 17.716 | 5.840 | 0.033 |
| 4 | 19.61 | 0.577 | 17.705 | 5.840 | 0.036 |
| 5 | 19.61 | 0.580 | 17.714 | 5.839 | 0.035 |
| Mean | 19.61 | 0.580 | 17.702 | 5.840 | 0.035 |
| SD | ±0.01 | ±0.009 | ±0.020 | ±0.003 | ±0.003 |
| CV | 0.00 | 0.015 | 0.001 | 0.001 | 0.085 |

Table 8.2 Optocraft reproducibility results

And finally for the Optical Bench, 5 more trials of a 24.5D, three piece blue blocking IOL, 7mm optic diameter were taken. Results are shown in Table 8.3.

| Trial | Measured Power (D) | USAF (Group: Element) | Resolution (%) |
|-------|--------------------|-----------------------|----------------|
| 1 | 24.18 | 4:4 | 73% |
| 2 | 24.29 | 4:4 | 73% |
| 3 | 24.23 | 4:4 | 73% |
| 4 | 24.23 | 4:4 | 73% |
| 5 | 24.20 | 4:3 | 65% |
| Mean | 24.23 | 4.4 | 71% |
| SD | ±0.04 | ± 0.1 | ±4% |
| CV | 0.00 | ND | 0.05 |

Table 8.3 Optical bench reproducibility results

A good reproducibility was found in all cases with small SD values and coefficients of variance less than 0.1 (10%) in all cases. For dioptric power, the IOLA plus showed the poorest reproducibility compared with both the Optocraft and Optical Bench, while for MTF values, the Optocraft had a better reproducibility than the IOLA plus. In addition, the IOLA plus appeared to have overestimated the manufacturer's given power of 24.5D by 0.64D, which is more than the proposed ISO 11979 tolerance of ±0.4D (Sverker Norrby et al., 1996).

8.3 Results

8.3.1 Stage One

Out of the 50 treated lenses, only 30 IOLs (60%) developed glistenings after being subjected to various thermal gradients. For those lenses, pre and post treatment measurements were compared. Subjective grading of glistenings did not exceed grade 3, therefore the IOLs measured were all of a low to moderate severity of glistenings. Moreover, only 2 out of the 30 (6.6%) were grade 3, 6 out of the 30 (20%) were grade 2 and the remaining 22 IOLs (73.4%) were grade 1. The sample therefore does not contain a uniform distribution of glistenings severity.

8.3.1.1 Wavefront Aberrations

As described in paragraph 8.2.3, the Seidel defocus, M, spherical RMS and higher-order RMS were evaluated, pre and post treatment. The calculated mean values and standard deviations are shown in Table 8.4.

| | Seidel Defocus M (D) | RMS sph (μm) | RMS HO (μm) |
|------|----------------------|---------------------------|--------------------------|
| Pre | 17.61 ± 0.64 | 5.833 ± 0.127 | 0.044 ± 0.032 |
| Post | 17.61 ± 0.63 | 5.833 ± 0.127 | 0.044 ± 0.038 |

Table 8.4 Stage 1: Wavefront metrics, pre and post treatment. All data are mean \pm SD.

A Mann-Whitney test was used to compare the pre and post thermal results. No statistically significant differences were found in Seidel Defocus ($p=0.94$), Spherical RMS ($p=0.95$) or Higher Order RMS ($p=0.67$).

8.3.1.2 Power and MTF

Dioptric Power and MTF measurements were evaluated with both the Optocraft and IOLA plus. Results are shown in Table 8.5 below.

| | Optocraft | | IOLA plus | |
|------|------------------|-------------------|------------------|-------------------|
| | Power (D) | MTF | Power (D) | MTF |
| Pre | 19.60 ± 0.44 | 0.563 ± 0.074 | 20.48 ± 0.41 | 0.602 ± 0.098 |
| Post | 19.60 ± 0.44 | 0.554 ± 0.082 | 20.33 ± 0.42 | 0.584 ± 0.094 |

Table 8.5 Stage 1: Power and MTF, tested with Optocraft and IOLA plus.

No statistical difference was found for Optocraft in Dioptric power ($p=0.98$) and MTF ($p=0.61$). This was also the case for the IOLA plus where Dioptric Power had no statistically significant change ($p=0.13$) as did MTF ($p=0.23$).

8.3.1.3 Resolution limit – USAF target

The optical resolution limit was also evaluated. Results are shown in Table 8.6.

| | Power (D) | Resolution (%) |
|------|------------------|-----------------|
| Pre | 19.81 ± 0.44 | $78\% \pm 8\%$ |
| Post | 19.76 ± 0.46 | $71\% \pm 11\%$ |

Table 8.6 Resolution limit measured with Optical Bench.

The change in power was not statistically significant ($p=0.86$) while for resolution a statistically significant decrease was found ($p=0.04$). No statistically significant correlation was found between subjective glistenings grading and resolution changes ($p=0.72$). Although the average resolution change among all measured IOLs was -6% ($\pm 12\%$), it was interesting to investigate individually the change in resolution for IOLs. This is illustrated in Figure 8.8 below.

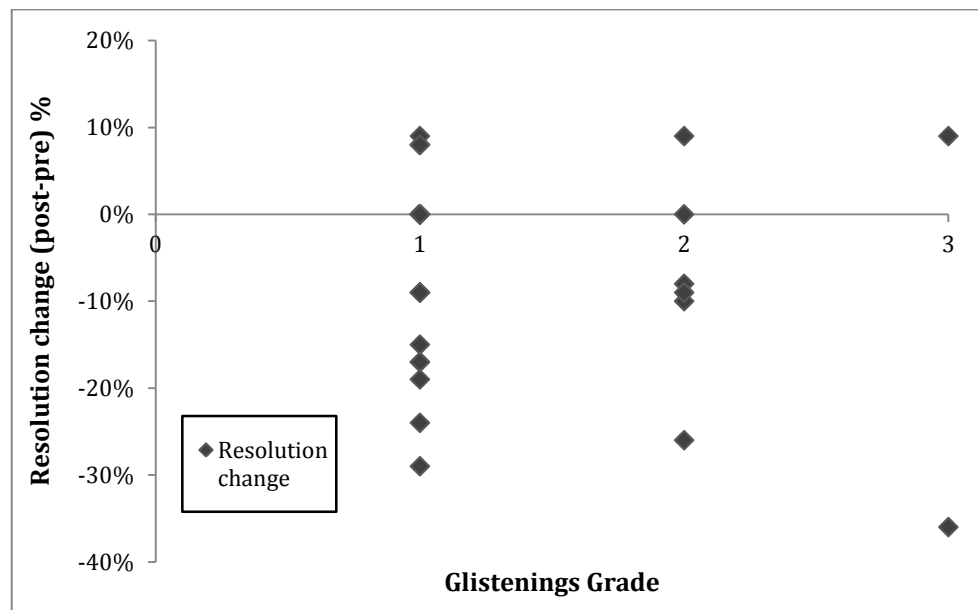


Figure 8.8 Number of lenses on different glistenings grades showing a negative, a positive or no resolution change.

The number of lenses with a negative impact on resolution was 14 out of the total 30, 46.7% of the total number of IOLs. Among these lenses, the mean resolution change was -17% ($\pm 9\%$). However, a considerable number of IOLs (33.3%) showed no difference in

resolution. Finally, a smaller number (20%) showed an improvement in optical resolution; the mean change though was just 8% ($\pm 1\%$) which is interpreted as a change in only one element on the USAF target, therefore it is a change that is within the range of the observational error and reproducibility error, as shown in paragraph 8.2.4.

8.3.2 Stage Two

From a total of 63 IOLs, 41 (65.1%) developed glistenings. Lenses were categorized according to their nominal dioptric power.

8.3.2.1 Correlation of Glistenings with Dioptric Power

Three dioptric power values were chosen with 21 in each group. This allowed the relationship between power and glistenings formation to be investigated. The number of IOLs that developed glistenings post thermal treatment in each group is given in Table 8.7.

| Group | Total IOLs Number | Total IOLs with Glistenings | Percentage |
|-------|-------------------|-----------------------------|------------|
| 15.0D | 21 | 8 | 38.1% |
| 20.0D | 21 | 13 | 61.9% |
| 25.0D | 21 | 20 | 95.2% |

Table 8.7 Percentage of lenses among the three dioptric groups, that developed glistenings after being subjected in same thermal grading conditions.

It was evident that the greater the dioptric power of the lens, the more likely the IOL is to show glistenings. Subjective grading varied from 0 to level 4, therefore no IOLs with high density grade 4+ glistenings were produced. Figure 8.9 shows the glistening grades with their corresponding dioptric power. It appeared that the higher the dioptric power of the lens, the greater the glistenings severity developed.

A statistically significant correlation was found between dioptric power and glistenings grade (Spearman coefficient of 0.56; $P=0.00$). While the number of IOLs with grade 0 glistenings was shown to drop when dioptric power increases, severity of glistenings among the lenses appeared to be positively related to the power; a notable result is apparent for the grades 3-4 where none of the 15.0D lenses showed a high density of glistenings compared to the 25.0D where almost a third (28.6%) were found in this category.

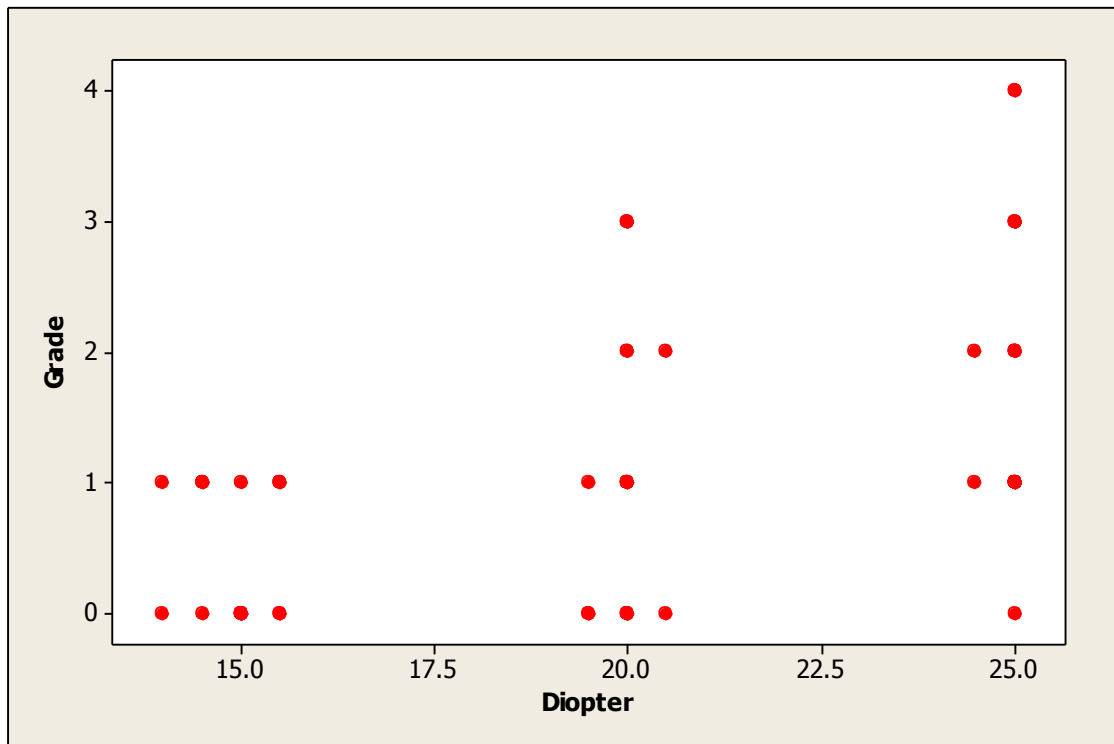


Figure 8.9 Grade of glistenings vs dioptric power.

8.3.2.2 MTF change

For study 2, lenses were only measured with the IOLA plus. Pre and post results were compared with a Mann-Whitney test. A statistically significant difference was found for the MTF values ($p=0.04$). The average change in MTF for all IOLs was $-0.026 (\pm 0.038)$. The change in MTF for each power group is shown in figure 8.10. Although the difference in MTF increased (absolute value) as the lens dioptric power increased, no statistically significant correlation was found between the MTF changes and the lens power ($p=0.97$) or the subjective glistenings grade ($p=0.47$).

8.3.2.3 Resolution limit

Resolution was evaluated using the Optical Bench (USAF target). Average resolution limit change was $-12\% (\pm 20\%)$ for all lenses. Pre and post treatment resolution values were compared with a Mann-Whitney test. A statistically significant difference was found ($p=0.02$). The results for the three dioptric power groups are shown in figure 8.11 below.

There was a decrease in resolution limit as dioptric power increased. A statistically significant negative correlation was found between the dioptric power and resolution change, ($r_s = -0.56$; $p=0.00$) as well as between subjective grading and the resolution changes, where the correlation coefficient was -0.53 ($p=0.00$).

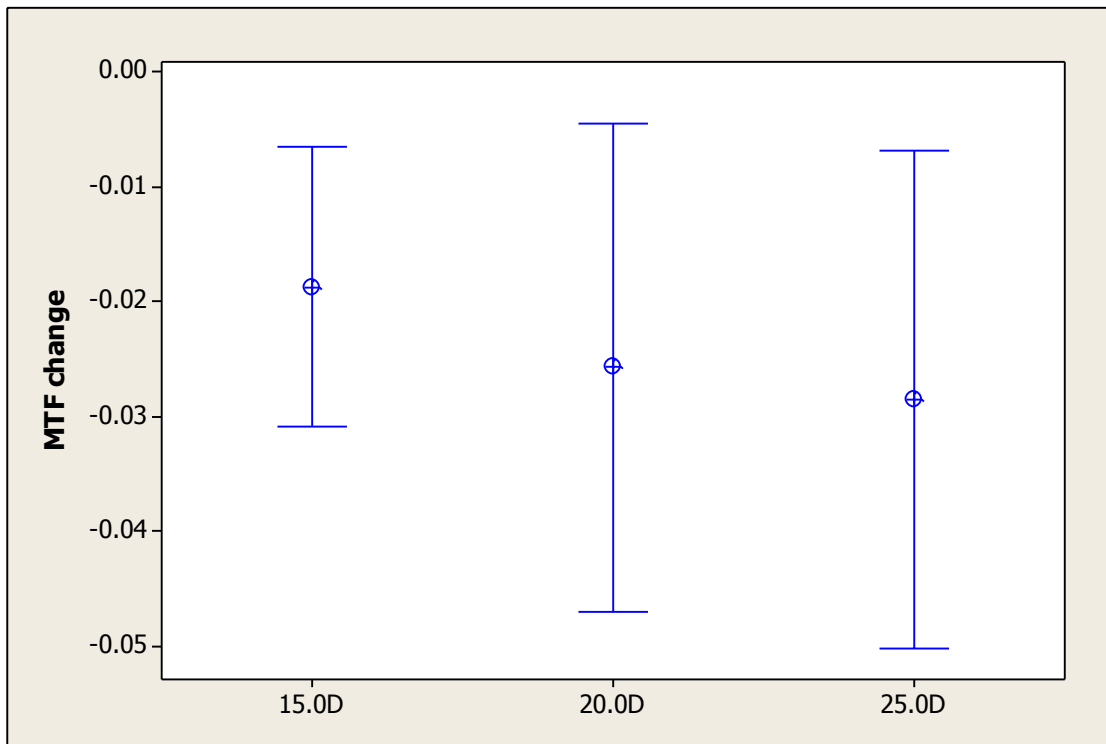


Figure 8.10 MTF changes mean values and standard deviations among the three dioptric power lens groups.

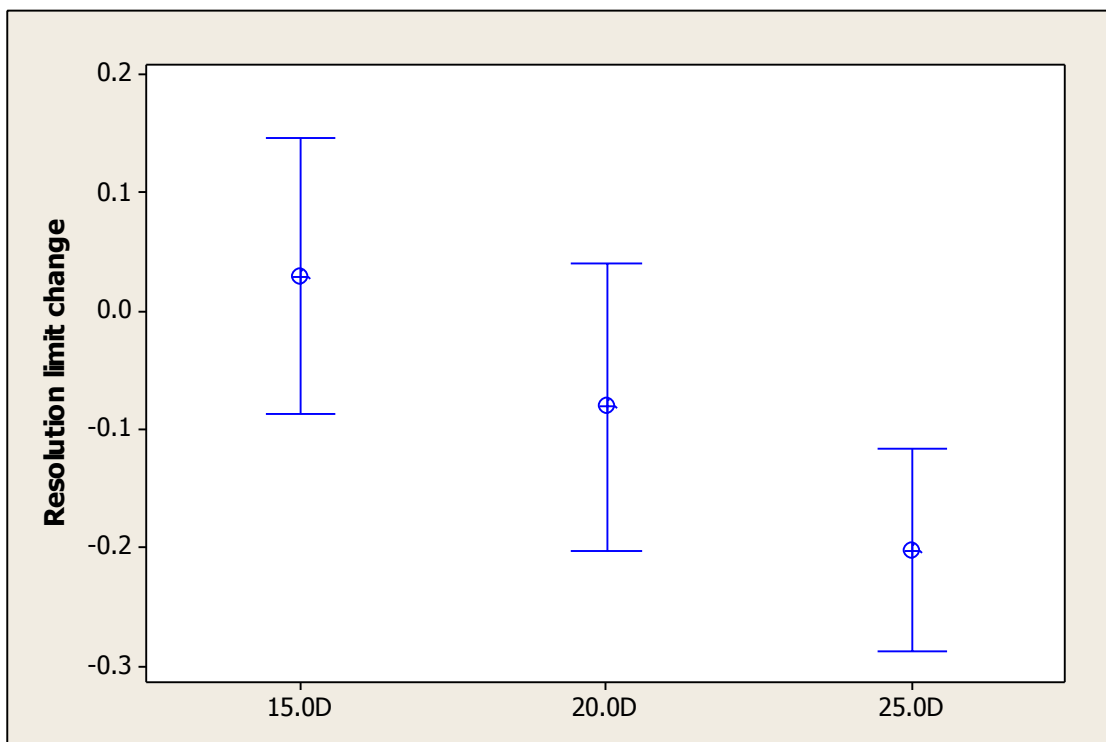


Figure 8.11 Resolution mean changes for each dioptric power IOL group.

8.4 Discussion

Despite the lack of high glistenings severity, a statistically significant decrease in resolution was observed both in Stage 1 and more obviously in Stage 2, which showed denser glistenings concentrations. Our previous results showed a rapid increase in light scatter for IOLs with higher grades of glistenings (4+ in our grading system). A similar finding has already been reported by Oshika et al (2001) when evaluating optical quality. Such high densities are not regularly observed but their existence has been clinically reported in case studies. Results from our bilateral study (Chapter 7), demonstrated that even modern designs of hydrophobic acrylic materials are likely to reach straylight levels equivalent to a cataractous lens.

Results from Study 1 show no significant change in wavefront spherical equivalent or higher-order aberrations. Moreover no significant change was found for any of the MTF results. The fact that subjective glistenings grade did not exceed a moderate severity of glistenings could explain these results; as shown in previous chapters, intraocular lenses with a considerable impact on scatter function were only the ones of high subjective grading. Consequently, any possible impact on MTF performance or wavefront aberrations may only be expected for higher levels of glistenings, in agreement with previous studies (Oshika et al., 2001).

A difference in MTF results was observed when comparing IOLA plus and Optocraft measurements. Variation of MTF measurements under identical conditions has been previously reported when comparing the results of a wavefront sensor with an interferometric technique (Liang and Williams, 1997); on average the wavefront sensor demonstrated higher MTF values, especially for the high frequencies. In our study there was little difference between the two methods; the results were equivalent, on average, to the reproducibility's standard deviation. This may have been due to the fact that the majority of the lenses showed grade 1 glistenings, therefore changes in MTF were expected to be minimal. It was also observed that the Optocraft produced smaller standard deviation values than the IOLA plus in both the measured power and MTF. A possible explanation for this is that a slight tilt of the IOL would often be caused by the cuvette's holder necessitating adjustment and repeat the measurements in many cases.

In study 2, a correlation between IOL dioptric power and severity of glistenings was found. Agbessi et al (2014) have recently reported in conference posters presented both at ARVO 2014, Orlando US (Agbessi et al., 2014) and ESCRS 2014, London, UK, that

glistenings' density was positively related to IOL dioptric power. Association between IOL power and both light scattering and glistenings' subjective grading has also been reported in previous studies (Mönestam et al., 2011, Colin et al., 2009). The most likely explanation could be the difference in lens thickness; the greater the dioptric power, the greater the lens thickness (provided that the same material and hence same refractive index, is compared). Greater lens volume could be a predictive factor for glistenings development.

In addition, stage 2 of the study showed a statistically significant difference in both MTF and Resolution limit, pre and post thermal treatment. A negative correlation was found between resolution and the subjective grading of glistenings. Consequently, resolution was also correlated negatively with lens dioptric power.

Chapter 9

Conclusions and Future Work

The studies described in this thesis investigate some of the aspects of forward light scatter caused by glistenings in intraocular lenses. The principal findings are summarised and discussed in this chapter together with suggestions for further work.

Chapter 4 – Clinical Grading

Subjective methods for grading intraocular lens glistenings poorly predict the increase in forward light scatter. It has been clearly shown in our study that IOLs with high grades of glistenings not only demonstrate high levels of light scatter but these straylight changes can be considered as potentially significant for visual function since they exceed the CIE standards for normal eyes. Moreover, our results have demonstrated that straylight changes with eccentricity angle, therefore evaluation should be carried out at more than one angle.

Chapter 5 – Glistenings Detection Programme

To better understand glistenings parameters that have an effect on forward light scatter and hence visual function, an objective method of glistenings grading is necessary. Image processing software has been developed, in collaboration with Thammasat University in Thailand and Kingston University in the UK. The Glistenings Detection Programme (GDP) is Matlab based software which analyzes *en face*, *in vitro* digital images of intraocular lenses captured using a slit-lamp and quantifies the glistenings' size, density and distribution.

Size is quantified using the minimum and maximum dimensions of the glistenings; this allows for elliptical glistenings, an innovation that no other study has considered although

there is evidence that non-spherical glistenings might exist. In addition, unlike previous glistenings quantification studies that use images from an illuminated slit section of the IOL or coronal projection images derived from Scheimpflug photography, our studies used whole lens images allowing metrics to be derived that don't make assumptions about the distribution of glistenings in the lens. The Glistenings Detection Programme was also modified to calculate metrics for three different pupil sizes (lens zones) so that light scatter and glistenings parameters can be related to changing pupil size under different lighting conditions (photopic/mesopic).

Evaluation metrics for the GDP (accuracy, sensitivity, specificity and area under the ROC curve), indicate a very good performance of the detection software. This gave us confidence in using the GDP for objective quantification of glistenings in our further studies.

Further development of the software as a future study is important to improve the accuracy, allow further automation and incorporate a method for analyzing both in vitro and in vivo images.

Chapter 6 – Objective Grading

In general, forward light scatter is positively correlated with the number and density of glistenings. Although the straylight parameter has been shown to increase as glistenings' severity increases, correlation was not clear either with the number, the cross-section or the density of glistenings. Therefore, although straylight is a clinical indicator for the visual importance, we have not found any relationship with glistenings morphology. This may be why studies looking at the visual impact of glistenings have failed to find consistent results.

Distribution of glistenings is not always uniform, with a trend for the centre to be denser in glistenings. The non-uniform distribution can cause a correlation of pupil size and light scattering if the change is significant. Glistenings are not ideal spherical particles; they are better approximated as ellipsoids, which in the case of large sizes could be a considerable factor for light scattering modelling and distribution.

Objective quantification tools of glistenings characterization offer better evaluation and association with light scattering. Number of glistenings is the dominant scattering factor; however, size of glistenings has been shown to be associated with increased light scattering. Additional measurements of IOLs, with a greater variety of different population densities and glistenings sizes are required to reach clearer conclusions.

The IOLs used in our studies appeared to develop larger numbers of microvacuoles greater than 20 μ m. The greater a microvacuole's size (cross-section) the more light propagation can be described with geometrical optics and diffraction (Van De Hulst, 1957). Laser diffraction is a method that is used experimentally for the size and shape characterization of scattering particles within a wide dimensional range. This could potentially be applied to glistenings studies, as illustrated in figure 9.1.

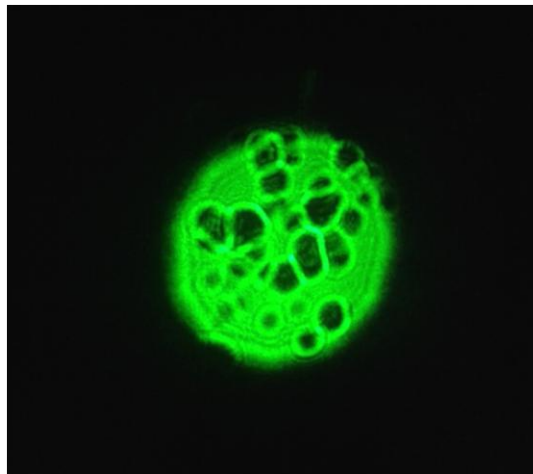


Figure 9.1 A diffraction topography of the IOL as projected on a black screen (shield) when exiting beam is diverging, offering a magnified projection of a relatively small central area of the lens. A modified version of this technique could be used for glistenings imaging and characterization.

Chapter 7 – Bilateral study

The Eternity Natural Uni NW-60 IOL material was found not to be a glistenings-free material under laboratory conditions but developed a small number of larger glistenings on average. However, since the laboratory conditions exaggerate the in vivo changes due to the artificial thermal gradients, the Eternity Natural Uni can be considered as material that strongly resists the development of glistenings with low VUSF and straylight parameter values. In contrast, the Acrysof NS60WF material developed a significant number of glistenings of less than 20microns from laboratory thermal cycling. A significant variation though was found between the Acrysof lenses for the number of

developed glistenings and corresponding VUSF values. This may suggest that, under normal in vivo conditions, not all Acrysof NS60WF IOLs are likely to cause a noticeable impact on visual function. However, in some cases, results were equivalent or much worse than those derived from a cataractous lens.

Chapter 8 – Optical performance

Our results suggest that the optical performance of an intraocular lens may not be affected by low to moderate glistenings' density. This may explain the lack of correlation between glistenings and visual performance in many clinical studies (Mönestam et al., 2011, Colin et al., 2012, Oshika et al., 2001, Colin and Orignac, 2011). However, IOLs developing high numbers of glistenings have been reported and are likely to exist even in modern designs of hydrophobic acrylic materials. A future optical performance study on the high density glistenings in IOLs is necessary to test the impact on MTF and resolution, as well as the corresponding impact on visual function.

Dioptric power was correlated with the potential of the intraocular lens to develop glistenings; this is a little known result that should be further considered and investigated as a factor in the mechanism of glistenings formation.

Concluding Remarks

The results from our studies suggest that glistenings in intraocular lenses have a direct effect on forward light scatter. Low to moderate glistenings density appeared to have little effect on light scatter when compared with the normal CIE standards. High glistenings density, on the other hand, showed results comparable with those of a cataractous crystalline lens.

Forward light scatter was shown to be inversely proportional to pupil size. Glistenings distribution was found to be non-uniform with a higher density of glistenings in the centre of the IOL than in the periphery.

The number of glistenings is the main factor affecting light scatter.; However, size and morphology of glistenings may play a considerable role on scattered light levels and distribution. It was shown that glistenings size differs among different materials; the

awareness of whether a material tends to develop small or large size of glistenings affects forward light scatter and could affect visual functional impairment.

Further clinical studies are necessary to realize the in vivo effect of glistenings, focusing on visual tests such as glare and contrast sensitivity. The objective quantification of glistenings in vivo would allow us to bring together in vitro measurement of light scatter and tests of visual function in vivo.

Appendix

Software for the Quantification of Glistenings in Intra-Ocular Lenses

Teeranoot Japunya, Parisut Jitpakdee, Bunyarit Uyyanonvara, Pakinee Aimmanee, Eva Philippaki, Chris Hull, and Sarah Barman

Abstract—An intraocular lens (IOL) is implanted in the eye after a cataract surgery. When an IOL is in an aqueous environment, glistenings that are fluid-filled microvacuoles are often observed. Previously, studies of glistenings involved tedious work of manual glistenings labeling and rough estimation of glistening distribution. This paper proposes a software that can be used for automatic glistenings detection. The software evaluates glistenings appearance in a lens, separating the IOL lens into 3 zones and accurately computing the average area, density and distribution to assist the user. The results are compared with clinicians hand-drawn ground truth for validation. The proposed GUI front-end is easy to use and very suitable for users who want accurate and quick glistenings detection. Numerical results can be achieved without manual drawing and rough estimation.

Index Terms—Medical Image Processing, Intra-Ocular Lens, Medical Software, Software Development, Glistening Detection.

I. INTRODUCTION

Following cataract or refractive lens surgery, the crystalline lens of the human eye is replaced by an artificial intraocular lens (IOL) typically inserted into the capsular bag [1]. When the IOL is in an aqueous environment, glistenings, which are fluid-filled microvacuoles, can be observed [2], [3], [4], [5], [6], [7]. Many studies report the formation of glistenings although the times of onset can be different [see 2 for a review]. The earliest reported onset of glistenings is one week postoperatively [2]. although, in some patients, glistenings were not found up to 6 months post implantation [2]. Irrespective of time of onset, the general trend is for the density of glistenings to increase with time [2], [5], [8]. There are many factors influencing the formation of glistenings, for example change in temperature, IOL material composition, IOL manufacturing technique, IOL packaging [2], [4], [5], [9], [10], [11].

Manuscript received March 14, 2014; revised April 9, 2014 This work was supported in part by the National Research University Project of Thailand Office of Higher Education Commission (Thammasat University), Thailand Advanced Institute of Science and Technology (TAIST), National Science and Technology Development Agency (NSTDA), Tokyo Institute of Technology, and Sirindhorn International Institute of Technology (SIIT), Thammasat University (TU) under the TAIST Tokyo Tech Program.

Teeranoot Japunya Author is with Thailand Advanced Institute of Science and Technology (TAIST), Sirindhorn International Institute of Technology, Thammasat University, Thailand (e-mail: teeranoot.j@gmail.com).

Parisut Jitpakdee, Bunyarit Uyyanonvara, Pakinee Aimmanee Authors are with Sirindhorn International Institute of Technology, Thammasat University, Thailand (e-mail: parisut@gmail.com, pakinee@siit.tu.ac.th, and bunyarit@siit.tu.ac.th, respectively).

Eva Philippaki and Chris Hull Authors are with Applied Vision Research Centre, School of Health Sciences, City University London, Northampton Square, United Kingdom (e-mail: Evangelia.Filippaki.1@city.ac.uk and C.C.Hull@city.ac.uk, respectively).

Sarah Barman Author is with Digital Imaging Research Centre, Faculty of Science, Engineering and Computing, Kingston University, Penrhyn Road, United Kingdom (e-mail: S.Barman@kingston.ac.uk).

Glistenings are important because they can affect vision by increasing forward light scatter [12], [13], [14]. The amount of light scatter is likely to be affected by the size, density and location of the glistening. To our best knowledge, no algorithm has been published for glistenings detection although a few studies suggest that other groups have looked at detection using image processing [15].

Exudates are lipids and leakage of proteins [16], [17]. Hard exudates are seen as bright yellow lesions with different sizes, shapes, and locations [16]. Blobs are defined as a brighter or darker region compared with the surrounding area or in the same color in the image or video [18], [19]. The techniques used for the detection of exudates and blobs can be adapted to use as glistenings detection.

In this paper, a collaboration between researchers from Thammasat University in Thailand, Kingston University and City University in London, we propose an effective intraocular lens glistenings quantification software. This novel software has a user friendly front-end and is designed to semi-automatically detect glistenings. Once detected, the software computes and displays important properties for the user. Its GUI is designed for the convenience of users who are typically clinicians or scientists with little image processing knowledge. The software is built based on Matlab.

The paper is organized as follows: Section 2 briefly describes the procedure for glistenings detection; Section 3 presents a detail of software features; The conclusion and future work are showed in Section 4.

II. PROCEDURE FOR GLISTENINGS QUANTIFICATION

A. Overall Procedure

For the quantification of the glistenings on an IOL, the boundary of the lens is detected. The radius is then calculated and the area of interest is divided into zones. Then glistenings are detected and the software calculates many properties such as area, density and glistenings distribution. The software contains an option to validate the glistenings detection result by comparing with the hand-drawn ground-truth image. The overall procedure is shown in Fig. 1.

B. Lens Detection and Zoning

The lens is detected within the image by finding the circumference of the lens. We assume that the radius of the IOL Lens is 6 mm and then divide the lens into 3 concentric zones; 3 mm, 4 mm, and 5 mm, representing the different pupil sizes. Glistenings are quantified within the different zones for further analysis that can be related to real world situations. Fig. 2 shows the zoning system described in this paper.

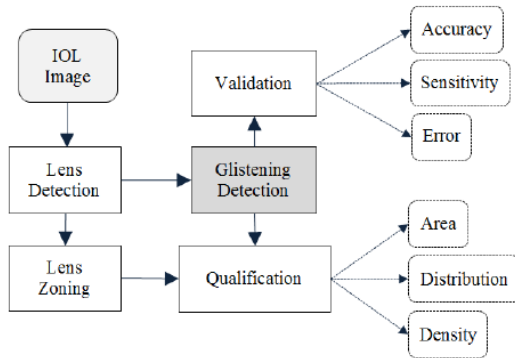


Fig. 1. The procedure of glistenings quantification.

C. Glistenings detection

Image processing techniques are used to detect the glistenings. The Sobel operator is employed to detect the edge of the glistenings. The Sobel filter is a mask operation which is a first order differential edge detection. In our method we applied both x and y coordinates and combined the two results into one image. Due to Sobel mask have line of high contrast in the image. The dilation operation is used for connecting broken lines. All gaps as a result of the dilation operation will be filled. After these operations, we get the glistenings area is output but it is combined with other smaller areas as a result of noise in the image.. To post-process, we use the erosion operator to remove areas which are smaller or larger than our expecting target size.

D. Glistenings Quantification

All detected glistenings will be used in the calculation of its properties, namely, area, distribution and density in all 4 regions: within the whole lens, within the 3mm zone, 4mm zone, and 5mm zone. An area of each microvacuole is a number of pixels detected as glistenings. The average area of each zone is used to compare with the sizes of glistenings. The distribution shows whether glistenings are located on the lens evenly or if most of them are located on certain zones. Then the density of glistenings of each zone is calculated by the summation of the areas of glistenings divided by the area of the zone.

An area of each microvacuole is a number of pixels detected as glistenings. The average area of each zone is used to compare with the sizes of glistenings. The distribution shows whether glistenings are located on the lens evenly or if most of them are located on certain zones. Then the density of glistenings of each zone is calculated by the summation of the areas of glistenings divided by the area of the zone.

E. Result Validation

The accuracy, sensitivity and error are used to inspect the performance comparing the glistenings detection result with the ground truth. The glistenings in ground truth images are hand marked in the red color by an expert in glistening (EP), as shown in Fig 3.

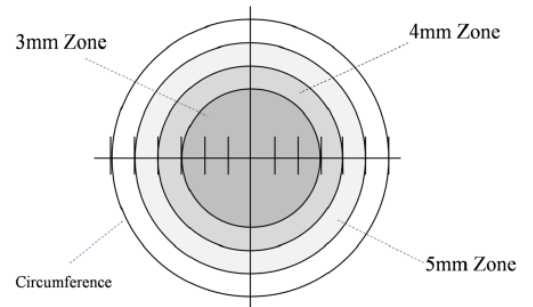


Fig. 2. Lens Zoning: 3mm, 4mm, and 5mm zones.

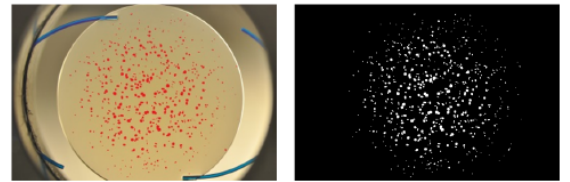


Fig. 3. Example ground truth image. Left hand side: Red marked Glistenings Image and Right hand side: White marked Glistenings.

III. SOFTWARE FEATURES

A user interface that can cope with different images of glistening has been created to allow for their different formation, size, density and position. Its features include IOL image selection and display, lens detection, parameter configuration and glistenings detection, ground truth selection, layer selection, quantification result and validation details.

A. IOL Image Selection and display

The user can select the IOL image by opening the image file. The IOL image can be 4 types: JPG, TIFF, PNG, or GIF.

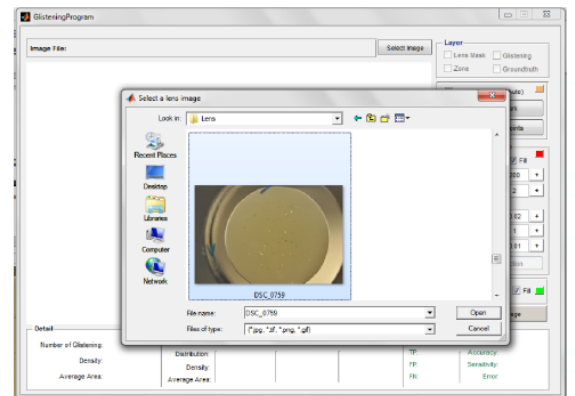


Fig. 4. IOL image saving window.

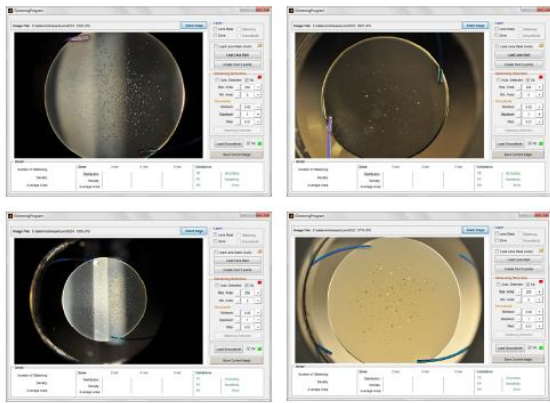


Fig. 5. IOL Image Showing Examples.



Fig. 6. IOL image and its lens mask.

B. Lens Detection

Before the glistenings detection process can be applied, we need to specify the region of the lens. This front-end includes 2 ways to identify the boundary of the lens. First, the user can load the lens mask by selecting the lens mask image file where the white area is the region of interest of the lens. Fig. 6 shows the example of the IOL image and its lens mask image. If the user doesn't have a mask, the user can create a mask semi-automatically by specifying 5 different locations on the lens boundary. The lens mask area is then created by the program and shown on the screen. Fig. 7 shows the example of lens mask creation by clicking on the IOL image 5 times.

C. Glistenings detection

In the glistenings detection part of the software, the user can adjust many parameters for a variety of glistenings image input. There are 5 variables in this part consisting of Maximum area of glistenings (Max. area), Minimum area of glistenings (Min. area), Minimum Threshold, Maximum Threshold and step. The user can choose the color of the glistenings and choose to show only the boundary line or the glistenings area filled with color. Fig. 8 shows the example of the glistenings area filled with color and Fig. 9 shows an example of the glistenings boundary line and lens mask line.

D. Ground truth Selection (for development phase)

During the program validation phase, the user can load a ground truth image and compare it with the automatic glistenings detection result. Specificity and Sensitivity will be automatically calculated.

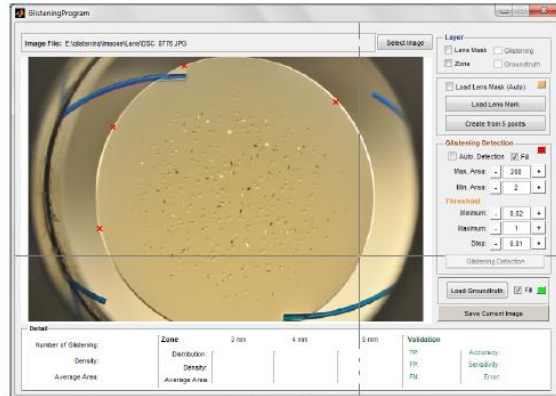


Fig. 7. 5 points clicking to create lens mask.

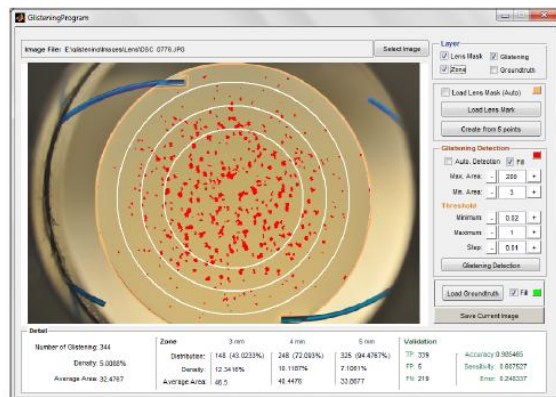


Fig. 8. Screen of program, shows filled-glistenings, lens mask and zone boundaries.

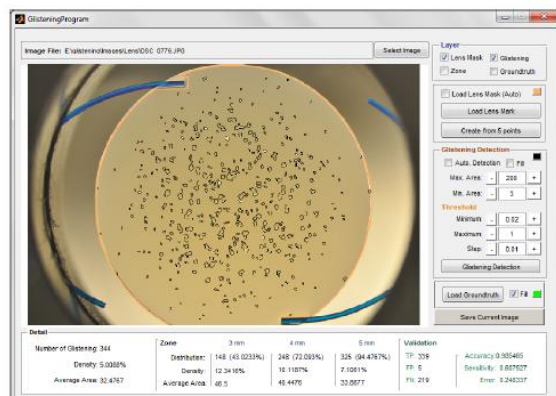


Fig. 9. Screen of program, shows the edges of glistenings and the lens mask line.

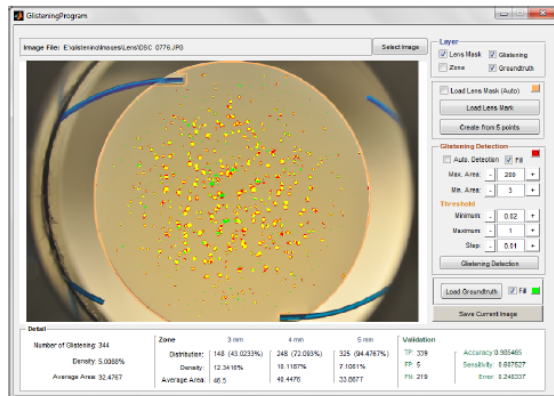


Fig. 10. Screen of program, shows the comparison of detected glistenings and the ground truth.

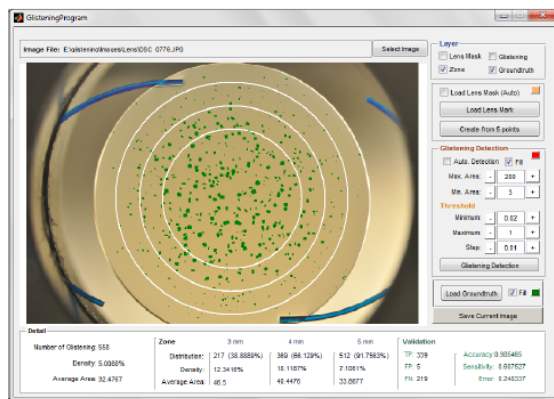


Fig. 11. Screen of program, shows the filled-glistenings from ground truth and zone boundary.

E. Layer Selection

The user can select the layers to be shown on the IOL image. There are 4 layers; Lens Mask, Zone, Glistenings, and Ground truth. The example of the comparing of detected glistenings, ground truth area and lens mask are shown in Fig. 10 and the filled-glistenings from ground truth and zone boundary are shown in Fig. 11.

F. Image Saving

A Save Current Image button is also added to help the user save the current processed image.

G. Quantification results

The results of the glistenings detection is shown on the Quantification Detail. The Overall result is shown on the left hand side of the screen for easy access. The results consist of the number of glistenings, density and average area. The next panel shows results from each zone of the IOL lens. The results show the distribution, density and average area of each zone.

H. Validation Result

The accuracy and sensitivity are used to compute front-end performance. The accuracy is the result of the correct

result divided by the total number of classifications and sensitivity is the result of the true positive and the condition negative. After the user chooses a ground truth image, the true positive (TP), false positive (FP), false negative (FN), accuracy, sensitivity and error are shown on the right hand side of the detail section.

IV. CONCLUSION & FUTURE WORK

This paper proposed a software that is designed to detect glistenings and accurately compute important properties for the user. Glistenings detection results along with its properties are shown on the screen, and comfortably help the user to analyze glistenings in real time. Its GUI is simplified for the convenience of users, so that even a first time user can find it easy to use. The software is built based on Matlab. It has an easy-to-use GUI and a semi-automatic algorithm to detect and quantify the glistenings. It is suitable for users who want accurate and quick glistenings detection. Numerical results can be achieved without manual drawing and rough estimation.

There are still limitations on the currently proposed software that need to be developed. The size of the IOL is considered as standard at 6mm while there are IOLs in the market with different diameters. In the case of glistenings overlapping, the software is still weak to distinguish this feature.

For future work, we will focus on the efficient algorithm for glistenings detection. We intend to develop a new technique which is more accurate and effective.

ACKNOWLEDGMENT

We would like to thank the Applied Vision Research Centre, School of Health Sciences, City University London, for the IOL images and ground truth data.

REFERENCES

- [1] R. Bellucci, "An introduction to intraocular lenses: material, optics, haptics, design and aberration," 2013.
- [2] L. Werner, "Glistenings and surface light scattering in intraocular lenses," *Journal of Cataract & Refractive Surgery*, vol. 36, no. 8, pp. 1398 – 1420, 2010. [Online]. Available: <http://www.sciencedirect.com/science/article/pii/S0886335010008308>
- [3] K. Hayashi, A. Hirata, M. Yoshida, K. Yoshimura, and H. Hayashi, "Long-term effect of surface light scattering and glistenings of intraocular lenses on visual function," *American Journal of Ophthalmology*, vol. 154, no. 2, pp. 240 – 251.e2, 2012. [Online]. Available: <http://www.sciencedirect.com/science/article/pii/S0002939412002024>
- [4] D. Tognetto, L. Toto, G. Sanguinetti, and G. Ravalico, "Glistenings in foldable intraocular lenses," *Journal of Cataract & Refractive Surgery*, vol. 28, no. 7, pp. 1211 – 1216, 2002. [Online]. Available: <http://www.sciencedirect.com/science/article/pii/S0886335002013536>
- [5] N. Mamalis, "Intraocular lens glistenings," *Journal of Cataract & Refractive Surgery*, vol. 38, no. 7, pp. 1119 – 1120, 2012. [Online]. Available: <http://www.sciencedirect.com/science/article/pii/S088633501200675X>
- [6] J. Colin, I. Orignac, and D. Touboul, "Glistenings in a large series of hydrophobic acrylic intraocular lenses," *Journal of Cataract & Refractive Surgery*, vol. 35, no. 12, pp. 2121 – 2126, 2009. [Online]. Available: <http://www.sciencedirect.com/science/article/pii/S0886335009007822>
- [7] U. Gunenc, F. Oner, S. Tongal, and M. Feriel, "Effects on visual function of glistenings and folding marks in acrylic intraocular lenses," *Journal of Cataract & Refractive Surgery*, vol. 27, no. 10, pp. 1611 – 1614, 2001. [Online]. Available: <http://www.sciencedirect.com/science/article/pii/S0886335001009956>

- [8] J. Colin, D. Praud, D. Touboul, and C. Schweitzer, "Incidence of glistenings with the latest generation of yellow-tinted hydrophobic acrylic intraocular lenses," *Journal of Cataract & Refractive Surgery*, vol. 38, no. 7, pp. 1140 – 1146, 2012. [Online]. Available: <http://www.sciencedirect.com/science/article/pii/S0886335012004762>
- [9] K. Kato, M. Nishida, H. Yamane, K. Nakamae, Y. Tagami, and K. Tetsumoto, "Glistening formation in an acrysof lens initiated by spinodal decomposition of the polymer network by temperature change," *Journal of Cataract & Refractive Surgery*, vol. 27, no. 9, pp. 1493 – 1498, 2001. [Online]. Available: <http://www.sciencedirect.com/science/article/pii/S0886335001008951>
- [10] N. Z. Gregori, T. S. Spencer, N. Mamalis, and R. J. Olson, "In vitro comparison of glistening formation among hydrophobic acrylic intraocular lenses," *Journal of Cataract & Refractive Surgery*, vol. 28, no. 7, pp. 1262 – 1268, 2002. [Online]. Available: <http://www.sciencedirect.com/science/article/pii/S0886335002012245>
- [11] T. Oshika, Y. Shiokawa, S. Amano, and K. Mitomo, "Influence of glistenings on the optical quality of acrylic foldable intraocular lens," *British Journal of Ophthalmology*, vol. 85, no. 9, pp. 1034–1037, 2001. [Online]. Available: <http://bj.o.bmj.com/content/85/9/1034.abstract>
- [12] E. Mnestam and A. Behndig, "Impact on visual function from light scattering and glistenings in intraocular lenses, a long-term study," *Acta Ophthalmologica*, vol. 89, no. 8, pp. 724–728, 2011. [Online]. Available: <http://dx.doi.org/10.1111/j.1755-3768.2009.01833.x>
- [13] K. Hayashi, A. Hirata, M. Yoshida, K. Yoshimura, and H. Hayashi, "Long-term effect of surface light scattering and glistenings of intraocular lenses on visual function," *American Journal of Ophthalmology*, vol. 154, no. 2, pp. 240 – 251.e2, 2012. [Online]. Available: <http://www.sciencedirect.com/science/article/pii/S0002939412002024>
- [14] M. van der Mooren, L. Franssen, and P. Piers, "Effects of glistenings in intraocular lenses," *Biomed. Opt. Express*, vol. 4, no. 8, pp. 1294–1304, Aug 2013. [Online]. Available: <http://www.opticsinfobase.org/boe/abstract.cfm?URI=boe-4-8-1294>
- [15] C. J and O. I, "Glistenings on intraocular lenses in healthy eyes: effects and associations," *Journal of Refractive Surgery (Thorofare, N.J. : 1995)*, pp. 869–875, 2011.
- [16] D. Youssef, N. Solouma, A. El-dib, M. Mabrouk, and A.-B. Youssef, "New feature-based detection of blood vessels and exudates in color fundus images," in *Image Processing Theory Tools and Applications (IPTA), 2010 2nd International Conference on*, July 2010, pp. 294–299.
- [17] H. Jaafar, A. Nandi, and W. Al-Nuaimy, "Detection of exudates in retinal images using a pure splitting technique," in *Engineering in Medicine and Biology Society (EMBC), 2010 Annual International Conference of the IEEE*, Aug 2010, pp. 6745–6748.
- [18] L. Wang and H. Ju, "A robust blob detection and delineation method," in *Education Technology and Training, 2008. and 2008 International Workshop on Geoscience and Remote Sensing. ETT and GRS 2008. International Workshop on*, vol. 1, Dec 2008, pp. 827–830.
- [19] Z. Qiu, L. Yang, and W. Lu, "A new feature-preserving nonlinear anisotropic diffusion for denoising images containing blobs and ridges," *Pattern Recognition Letters*, vol. 33, no. 3, pp. 319 – 330, 2012. [Online]. Available: <http://www.sciencedirect.com/science/article/pii/S016786551100376X>

References

- Agbessi, L., Mascali, R., Cochener, B., Orignac, I. & Schweitzer, C. (2014) 'Glistenings in multifocal intraocular lenses: Visual outcomes and risk factors', *Investigative Ophthalmology and Visual Science*, 55 (5), pp. 2522.
- Altman, D. G. (1990). *Practical statistics for medical research*, CRC Press.
- Amaral, F. T. & Monteiro, D. W. D. L. (2013) 'Alternative methodology for intraocular lens characterisation', *Ophthalmic & physiological optics : the journal of the British College of Ophthalmic Opticians (Optometrists)*, 33 (4), pp. 427-433.
- Apple, D. J., Peng, Q. & Ram, J. (1999) 'The 50th anniversary of the intraocular lens and a quiet revolution', *Ophthalmology*, 106 (10), pp. 1861-1862.
- Artal, P. & Navarro, R. (1994) 'Monochromatic modulation transfer function of the human eye for different pupil diameters: an analytical expression', *JOSA A*, 11 (1), pp. 246-249.
- Atchison, D. A., Smith, G. O. & Elsevier, E. B. S. (2000). *Optics of the human eye*, Oxford; Boston, Butterworth-Heinemann.
- Attia, J. (2003) 'Moving beyond sensitivity and specificity: using likelihood ratios to help interpret diagnostic tests', *Australian prescriber*, 26 (5), pp. 111-113.
- Ayaki, M., Nishihara, H., Yaguchi, S. & Koide, R. (2006) 'Surfactant induced glistenings: surface active ingredients in ophthalmic solutions may enhance water entry into the voids of implanted acrylic intraocular lenses', *Journal of long-term effects of medical implants*, 16 (6).

- Bamber, D. (1975) 'The area above the ordinal dominance graph and the area below the receiver operating characteristic graph', *Journal of mathematical psychology*, 12 (4), pp. 387-415.
- Barbero, S., Marcos, S. & Jiménez-Alfaro, I. (2003) 'Optical aberrations of intraocular lenses measured *in vivo* and *in vitro*', *JOSA A*, 20 (10), pp. 1841-1851.
- Barboriak, D. P., Padua, A. O., York, G. E. & Macfall, J. R. (2005) 'Creation of DICOM—aware applications using ImageJ', *Journal of digital imaging*, 18 (2), pp. 91-99.
- Barbur, J., Edgar, D. & Woodward, E. (1995) 'Measurement of the scattering characteristics of the eye in relation to pupil size', *Vision Science and its Applications*, 1, pp. 250-253.
- Behndig, A., Mönestam, E., Medicinska, F., Oftalmiatrik, Institutionen För Klinisk, V. & Umeå, U. (2009) 'Quantification of glistenings in intraocular lenses using Scheimpflug photography', *Journal of Cataract & Refractive Surgery*, 35 (1), pp. 14-17.
- Beiko, G. H. & Grzybowski, A. (2013) 'Glistenings in hydrophobic acrylic intraocular lenses do affect visual function', *Clinical ophthalmology (Auckland, N.Z.)*, 7, pp. 2271-2274.
- Bellucci, R. (2013) 'An introduction to intraocular lenses: material, optics, haptics, design and aberration', *Cataract*, 3, pp. 39.
- Bellucci, R., Morselli, S. & Piers, P. (2004) 'Comparison of wavefront aberrations and optical quality of eyes implanted with five different intraocular lenses', *Journal Of Refractive Surgery (Thorofare, N.J.: 1995)*, 20 (4), pp. 297-306.
- Boynton, R. M., Enoch, J. M. & Bush, W. R. (1954) 'Physical Measures of Stray Light in Excised Eyes', *Journal of the Optical Society of America*, 44 (11), pp. 879-886.
- Bradley, A. P. (1997) 'The use of the area under the ROC curve in the evaluation of machine learning algorithms', *Pattern recognition*, 30 (7), pp. 1145-1159.

- Burton, G. & Haig, N. (1984) 'Effects of the Seidel aberrations on visual target discrimination', *JOSA A*, 1 (4), pp. 373-385.
- Camparini, M., Macaluso, C., Reggiani, L. & Maraini, G. (2000) 'Retroillumination versus reflected-light images in the photographic assessment of posterior capsule opacification', *Investigative ophthalmology & visual science*, 41 (10), pp. 3074-3079.
- Campbell, F. & Green, D. (1965) 'Optical and retinal factors affecting visual resolution', *The Journal of Physiology*, 181 (3), pp. 576.
- Cerviño, A., Bansal, D., Hosking, S. L. & Montés-Micó, R. (2008) 'Objective measurement of intraocular forward light scatter using Hartmann-Shack spot patterns from clinical aberrometers: Model-eye and human-eye study', *Journal of Cataract & Refractive Surgery*, 34 (7), pp. 1089-1095.
- Chang, A., Behndig, A., Rønbeck, M. & Kugelberg, M. (2013) 'Comparison of posterior capsule opacification and glistenings with 2 hydrophobic acrylic intraocular lenses: 5- to 7-year follow-up', *Journal of Cataract & Refractive Surgery*, 39 (5), pp. 694-698.
- Chang, D. (2004) 'Single versus three piece acrylic IOLs', *British journal of ophthalmology*, 88 (6), pp. 727-728.
- Chou, J.-S., Blake, L. W., Fridge, J. M. & Fridge, D. A. (1995) 'MTF measurement system that simulates IOL performance in the human eye'. 1995. 271-279.
- Christiansen, G., Durcan, F. J., Olson, R. J. & Christiansen, K. (2001) 'Glistenings in the AcrySof intraocular lens: pilot study', *Journal of cataract and refractive surgery*, 27 (5), pp. 728-733.
- Chylack Jr, L. T., Jakubicz, G., Rosner, B., Khu, P., Libman, J., Wolfe, J. K., Padhye, N. & Friend, J. (1993) 'Contrast sensitivity and visual acuity in patients with early cataracts', *Journal of Cataract & Refractive Surgery*, 19 (3), pp. 399-404.

- Cisneros-Lanuza, A., Hurtado-Sarrió, M., Duch-Samper, A., Gallego-Pinazo, R. & Menezo-Rozalén, J. L. (2007) 'Glistenings in the Artiflex phakic intraocular lens', *Journal of Cataract & Refractive Surgery*, 33 (8), pp. 1405-1408.
- Cobb, P. W. (1911) 'The influence of illumination of the eye on visual acuity', *American Journal of Physiology--Legacy Content*, 29 (1), pp. 76-99.
- Colin, J. & Orignac, I. (2011) 'Glistenings on intraocular lenses in healthy eyes: effects and associations', *Journal of refractive surgery (Thorofare, N.J.: 1995)*, 27 (12), pp. 869-875.
- Colin, J., Orignac, I. & Touboul, D. (2009) 'Glistenings in a large series of hydrophobic acrylic intraocular lenses', *Journal of Cataract & Refractive Surgery*, 35 (12), pp. 2121-2126.
- Colin, J., Praud, D., Touboul, D. & Schweitzer, C. (2012) 'Incidence of glistenings with the latest generation of yellow-tinted hydrophobic acrylic intraocular lenses', *Journal of Cataract & Refractive Surgery*, 38 (7), pp. 1140-1146.
- Cox, M. E. (1979) 'The lens-pinhole spatial filter (teaching)', *Physics Education*, 14 (1), pp. 56-57.
- Curcio, C., Millican, C., Allen, K. & Kalina, R. (1993) 'Aging of the human photoreceptor mosaic: evidence for selective vulnerability of rods in central retina', *Investigative ophthalmology & visual science*, 34 (12), pp. 3278-3296.
- Cuthbertson, F. M., Peirson, S. N., Wulff, K., Foster, R. G. & Downes, S. M. (2009) 'Blue light-filtering intraocular lenses: Review of potential benefits and side effects', *Journal of Cataract & Refractive Surgery*, 35 (7), pp. 1281-1297.
- Das, K. K., Stover, J. C., Schwiegerling, J. & Karakelle, M. (2013) 'Technique for measuring forward light scatter in intraocular lenses', *Journal of Cataract & Refractive Surgery*, 39 (5), pp. 770-778.

- De Waard, P. W., Ijspeert, J. K., Van Den Berg, T. J. & De Jong, P. T. (1992) 'Intraocular light scattering in age-related cataracts', *Investigative ophthalmology & visual science*, 33 (3), pp. 618-625.
- De Wit, G. C. & Coppens, J. E. (2003) 'Stray light of spectacle lenses compared with stray light in the eye', *Optometry & Vision Science*, 80 (5), pp. 395-400.
- De Wit, G. C., Franssen, L., Coppens, J. E. & Van Den Berg, T. J. T. P. (2006) 'Simulating the straylight effects of cataracts', *Journal of Cataract & Refractive Surgery*, 32 (2), pp. 294-300.
- Dehoog, E. & Doraiswamy, A. (2014) 'Evaluation of the impact of light scatter from glistenings in pseudophakic eyes', *Journal of Cataract & Refractive Surgery*, 40 (1), pp. 95-103.
- Dhaliwal, D. K., Mamalis, N., Olson, R. J., Crandall, A. S., Zimmerman, P., Alldredge, O. C., Durcan, F. J. & Omar, O. (1996) 'Visual significance of glistenings seen in the AcrySof intraocular lens', *Journal of Cataract & Refractive Surgery*, 22 (4), pp. 452-457.
- Duanggate, C., Uyyanonvara, B., Makhanov, S. S., Barman, S. & Williamson, T. (2011) 'Object detection with feature stability over scale space', *Journal of Visual Communication and Image Representation*, 22 (4), pp. 345-352.
- Eliceiri, K. W. & Rueden, C. (2005) 'Tools for visualizing multidimensional images from living specimens', *Photochemistry and photobiology*, 81 (5), pp. 1116-1122.
- Eppig, T., Gillner, M., Zoric, K., Jäger, J., Löffler, A. & Langenbucher, A. (2013) 'Biomechanical eye model and measurement setup for investigating accommodating intraocular lenses', *Zeitschrift für Medizinische Physik*, 23 (2), pp. 144-152.
- Eshel, G., Levy, G., Mingelgrin, U. & Singer, M. (2004) 'Critical evaluation of the use of laser diffraction for particle-size distribution analysis', *Soil Science Society of America Journal*, 68 (3), pp. 736-743.

- Farbowitz, M. A., Zabriskie, N. A., Crandall, A. S., Olson, R. J. & Miller, K. M. (2000) 'Visual complaints associated with the AcrySof acrylic intraocular lens', *Journal of Cataract & Refractive Surgery*, 26 (9), pp. 1339-1345.
- Finney, R. L., Weir, M. D., Giordano, F. R. & Thomas, G. B. (2001). *Thomas' calculus*, Boston, Mass; London, Addison-Wesley.
- Franssen, L., Coppens, J. E. & Van Den Berg, T. J. (2006) 'Compensation comparison method for assessment of retinal straylight', *Investigative ophthalmology & visual science*, 47 (2), pp. 768-776.
- Franssen, L., Tabernero, J., Coppens, J. E. & Van Den Berg, T. J. T. P. (2007) 'Pupil Size and Retinal Straylight in the Normal Eye', *Investigative ophthalmology & visual science*, 48 (5), pp. 2375-2382.
- Fraz, M. M., Remagnino, P., Hoppe, A., Uyyanonvara, B., Rudnicka, A. R., Owen, C. G. & Barman, S. A. (2012) 'Blood vessel segmentation methodologies in retinal images--a survey', *Computer methods and programs in biomedicine*, 108 (1), pp. 407-433.
- Fry, G. A. & Alpern, M. (1953) 'The effect of a peripheral glare source upon the apparent brightness of an object', *JOSA*, 43 (3), pp. 189-195.
- Ginis, H., Pentari, I., De Brouwere, D., Bouzoukis, D., Naoumidi, I. & Pallikaris, I. (2009) 'Narrow angle light scatter in rabbit corneas after excimer laser surface ablation', *Ophthalmic and Physiological Optics*, 29 (3), pp. 357-362.
- Gray, R., Perkins, S. A., Suryakumar, R., Neuman, B. & Maxwell, W. A. (2011) 'Reduced effect of glare disability on driving performance in patients with blue light-filtering intraocular lenses', *Journal of Cataract & Refractive Surgery*, 37 (1), pp. 38-44.
- Gregori, N. Z., Spencer, T. S., Mamalis, N. & Olson, R. J. (2002) 'In vitro comparison of glistening formation among hydrophobic acrylic intraocular lenses', *Journal of Cataract & Refractive Surgery*, 28 (7), pp. 1262-1268.

- Greiner, M., Pfeiffer, D. & Smith, R. (2000) 'Principles and practical application of the receiver-operating characteristic analysis for diagnostic tests', *Preventive veterinary medicine*, 45 (1), pp. 23-41.
- Guirao, A., Gonzalez, C., Redondo, M., Geraghty, E., Norrby, S. & Artal, P. (1999) 'Average optical performance of the human eye as a function of age in a normal population', *Investigative Ophthalmology & Visual Science*, 40 (1), pp. 203-213.
- Guirao, A., Porter, J., Williams, D. R. & Cox, I. G. (2002) 'Calculated impact of higher-order monochromatic aberrations on retinal image quality in a population of human eyes: erratum', *JOSA A*, 19 (3), pp. 620-628.
- Gunenc, U., Oner, F. H., Tongal, S. & Ferliel, M. (2001) 'Effects on visual function of glistenings and folding marks in AcrySof intraocular lenses', *Journal of Cataract & Refractive Surgery*, 27 (10), pp. 1611-1614.
- Gupta, S. & Mazumdar, S. G. (2013) 'Sobel edge detection algorithm', *International journal of computer science and management Research*, 2 (2), pp. p1578-1583.
- Hanley, J. A. & Mcneil, B. J. (1982) 'The meaning and use of the area under a receiver operating characteristic (ROC) curve', *Radiology*, 143 (1), pp. 29-36.
- Harangi, B., Lazar, I. & Hajdu, A. (2012) 'Automatic exudate detection using active contour model and regionwise classification'. Engineering in Medicine and Biology Society (EMBC), 2012 Annual International Conference of the IEEE, 2012. IEEE, 5951-5954.
- Hayashi, K., Hirata, A., Yoshida, M., Yoshimura, K. & Hayashi, H. (2012) 'Long-term effect of surface light scattering and glistenings of intraocular lenses on visual function', *American Journal of Ophthalmology*, 154 (2), pp. 240-251.
- Hecht, E. (2002). *Optics*, San Francisco; London, Addison-Wesley.
- Hennelly, M., Barbur, J., Edgar, D. & Woodward, E. (1997) 'Factors affecting the integrated straylight parameter in the normal human eye'. *Investigative*

Ophthalmology & Visual Science, 1997. LIPPINCOTT-RAVEN PUBL 227
EAST WASHINGTON SQ, PHILADELPHIA, PA 19106, 4721-4721.

Hennelly, M. L., Barbur, J. L., Edgar, D. F. & Woodward, E. G. (1998) 'The effect of age on the light scattering characteristics of the eye', *Ophthalmic and Physiological Optics*, 18 (2), pp. 197-203.

Holladay, L. (1927) 'Action of a light-source in the field of view in lowering visibility', *JOSA*, 14 (1), pp. 1-1.

Hosmer Jr, D. W. & Lemeshow, S. (2004). *Applied logistic regression*, John Wiley & Sons.

Hull, C. C., Cleary, G., Zhang, J. J., Spalton, D. J. & Marshall, J. (2009) 'Forward Light Scatter Measurements in an in vitro Model of Posterior Capsule Opacification', *Invest. Ophthalmol. Vis. Sci.*, 50 (5), pp. 6128-.

Ijspeert, J., De Waard, P., Van Den Berg, T. & De Jong, P. (1990) 'The intraocular straylight function in 129 healthy volunteers; dependence on angle, age and pigmentation', *Vision research*, 30 (5), pp. 699-707.

Ijspeert, J. K., Van Den Berg, T. J. T. P. & Spekreijse, H. (1993) 'An improved mathematical description of the foveal visual point spread function with parameters for age, pupil size and pigmentation', *Vision Research*, 33 (1), pp. 15-20.

Jahns, J. & Lohmann, A. W. (1979) 'The Lau effect (a diffraction experiment with incoherent illumination)', *Optics Communications*, 28 (3), pp. 263-267.

Japunya, T., Jitpakdee, P., Uyyanonvara, B., Aimmanee, P., Philippaki, E., Hull, C. & Barman, S. (2014) 'Software for the Quantification of Glistenings in Intra-Ocular Lenses'. Proceedings of the World Congress on Engineering, 2014.

Jin, Y. & Dunbrack, R. L. (2005) 'Assessment of disorder predictions in CASP6', *Proteins: Structure, Function, and Bioinformatics*, 61 (S7), pp. 167-175.

Kasper, T., Bühren, J. & Kohnen, T. (2006) 'Visual performance of aspherical and spherical intraocular lenses: intraindividual comparison of visual acuity, contrast

sensitivity, and higher-order aberrations', *Journal of Cataract & Refractive Surgery*, 32 (12), pp. 2022-2029.

Kato, K., Nishida, M., Yamane, H., Nakamae, K., Tagami, Y. & Tetsumoto, K. (2001) 'Glistening formation in an AcrySof lens initiated by spinodal decomposition of the polymer network by temperature change', *Journal of cataract and refractive surgery*, 27 (9), pp. 1493-1498.

Kawai, K. (2012) 'Comparative Study on Changes in Turbidity and Resolution of Colored Acrylic Intraocular Lenses in an Accelerated Aging Test under Severe Conditions.'. ARVO, 2012 Fort Lauderdale, Fla. USA. poster 3062.

Kawamorita, T. & Uozato, H. (2005) 'Modulation transfer function and pupil size in multifocal and monofocal intraocular lenses in vitro', *Journal of Cataract & Refractive Surgery*, 31 (12), pp. 2379-2385.

Khan, M. F., Saqib, M., Siddiqui, A. M. & Iqbal, N. (2011) 'Removal of blobs from retinal videos using intra-video registration'. Biomedical Engineering and Informatics (BMEI), 2011 4th International Conference on, 2011. IEEE, 462-466.

Kim, D.-H., James, R. H., Landry, R. J., Calogero, D., Anderson, J. & Ilev, I. K. (2011) 'Quantification of glistenings in intraocular lenses using a ballistic-photon removing integrating-sphere method', *Applied optics*, 50 (35), pp. 6461-6467.

Klein, R., Wang, Q., Klein, B., Moss, S. E. & Meuer, S. M. (1995) 'The relationship of age-related maculopathy, cataract, and glaucoma to visual acuity', *Investigative ophthalmology & visual science*, 36 (1), pp. 182-191.

Klos, K., Richter, R., Schnaudigel, O.-E. & Ohrloff, C. (1999) 'Image analysis of implanted rigid and foldable intraocular lenses in human eyes using Scheimpflug photography', *Ophthalmic research*, 31 (2), pp. 130-133.

Koch, D. D. (1989) 'Glare and contrast sensitivity testing in cataract patients', *Journal of Cataract & Refractive Surgery*, 15 (2), pp. 158-164.

- Kohnen, T., Dick, B. & Jacobi, K. W. (1995) 'Comparison of the induced astigmatism after temporal clear corneal tunnel incisions of different sizes', *Journal of Cataract & Refractive Surgery*, 21 (4), pp. 417-424.
- Kokhanovsky, A. A. (2008). *Light Scattering Reviews 3: Light Scattering and Reflection*, Springer.
- Kuroda, T., Fujikado, T., Maeda, N., Oshika, T., Hirohara, Y. & Mihashi, T. (2002) 'Wavefront analysis in eyes with nuclear or cortical cataract', *American journal of ophthalmology*, 134 (1), pp. 1-9.
- Lalkhen, A. G. & Mccluskey, A. (2008) 'Clinical tests: sensitivity and specificity', *Continuing Education in Anaesthesia, Critical Care & Pain*, 8 (6), pp. 221-223.
- Laven, P. (2003) 'Simulation of rainbows, coronas, and glories by use of Mie theory', *Applied Optics*, 42 (3), pp. 436-444.
- Laven, P. (2006) 'MiePlot: a computer program for scattering of light from a sphere using Mie theory & the Debye series', *PhilipLaven.com*, 10.
- Le Grand, Y. (1937) 'Recherches sur la diffusion de la lumière dans l'oeil humain', *Rev. opt*, 16, pp. 240-266.
- Leaming, D. V. (2004) 'Practice styles and preferences of ASCRS members—2003 survey', *Journal of Cataract & Refractive Surgery*, 30 (4), pp. 892-900.
- Lee, K., Yoon, M. H., Seo, K. Y., Kim, E. K. & Kim, T.-I. (2013) 'Comparisons of Clinical Results after Implantation of Three Aspheric Intraocular Lenses', *Journal of the Korean Ophthalmological Society*, 54 (8), pp. 1213-1218.
- Leydolt, C., Schriebl, S., Stifter, E., Haszcz, A. & Menapace, R. (2013) 'Posterior Capsule Opacification with the iMics1 NY-60 and AcrySof SN60WF 1-Piece Hydrophobic Acrylic Intraocular Lenses: 3-Year Results of a Randomized Trial', *American Journal of Ophthalmology*, 156 (2), pp. 375-381.e2.
- Liang, J. & Williams, D. R. (1997) 'Aberrations and retinal image quality of the normal human eye', *JOSA A*, 14 (11), pp. 2873-2883.

- Ma, Z., Merkus, H. G., De Smet, J. G., Heffels, C. & Scarlett, B. (2000) 'New developments in particle characterization by laser diffraction: size and shape', *Powder Technology*, 111 (1), pp. 66-78.
- Mackool, R. J. & Colin, J. (2009) 'Limitations of Scheimpflug photography in quantifying glistenings', *Journal of Cataract & Refractive Surgery*, 35 (8), pp. 1480-1481.
- Mainster, M. A. & Turner, P. L. (2010) 'Blue-blocking IOLs decrease photoreception without providing significant photoprotection', *Survey of ophthalmology*, 55 (3), pp. 272-283.
- Mamalis, N. (2012) 'Intraocular lens glistenings', *Journal of Cataract & Refractive Surgery*, 38 (7), pp. 1119-1120.
- Matsui, E. (2006) 'Generation of glistening particles in the intraocular lens', *JAPANESE JOURNAL OF CLINICAL OPHTHALMOLOGY*, 60 (2), pp. 201.
- Mclaren, J. W., Trocme, S. D., Relf, S. & Brubaker, R. F. (1990) 'Rate of flow of aqueous humor determined from measurements of aqueous flare', *Investigative ophthalmology & visual science*, 31 (2), pp. 339-346.
- Mclellan, J. S., Marcos, S. & Burns, S. A. (2001) 'Age-related changes in monochromatic wave aberrations of the human eye', *Investigative ophthalmology & visual science*, 42 (6), pp. 1390-1395.
- Michael, R., Barraquer, R. I., Rodríguez, J., Tuñi I Picado, J., Jubal, J. S., González Luque, J. C. & Van Den Berg, T. (2010) 'Intraocular straylight screening in medical testing centres for driver licence holders in Spain', *Journal of optometry*, 3 (2), pp. 107-114.
- Mie, G. (1908) 'Beiträge zur Optik trüber Medien, speziell kolloidaler Metallösungen', *Annalen der Physik*, 330 (3), pp. 377-445.
- Mihashi, T., Hirohara, Y., Bessho, K., Maeda, N., Oshika, T. & Fujikado, T. (2006) 'Intensity analysis of Hartmann-Shack images in cataractous, keratoconic, and

- normal eyes to investigate light scattering', *Japanese journal of ophthalmology*, 50 (4), pp. 323-333.
- Minami, K., Maruyama, Y., Honbo, M., Matsunaga, J. & Miyata, K. (2014) 'In vitro examination of surface light scattering in hydrophobic acrylic intraocular lenses', *Journal of Cataract & Refractive Surgery*, 40 (4), pp. 652-656.
- Miura, M., Osako, M., Elsner, A. E., Kajizuka, H., Yamada, K. & Usui, M. (2004) 'Birefringence of intraocular lenses', *Journal of Cataract & Refractive Surgery*, 30 (7), pp. 1549-1555.
- Miyata, A. (2007) 'Water accumulation in polymers', *IOL&RS*, 21, pp. 59-62.
- Miyata, A. 2014. Glistenings and Their Influence on Visual Function. *Cataract Surgery: Maximizing Outcomes Through Research*. Springer.
- Miyata, A., Uchida, N., Nakajima, K. & Yaguchi, S. (2001) 'Clinical and experimental observation of glistening in acrylic intraocular lenses', *Japanese journal of ophthalmology*, 45 (6), pp. 564-569.
- Miyata, K., Honbo, M., Otani, S., Nejima, R. & Minami, K. (2012) 'Effect on visual acuity of increased surface light scattering in intraocular lenses', *Journal of Cataract & Refractive Surgery*, 38 (2), pp. 221-226.
- Mönestam, E., Behndig, A., Medicinska, F., Oftalmiatrik, Institutionen För Klinisk, V. & Umeå, U. (2011) 'Impact on visual function from light scattering and glistenings in intraocular lenses, a long-term study', *Acta Ophthalmologica*, 89 (8), pp. 724-728.
- Moreno-Barriuso, E. & Navarro, R. (2000) 'Laser ray tracing versus Hartmann–Shack sensor for measuring optical aberrations in the human eye', *JOSA A*, 17 (6), pp. 974-985.
- Moreno-Montañés, J., Alvarez, A., Rodríguez-Conde, R. & Fernández-Hortelano, A. (2003) 'Clinical factors related to the frequency and intensity of glistenings in AcrySof intraocular lenses', *Journal of cataract and refractive surgery*, 29 (10), pp. 1980-1984.

- Nanavaty, M. A., Spalton, D. J. & Boyce, J. F. (2011) 'Influence of different acrylic intraocular lens materials on optical quality of vision in pseudophakic eyes', *Journal of Cataract & Refractive Surgery*, 37 (7), pp. 1230-1238.
- Navarro, R., Ferro, M., Artal, P. & Miranda, I. (1993) 'Modulation transfer functions of eyes implanted with intraocular lenses', *Applied Optics*, 32 (31), pp. 6359-6367.
- Nishi, Y., Rabsilber, T. M., Limberger, I.-J., Reuland, A. J. & Auffarth, G. U. (2007) 'Influence of 360-degree enhanced optic edge design of a hydrophilic acrylic intraocular lens on posterior capsule opacification', *Journal of Cataract & Refractive Surgery*, 33 (2), pp. 227-231.
- Nishihara, H., Kageyama, T., Ohnishi, T., Koike, M., Imai, M., Shibuya, A. & Yaguchi, S. (2000) 'Glistenings in lathe-cut acrylic intraocular lens', *Ganka Shujutsu*, 13, pp. 227-230.
- Nishihara, H., Yaguchi, S., Onishi, T., Chida, M. & Ayaki, M. (2003) 'Surface scattering in implanted hydrophobic intraocular lenses', *Journal of Cataract & Refractive Surgery*, 29 (7), pp. 1385-1388.
- Nolan, J. M., O'reilly, P., Loughman, J., Stack, J., Loane, E., Connolly, E. & Beatty, S. (2009) 'Augmentation of macular pigment following implantation of blue light-filtering intraocular lenses at the time of cataract surgery', *Investigative ophthalmology & visual science*, 50 (10), pp. 4777-4785.
- Ogura, Y., Ong, M. D., Akinay, A., Carson, D. R., Pei, R. & Karakelle, M. (2014) 'Optical performance of hydrophobic acrylic intraocular lenses with surface light scattering', *Journal of Cataract & Refractive Surgery*, 40 (1), pp. 104-113.
- Ollerton, A., Werner, L., Fuller, S. R., Kavoussi, S. C., McIntyre, J. S. & Mamalis, N. (2012) 'Evaluation of a new single-piece 4% water content hydrophobic acrylic intraocular lens in the rabbit model', *Journal of Cataract & Refractive Surgery*, 38 (10), pp. 1827-1832.

- Omar, O., Pirayesh, A., Mamalis, N. & Olson, R. J. (1998) 'In vitro analysis of AcrySof intraocular lens glistenings in AcryPak and Wagon Wheel packaging', *Journal of Cataract & Refractive Surgery*, 24 (1), pp. 107-113.
- Ong, M. D., Callaghan, T. A., Pei, R. & Karakelle, M. (2012) 'Etiology of surface light scattering on hydrophobic acrylic intraocular lenses', *Journal of Cataract & Refractive Surgery*, 38 (10), pp. 1833-1844.
- Oshika, T., Shiokawa, Y., Amano, S. & Mitomo, K. (2001) 'Influence of glistenings on the optical quality of acrylic foldable intraocular lens', *British journal of ophthalmology*, 85 (9), pp. 1034-1037.
- Packer, M., Fry, L., Lavery, K. T., Lehmann, R., McDonald, J., Nichamin, L., Bearie, B., Hayashida, J., Altmann, G. E. & Khodai, O. (2013) 'safety and effectiveness of a glistening-free single-piece hydrophobic acrylic intraocular lens (enVista)', *Clinical ophthalmology (Auckland, NZ)*, 7, pp. 1905.
- Packer, M., Rajan, M., Ligabue, E. & Heiner, P. (2014) 'Clinical properties of a novel, glistening-free, single-piece, hydrophobic acrylic IOL', *Clinical ophthalmology (Auckland, NZ)*, 8, pp. 421.
- Pagnouille, C., Bozukova, D., Gobin, L., Bertrand, V. & Gillet-De Pauw, M.-C. (2012) 'Assessment of new-generation glistening-free hydrophobic acrylic intraocular lens material', *Journal of Cataract & Refractive Surgery*, 38 (7), pp. 1271-1277.
- Panagopoulou, S. I. & Pallikaris, I. G. (2001) 'Wavefront customized ablations with the WASCA Asclepion workstation', *Journal of Refractive Surgery*, 17 (5), pp. S608-S612.
- Philippaki, E., Plainis, S., Pallikaris, A., Papadiamantis, A. & Pallikaris, I. G. (2009) 'Wavefront map analysis of single vision and progressive ophthalmic lenses', *Acta Ophthalmologica*, 87, pp. 0-0.
- Richter-Mueksch, S., Kahraman, G., Amon, M., Schild-Burggasser, G., Schauersberger, J. & Abela-Formanek, C. (2007) 'Uveal and capsular biocompatibility after implantation of sharp-edged hydrophilic acrylic, hydrophobic acrylic, and silicone

- intraocular lenses in eyes with pseudoexfoliation syndrome', *Journal of cataract and refractive surgery*, 33 (8), pp. 1414-1418.
- Rønbeck, M., Behndig, A., Taube, M., Koivula, A., Kugelberg, M., Medicinska, F., Oftalmiatrik, Institutionen För Klinisk, V. & Umeå, U. (2013) 'Comparison of glistenings in intraocular lenses with three different materials: 12-year follow-up', *Acta Ophthalmologica*, 91 (1), pp. 66-70.
- Rossi, E. A. & Roorda, A. (2010) 'The relationship between visual resolution and cone spacing in the human fovea', *Nat Neurosci*, 13 (2), pp. 156-157.
- Sacu, S., Findl, O., Menapace, R., Buehl, W. & Wirtitsch, M. (2004) 'Comparison of posterior capsule opacification between the 1-piece and 3-piece Acrysof intraocular lenses', *Ophthalmology*, 111 (10), pp. 1840-1846.
- Sakuraba, T. (2006) 'Optical quality measurements of hydrophobic acrylic intraocular lenses', *Journal of refractive surgery (Thorofare, N.J.: 1995)*, 22 (8), pp. 824.
- Saylor, D. M., Coleman Richardson, D., Dair, B. J. & Pollack, S. K. (2010) 'Osmotic cavitation of elastomeric intraocular lenses', *Acta biomaterialia*, 6 (3), pp. 1090-1098.
- Schauersberger, J., Amon, M., Kruger, A., Abela, C., Schild, G. & Kolodjaschna, J. (2001) 'Comparison of the biocompatibility of 2 foldable intraocular lenses with sharp optic edges', *Journal of cataract and refractive surgery*, 27 (10), pp. 1579-1585.
- Schramm, S., Seifert, B.-U., Schikowski, P., Prehl, J., Kunert, K. S., Blum, M., Kaeding, A. & Haueisen, J. (2013) 'A modified Hartmann–Shack aberrometer for measuring stray light in the anterior segment of the human eye', *Graefes Archive for Clinical and Experimental Ophthalmology*, 251 (8), pp. 1967-1977.
- Schweitzer, C., Orignac, I., Praud, D., Chatoux, O. & Colin, J. (2013) 'Glistening in glaucomatous eyes: visual performances and risk factors', *Acta ophthalmologica*.
- Sebag, J. (1987) 'Ageing of the vitreous', *Eye*, 1 (2), pp. 254-262.

- Sher, J. H., Gooi, P., Dubinski, W., Brownstein, S., El-Defrawy, S. & Nash, W. A. (2008) 'Comparison of the incidence of opacification of Hydroview hydrogel intraocular lenses with the ophthalmic viscosurgical device used during surgery', *Journal of cataract and refractive surgery*, 34 (3), pp. 459-464.
- Shiba, T., Mitooka, K. & Tsuneoka, H. (2002) 'In vitro analysis of AcrySof intraocular lens glistening', *European journal of ophthalmology*, 13 (9-10), pp. 759-763.
- Sopharak, A., Uyyanonvara, B. & Barman, S. (2009) 'Automatic exudate detection from non-dilated diabetic retinopathy retinal images using fuzzy c-means clustering', *Sensors*, 9 (3), pp. 2148-2161.
- Spalton, D. J. (1999) 'Harold Ridley's first patient', *Journal of Cataract & Refractive Surgery*, 25 (2), pp. 156.
- Stiles, W. S. (1929) 'The effect of glare on the brightness difference threshold', *Proceedings of the Royal Society of London. Series B, Containing Papers of a Biological Character*, pp. 322-351.
- Stiles, W. S. & Crawford, B. H. (1937) 'The Effect of a Glaring Light Source on Extrafoveal Vision', *Proceedings of the Royal Society B: Biological Sciences*, 122 (827), pp. 255-280.
- Sverker Norrby, N., Grossman, L. W., Geraghty, E. P., Kreiner, C. F., Mihori, M., Patel, A. S., Portney, V. & Silberman, D. M. (1996) 'Accuracy in determining intraocular lens dioptric power assessed by interlaboratory tests', *Journal of Cataract & Refractive Surgery*, 22 (7), pp. 983-993.
- Tetz, M., Werner, L., Schwahn-Bendig, S. & Battle, J. (2009) 'A prospective clinical study to quantify glistenings in a new hydrophobic acrylic IOL'. American Society of Cataract and Refractive Surgery (ASCRS) Symposium & Congress, 2009.
- Thibos, L. N. (2000) 'Principles of hartmann-shack aberrometry'. Vision Science and its Applications, 2000. Optical Society of America, NW6.

- Thibos, L. N., Hong, X., Bradley, A. & Cheng, X. (2002) 'Statistical variation of aberration structure and image quality in a normal population of healthy eyes', *JOSA A*, 19 (12), pp. 2329-2348.
- Thomes, B. E. & Callaghan, T. A. (2013) 'Evaluation of in vitro glistening formation in hydrophobic acrylic intraocular lenses', *Clinical ophthalmology (Auckland, NZ)*, 7, pp. 1529.
- Tognetto, D., Toto, L., Sanguinetti, G. & Ravalico, G. (2002) 'Glistenings in foldable intraocular lenses', *Journal of cataract and refractive surgery*, 28 (7), pp. 1211-1216.
- Van De Hulst, H. C. (1957). *Light scattering by small particles*, New York, Dover Publications.
- Van Den Berg, T., Ijspeert, J. & De Waard, P. (1991) 'Dependence of intraocular straylight on pigmentation and light transmission through the ocular wall', *Vision research*, 31 (7), pp. 1361-1367.
- Van Den Berg, T. J. (1995) 'Analysis of intraocular straylight, especially in relation to age', *Optometry and vision science : official publication of the American Academy of Optometry*, 72 (2), pp. 52-59.
- Van Den Berg, T. J., Franssen, L. & Coppens, J. E. (2009) 'Straylight in the human eye: testing objectivity and optical character of the psychophysical measurement', *Ophthalmic and Physiological Optics*, 29 (3), pp. 345-350.
- Van Den Berg, T. J., Franssen, L., Kruijt, B. & Coppens, J. E. (2013) 'History of ocular straylight measurement: a review', *Zeitschrift für Medizinische Physik*, 23 (1), pp. 6-20.
- Van Den Berg, T. J. & Ijspeert, J. K. (1992) 'Clinical assessment of intraocular stray light', *Applied Optics*, 31 (19), pp. 3694-3696.
- Van Den Berg, T. J. T. P. & Ijspeert, J. K. (1995) 'Light scattering in donor lenses', *Vision research*, 35 (1), pp. 169-177.
- Van Der Mooren, M., Coppens, J., Bandhauer, M. & Van Den Berg, T. (2007) 'Light scatter characteristics of acrylic intraocular lenses', *Invest. Ophthalmol. Vis. Sci*, 48.

- Van Der Mooren, M., Franssen, L. & Piers, P. (2013) 'Effects of glistenings in intraocular lenses', *Biomedical optics express*, 4 (8), pp. 1294-1304.
- Van Der Mooren, M., Van Den Berg, T., Coppens, J. & Piers, P. (2011) 'Combining in vitro test methods for measuring light scatter in intraocular lenses', *Biomedical optics express*, 2 (3), pp. 505-510.
- Vos, J. & Bouman, M. (1959) 'Disability glare: theory and practice', *CIE Publication*, (5), pp. 298-307.
- Vos, J. & Van Den Berg, T. (1999) 'Report on disability glare', *CIE collection*, 135 (1), pp. 1-9.
- Vos, J. J. (1963) 'On mechanisms of glare'.
- Vos, J. J. (1984) 'Disability glare-a state of the art report', *CIE Journal*, 3 (2), pp. 39-53.
- Waite, A., Faulkner, N. & Olson, R. J. (2007) 'Glistenings in the single-piece, hydrophobic, acrylic intraocular lenses', *Am J Ophthalmol*, 144 (1), pp. 143-144.
- Wallin, T. R., Hinckley, M., Nilson, C. & Olson, R. J. (2003) 'A clinical comparison of single-piece and three-piece truncated hydrophobic acrylic intraocular lenses', *American journal of ophthalmology*, 136 (4), pp. 614-619.
- Walraven, J. (1973) 'Spatial characteristics of chromatic induction; the segregation of lateral effects from straylight artefacts', *Vision research*, 13 (9), pp. 1739-1753.
- Wang, L. & Ju, H. (2008) 'A robust blob detection and delineation method'. Education Technology and Training, 2008. and 2008 International Workshop on Geoscience and Remote Sensing. ETT and GRS 2008. International Workshop on, 2008. IEEE, 827-830.
- Werner, L. (2010) 'Glistenings and surface light scattering in intraocular lenses', *Journal of Cataract & Refractive Surgery*, 36 (8), pp. 1398-1420.

- Werner, L., Storsberg, J., Mauger, O., Brasse, K., Gerl, R., Müller, M. & Tetz, M. (2008) 'Unusual pattern of glistening formation on a 3-piece hydrophobic acrylic intraocular lens', *Journal of Cataract & Refractive Surgery*, 34 (9), pp. 1604-1609.
- Whitaker, D., Steen, R. & Elliott, D. B. (1993) 'Light scatter in the normal young, elderly, and cataractous eye demonstrates little wavelength dependency', *Optometry & Vision Science*, 70 (11), pp. 963-968.
- Wilkins, E. & Olson, R. J. (2001) 'Glistenings with long-term follow-up of the Surgidev B20/20 polymethylmethacrylate intraocular lens', *American journal of ophthalmology*, 132 (5), pp. 783-785.
- Williams, D., Yoon, G.-Y., Porter, J., Guirao, A., Hofer, H. & Cox, I. (2000) 'Visual benefit of correcting higher order aberrations of the eye', *Journal of Refractive Surgery*, 16 (5), pp. S554-S559.
- Winn, B., Whitaker, D., Elliott, D. B. & Phillips, N. J. (1994) 'Factors affecting light-adapted pupil size in normal human subjects', *Investigative Ophthalmology & Visual Science*, 35 (3), pp. 1132-1137.
- Wong, H. B. & Lim, G. H. (2011) 'Measures of diagnostic accuracy: sensitivity, specificity, PPV and NPV', *Proceedings of Singapore Healthcare Volume*, 20 (4).
- Wriedt, T. (1998) 'A review of elastic light scattering theories', *Particle & particle systems characterization*, 15 (2), pp. 67-74.
- Xu, M., Lax, M. & Alfano, R. (2003) 'Anomalous diffraction of light with geometrical path statistics of rays and a Gaussian ray approximation', *Optics letters*, 28 (3), pp. 179-181.
- Yaguchi, S., Nishihara, H., Kambhiranond, W., Stanley, D. & Apple, D. (2007) 'Light scatter on the surface of AcrySof intraocular lenses: part II. Analysis of lenses following hydrolytic stability testing', *Ophthalmic surgery, lasers & imaging: the official journal of the International Society for Imaging in the Eye*, 39 (3), pp. 214-216.

- Yaguchi, S., Nishihara, H., Kambhiraonond, W., Stanley, D. & Apple, D. J. (2008) 'Light scatter on the surface of AcrySof intraocular lenses: part I. Analysis of lenses retrieved from pseudophakic postmortem human eyes', *Ophthalmic surgery, lasers & imaging: the official journal of the International Society for Imaging in the Eye*, 39 (3), pp. 209.
- Yellott, J. I. (1983) 'Spectral Consequences of Photoreceptor Sampling in the Rhesus Retina', *Science*, 221 (4608), pp. 382-385.
- Yoshida, S., Matsushima, H., Nagata, M., Senoo, T., Ota, I. & Miyake, K. (2011) 'Decreased visual function due to high-level light scattering in a hydrophobic acrylic intraocular lens', *Japanese Journal of Ophthalmology*, 55 (1), pp. 62-66.
- Youssef, D., Solouma, N., El-Dib, A., Mabrouk, M. & Youssef, A.-B. (2010) 'New feature-based detection of blood vessels and exudates in color fundus images'. *Image Processing Theory Tools and Applications (IPTA), 2010 2nd International Conference on*, 2010. IEEE, 294-299.
- Zhou, C., Lui, S., Yan, T. & Tao, W. 2014. Noise Removal Using Fourth Order PDEs Based on Nonlocal Derivative. *Intelligent Computing Theory*. Springer.
- Zhou, X.-H., Obuchowski, N. A. & Mcclish, D. K. (2011). *Statistical methods in diagnostic medicine*, John Wiley & Sons.
- Zweig, M. H. & Campbell, G. (1993) 'Receiver-operating characteristic (ROC) plots: a fundamental evaluation tool in clinical medicine', *Clinical chemistry*, 39 (4), pp. 561-577.

